Hyperspectral Coherent Anti-Stokes Raman Scattering Microscopy

Kavanagh, Thomas Christopher

Awarding institution:
King's College London

Hyperspectral Coherent Anti-Stokes Raman Scattering Microscopy

By Thomas Kavanagh

Department of Physics, King's College London

A thesis submitted to King's College London as partial fulfilment of the requirements for the degree of Doctor of Philosophy

2016

Acknowledgements

I would like to take this opportunity to express my deepest gratitude to everybody who supported me during my Ph.D. studies.

Throughout the last 9 years (including my undergraduate studies) the King's College London physics department has been like a home away from home, possessing a uniquely warm familial atmosphere, in which I have always felt included and valued.

First and foremost, I would like to thank Professor David Richards, who is not only my first supervisor but was also my undergraduate personal tutor, for his patience, wisdom and trust over these many years. His support and seemingly inexhaustible supply of technical insight have been invaluable. I can honestly say that our weekly meetings, although occasionally confusing, have always left me feeling inspired and invigorated for the challenges to come. It has been my sincerest pleasure to complete my Ph.D. with David as my mentor.

I am also exceptionally grateful to Dr. Bradley Littleton, with whom I worked in the lab on a daily basis: always patient, always willing to impart practical skills and a good friend. His genuine enthusiasm for the subject and conscientious but relaxed demeanour has been, and will continue to be, a great inspiration.

I would like extend my gratitude to my second supervisor, Dr. Frederic Festy, for use of his facilities and expertise regarding Raman cluster analysis.

I thank all my friends, but in particular Alix and Basma for the many interesting conversations, scientific, and otherwise, shared over coffee.

I would like to say how deeply appreciative I am of my girlfriend, Nell, her love, support, and calming influence have kept me going, especially whilst writing this thesis.

Last but not least, I wish to thank my mum and dad, without their unconditional love, support and understanding throughout, this would not have been possible.

Table of Contents

Abstract

Possessing high three dimensional optical sectioning capabilities and deriving chemical contrast from the intrinsic molecular vibrations of the sample, coherent anti-Stokes Raman scattering (CARS) microscopy has the ability to deliver high sensitivity non-invasive biological imaging. It is, however, accompanied by a deleterious non-resonant background (NRB) which acts to reduce the contrast and severely complicate analysis. Computational approaches are currently favoured for removing this NRB; however, these result in significant spectrally varying errors. This thesis concerns the development and subsequent implementation of a CARS platform employing a novel, all-optical, non-resonant background removal mechanism: Spectral Interferometric Polarisation Coherent Anti-Stokes Raman Scattering (SIPCARS). Exploiting the phase change that accompanies a Raman resonance and employing an elliptical pump/probe beam and linear Stokes beam, SIPCARS allows the complete removal of the NRB. The resulting SIPCARS spectra encode mode symmetry information into the amplitude response which can be directly related to polarisation resolved spontaneous Raman scattering spectra.

Verification of the SIPCARS methodology was achieved using spectra acquired from pure liquid samples which were in complete agreement with the corresponding polarisation resolved spontaneous Raman scattering spectra. The multiplexing limit of the system was assessed using several multi-component polymer bead mixtures and a lower limit of four determined. High signal-to-noise ratio SIPCARS imaging of a HeLa cell in the vibrational fingerprint region was acquired, from which it was possible to identify lipid droplets and subsequently, by producing ratio images, assess their degree of lipid unsaturation and the level of oxidised lipid content. The effect of a naturally derived phytotherapeutic lipid metabolism altering drug on the lipid droplets, contained within wild type N2 *Caenorhabditis elegans* nematodes, was addressed using SIPCARS. Assessing lipid unsaturation and area fraction, the drug was shown to produce a marked effect: a significant reduction in storage of saturated fatty acids post exposure. Additionally the ability of SIPCARS to differentiate between a variety of different *C. elegans* mutants was also demonstrated.

SIPCARS currently provides perhaps the only viable route to attain truly quantitative NRB-free CARS data; however, expanding on the foundation provided by this thesis, and following further development, it has the potential for profound implications in a wide range of areas including fundamental life sciences research, novel drug characterisation and histopathology.

Table of Figures

List of Abbreviations

KCL	=	King's College London
CRS	=	Coherent Raman scattering
SRS	=	Simulated Raman scattering
CARS	=	Coherent anti-Stokes Raman scattering
SIPCARS	=	Spectral Interferometric Polarised CARS
F-CARS	=	Forward propagating CARS
BCARS	=	Broadband CARS
PCARS	=	Polarisation-sensitive detection CARS
DQSI	=	Dual-quadrature spectral interferometry
NRB	=	Non-resonant background
FPR	=	Fingerprint region
PCF	=	Photonic crystal fibre
EMCCD	=	Electron multiplying charge coupled device
TDKK	=	Time domain Kramers - Kronig
MEM	=	Maximum entropy method
LO	=	Local oscillator
IFD	=	Instantaneous frequency difference
SNR	=	Signal-to-noise ratio
NIST	=	National Institute of Standards and Technology
PCA	=	Principle components analysis
PMMA	=	Poly (methyl methacrylate)
PAN	=	Polyacrylonitrile
LD	=	Lipid droplet

1. Introduction

The non-invasive characterisation of biological molecules within complex heterogeneous systems, by optical microscopy, is a foremost area of interest for the life sciences [1]. In order to achieve this accurately in a three dimensional heterogeneous sample it is imperative to attain a high degree of spatial resolution and chemical sensitivity. One approach to achieving high resolution three dimensional optical sectioning is fluorescence microscopy, in conjunction with either confocal detection [2] or two-photon excitation [3], with chemical specificity derived from labelling with a variety of fluorescent probes [4]. The typically broad emission peaks coupled with the potential toxicity of many fluorescent probes can, however, limit the applicability of this technique within biological samples.

Rather than introduce exogenous probes, it is possible, instead, to utilise the intrinsic molecular vibrations of the chemical species within the sample as a contrast mechanism. Spontaneous Raman scattering [5] spectroscopy facilitates this, allowing direct acquisition of the vibrational spectra of the constituent molecules of the sample. When coupled with confocal detection and performed in the visible or near-infrared region, confocal spontaneous Raman scattering microscopy has high three dimensional optical sectioning capability and, thus, would appear ideally suited for non-invasive characterisation of biological samples. The spontaneous Raman scattering cross section of many biological molecules, however, is exceptionally weak and, thus, necessitates either long detection times or high laser power, subsequently reducing the applicability of spontaneous Raman scattering microscopy for fragile samples and/or observing biological dynamics [6].

In order to circumvent this limitation it is necessary to employ non-linear coherent Raman scattering (CRS) techniques, most notably stimulated Raman scattering (SRS) and coherent anti-Stokes Raman scattering (CARS), the details of which will be discussed at length in subsequent chapters. The signal levels derived from these techniques are typically many orders of magnitude greater than spontaneous Raman scattering allowing significantly reduced acquisition times whilst still retaining comparable levels of chemical sensitivity. CARS and SRS are accompanied by deleterious backgrounds, albeit stemming from different sources. In the case of CARS this corresponds to the non-resonant background (NRB) which is non-linearly mixed with the CARS signal.

There are several objectives of this research; firstly, to build a functional broadband CARS micro-spectroscopy system based on a low cost commercially available supercontinuum system. Secondly, to implement and characterise an all optical NRB removal mechanism. Thirdly, to acquire data from model biological systems such as HeLa cells and *C. elegans* nematodes. Finally,

to apply the system to a novel biological hypothesis, for example the efficacy of a lipid metabolism altering drug within a model organism.

The ultimate motivation for this research programme is to develop a novel low cost CARS imaging system encompassing an all optical NRB removal mechanism which can be commercialised, for use as a novel drug characterisation, histopathology or fundamental life sciences research instrument.

Owing to the largely developmental nature of the work reported within this thesis much of it was performed in close collaboration with Dr. Bradley Littleton. Throughout the developmental phase of this project (chapters 7, 8 and 9) it is an accurate appraisal that the work performed by each person overlapped considerably. As the final chapters of this thesis concern more delimited bodies of work, in order to provide clarity as to who took the lead, a short paragraph will be included at the start of each.

2. Background theory

2.1 Optical processes

Both linear and non-linear optical processes stem from the response of the charged particles within material to the electric field component of incident electromagnetic radiation. Whilst the nuclei are too large to follow the high frequency (in the 10^3 THz range) driving force adiabatically; electrons, however, being sufficiently light, follow the rapid oscillations of the driving field [7]. As a result optical resonances are principally due to the motion of the electron. This displacement of the electrons from their equilibrium position results in an induced electric dipole $\mu(t)$:

$$\mu(t) = -e \cdot r(t) \tag{1}$$

where e the fundamental electron charge and $r(t)$ is the time varying displacement [8]. The result of this is a macroscopic polarisation (P) which is dependent on the number of dipoles per unit volume (N):

$$P(t) = N\,\mu(t) \tag{2}$$

In the limit of weak applied field this can be written as:

$$\mathrm{P(t)} = \varepsilon_0\,\chi^{(1)}\mathrm{E(t)} \tag{3}$$

where ε_0 is the electric permittivity in a vacuum, $\chi^{(n)}$ is the nth order susceptibility and E(t) is the electric field. It is trivial to see that in this weak field limit the induced polarisation has a linear dependence on the electric field. This expression, therefore, characterises all linear optical effects including spontaneous Raman scattering.

If, however, a strong field is applied that consequently gives rise to a significantly larger displacement of the electrons from their equilibrium positions, it is insufficient to consider a simple harmonic binding potential and higher order terms must be incorporated into the expression for induced polarisation:

$$P(t) = \varepsilon_0\left(\chi^{(1)}E(t) + \chi^{(2)}E^2(t) + \chi^{(3)}E^3(t) + \cdots\right) \tag{4}$$

$$P(t) = P^{(1)}(t) + P^{(2)}(t) + P^{(3)}(t) + \cdots \tag{5}$$

where $P^{(n)}$ is the nth order polarisation. All non-linear optical effects are characterised by second and higher order non-linear susceptibilities [7]. All coherent Raman scattering (CRS) effects referred to in this thesis are dependent on the third-order non-linear susceptibility: $\chi^{(3)}$.

2.2 Spontaneous Raman scattering

Spontaneous Raman scattering is dependent on the inelastic scattering of photons by the system either creating or annihilating a molecular vibration ($\hbar\omega_{incident} = \hbar\omega_{scattered} \pm \hbar\omega_{vibration}$) [5]. Photon scattering events correspond to the absorption of an incident photon by the system, and thus subsequent excitation and relaxation of an electron from an initial state to a final state via a virtual state and consequently the re-emission of a photon. The majority of photons interacting with a material undergo Rayleigh scattering (i.e. initial and final states are equivalent) being absorbed and re-emitted with the same frequency (elastically) [5]. Spontaneous Raman scattering, however, occurs when the initial and final state are not equivalent, and thus the photon is re-emitted with a different frequency (inelastically). Stokes Raman scattering occurs when a photon is re-emitted with a lower frequency, with the energy discrepancy due to the creation of a molecular vibration within the system. Anti-Stokes Raman scattering equates to the photon being re-emitted with a higher frequency, the energy discrepancy due to the annihilation of a molecular vibration within the system [5] (see figure 2.1).

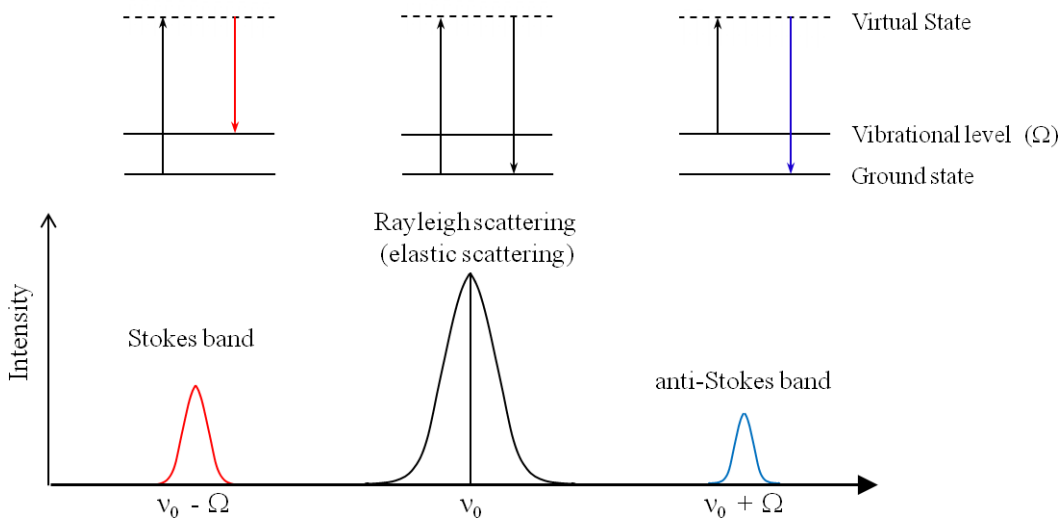

Figure 2.1 Diagram illustrating three major types of scattering that occur within a material [18].

Using the common framework for describing linear and non-linear optical effects outlined in the previous section a brief derivation of the pertinent aspects of polarisation resolved spontaneous Raman scattering are given below [5] [7] [8].

Before deriving the frequencies of the Stokes and anti-Stokes Raman scattering components it is important firstly to introduce the concept of polarisability [5] [8]. Whilst, as previously stated, optical resonances are predominantly mediated by the motion of the electrons within a material, the motion of the nuclei alters the polarisability (the extent to which the electron cloud of a molecular bond may be distorted from its equilibrium shape by an incident electric field and thus form an instantaneous dipole). Considering this, under the assumption that the driving frequency

is significantly displaced from electronic resonances (where interactions with real electronic states cannot be neglected and severely complicate any derivation [10]), it is possible to re-write the induced electric dipole as:

$$\mu(t) = \alpha_{ij}(t)\, E(t) \tag{6}$$

Here the second rank polarisability tensor, $\alpha_{ij}(t)$ (where indices i and j denote the specific tensor elements), describes the combined motion of the electrons and nuclei at any given time characterising the overall polarisability of the molecular bond. The details of this tensor are given in appendix I.

It is now possible to proceed with a classical derivation of the Stokes and anti-Stokes Raman scattering frequencies by considering a Taylor expansion of the polarisability tensor about the equilibrium nuclear position:

$$\alpha_{ij}(t) = \alpha_{ij}(0) + \left(\partial\alpha_{ij}/\partial q\right)_0 q(t) + \ldots \tag{7}$$

The nuclear motion, $q(t)$, may be assumed to be that of a classical harmonic oscillator and thus can be re-written as:

$$q(t) = q_0 \cos(\Omega t) \tag{8}$$

Additionally, if the incident field is assumed to be a plane wave, $E(t) = E_0 \cos(\omega t)$, the induced electric dipole has the following form:

$$\mu(t) = \alpha_{ij}(0)\, E(t) + \left(\partial\alpha_{ij}/\partial q\right)_0 q(t)\, E(t) \tag{9}$$

$$= \alpha_{ij}(0)\, E_0 \cos(\omega t) + \frac{1}{2}\left(\partial\alpha_{ij}/\partial q\right)_0 q_0\, E_0\, [\cos(\omega + \Omega)t + \cos(\omega - \Omega)t] \tag{10}$$

The first term of this expression corresponds to elastic Rayleigh scattering, oscillating at the incident frequency, whilst the final term describes spontaneous Raman scattering with a Stokes and anti-Stokes frequency of $(\omega - \Omega)$ and $(\omega + \Omega)$ respectively.

This equation also provides the selection rule for Raman active modes [11]:

$$\left(\partial\alpha_{ij}/\partial q\right)_0 \neq 0 \tag{11}$$

In essence this expression means that a polarisability of a molecular bond can be neither at its maximum nor minimum value at the nuclear equilibrium position for spontaneous Raman scattering to occur.

To derive the Raman scattering intensity it is necessary to employ a full quantum field description; however, this is beyond the scope of this thesis. Classically the intensity of the Stokes scattered light is given by [7]:

$$I(\omega_s) = N \; {\omega_s^4}/{12\pi\varepsilon_0 c^3} \; q_0^2 \left({\partial\alpha_{ij}}/{\partial q}\right)^2 I_0 = N\,\sigma(\omega_s)\; I_0 \tag{12}$$

where σ is the Raman scattering cross section.

Although this equation is only an approximation it correctly predicts several important features of spontaneous Raman scattering: the fourth order dependence on frequency and the linear dependence on both number of molecular bonds in focal volume and incident intensity. Additionally, while not explicitly included in this derivation, it is worthwhile noting that the dependency of each scattering event (i.e. the scattered light from each individual molecular bond) on nuclear motion, which, at equilibrium, is uncorrelated, gives rise to the inherently incoherent nature of spontaneous Raman scattering.

The full quantum field description of spontaneous Raman scattering yields a scattered intensity which is directly proportional to the imaginary component of the complex resonant third order susceptibility (see section 2.3.1): $Im\left\{\chi^{R(3)}\right\}$ [12]. An intuitive explanation for this has been ventured in appendix II. In addition, while the classical approach correctly predicted a fourth order dependence on frequency (albeit only partially correct) the full quantum field description is required to reveal that this, in actuality, corresponds to $\omega_s^3\omega_p$ [12].

Polarisation resolved spontaneous Raman scattering is closely related to conventional spontaneous Raman scattering; however, in addition to the resonant frequency, the symmetry of the molecular bond is also probed. The resulting intensity is, therefore, dependent on both the conventional spontaneous Raman intensity and the depolarisation ratio (ρ). The depolarisation ratio is determined by the relative contribution from diagonal and off diagonal components of the polarisability tensor. The relative magnitudes of these components are, in themselves, determined by the symmetry of the probed molecular mode (further detail is given in appendix I). The depolarisation ratio is limited to values from 0 to 0.75 $(0 \geq \rho \geq 0.75)$ and a given mode is said to be depolarised if $\rho = 0.75$ or polarised for any other value.

Experimentally the depolarisation ratio is equal to [9], [10]:

$$\rho = \frac{I_{\perp}}{I_{\parallel}} \tag{13}$$

where $I_{\perp}$ and $I_{\parallel}$ correspond to the intensities of the perpendicular and parallel (in relation to the excitation polarisation) components of the scattered light respectively.

Spectra obtained using this technique contain additional mode symmetry information that is not easily acquired by other means.

2.3 Coherent anti-Stokes Raman scattering spectroscopy

2.3.1 Fundamental principles

CARS spectroscopy is a non-linear four wave parametric mixing process involving the interaction of three laser fields, pump $E_p(\omega_p)$, Stokes $E_s(\omega_s)$ and probe $E_{pr}(\omega_{pr})$ with a sample to generate a fourth anti-Stokes $E_{as}(\omega_{as})$ field (see figure 2.2a) [8].

The frequency of the anti-Stokes field is then given by [13]:

$$\omega_{as} = (\omega_p - \omega_s) + \omega_{pr} \tag{14}$$

The majority of experiments employ a frequency degenerate pump and probe field (both derived from a single laser) and subsequently the assumption that $E_{pr} = E_p$ will be made for all further derivations except where explicitly stated otherwise.

The anti-Stokes frequency is then given by:

$$\omega_{as} = 2\omega_p - \omega_s \tag{15}$$

The three incident laser fields have the effect of inducing a third order polarisation within the sample, which can be expressed as follows [13] [14]:

$$P^{(3)} = \chi^{(3)} E_p^2 E_s^* = \left(\chi^{R(3)} + \chi^{NR(3)}\right) E_p^2 E_s^* \tag{16}$$

where the indices *R* and *NR* correspond to the resonant and non-resonant components of third order susceptibility respectively.

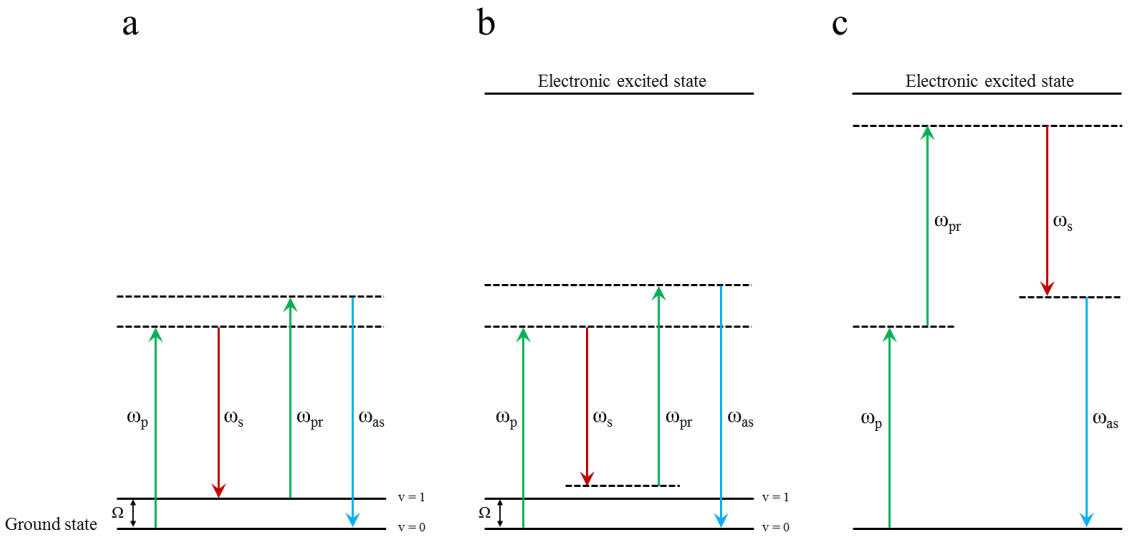

Figure 2.2 Energy level diagram of a) resonant, b) non-resonant and c) two-photon non-resonant CARS [15]. Where the dotted lines denote virtual states and Ω equates to the resonant frequency of a vibrational state.

The complex resonant third order susceptibility $\chi^{R(3)}$ corresponds to the Raman response of the molecules and is enhanced when $(\omega_p - \omega_s)$ corresponds to Ω (see figure 2.1a) [16], which therefore provides the contrast mechanism for CARS spectroscopy. Conversely the non-resonant third order susceptibility $\chi^{NR(3)}$ relates to all other electronic contributions, and may manifest as either a single (see figure 2.1b) or two-photon process (see figure 2.1c) [15]. Assuming the incident laser frequencies are sufficiently displaced from one or two photon electronic transitions, $\chi^{NR(3)}$ is essentially a frequency independent real quantity. It therefore appears as a non-specific background signal, consequently reducing vibrational contrast and spectral resolution [6]. This background is known as the non-resonant background and due to its deleterious effect on CARS spectra many removal techniques have been developed (see section 3.2).

The overall CARS intensity (including non-resonant contributions) is then given by the total incident intensities multiplied by the square modulus of the third order susceptibility [6]:

$$I_{CARS} = \left|\chi^{(3)}\right|^2 I_p^2 I_s \tag{17}$$

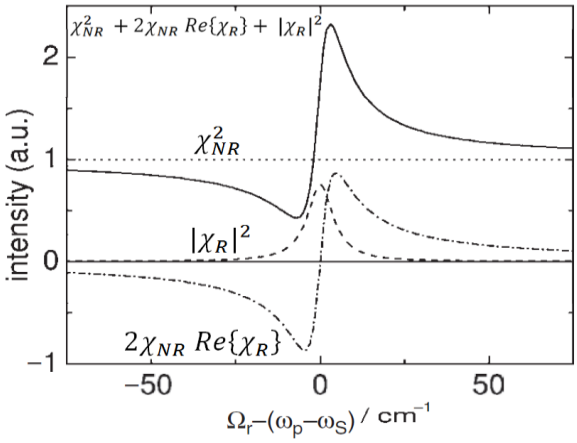

Figure 2.3 Diagram illustrating the spectral form of the terms in equation 18 at an isolated resonance. The resultant characteristic dispersive CARS line shape (————) is also shown. (Reproduced from [16])

Expanding the third order susceptibility gives insight into the characteristic line shape of CARS:

$$I_{CARS} \propto (\chi^{NR})^2 + 2\chi^{NR}\,\mathrm{Re}\{\chi^R\} + |\chi^R|^2 \tag{18}$$

Whilst the purely resonant contribution is symmetric and centred on the resonance, the first term constitutes a ubiquitous constant background and the second term is asymmetric and shifted to a slightly higher vibrational frequency (see figure 2.3). The sum of these components gives rise to the characteristic dispersive shifted line shape of CARS. As previously stated it has been shown that the imaginary component of χ^Rcan be directly related to spontaneous Raman scattering [12] and it is this that NRB removal techniques attempt to retrieve (see section 3.2). Additionally this proportionality also illustrates the desirable nature of the second term, as it is both linear with respect to the χ^R and amplified by χ^{NR} and is subsequently the focus of interferometric NRB removal techniques.

2.3.2 Phase matching criteria

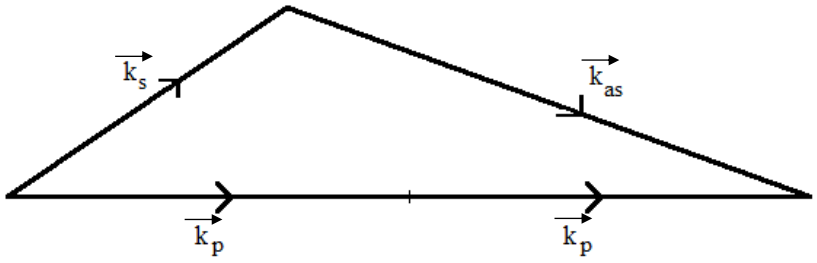

Figure 2.4 Diagram showing the phase matching criteria of CARS spectroscopy [6]. Where k is the wave vector, and the indices p, s and as correspond to pump, Stokes and anti-Stokes respectively.

In order to observe CARS within a system the wave vectors (k) of the incident fields must be matched with the resultant field (see figure 2.4), thus satisfying the following equations [6] [17]:

$$l < l_c \tag{19}$$

$$|k_{as}| = \left|\left(2k_p - k_s\right)\right| \tag{20}$$

where l is the interaction length within the sample, l_c is the coherence length, and k is the wave vector.

The initial condition stipulates that the interaction between the three incident fields and the sample must occur within the coherence length so as to avoid decoherence [6]. The second condition states that in order to achieve appreciable constructive interference on a macro scale the wave vectors of the incident fields must equate to that of the CARS field [8].

2.3.3 Coherent anti-Stokes Raman scattering micro-spectroscopy

CARS spectroscopy was first described by *Maker and Terhune* (1965) [18] and over the years has taken a multiplicity of different configurations, including, but not limited to, different detection geometries (BOXCARS, epi-CARS or C-CARS) and different laser sources (continuous wave, pulsed, narrowband or broadband), a full review of which can be found elsewhere [16].

The popularity of the technique, however, largely dwindled throughout the 1970's, 1980's and early 1990's (one notable exception being Duncan *et al* (1982) [19]) until the invention of a tight focusing geometry by Zumbusch *et al.* in 1999 [20]. The effect of this was to transform CARS, previously low spatially resolution, into a high resolution micro-spectroscopy technique with a probed interaction volume equivalent to comparable multiphoton microscopy techniques. This in turn stimulated an upsurge in work related to CARS as an analytical method for complex biological systems. A renaissance, which to this day, has resulted in several successful groups still active in the field.

Save for a few elaborate techniques designed to gain insight into the fundamental physics underlying non-linear optics and/or the CARS process itself the vast majority of major groups, including King's College London (KCL), now use variants of tight focusing CARS (therefore further discussion will be restricted to this experimental geometry). More specifically, most groups use frequency degenerate tight focused forward propagating CARS micro-spectroscopy as this reduces the experimental complexity whilst also producing the maximum signal-to-noise ratio for majority of biological samples [16] .

Forward propagating CARS (F-CARS) corresponds to directing the two incident laser fields onto the top surface of the sample then proceeding to collect the CARS field from the bottom surface of the sample. This method of detection provides both the strongest CARS signal for samples of comparable or larger size than the excitation wavelength (most biological structures of interest), and also facilitates easy realisation of the phase matching conditions in comparison to backward propagating CARS spectroscopy (epi-CARS) [21].

There are, however, a variety of inherent limitations of F-CARS. Dependent on the intensity of the incident laser fields and the transparency of the sample at the incident wavelengths there is a maximum thickness for which appreciable CARS signal can be attained [22]. F-CARS, as previously stated, provides strong intensity for samples of comparable or larger size than the excitation wavelength, however, in the absence of a NRB removal mechanism, the contrast for smaller samples is significantly limited by the non-resonant contributions of the surrounding medium [21]. A further disadvantage of F-CARS is the requirement of both a pre and post sample objective lens.

In a tight focused F-CARS detection geometry the three incident laser fields are tightly focused within the sample using a high numerical aperture (NA > 1.3) oil immersion lens and the subsequent CARS signal is also collected via a high numerical aperture lens. There are significant advantages to this form of tight focusing geometry. Foremost is that the normal phase matching conditions (previously discussed in section 2.3.2) are relaxed, being automatically satisfied in a collinear system due to the small interaction volume and large cone angle of the two incident fields [6]. A further considerable advantage stems from the use of high numerical aperture lenses for focusing and subsequent collection resulting in small interaction volume, which consequently provides intrinsic three dimensional optical sectioning.

3. CRS micro-spectroscopy techniques

Unlike spontaneous Raman scattering, where an entire spectrum of the sample is automatically acquired, CRS techniques require additional elements to achieve this. In relation to CARS this corresponds to a different excitation profile: broadband CARS (BCARS).

3.1 Broadband CARS

Broadband CARS, an early proponent of which was the Cicerone group [23], corresponds to the use of a broadband, rather than narrowband, Stokes beam as illustrated in figure 3.1. This excitation scheme allows multiple vibration levels to be accessed simultaneously and therefore, when coupled with a dispersive optical element and a CCD, has the potential to allow the entire spectrum of a sample to be attained in a single measurement: analogous to spontaneous Raman scattering. The spectral resolution of a BCARS system is ultimately limited by the spectral width of the narrowband pump/probe beam whilst the spectral coverage is determined by the width of the Stokes beam.

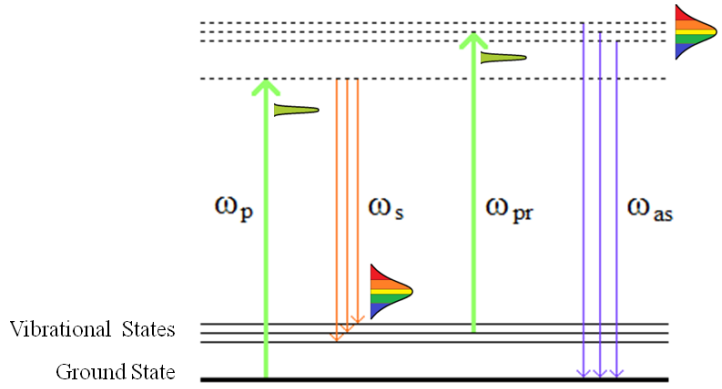

Figure 3.1 Energy level diagram of broadband CARS. Where the dotted lines denote virtual states.

This approach significantly reduces the amount of time and realignment required to attain CARS spectra over a wide variety of vibrational excitations as wavelength scanning is not required to build up spectral information. Additionally BCARS lends itself to hyperspectral imaging (discussed in further detail in a chapter 5) as the multiple narrow spectral features found in the region 500 - 1800 cm^{-1}, of biological spectra, serve as a unique fingerprint: the so-called fingerprint region (FPR). Importantly this allows a significantly higher number of distinct molecular species to be simultaneously detected than with other comparable optical techniques. As BCARS is the non-linear analogue of spontaneous Raman scattering, after removal of the NRB, the wealth of linear multivariate analysis techniques such as principle component analysis [24], that have found extensive use in spontaneous Raman scattering, can be applied.

Generation of a broadband supercontinuum Stokes beam is a necessity for a viable BCARS system. There are two possible routes to attain such a broad beam: transform limited ultra-short pulses or optical fibre. To generate a broadband beam, solely using the spectral characteristics of an ultrafast laser, capable of addressing the whole Raman spectrum of interest (500-3400 cm^{-1}) is an exceptionally complex endeavour requiring precise dispersion compensation and a pulse duration of significantly less that 10 fs at the sample. This has only very recently become technically possible; however, it has yet to be applied to conventional BCARS and would be an enormous experimental challenge. The other, more feasible, method stems from using specialised optical fibres which exhibit extraordinarily high non-linear coefficients due to manipulation of their refractive index.

The most extensively used is photonic crystal fibre (PCF) where the region around the core is structured on a micrometre scale, the so-called 'holey' region [25] [26], which leads to spatial discontinuities of the refractive index and accordingly a high non-linear coefficient (see figure 3.2). PCFs are typically pumped with high intensity femtosecond or picosecond pulses due to the requirement of high peak power to achieve appreciable broadening. The mechanisms by which broadening is achieved depends on the pump wavelength relative to the zero dispersion wavelength: the characteristic wavelength at which the group delay dispersion of the PCF is zero. Additionally the pump pulse duration is also important in determining the specifics of the broadening mechanisms. The detailed mechanisms of the various regimes can be found elsewhere [27]. It should be noted that the principle broadening mechanism that results from two picosecond pumping with wavelength greater than the zero dispersion wavelength (anomalous group velocity dispersion regime) is soliton fission. Whilst PCF offers an attractive solution for supercontinuum generation soliton fission is; however, a stochastic process that inexorably leads to an intrinsically noisy supercontinuum [27].

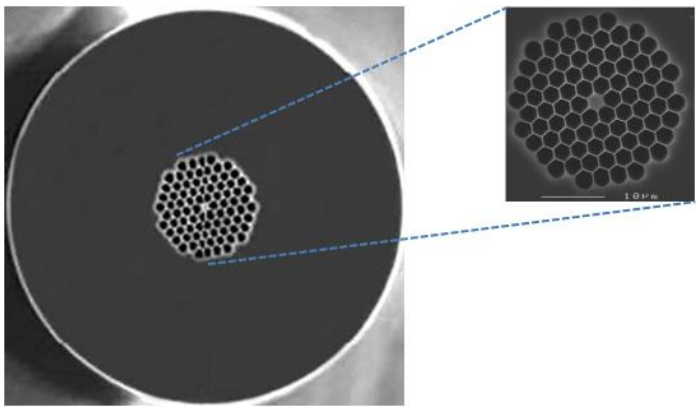

Figure 3.2 Picture of the end of a PCF with an expanded view of the core and 'holey' region. Scale bar: 1µm. (Images taken from [28])

Supercontinuum generation by exploiting the spectral characteristics of a transform limited pulse, or via an optical fibre, both require the use of a high peak power ultra-short pulsed laser (albeit with less rigorous constrains for the optical fibre based approach). There are several different types of laser, or combinations of lasers, capable of producing the narrow and broadband beams required for BCARS and, as such, rather than attempt to describe all possible configurations they will be dealt with on a group by group basis in the following sections.

3.2 Non-resonant background suppression/removal

As expected, given the significant detrimental effect on the quality of CARS spectral information caused by the presence of the NRB (see section 2.3.1), especially in the FPR of biological systems where it may be orders of magnitude greater than the resonant component [29], a variety of NRB removal techniques have been developed. These broadly can be split into three categories: detection of only the resonant components (non-interferometric), interferometric CARS, and phase retrieval/extraction [30]. The most simple are the non-interferometric techniques which, by means of either polarisation sensitive or time resolved detection, reject the first two terms of equation 18 recovering a, typically small, proportion of the third term. More sophisticated interferometric techniques focus on the second term of the aforementioned equation and seek to retrieve the $Im\{\chi^R\}$ by interference with either an externally or internally generated local oscillator (LO) [31]. Finally, the phase retrieval/extraction methods that are comprised of the maximum entropy method (MEM), and the time domain Kramers - Kronig (TDKK) approach or variants thereof.

3.2.1 Analysis by type

Although many of the following techniques are obsolete they merit an individual section as they contributed to the development of CARS, more specifically the removal of the NRB, and therefore any discussion about the present generation of CARS systems would be left wanting without their inclusion. It should be noted that many of these techniques were only ever demonstrated in a single line/spectral scanning configuration and were superseded by BCARS prior to further development.

3.2.1.1 Non - interferometric NRB removal

Time resolved NRB removal techniques rely on the finite decay life time of a Raman resonance in relation to the instantaneous relaxation of the NRB. This type of removal mechanism requires the use of three distinct excitation beams as the initial pump and Stokes beams pair is temporally overlapped whilst the final beam serves to probe the system after a given time delay. In this way the resulting spectrum does not contain any contributions from the NRB [21].

Polarisation sensitive NRB removal techniques (PCARS) rely on adjusting the polarisation of the input fields such that the resultant resonant and non-resonant components of the CARS signal are differentiated in terms of polarisation orientation (see figure 3.3) [16]. By employing orthogonal detection in relation to the non-resonant component of the CARS signal (I_{NR}), using a linear analyser, it is therefore possible to remove this component resulting in NRB free spectrum.

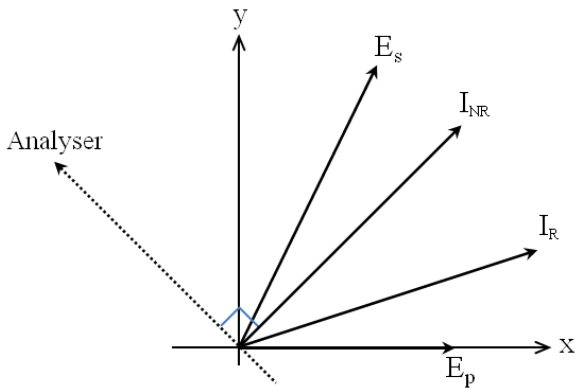

Figure 3.3 Diagram showing the polarization of the incident laser fields and the resultant polarisation of the resonant and non-resonant components of the CARS intensity (I), where the indices R and NR correspond to resonant and non-resonant respectively. The required detection geometry, as indicated by the linear analyser, is also shown.

In principle both of the aforementioned non-interferometric NRB removal techniques can produce NRB free spectra; however they do so at the expense of the resonant signal typically recovering only a small portion of the energy in the third term of equation 18. It has previously been shown that CARS, for biologically relevant excitation powers, can exceed the signal produced by spontaneous Raman scattering only if the second interferometric term is detected [32] [33] and therefore hetero/homodyne amplification achieved. These techniques therefore, whilst technically valid, are of limited value for biological samples.

There were three noteworthy extensions of the PCARS technique IP-CARS [34], HP-CARS [35] and HIP-CARS [36], each of which sought to redress the lack of signal through heterodyne amplification: interfering the CARS signal with a local oscillator. Whilst it is true that each of these techniques includes heterodyne amplification of the PCARS signal they are not true interferometric techniques as the mixing (interferometric term of equation 18) term is rejected along with the NRB. The principle of each of these techniques is fundamentally the same as PCARS, rejecting the NRB by detecting in the orthogonal axis through an analyser, therefore leading to the same drawback. As the initial PCARS signal is typically exceptionally weak, even with significant heterodyne amplification, these techniques do not generate enough total signal for meaningful biological application (beyond single cell measurements of the strongest scattering molecular bonds).

3.2.1.2 Interferometric NRB removal

Interferometric NRB removal techniques attempt to retrieve the $Im\{\chi^R\}$ from the second term of equation 18 by interference with a local oscillator. Whilst this LO may be either produced externally or internally, with respect to the sample, these techniques share a common ancestor: dual-quadrature spectral interferometry (see figure 3.4).

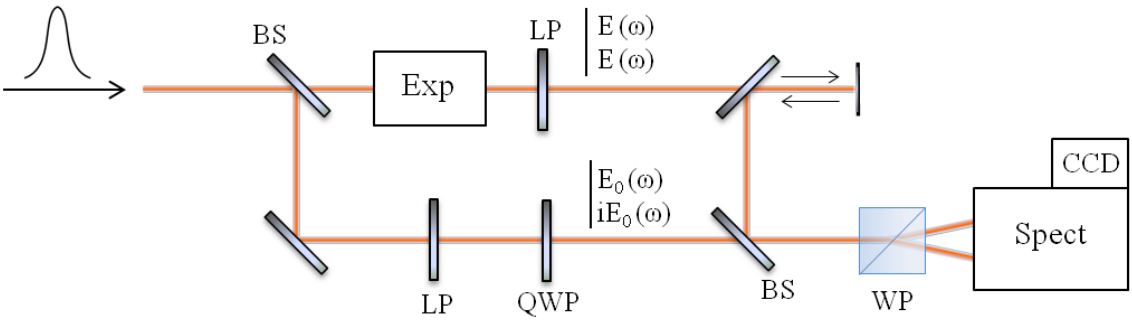

Figure 3.4 Diagram of the components of a dual-quadrature spectral interferometer; where BS equates to beam splitter, EXP to an arbitrary sample/experiment, LP to linear polariser, QWP to quarter waveplate and WP to Wollaston prism. Shown adjacent to each beam are the constituent orthogonal linear polarisation components.

Dual-quadrature spectral interferometry (DQSI) stems from the requirement to extract both phase and amplitude information from a given measurement [37]. This is achieved using a Mach-Zehnder type interferometer introducing an additional fully characterised (i.e. amplitude and phase precisely known) reference arm ($E_0(\omega)$) and subsequently allowing interference between the sample and reference beam to occur at the final beam splitter. By introducing a quarter waveplate into the reference arm and consequently circularly polarising the reference beam, the reference beam can then be thought of in terms of a superposition of two distinct linearly polarised [$E_0(\omega)$, $iE_0(\omega)$] beams phase shifted by $\pi/2$. The subsequent interference between reference and sample beam can therefore be separated into two independent perpendicular polarisation components (± 45° with respect to the linear polariser in the sample arm) and analysed independently:

$$|E_0(\omega) + E(\omega)|^2 = |E_0(\omega)|^2 + |E(\omega)|^2 + 2Re\{E_0(\omega)^* E(\omega)\} \quad (21)$$

$$|iE_0(\omega) + E(\omega)|^2 = |E_0(\omega)|^2 + |E(\omega)|^2 + 2Im\{E_0(\omega)^* E(\omega)\} \quad (22)$$

Using a Wollaston prism the relative contribution of each of these beams can be separated on to two tracks of a CCD. By sequentially blocking each arm of the interferometer it is then possible to remove the non-interferometric (i. e. $|E_0(\omega)|^2 + |E(\omega)|^2$) portion from each contribution after which it is then possible, given that the exact phase and amplitude of $E_0(\omega)$ is known, to extract the phase and amplitude of $E(\omega)$ (specifics detailed in [38]).

Whilst DQSI would appear to be an appealing method to retrieve the $Im\{\chi^R\}$ (phase information) of CARS measurements using an external LO (see appendix III), as in the case of DQSI CARS, (see figure 3.5) it leads to a significant additional level of complexity [39]. This complexity stems from the addition of the Stokes beam and, unlike DQSI where, with the exception of introducing a quarter waveplate, the reference beam is unaltered through the system, both the pump and Stokes reference beams must be passed through a suitable (non-resonant) material in order to generate a LO (although epi-detection is used in this case the same principles apply for forward detection). Given the nature of this experimental setup it is also no longer trivial to retrieve the $Im\{\chi^R\}$ as an additional measurement, from a non-resonant sample, of the relative phase difference imparted by the optics of each arm is necessary. Whilst using this system it is possible to attain NRB free spectra, the additional reference measurement, in conjunction with the complexity of this system, results in an exceptionally high stability requirement. An additional requirement of this system, and other similar DQSI CARS - type systems, attempting to acquire single shot broad spectra is the necessity for broad transform limited pump and Stokes beams: precluding the use of PCF (see appendix III) [40].

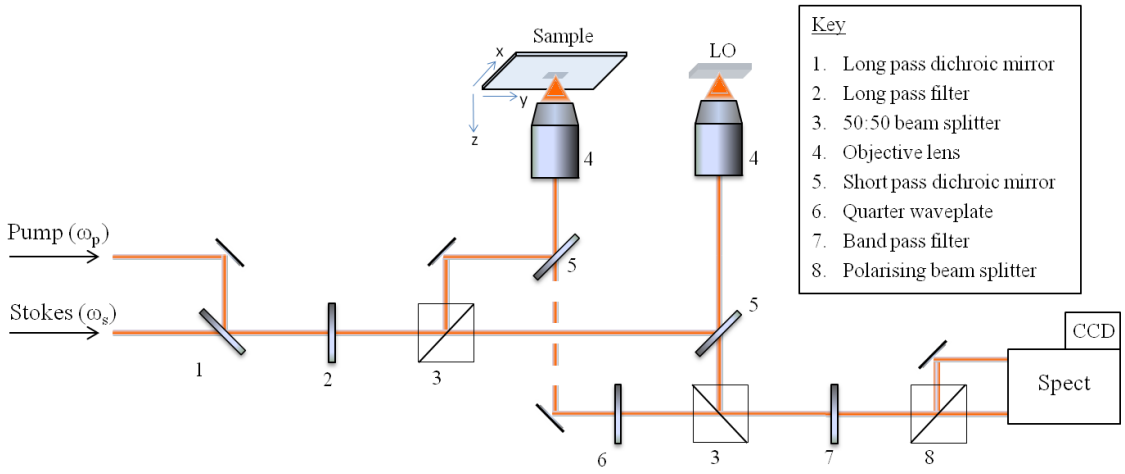

Figure 3.5 Diagram of the components necessary to perform DQSI CARS.

As previously stated it is also possible to use an internally generated LO to perform DQSI CARS. Previous attempts using the NRB as a LO in conjunction with phase and polarization-controlled laser pulses to attain single beam multiplex CARS, however, have yielded only approximations of NRB free CARS spectra as they require assumptions to be made as to the relative strengths of the resonant (P^R) and non-resonant components (P^{NR}): $P^{NR} \gg P^R$ [41] or $P^R \gg P^{NR}$ [42]. Additionally, given the requirement to precisely control both the phase, and, to a lesser extent, polarisation with a liquid crystal spatial light modulator, broad transform limited pulses are again required.

3.2.1.3 Computational NRB removal

By far the most widely adopted NRB removal methods are the computational approaches. These consist of the maximum entropy method and the time domain Kramers-Kronig (or variants thereof) algorithms, both of which attempt to infer $Im\{\chi^R\}$ from the second term of equation 18. The detailed workings of these approaches are outside the scope of this thesis; however, a full description of both techniques, as applied to CARS, can be found elsewhere [29] [30] [43].

These techniques are both defined over infinite spectral ranges and thus, by definition, can reproduce only an estimation of the $Im\{\chi^R\}$ of a discrete raw CARS spectrum, even in idealised cases. The results produced by these techniques have been shown to be quantitatively equivalent both producing output spectra exhibiting spectrally varying residual errors of up to 10% at resonances [30]. Additionally, both techniques require a non- resonant reference (normally glass) sample as an input with which to normalise the raw CARS spectrum prior to NRB removal [30]. The possibility that the reference material itself may have residual resonances present is often neglected further compounding the spectrally varying residual errors.

3.2.2 Analysis by research group (period covered: 2011-2015)

This section represents the 'state-of-the-art' with respect to biologically applicable quantitative broadband CARS. A brief summary, with associated references, has been given for each research group (the principle investigator has been indicated within the brackets). There is some contention as to whether, given the variety of assumptions (elaborated in later sections), these techniques are quantitative or merely semi-quantitative. A conscious decision, however, has been made to exclude any obviously solely qualitative techniques.

University of Konstanz (A. Zumbusch) group [44]:

The Zumbusch group at the University of Konstanz essentially perform an ultra broadband time resolved version of CARS using two co-seeded Er:fibre oscillators (1550 nm fundamental wavelength). The first, in conjunction with a highly non-linear fibre [45], to create a broadband pulse (0-4000 cm^{-1}, ~11 fs) containing both the pump and Stokes components, and the second, via frequency doubling using a periodically poled lithium niobate (PPLN) crystal, to produce a 3 ps flattop pulse with a 200 fs rise time which is used as the probe beam. By exploiting the finite decay life time of the resonant response in relation to the instantaneous relaxation of the purely electronic NRB a combination of impulsive excitation via the short lived broadband pulse and the longer probe pulse results in suppression of the NRB. This technique has been demonstrated on a bulk liquid film and *C. elegans* (although notably only in the C-H stretch region).

University of Ottawa (A. Stolow) group [46] [47]:

This group performs a variant of spectral focusing CARS where the pump/probe pulse and the Stokes pulse are equally linearly chirped, normally by means of glass blocks, and temporally overlapped. The instantaneous frequency difference (IFD), the difference in frequency between the pump and Stokes which defines the Raman shift being probed, is then scanned to build up spectral information.

The particular system employed by this group utilises a titanium sapphire (Ti-Sapph) oscillator (variable wavelength, 60 fs) from which the pump is derived directly, and a broadband Stokes pulse created via a PCF. This system allows scanning between 850 cm^{-1} and 3300 cm^{-1} (albeit with great complexity below 1100 cm^{-1}) at a spectral resolution of 27 cm^{-1}. NRB removal is accomplished by TDKK. This technique has been demonstrated on cellulose fibres and bulk bone samples.

University of Cardiff (P. Borri/W. Langbein) group [48]:

The Cardiff group utilise a similar type of CARS system to the Ottawa group above, however, favouring a shorter Ti-Sapph oscillator pulse duration (5 fs) from which both the pump (<730 nm, bandwidth 65 nm) and Stokes (> 730 nm, bandwidth 200 nm) can be directly extracted without the need for a PCF. As before the two pulses are equally linearly chirped and spectral information retrieved by scanning the IFD. The instantaneous temporal overlap is ~ 1 ps resulting in a spectral resolution of ~10 cm^{-1} over a 1200 cm^{-1} and 3300 cm^{-1} spectral range. NRB removal is accomplished by phase-corrected Kramers - Kronig (PCKK) [49]: a computationally less expensive variant of TDKK. This technique has been demonstrated on HeLa cells, mouse tail and human adipose tissue.

University of Tokyo (H. Hamaguchi/H. Kano) group [50] [51]:

The Tokyo group use an 800 ps passively Q-switched Nd:YAG laser to perform non-degenerate coherent Raman scattering, both CARS and coherent Stokes Raman scattering (CSRS), deriving the pump from the 1064 nm fundamental, the probe, at 532 nm, from frequency doubling, and the Stokes, between 1100-1700 nm (> 3500 cm^{-1}), via a 6 metre PCF. Given the long pulse duration the spectral resolution of this system is <0.1 cm^{-1}. Displacing the probe wavelength with respect to the pump allows both the CARS and CSRS signals to be simultaneously collected. Removal of the NRB is achieved by means of the MEM, however the number of correlation coefficients (normally determined empirically by minimising high frequency noise) is determined by minimising the difference between $Im\{\chi^R\}_{CARS}$ and $Im\{\chi^R\}_{CSRS}$. This technique has been demonstrated on yeast cells and mayonnaise.

National Institute of Standards and Technology (NIST), Gaithersburg, U.S.A (M. Cicerone) group [52] [53]:

The Cicerone group use co-seeded Er:fibre lasers producing a flattop narrow band (3.4 ps) probe at 770 nm and a broadband supercontiuum (16 fs), via a highly non-linear fibre, at 900-1350 nm to perform hybrid two colour/three colour CARS (see figure 3.6). The actual laser configuration is based on a collaborative design between the Zumbusch group and Toptica GmbH. (*cf.* University of Konstanz). By spectrally separating the broad and narrowband beams and exploiting a combination of narrowband pump broadband Stokes (2-colour CARS) and broadband pump broadband Stokes (3-colour CARS) this system is able efficiently to stimulate Raman transitions in both the fingerprint region and also the C-H stretch region. The system is able to interrogate a spectral range of 500-3500 cm^{-1} with a spectral resolution of <10 cm^{-1}. NRB removal is accomplished using TDKK. This technique has been demonstrated on murine liver, pancreas and tumorous brain tissue encapsulated by healthy brain matter.

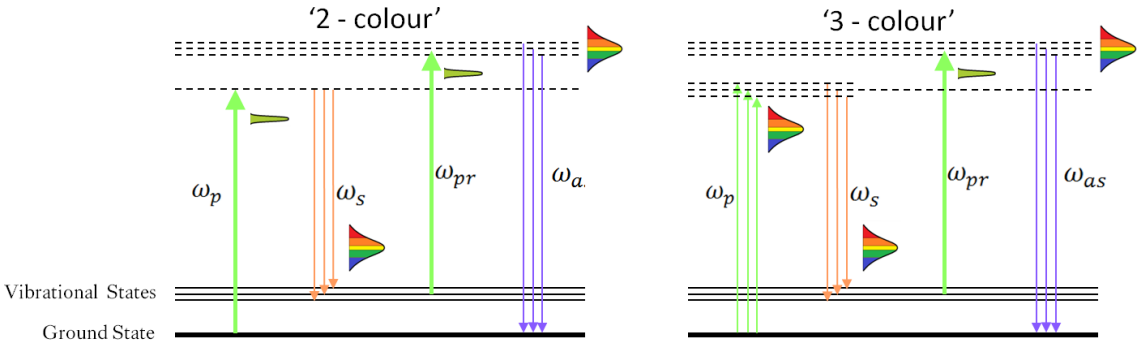

Figure 3.6 Energy level diagrams of 2 and 3 colour CARS. Where the dotted lines denoting virtual states.

University of Heidelberg (M. Motzkus) group [54]:

The Motzkus group perform CARS by means of a Ti-Sapph oscillator (785 nm, 100 fs) from which a narrowband pump is created by means of a spectral filter (1 nm bandwidth), and broadband Stokes pulse (785-1100 nm) is produced via a PCF. These two pulses are spatio-temporally overlapped onto the sample and the resultant CARS collected over a 500-3400 cm^{-1} spectral range with a spectral resolution of 30 cm^{-1}. The NRB is removed using the MEM algorithm. This technique has been demonstrated on murine brain matter.

Whilst the approach adopted by the Zumbusch group would appear to be one of the most initially compelling solutions for acquiring broadband CARS, the method by which the NRB is rejected also results in the interferometric term being neglected and, as such, no hetro/homodyne amplification of the CARS signal can occur. This technique is realistically limited to only the C-H stretch region and is, therefore, not truly feasible for broadband CARS (and will be discounted from further discussion accordingly).

There are a multiplicity of other possible configurations by which broadband CARS can be attained; however, these can be essentially reduced to two approaches: spectral focusing or a PCF/highly non-linear fibre generated Stokes beam in conjunction with a narrowband probe beam. The main advantage of spectral focusing CARS is the extent to which it can be made multimodal. Both the Ottawa and Cardiff groups have successfully incorporated the ability to collect SHG and TPF within their CARS systems. An additional benefit of this type of system is the ability to acquire rapid single line CARS (~10 μs). Whilst the pixel dwell times (estimated for a hyperspectral image with an equivalent signal-to-noise ratio) of these systems in comparison to the PCF based techniques are competitive over a limited spectral range, their main drawback stems from the requirement to change glass blocks and/or filters between spectral ranges to maintain the linear chirp of each beam. As result of this the acquisition times required to collect spectra over the entire biologically relevant spectral window are significantly increased.

Fibre based CARS systems, which do not rely on scanning an IFD to build up spectral information, do not suffer from this drawback and can attain data over the entire relevant spectral region in a single shot. With the exception of the Cicerone group, the current operational fibre based CARS systems inefficiently stimulate Raman transitions in the fingerprint region and are thus limited to those modes with the highest Raman cross section. The Cicerone group, however, employs a hybrid two colour/three colour CARS as a means to circumvent this limitation, and in so doing can acquire with pixel dwell times of 3.5 ms (an order of magnitude less than the majority of other systems) with full access to the entirety of spectral information in the fingerprint region (arguably the first true realisation of broadband CARS analogous to spontaneous Raman scattering).

Another fundamental difference between the various approaches is the chosen method of NRB removal. Each of the above groups rely on a computational approach whether MEM, TDKK or a modified/optimised variant. Whilst these methods do provide hetro/homodyne amplification by the NRB they, irrespective of the particular variant, all result in spectrally varying residual errors of up to 10% at resonances and, as such, are only approximations of the actual spectral form.

If quantitative broadband CARS, as opposed to multimodality, is the only consideration then fibre based systems, when coupled with hybrid two colour/three colour CARS, have a distinct advantage in terms of speed whilst maintaining a comparable level of spectral content. The laser

employed by the various techniques is another point of differentiation; however, for a laser system to be capable of supporting two colour/three colour CARS the Stokes beam must be sufficiently compressible (temporally). This precludes the use of the 800 ps passively Q-switched Nd:YAG in conjunction with 6 metre PCF employed by the Tokyo group. The femtosecond Ti-Sapph lasers utilised by the Cardiff and Heidelberg groups would, in fact, be capable of producing an appropriate supercontinuum; however, doubling the narrowband pulse (~ 780 nm) would result in an unobtainable two colour CARS.

In conclusion, the ideal system for conducting quantitative broadband CARS would be the system employed by the Cicerone group; however, with the amendment of an all optical NRB removal mechanism, as opposed to the TDKK currently used. Such an all optical NRB removal mechanism is demonstrated in the following chapter.

3.3 Other CRS techniques

In addition to CARS there are several other CRS techniques such as fifth-order non-linear CRS [55], Raman induces Kerr effect spectroscopy [56], Raman optical activity [57] and stimulated Raman scattering (SRS). Of these, however, at present only SRS has benefited from any sustained development. This does not, however, reflect negatively on the viability of the other techniques as, especially performed in conjunction with balanced detection, they do exhibit significant potential.

A conspicuous absence from the above group by group analysis of the CARS 'state-of-the-art' is the University of Harvard (Xie) group as they were instrumental in its initial proliferation; however, over approximately the last 3 years there has been a sea-change as regards to their focus from CARS to SRS. In fact this has been characteristic of many of the groups in this field with only the King's College London, Cardiff and NIST groups remaining solely CARS based.

In contrasting the two techniques, CARS and SRS, the reason for this will become apparent. Firstly, in brief, SRS corresponds to the interaction of two incident laser fields, pump and Stokes, with the sample [58], and is analogous to simulated emission [59] (see figure 3.7). When the difference frequency between the two incident fields coincides with a resonance the molecules within the sample then simultaneously interact with both of the incident laser fields allowing a parametric energy exchange to occur. The amplitude of the stimulated emission, and thus the exchange of energy, are dependent on the intensity of the incident fields and polarisability of the species [8].

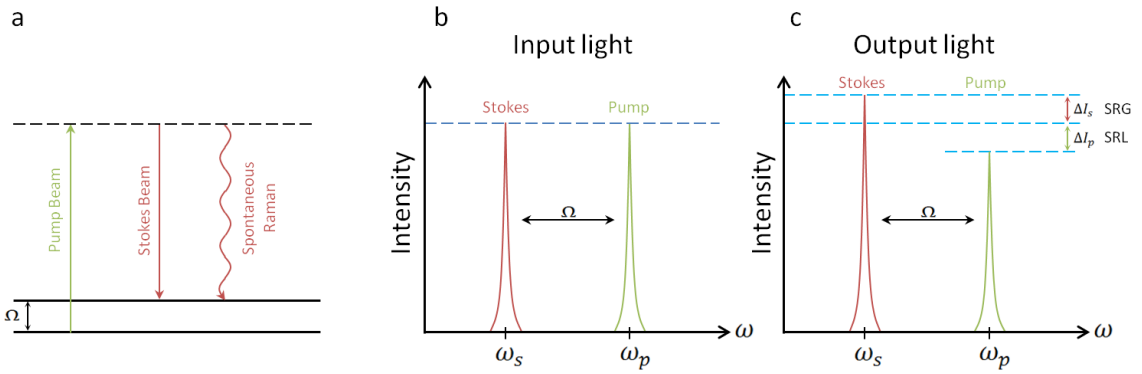

Figure 3.7 a) Energy level diagram of SRS shown with the corresponding spontaneous Raman scattering b) & c) SRS Input and output spectra. SRS leads to an intensity increase in the Stokes beam (SRG) and an intensity decrease in the pump beam (SRL). Diagram reproduced from [58].

Experimentally, via high frequency modulation of the incident Stokes beam, the resulting energy exchange, in SRL mode, can be detected as an exceptionally small (many orders of magnitude) modulation of the otherwise DC pump beam. Typically a lock-in amplifier is used to extract this small AC component. Herein lies the first major distinction between the two techniques: the CARS signal maybe detected directly without the use of expensive specialised lock-in amplification.

Another significant distinction between these two techniques is the origin of their respective backgrounds. Whilst the NRB is a well established phenomenon of CARS, proponents of SRS often state that it is a background free technique: this is not the case. The nature of the SRS background is just somewhat different from the coherently generated background of CARS. The SRS background stems from unwanted parasitic non-linear effects: primarily cross-phase modulation [60]. The effect of this is to introduce clipping on the pre-detector pinhole (or physical extent of the detector) and thus subsequently reduce the signal, complicating quantitative interpretation of the data. This necessitates large area detectors; however, this often only partially alleviates problem.

Finally, and probably most decisively, another difference is the typical wavenumber range accessible with each technique. Broadband CARS, as stated above, has the ability to interrogate, simultaneously, the whole spectrum of any given sample whilst SRS is normally limited to approximately 300 cm^{-1}. In essence this is due to the method by which SRS data is acquired: rapid wavelength scanning using a lock-in amplifier to extract the signal. Whilst the wavenumber range accessible to BCARS is significantly larger, acquisition times are also considerably longer, on the order of several milliseconds per pixel [53] in comparison to hundreds of nanoseconds (per pixel equivalent) for SRS [61]. A full comparison between BCARS and SRS is given in full elsewhere [62]. There have, however, been two noteworthy recent improvement of SRS: phase encoding [63] and lock-in free acquisition using a tuned amplifier array [64].

In practical terms the choice of technique comes down to necessity. If acquisition speed is of the essence, such as in large area imaging, 3D imaging or sample dynamics, but spectral detail is of less importance then SRS is likely to be the most appropriate. This typically corresponds to the situation where the chemical species/bonds of interest are well known and thus a judicious choice of narrow wavelengths will suffice. If, however, as is the case with a significant amount of biomedical imaging, the sample is not necessarily well characterised prior to Raman imaging then it is essential to obtain as much spectral information as possible. To give an example, it was recently shown that by identifying the required proteins, viral replication could be tracked and localised within a human cell *in vitro* [65]. This would have been impossible using SRS as there would have been insufficient spectral detail to distinguish the variety of proteins let alone track viral development.

These two techniques are often thought of as competitors yet, at present, they produce complimentary data: BCARS addressing the myriad of spectral detail that can be obtained primarily from the FPR of a biological species on minute time scale (per image) whilst SRS is focused more on recording the real time dynamics of a smaller subset of chemical bonds, typical lipid, via the CH stretch region.

While in comparison with SRS the acquisition times may appear slow the single largest impediment of BCARS is the NRB which, using current removal methods, results in only a semi-quantitative outcome. The Spectral Interferometric Polarised CARS (SIPCARS) NRB removal technique developed at King's College London yields an entirely quantitative BCARS measurement.

4. Spectral Interferometric Polarised Coherent Anti-Stokes Raman Scattering

In detailing the various BCARS approaches in the previous chapter it is immediately apparent that the technique which has both shown the most potential and proved most successful is the hybrid 2-colour/3-colour BCARS developed by NIST (Cicerone group). Whilst their excitation profile allows the highest efficiency stimulation of the CARS process and consequently the greatest signal-to-noise ratio per unit pixel dwell time, the method by which the NRB is removed, TDKK, is fundamentally flawed.

This chapter, and associated appendices, give a comprehensive description of the theory of Spectral Interferometric Polarised Coherent Anti-Stokes Raman Scattering (SIPCARS) developed at King's College London over the course of this Ph.D. This novel technique completely removes the NRB without prior or post assumption of the CARS spectral form and without the need for normalisation by a non-resonant reference material.

4.1 Fundamental theory

Whilst, in reality, an elliptically polarised pump/probe and linearly polarised Stokes beam are used to generate SIPCARS, it is conceptually easier, in the first instance, to derive the underlying theory with a (right-hand) circularly polarised Stokes (E_s) and linearly polarised pump/probe (E_p) beam, as shown in figure 4.1. The normal beam order convention within the third order susceptibility tensor, $\chi^{(3)}_{ijkl}$, has been followed: where *i*, *j*, *k* and *l* correspond to anti-Stokes, pump, probe and Stokes respectively. $\chi^{(3)}_{ijkl}$ can be readily separated into diagonal $\left(\chi^{(3)}_{iiii}\right)$ and off-diagonal $\left(\chi^{(3)}_{ijij}, \chi^{(3)}_{ijji}, \chi^{(3)}_{iijj}\right)$ elements where the off-diagonal terms mediate the coupling of orthogonally polarized excitations into the detected polarization. It should be noted that in an isotropic medium, for reasons of symmetry, that any $\chi^{(3)}$tensor element where the same index appears three times (e.g. $\chi^{(3)}_{ijjj}$) is equal to 0 [66].

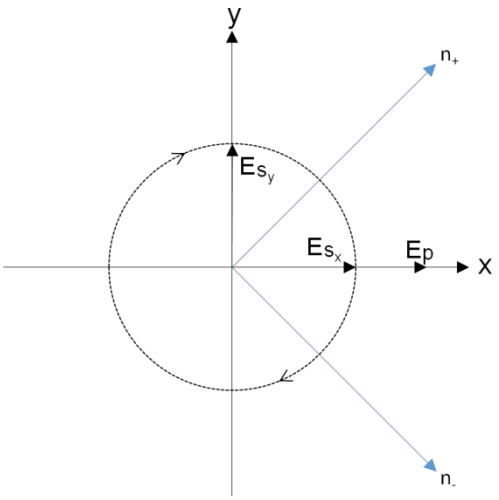

Figure 4.1 Polarisations for SIPCARS with a right-hand circularly polarised Stokes beam (E_s), indicated by the dashed circle, and linearly polarised pump/probe (E_p) beam. Detection is performed along the n_+ and n_- axis (orthogonal blue lines).

The detected anti-Stokes intensity is determined by the square modulus of the third order non-linear polarisability:

$$I_{CARS} \propto \left|P^{(3)}\right|^2 = \left|\left(\chi^{R(3)} + \chi^{NR(3)}\right) {E_p}^2 E_s^*\right|^2 \tag{23}$$

In order to gain an intuitive understanding of the all optical NRB removal achieved by SIPCARS, expressions for the induced polarisations P_+ and P_- along the detection axes n_+ and n_-, respectively, are determined as follows:

$$P_+ = \frac{1}{2}\left(\chi^{(3)}_{1111}\, {E_p}^2 E_s^{+*} + \chi^{(3)}_{1221}\, {E_p}^2 E_s^{+*} + \chi^{(3)}_{1122}\, {E_p}^2 E_s^{-*} + \chi^{(3)}_{1212}\, {E_p}^2 E_s^{-*}\right) \tag{24}$$

$$P_- = \frac{1}{2}\left(\chi^{(3)}_{2222}\, {E_p}^2 E_s^{-*} + \chi^{(3)}_{2112}\, {E_p}^2 E_s^{-*} + \chi^{(3)}_{2211}\, {E_p}^2 E_s^{+*} + \chi^{(3)}_{2121}\, {E_p}^2 E_s^{+*}\right) \tag{25}$$

where E_s^+ and E_s^- denote the components of the Stokes field along n_+ and n_- respectively. As might be expected these two expressions share a common form and it is apparent that they differ only in that the orientation of the Stokes field is swapped for each respective term.

Noting that:

$$E_s^+ = iE_s^- \qquad \& \qquad E_s^- = {E_s^+}/{i} \tag{26}$$

It is possible to recast the expressions for the polarisations as:

$$P_+ = \frac{1}{2}\left[\chi^{(3)}_{1111}\, {E_p}^2 E_s^{+*} + \chi^{(3)}_{1221}\, {E_p}^2 E_s^{+*} + \chi^{(3)}_{1122}\, {E_p}^2 \left({E_s^+}/{i}\right)^* + \chi^{(3)}_{1212}\, {E_p}^2 \left({E_s^+}/{i}\right)^*\right] \tag{27}$$

$$= \frac{1}{2}\left[\chi^{(3)}_{1111}\, {E_p}^2 E_s^{+*} + \chi^{(3)}_{1221}\, {E_p}^2 E_s^{+*} + i\left(\chi^{(3)}_{1122}\, {E_p}^2 E_s^{+*} + \chi^{(3)}_{1212}\, {E_p}^2 E_s^{+*}\right)\right] \tag{28}$$

$$P_{-} = \frac{1}{2}\left[\chi^{(3)}_{2222}\, {E_p}^2 E_s^{-*} + \chi^{(3)}_{2112}\, {E_p}^2 E_s^{-*} + \chi^{(3)}_{2211}\, {E_p}^2 (iE_s^{-})^* + \chi^{(3)}_{2121}\, {E_p}^2 (iE_s^{-})^*\right] \quad (29)$$

$$= \frac{1}{2}\left[\chi^{(3)}_{2222}\, {E_p}^2 E_s^{-*} + \chi^{(3)}_{2112}\, {E_p}^2 E_s^{-*} - i\left(\chi^{(3)}_{2211}\, {E_p}^2 E_s^{-*} + \chi^{(3)}_{2121}\, {E_p}^2 E_s^{-*}\right)\right] \quad (30)$$

Simple inspection of these two expressions shows that the latter two terms of each expression are phase shifted by $\pi/2$ with respect to the former. As the imaginary components are, themselves, shifted by $\pi/2$ with respect to the real component, so the imaginary components of the phase shifted latter terms are bought into phase with the real components of the first two terms and are, therefore, able to interfere. In the case of P_{+} these terms lag behind (in terms of time and therefore phase) the first terms aligning along the negative n_{-} axis. This results in the imaginary components adding to the real components aligned along the n_{+} axis. In contrast for P_{-} the latter terms lead the former and are therefore aligned along the n_{+} axis. This results in the imaginary term aligning along the negative n_{-} axis (equivalent to the negative imaginary term aligned along the positive n_{-} axis) and therefore along the n_{-} axis the imaginary components are subtracted from the real components. In summary the induced polarisations along the n_{+} and n_{-} are:

$$\text{Along } n_{+}: \quad Real\ components + Imaginary\ components$$
$$\text{Along } n_{-}: \quad Real\ components - Imaginary\ components$$

From which it is trivial to deduce that a simple subtraction yields only the imaginary components which are directly related to the spontaneous Raman spectrum.

Whilst this approach highlights the elegant simplicity of SIPCARS, to derive a quantitative expression it is necessary to start, instead, by obtaining expressions for the induced polarisations along the x and y axes as denoted by P_{x} and P_{y} respectively. To avoid overly complicating the following derivation the superscript $^{(3)}$, signifying the order of the non-linear susceptibility, has been omitted and can be assumed henceforth unless otherwise stated. Given that $E_{s_x} = E_s/\sqrt{2}$ and $E_{s_y} = iE_s/\sqrt{2}$ and that the pump/probe polarisation is confined along the x axis is possible to obtain the following succinct expressions:

$$P_x = 1/\sqrt{2}\ \chi_{1111}\, E_p^2 E_s^* \quad (31)$$

$$P_y = -i/\sqrt{2}\ \chi_{2112}\, E_p^2 E_s^* \quad (32)$$

It is now possible to state the induced polarisation along n_+ and n_- in terms of P_x and P_y (including a $\frac{1}{\sqrt{2}}$ normalisation factor):

$$P_+ = {}^1/_{\sqrt{2}}\,(P_x + P_y) \tag{33}$$

$$P_- = {}^1/_{\sqrt{2}}\,(P_x - P_y) \tag{34}$$

SIPCARS intensity is determined by the square modulus of the third order non-linear polarisability therefore the signal intensity (S) along n_+ and n_- can be defined as (constants absorbed into the proportionality):

$$S_+ \propto P_+ P_+^* \qquad \& \qquad S_- \propto P_- P_+^* \tag{35}$$

Therefore:

$$S_+ \propto (P_x + P_y)(P_x + P_y)^* \propto (P_x P_x^* + P_x P_y^* + P_y P_x^* + P_y P_y^*) \tag{36}$$

$$S_- \propto (P_x - P_y)(P_x - P_y)^* \propto (P_x P_x^* - P_x P_y^* - P_y P_x^* + P_y P_y^*) \tag{37}$$

The sum signal (which is the polarised equivalent of a conventional CARS signal: see appendix IV), $\sum S = S_+ + S_-$, is then given by:

$$\sum S \propto (P_x P_x^* + P_y P_y^*) \tag{38}$$

Whilst the SIPCARS signal (ΔS), the difference signal, is given by:

$$\Delta S \propto (P_x P_y^* + P_y P_x^*) \propto (P_x P_y^* + (P_x P_y^*)^*) \tag{39}$$

Fully expanding this expression results in the following:

$$\Delta S \propto \frac{1}{2} i\,(\chi_{1111}\,\chi_{2112}^* - \chi_{1111}^*\,\chi_{2112})\,I_p^2 I_s \tag{40}$$

where I is the intensity of the respective input beams. Using the identity $-z^* = 2i\,Im\{z\}$, where z is a complex number, it is possible to simplify the above proportionality to:

$$\Delta S \propto Im\{\chi_{1111}\,\chi_{2112}^*\}\,I_p^2 I_s \tag{41}$$

As previously stated (see chapter 2) the third order susceptibility can be separated into its resonant and non-resonant components, $\chi_{ijkl} = \chi^{R}_{ijkl} + \chi^{NR}_{ijkl}$. Making this substitution into equation 41 yields the following expression:

$$\Delta S \propto Im\{(\chi^{R}_{1111} + \chi^{NR}_{1111})(\chi^{R}_{2112} + \chi^{NR}_{2112})^{*}\} I_P^2 I_s \quad (42)$$

$$\propto Im\{\chi^{R}_{1111}\chi^{R}_{2112}{}^{*} + \chi^{R}_{1111}\chi^{NR}_{2112}{}^{*} + \chi^{NR}_{1111}\chi^{R}_{2112}{}^{*} + \chi^{NR}_{1111}\chi^{NR}_{2112}{}^{*}\} I_P^2 I_s \quad (43)$$

The final term within the parenthesis is purely real and is therefore its imaginary component is equal to zero. Given that the resonant and non-resonant components are complex and real, respectively, a further simplification of the second and third terms can be achieved by careful application of the complex conjugation.

$$\Delta S \propto Im\{\chi^{R}_{1111}\chi^{R}_{2112}{}^{*} + \chi^{R}_{1111}\chi^{NR}_{2112} - \chi^{NR}_{1111}\chi^{R}_{2112}\} I_P^2 I_s \quad (44)$$

Whilst not immediately apparent the first term of this equation is also equal to zero (see appendix V) therefore:

$$\Delta S \propto Im\{\chi^{R}_{1111}\chi^{NR}_{2112} - \chi^{NR}_{1111}\chi^{R}_{2112}\} I_P^2 I_s \quad (45)$$

Assuming an isotopic medium, such that $\chi_{2112} = \chi_{1221}$ and $\chi_{1111} = \chi_{1212} + \chi_{1221} + \chi_{1122}$, and noting that away from resonance the third order susceptibility is essentially frequency independent and thus possesses Kleinman symmetry, $\chi^{NR}_{1111} = \chi^{NR}$ and $\frac{\chi^{NR}}{3} = \chi^{NR}_{1212} = \chi^{NR}_{1221} = \chi^{NR}_{1122}$ [67], it is possible to make further simplifications to 45.

$$\Delta S \propto \chi_{NR}\, Im\{\chi^{R}_{1111} - 3\chi^{R}_{1221}\} I_P^2 I_s \quad (46)$$

Introducing the CARS depolarisation ratio, $\rho = \chi^{R}_{1221} / \chi^{R}_{1111}$, this equation finally becomes:

$$\Delta S \propto (1 - 3\rho)\, \chi^{NR}\; Im\{\chi^{R}_{1111}\} I_P^2 I_s \quad (47)$$

Examining this equation carefully gives insight into the real strength of this technique. The first term, which includes the depolarisation ratio ρ, encodes mode symmetry into the resultant SIPCARS spectrum. This depolarisation ratio is equivalent to the spontaneous Raman depolarisation ratio and consequently, once normalised, the SIPCARS spectrum is identical to a polarisation resolved spontaneous Raman scattering spectrum.

The second term, χ_{NR}, results in homodyne amplification of the signal. This is a necessity for any CARS system if, at biologically relevant powers, it is to generate higher signal-to-noise ratio (SNR) spectra than spontaneous Raman [32] [68]. It is important to note that while SIPCARS automatically removes the NRB that is non-linearly mixed with the resonant signal, this

homodyne amplification term remains. The effect of which is to increase the SNR and thus allow faster image acquisition (whilst still remaining above the noise floor/detector noise). This term is subsequently removed by spatial normalisation (see section 8.3.4) having served its purpose.

The third term explicitly shows that the SIPCARS intensity is linear with respect to the imaginary component of χ^R_{1111} and thus has a linear analyte concentration dependence. As previously stated, $Im\{\chi^R_{1111}\}$ is directly proportional to the spontaneous Raman response. The final terms simply show that the signal is dependent on the square of the pump/probe beam intensity and is directly proportional to the intensity of the Stokes beam.

Although not typical of a doctoral thesis I have chosen to include, in appendix VI, a more informal description of SIPCARS that should be accessible to a wider, less specialist, audience.

The above derivation assumes a circularly polarised Stokes beam and a linearly polarised pump/probe beam; however, as previously stated, this is not, in reality, how the experiment is carried out owing to the complexity of precisely controlling the polarisation of a broadband beam. The full derivation is tackled in appendix VII.

The inherent simplicity of SIPCARS, requiring the addition of only passive polarisation optics in order to generate an elliptically polarised narrowband beam and detect in two orthogonal polarisation axes, renders it readily applicable to any laser system capable of producing a conventional CARS signal. With regards to a hybrid 2-colour/3-colour BCARS implementation complete NRB removal is guaranteed, provided that at least one of the three fields (pump, probe or Stokes) is elliptically polarised and aligned such that its major or minor axis is orientated along the linearly polarised fields. By simply exploiting the fundamental phase shift that accompanies a resonance, SIPCARS completely removes the NRB without any pre or post assumption as to the spectral form (resonant and non-resonant) of the sample and without the need for normalisation by a non-resonant reference material. As such, SIPCARS represents the only truly quantitative approach for retrieving a NRB-free broadband CARS spectrum/image of a sample (faster than spontaneous Raman scattering for biologically relevant powers).

5. Hyperspectral CRS imaging

This chapter highlights the benefits of hyperspectral imaging when examining complex biological systems and, in particular, the extent to which it is applicable to a variety of techniques. A hyperspectral image data cube corresponds to the acquisition of intensity with respect to wavelength in addition to the requisite Cartesian axes (see figure 5.1): in effect yielding a continuous spectrum at each pixel. There are several advantages of hyperspectral imaging; however, the most notable are a higher multiplexing limit (discussed in detail in the following section) and the ability to apply multivariate analysis techniques.

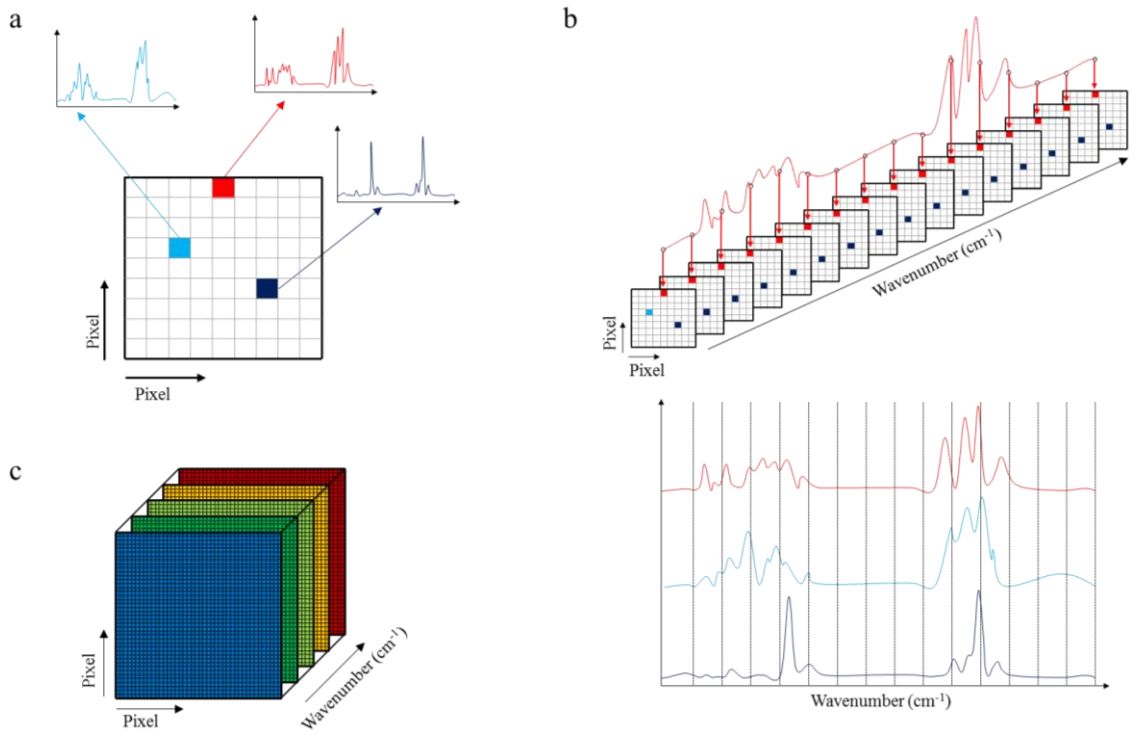

Figure 5.1 Hyperspectral image data. a) Acquisition: at each individual pixel an entire spectrum is acquired in a single shot. Only two dimensions have been shown, however, this can readily be extended in a third. b) Analysis: in this simplified pictographic representation, for easy of depiction, only the spectrum related to a single pixel has been directly indicated on the sequential wavenumber images. The spectra below correspond to the three highlighted pixels, the intensities of which are also mapped onto the corresponding wavenumber slices (denoted by the dotted line). This is the case for all of the pixels. c) Result: the spectral information contained within a hyperspectral data cube allows an intensity image to be created for any given wavenumber. In combination with Raman scattering this allows chemically specific maps of the sample to be created.

5.1 Hyperspectral imaging

Regardless of the particular chosen technique, imaging biological samples requires a high degree of spatial resolution and chemical specificity i.e. the ability to see small objects and correctly identify them. High spatial resolution is typically achieved with high NA lenses and/or multiphoton excitation; however, high chemical specificity can prove more elusive. Variants of two techniques fulfil both of these criteria: fluorescence microscopy and Raman scattering microspectroscopy. The ability, however, to spatially localise and identify a single chemical species within a sample is adequate only for a limited set of experiments. Compositional analysis or interaction characterisation, requiring the identification of multiple chemical components, are of significantly more importance when deciphering the fundamental biochemistry underlying many vital processes.

The number of distinct molecular species that can be simultaneously detected by a technique, normally termed the multiplexing limit, is largely dependent on two factors: the density of spectral information (number and width of distinct spectral lines) and the accessible spectral range. If fluorescence microscopy is considered, the spectral range is, in principle, limited only by the transmission characteristics of the various optics within the system and is typically greater than the visible region (360 to 750 nm). The inherently broad emission spectra of typical fluorescent probes (see figure 5.2b), however, restrict the multiplexing limit to a maximum of 6 distinct (tagged) molecular species [69]. This can be achieved only by means of a battery of different lasers and a truly judicious choice of probes (so as to avoid any possibility of cross talk). As such, the vast majority of fluorescence microscopy is performed with a maximum of three simultaneously tagged species.

To achieve a higher multiplexing limit it is, instead, necessary to use the intrinsic molecular vibrations of the biological molecules as a contrast mechanism. Although there are two techniques that accomplish this, intra-red spectroscopy and Raman scattering microspectroscopy, the former may be discounted as it is severely limited due to the inherent long excitation wavelengths, and thus low spatial resolution, coupled with the absorption of water [16].

A Raman scattering spectrum, as can be seen in figure 5.2a, contains a multiplicity of spectral features within the corresponding wavelength range of a single broad fluorescence peak. Additionally, whilst the peaks within a given spectrum, toluene in this particular example, stem from the constituent molecular bonds which may be common to many materials the overall spectrum, peak positions and intensity, is unique. This allows the spectrum to be used as a signature for a given material within a sample, analogous to a barcode in a warehouse. A Raman spectrum itself may be split into two distinct regions (see figure 5.3): the FPR, located between 500-1800cm^{-1}, and the CH-stretch region at 2600-3100cm^{-1}. Given the high density of spectral information located within the FPR it is primarily used to identify compounds. Conversely, since

all organic molecules, by definition, contain carbon and hydrogen, molecular identification using the CH-stretch region alone is problematic. It is, in fact, further complicated by the broad nature of the spectral features within this region and interference with overtones stemming from the FPR: so called Fermi resonances [70].

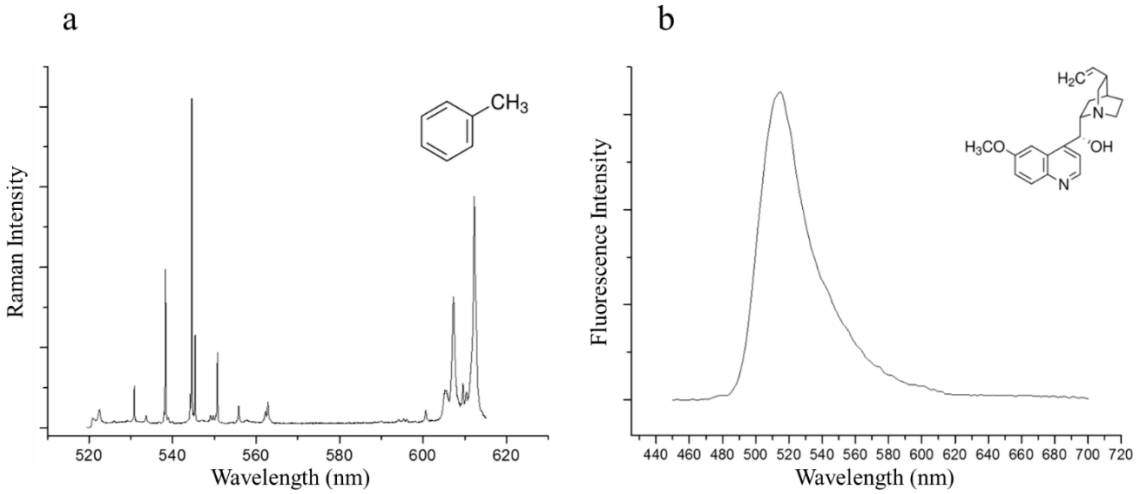

Figure 5.2 a) Spontaneous Raman spectrum of toluene acquired with a 514 nm laser. Inset: molecular structure of toluene. b) Fluorescence emission spectrum of quinine, a noteworthy standard fluorophore. Inset: molecular structure of quinine. Unconventionally the Raman intensity is displayed as a function of wavelength as opposed to wavenumber to allow a direct comparison between spectra. It should be noted that the wavelength range of the Raman spectrum is significantly smaller than the fluorescence spectrum. Additionally fluorescence emission is on average many orders of magnitude more intense than Raman scattering therefore the intensity axes are not comparable.

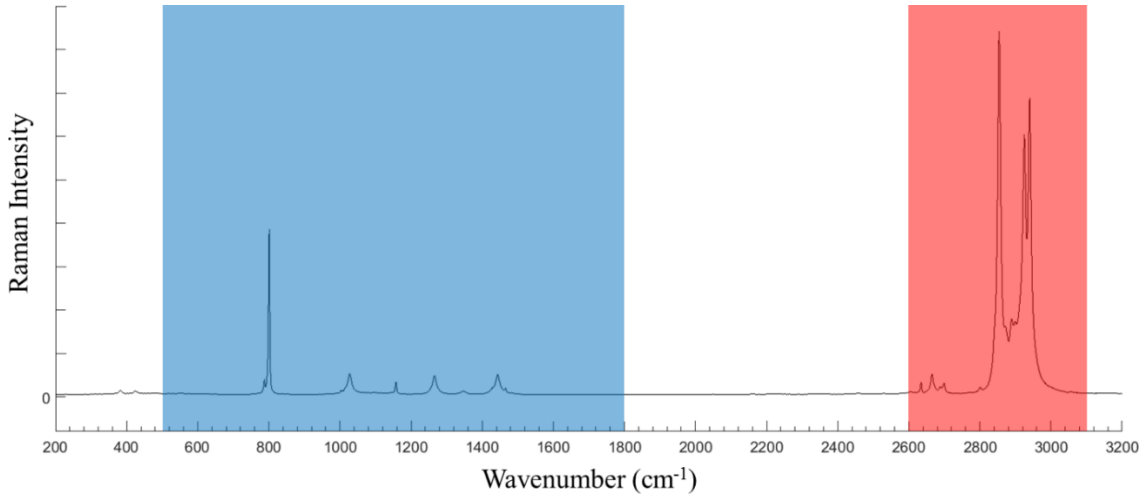

Figure 5.3 Spontaneous Raman spectrum of cyclohexane (C_6H_{12}) acquired with a 514nm laser. The FPR and CH-stretch regions are highlighted in blue and red respectively. The unhighlighted section (1800-2600 cm^{-1}) between the two regions is known as the quiescent or 'quiet' region and is not Raman active for the vast majority of biological molecules.

Overall the array of narrow spectral features found in a typical Raman spectrum, and thus the wealth of discriminatory information contained within a Raman hyperspectral data cube, allow the successful application of various multivariate analysis techniques: a staple of hyperspectral data processing [71]. One of the most prolific multivariate analysis techniques is principle components analysis (PCA) which, by means of orthonormal transformation, can decompose hyperspectral data into a set of orthogonal directions containing the largest variances. The data is then projected on to these directions to form the principal components (PC). The PC are ordered such that the first contains the largest variance after which the variance decreases with increasing component number. The PC are a linearly uncorrelated representation of the hyperspectral data set which, in principle, allow the sample to be segmented. A notable significant drawback of PCA is that that PC are not necessarily correlated with the Raman spectra of the constituents; however, in many cases they bear a close resemblance. The authentic component spectra, and thus images, may be, potentially, retrieved by further processing the data using non-negative matrix factorisation, the details of which are outside the scope of this discussion but may be found elsewhere [49] .

For any given data set the number of PC revealed may be as large as the number of input variables. In terms of Raman hyperspectral imaging this corresponds to the number of spectral bins spanning a spectrum. Practically, when using a CCD, this is normally dictated by the number of pixels on to which the spectrum is dispersed. As the physical number of unique constituents within a biological sample is exceptionally unlikely to be this high, a reasonable assumption can be made that the vast majority of PC contain only noise and thus maybe discarded without loss of SNR. In fact, with cautious application, this procedure can result in a significantly improved SNR and has, accordingly, been widely implemented. This 'de-noising' application of PCA is arguably of greater importance than PC retrieval given the above mentioned disadvantage.

A significant body of literature exists which pertains to the identification of the various Raman peaks/bands. These are too extensive to list in their entirety; however, classification of the vast majority can be accomplished from these select few sources [72]–[75].

In addition to simple band assignments there are several ratios between band intensities which are of note. Considering the 1450 cm^{-1} CH_2 degenerate deformation, 1650 cm^{-1} C=C bond, and 1740 cm^{-1} C=O ester bond, which alone are informative, by taking the ratio of 1650/1450 cm^{-1} a measure of lipid unsaturation (the ratio of double bonded to single bonded carbons in a fatty acid acyl chain) is attained. Likewise the degree of lipid oxidation of a sample can be determined by taking the ratio of 1740/1650 cm^{-1} peaks [76]. In the CH-stretch region is it possible, albeit significantly more complex (often requiring significant peak fitting procedures) and less reliable, to derive a measure of lipid unsaturation via the ratio between the 3020 cm^{-1} (=C-H) peak and the

integrated total lipid (2800-3100 cm^{-1}), while the ratio between 2845 cm^{-1} and 2930 cm^{-1} is indicative of acyl chain order [77] [78].

5.2 CRS hyperspectral imaging

The requirements of hyperspectral imaging for CRS and spontaneous Raman techniques are fundamentally equivalent: relying on the acquisition of wavelength in addition to spatial information.

There are two main methods, both applied by various CRS techniques, by which spatial data can be acquired: stage scanning and galvanometer based scanning. Stage scanning corresponds to physically moving the stage to which the sample is rigidly fixed in order to acquire spatial information. This method, although slow, is robust in nature. Galvanometer based scanning utilises rapid movements of mirrors (controlled by precise galvanometers) located in a Fourier plane to scan the laser focal spot over the imaging area. There are advantages and disadvantages to both approaches. Galvanometer based scanning is only advantageous if pixel dwell time is the limiting factor. For the majority of BCARS techniques applied to biological samples, however, this is simply not the case. It can, however, introduce image artefacts, especially if scanning in both x and y axes, due to the inability to place both mirrors in a Fourier plane [79]. Additionally, regular realignment/recalibration may be required to ensure optimal scanning. On the other hand stage scanning is completely unfeasible for 'state of the art' hyperspectral SRS techniques as the pixel dwell times required are on the order of hundreds of nanoseconds: well beyond the capabilities of even the fastest piezo driven stages.

A third option, recently applied by the NIST group [80], is a hybrid approach in which the fast axis is scanned using a galvanometer based approach and the slow axis with conventional stage scanning. This approach overcomes the major drawback of multi-axis galvanometer based scanning as only a single, correctly positioned, mirror is used whilst still significantly decreasing acquisition time (a major limiting factor for this particular implementation of BCARS).

There are also two main approaches for wavelength acquisition: spectral scanning (frame-by-frame wavelength tuning) in conjunction with a photodiode/photomultiplier tube, or a CCD coupled with a dispersive optical element. Typically, although there are exceptions (see chapter 3), SRS techniques adopt the photodiode/photomultiplier tube approach whilst CCD acquisition is the preserve of BCARS techniques. Although spectral scanning could be termed multispectral (multiple discrete spectral points) rather than hyperspectral imaging, the standard spectral resolution achieved by such systems is normally less than 10 cm^{-1} and is, therefore, in effect, the same as hyperspectral imaging. The typical pixel dwell times (at a single wavelength) and lock-in detection requirement of hyperspectral SRS techniques preclude the use of conventional CCDs (feasible with small area CCDs however with no apparent advantage) relying,

instead, on the use of photodiodes or photomultiplier tubes which on average have a rise time of less than 10 ns. In contrast, the pixel dwell times used in BCARS techniques have yet to approach the read out time of a conventional imaging CCD which, when coupled with a spectrometer, yields the required spectral discrimination.

Full spectral range (FPR and CH-stretch region) BCARS hyperspectral data, assuming complete NRB removal, is functionally equivalent to that produced via spontaneous Raman scattering in terms of multivariate analysis applicability. It is therefore entirely amenable to linear multivariate techniques including PCA denoising. An important caveat that must be taken into account is that these techniques are linear in nature and therefore produce erroneous results if even a small amount of NRB is still present.

SRS data is inherently linear (with respect to analyte concentration) in nature and thus multivariate analysis is readily applicable; however, as SRS is typically applied to the CH-stretch region, which usually lacks a high degree of spectral detail, it is of limited use. If, instead, the FPR is assessed using SRS then the current wavenumber range limitation (approximately 300 cm^{-1}) is an impediment for meaningful application of multivariate analysis as it, once again, reduces the amount of spectral detail accessible. Whilst the data produced by SRS is appropriate for multivariate analysis, at present, it is not efficient to do so.

The overarching objective of all CRS techniques is to be able to replicate the full spectral coverage of spontaneous Raman scattering in a fraction of the time and as such hyperspectral imaging is a necessity.

6. Polarisation resolved spontaneous Raman scattering

The worked detailed in this chapter, including upgrading the Renishaw Raman spectrometer, developing the alignment method and subsequently acquiring data, was the result of an individual effort on the part of the author.

6.1 Motivation

The theory of SIPCARS, as set out in chapter 4, clearly illustrates the importance of the Raman depolarisation ratio. Briefly, to recapitulate, within a SIPCARS spectrum the depolarisation ratio of a given Raman band plays a significant role in determining the intensity, and also exclusively governs the sign. It was, therefore, imperative during the initial development of the SIPCARS system/theory at KCL to have a method by which the Raman depolarisation ratio of various materials could be independently verified. The simplest (only direct linear optical approach) and consequently most robust method by which this information could be attained was polarisation resolved spontaneous Raman scattering. Whilst the use of polarisation resolved spontaneous Raman scattering, however, yields significantly more information than conventional spontaneous Raman scattering there are currently very few research groups, worldwide, that routinely acquire it. This, unfortunately, leads to the situation whereby direct comparison of SIPCARS intensity with the vast majority of current spontaneous Raman scattering literature requires the Raman depolarisation ratio to be known, and the data to be converted into an appropriate form. This point actually holds true for the majority of CRS techniques, which also neglect the molecular symmetry information that can be ascertained via a polarisation resolved approach. An additional effect of the rarity of polarisation resolved Raman measurements is the general lack of information regarding the Raman depolarisation ratios of even simple (less than four elemental constituents) compounds. This rendered access to an operational polarisation resolved spontaneous Raman spectrometer indispensable.

Given that direct comparison between polarisation resolved spontaneous Raman scattering and SIPCARS spectra is required, it is necessary to extract the difference spectrum from the polarisation resolved spontaneous Raman scattering data. This is achieved by multiplying the signal of the perpendicular polarisation geometry by a factor of three and subsequently subtracting it from the signal of the parallel polarisation. This is equivalent to manipulating the polarisation resolved spontaneous Raman scattering data into a form where it is equivalent to the Raman depolarisation ratio dependent pre-factor of the SIPCARS intensity (cf. equation 47):

$$(1-3\rho) = (1-3\,I_{\perp}/I_{\parallel}) = (I_{\parallel}-3I_{\perp}) \tag{48}$$

As, in principle, the Raman depolarisation ratio for a given bond is fixed and, therefore independent of the method by which it is ascertained, the above equation remains valid in all instances.

Prior to addressing the method behind polarisation resolved spontaneous Raman scattering the apparatus used is detailed below.

6.2 Apparatus

In order to perform polarisation resolved spontaneous Raman scattering spectroscopic measurements a Renishaw Raman spectrometer (InVia RM-100) (see figure 6.1 and figure 6.2) was renovated and repurposed for the task. This was then coupled with a Coherent Innova 70C argon-krypton ion laser operated at 514 nm.

The principle optical components within the spectrometer included an objective lens (numerical aperture and magnification of 0.4 and 20 respectively), an edge filter (rejection threshold of 10^{-4}) and a 2400 lines/mm diffraction grating. The edge filter is, in fact, a couplet actually consisting of two filters: an ultrasharp edge filter to allow successful acquisition of low wavenumber Raman scattering, and an additional moderately sharp edge filter to improve the rejection threshold and increase the width of the blocking band.

The necessary alterations to the Renishaw Raman spectrometer required to attain polarisation resolved spontaneous Raman scattering entailed the introduction of polarisation optics to ensure both a well-defined excitation polarisation, corresponding to either crossed (orthogonal excitation and detection polarisation) or parallel (parallel excitation and detection polarisation) polarisation, in addition to a linear detection polarisation. This was achieved by inserting a linear polariser and a half waveplate into the beam path before the Renishaw Raman system (see figure 6.1). Although typically the detection polarisation is rotated, due to the space limitations within the Renishaw system, which rendered rotating the analyser from cross to parallel positions between measurements both impractical and inaccurate, the inclusion of the half waveplate was necessary. The detection polarisation was then set using a linear analyser (see figure 6.2). In addition to allaying the practical difficulty of rotating the analyser, introducing a fixed analysis polarisation removed the requirement to account for the differing polarisation dependent reflectivities of the diffraction grating.

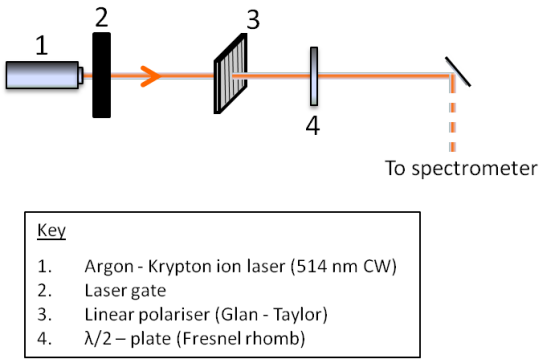

Figure 6.1 Diagram showing the main pre-Renishaw Raman system optics.

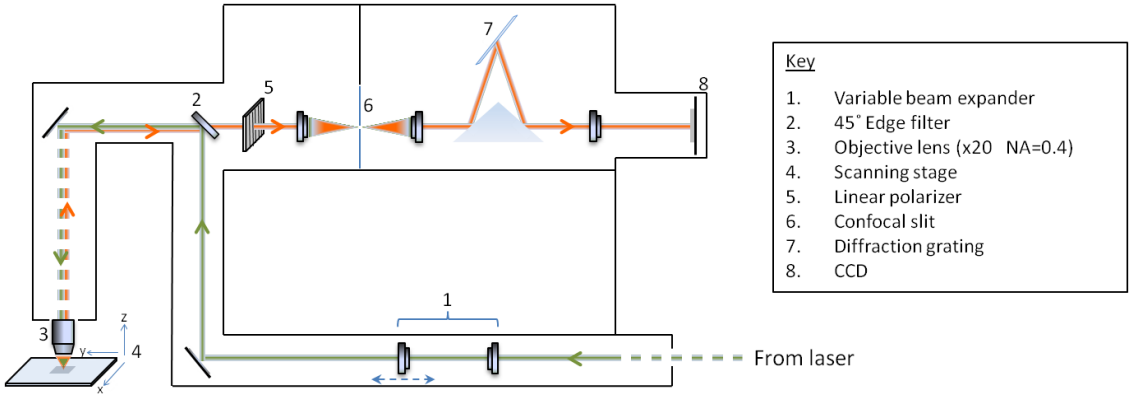

Figure 6.2 Diagram showing the main optics contained within a Renishaw Raman system.

6.3 Method

6.3.1 Sample preparation

Silicon samples were in the form of purchased pure/undoped wafers $\left(\text{top surface} : (110)\right)$. As is customary for silicon wafers the crystallographic axis was indicated by a straight cut in the side of the circular wafer. In this particular case the indicated axis was the $\langle 100 \rangle$. Due to sample size restrictions the large silicon wafers were cleaved, using a diamond scribe, along $\langle 100 \rangle$ to create smaller samples. Rotating the silicon samples by 54.7° allowed access to the $\langle 111 \rangle$ axis which was imperative for validating the polarisation alignment of the system [81].

All liquid samples used were of analytical standard ($\geq$ 99.9% purity): sourced from Sigma Alrdrich LLC. Two sample configurations were used to acquire spectra from liquids: dropcast on silicon, and encapsulated within a flow cell (developed and produced via 3D printing in house). The dimensions of the sample chamber within the flow cell were a 15 mm diameter clear aperture and sample thickness of approximately 40 μm.

One micrometre polystyrene beads samples (Sigma Aldrich LLC) were prepared by two different methods: on silicon, and on glass enclosed by a glycerol based mounting agent. The process of

mounting on silicon simply required dropcasting 8 µl of the polystyrene beads solution (10% w/v) onto a clean silicon wafer and allowing to air dry (under ambient conditions) for a minimum of 3 hours in a dust free location. The preparation on glass, again entailed dropcasting 8 µl of bead solution onto a standard microscope slide and allowing to air dry for a minimum of 3 hours. Once dry 8 µl of mounting agent was applied and left to dry for a further 3 hours prior to measurement.

The Polystyrene film used was provided with the Renishaw system as a purpose built spectroscopic grade test sample.

6.3.2 Polarisation resolved measurements

Careful alignment of the pre-Renishaw (excitation) and post sample (analyser) linear polarisers was required prior to any polarisation resolved measurements being acquired. Initially an intuitive approach was taken, firstly maximising the laser power passed by the excitation polariser (i.e. aligning the transmission axis of the polariser with the native polarisation of the laser) and subsequently setting the analyser orthogonal. In this configuration the action of the Fresnel - Rhomb would be solely to rotate the excitation polarisation by 90° and in so doing convert from crossed to parallel detection geometry and vice versa. The exceptionally strong plasma at line 520 nm (232 cm^{-1} shift in relation to the 514 nm Ar^{+} emission line) generated by the laser was used to characterise the extinction ratio with this polariser configuration[†]. This rudimentary approach, however, proved unsuccessful and thus an improved method was devised. This entailed rotating the Fresnel - Rhomb *in situ* to minimise the power, as measured by a power meter, through an additional polariser placed at the sample. Having determined the correct input polarisation to the Renishaw system, the analyser was incrementally rotated and the plasma line intensity monitored, via the CCD, to achieve the best extinction ratio.

As this approach yielded a considerably improved extinction ratio, testing of the system was then undertaken acquiring polarisation resolved data from silicon. Aligning the silicon [100] and [111] crystallographic axes with the set of orthogonal polarisation axes, defined in the sample plane by the Fresnel – Rhomb, allowed data to be acquired that could then be used to verify the polarisation alignment of the system by consulting the established literature.

Having verified the alignment of the system, polarisation resolved spontaneous Raman scattering spectra were acquired of several simple liquids (three elemental constituents or less and a molar mass < 100 g/mol): toluene, cyclohexane, ethylene Glycol and glycerol.

[†]Although experimentally often simpler, it is not possible to use the Rayleigh scattered light from silicon as it has an intrinsic polarisation behaviour that, analogous to Raman scattering, can be characterised by a depolarisation ratio. The expressions governing this behaviour are enormously complex and as such are significantly beyond the scope of this thesis. They can however be found in chapter 5 of reference [10].

Using a flow cell, the liquids were manually pumped into the acquisition chamber using a syringe. The pumping rate was determined by eye and chosen to minimise leaks and formation of bubbles whilst still ensuring a homogeneous liquid layer over the focal spot. Acquisition times were tailored to each sample with the aim of attaining high SNR spectra whilst taking into account the restrictions on flow rate and the possibility of cosmic rays impinging on the CCD.

As the CARS system developed, so the samples interrogated with polarisation resolved spontaneous Raman scattering progressed accordingly from bulk liquid samples onto more complex bead samples: a staple for characterising new microscopy systems.

In order to acquire the polarisation resolved spectrum of polystyrene beads, with minimal interference, the silicon substrate was aligned with the crystallographic [100] direction parallel/perpendicular to the polarisation of the incident light. Attempts to acquire spectra from several low bead density areas proved futile due to lack of signal. A spectrum from the dropcast polystyrene bead 'coffee ring' (the dense ring shaped region formed when the solvent in which particles are suspended is allowed to dry under ambient conditions) formed on silicon substrate was, therefore, acquired. Similarly a spectrum of the polystyrene beads enclosed in mounting agent on glass was also acquired again from the coffee ring region. As before the acquisition times were tailored to each sample with the aim of attaining high SNR spectra whilst avoiding saturation of the CCD and/or the detrimental effects of cosmic rays.

Sample spectra throughout were attained over the full spectral range (150-3250 cm^{-1}) in order to allow a complete comparison with SIPCARS data to be made.

6.4 Results and Analysis

The first attempt to align the excitation polariser and analyser orientations to acquire polarisation resolved spontaneous Raman measurements proved largely unsuccessful, yielding an extinction ratio of only 1:9. From the data acquired using a system with an extinction ratio of this magnitude it may be possible to perform a qualitative analysis of the whether a given peak is polar or depolar; however, this data would be of little use for quantitative measurements. After determination of the polarisation properties of each individual optical component within the Renishaw system it was evident that the edge filter couplet was responsible for the resultant extinction ratio. A new method taking into account the polarisation scrambling effect of the edge filter couplet was therefore devised. The resultant extinction ratio of this method was 1:50. This was a significant improvement and, whilst not as high as desired, still permitted quantitative analysis of spectral form and depolarisation ratio to be achieved. In order to improve this extinction ratio it was necessary to further compensate for the elipticity introduced by the edge filter couplet by introducing a quarter waveplate and iteratively tuning it *in situ*.

To ensure the validity of this alignment, spectra were then acquired using silicon test samples with known crystallographic axes (see figure 6.3) and compared with the literature [81] [82]. The resulting spectra closely conformed to those found in the literature exhibiting the correct one- and two- phonon peak positions and relative intensities. This strongly suggested that the Renishaw system had been correctly adapted and aligned to allow the successful acquisition of quantitative polarisation resolved spontaneous Raman scattering spectra.

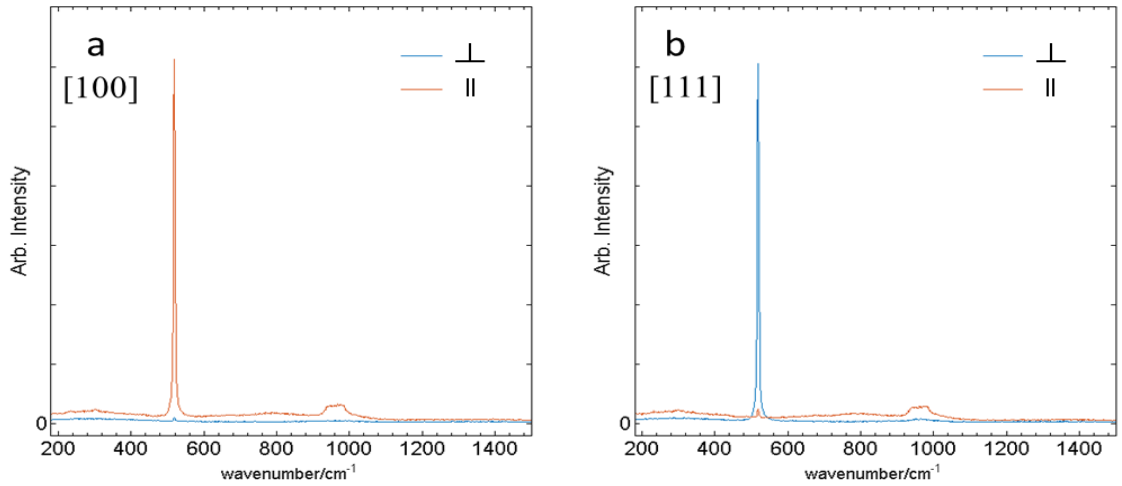

Figure 6.3 Polarisation resolved spontaneous Raman scattering of silicon aligned parallel (∥) and perpendicular (⊥) to the a) [100] and b) [111] crystallographic axes. The spectra have been cropped to remove featureless regions. Acquisition time: 20 seconds.

Initially chosen for both their simplistic isotropic nature, and relative ease of preparation for CARS microscopy (see chapter 7), toluene, cyclohexane, ethylene glycol and glycerol proved problematic. The liquid nature of these samples initially hampered attempts to acquire polarisation resolved spontaneous Raman scattering spectra as dropcasting on silicon, an expedient preliminary approach, proved unsuccessful due to evaporation or transient movement over the acquisition period. Considering this, a flow cell was developed in house and employed to negate these effects. The small internal diameter of the flow cell, approximately 400 μm sample thickness, resulted in a small but not insignificant glass background when acquiring with a 50 μm confocal slit. To correct this the alignment was refined and the slit reduced to 10 μm. Whilst significantly reducing the signal, and thus necessitating considerably longer acquisitions times, this did have the desired effect of producing spectra with a less substantial glass background (see figure 6.4). In addition to reducing the slit width the collection area of the CCD significantly narrowed in order to produce high SNR spectra.

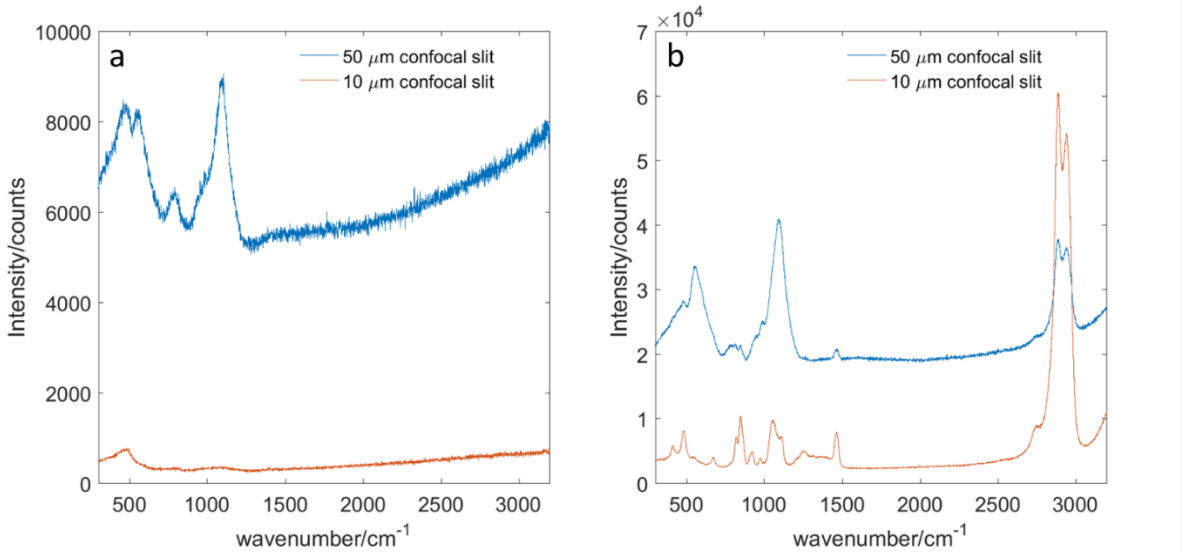

Figure 6.4 a) Spontaneous Raman spectra of an empty flow cell. Acquisition time 30 seconds. Spectra are corrected for differing incident power. The form of the spectrum acquired with a 50 μm confocal slit is equivalent to a typical borosilicate glass: containing large peaks at ~ 550 cm^{-1} and ~ 1090 cm^{-1}. b) Spontaneous Raman spectra of glycerol passing through the flow cell. Notably a fivefold increase in acquisition time was required after the slit width was decreased (from 60 to 300 seconds). The glass background has, however, been supressed. In both a) and b) the blue and red spectra were acquired with a 50 μm and 10 μm confocal slit widths respectively.

The spectra of toluene, cyclohexane, ethylene glycol and glycerol obtained using the flow cell in conjunction with a 10 μm confocal slit are shown in figure 6.5. It is immediately apparent that the spectra acquired have a high SNR and contain no discernible glass background. Additionally the approximate spectral resolution of the system (as determined from the FWHM of the Rayleigh scattered light) is ~ 3.5 cm^{-1} which, given the typical line width of a resonance within an organic compound is greater than 7 cm^{-1}, suggested that the observed spectra were, in fact, the native resonant signature of the sample with minimal interference from the system [22]. Comparing the spectra with the literature [75] [83] there is good agreement throughout (both spectral form and relative peak heights): all discrepancies are within the spectral resolution of the system. As potential calibration/test samples for the SIPCARS system the toluene and cyclohexane spectra appear promising, both containing a variety of intense narrow spectral features throughout the FPR and CH-stretch region. Whilst it is true the spectra of glycerol and ethylene glycol also have features in both regions they are significantly weaker and, in contrast to the previous two spectra, exhibit complex broad spectral features. It is for these reasons that toluene and cyclohexane were subsequently extensively used as SIPCARS samples. The process by which the difference spectra were extracted is detailed above; however, it is worthwhile emphasising that polarisation resolved Raman scattering yields spectra containing peaks that may be either positive, or negative. This is an expected result and although not often seen in contemporary Raman literature it is a revival of an antiquated approach as opposed to a novel method. The derived difference spectra further

illustrate the complex, non-trivial, nature of the peaks contained within the FPR of glycerol and ethylene glycol. Unusually there exists previous polarisation resolved Raman scattering data for toluene and cyclohexane which compares favourably with these present measurements.

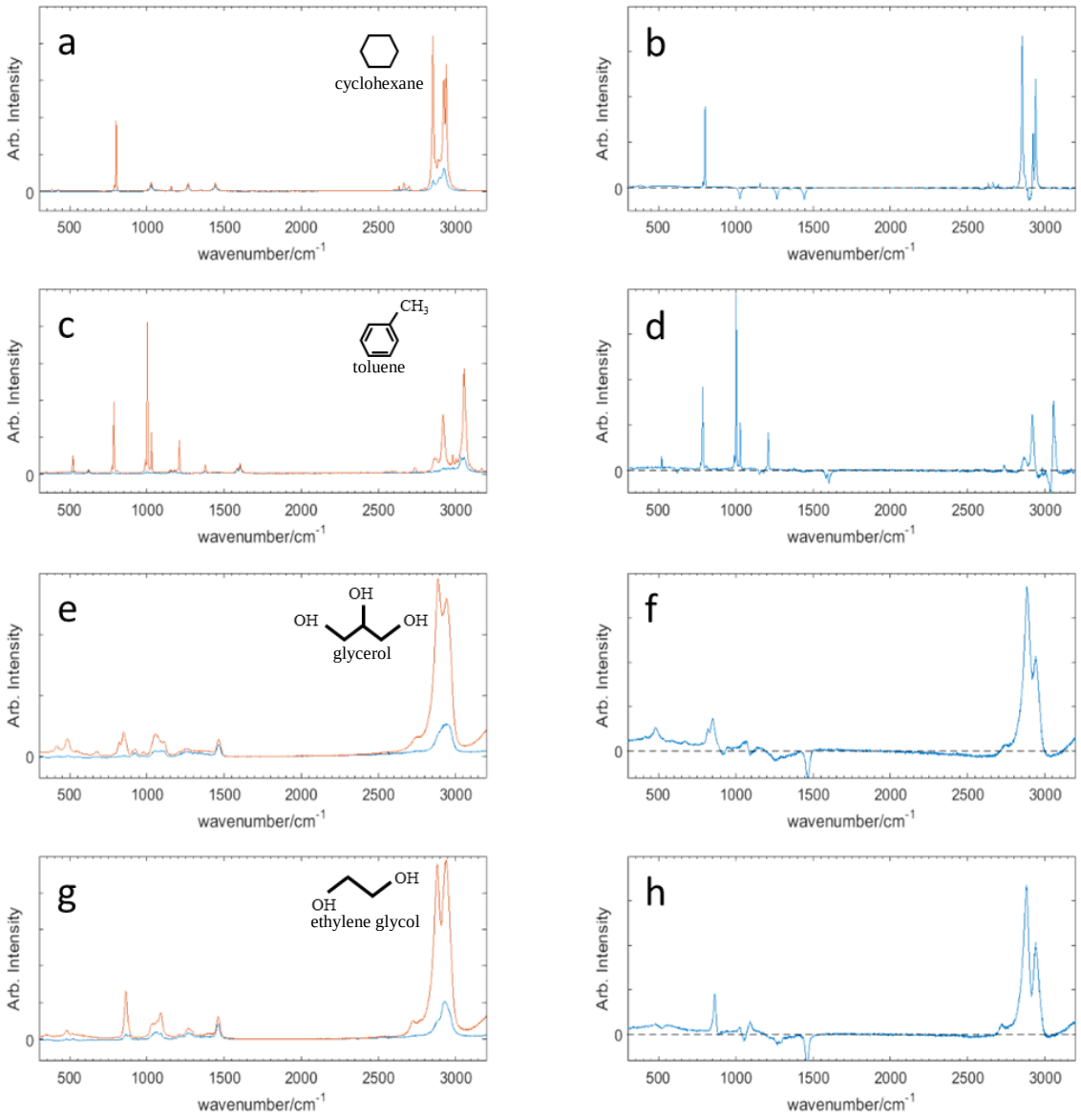

Figure 6.5 Polarisation resolved spontaneous Raman scattering measurements of the simple liquids samples. The spectra (a, c, e and g) derived from the parallel and perpendicular detection geometries, depicted in red and blue respectively, are shown adjacent to their respective $(I_{\parallel} - 3I_{\perp})$ spectra (b, d, f and h). Insets show the chemical structure of each liquids.

The most readily available and, consequently, the first candidate for polarisation resolved spontaneous Raman scattering beyond simple liquids, was polystyrene beads. Ideally, to compare the SIPCARS and polarisation resolved spontaneous Raman scattering spectrum of polystyrene the same bead-type sample would be used on both systems: but this did not prove feasible. Measurements attempted from isolated single beads (or clumps appearing to contain only a few beads) did not yield enough signal to perform a meaningful analysis, even with acquisition times in excess of 30 minutes. Furthermore measurements from within the densely populated coffee

ring resulted in an agglomeration of spherical beads within the focal volume of the Renishaw spontaneous Raman scattering system, and thus severe polarisation scrambling due to multiple reflections, which did not improve significantly with the addition of refractive index matching mounting medium. Figure 6.6 clearly illustrates the unphysical relationship between the spectra derived from the parallel and perpendicular detection geometries as several peaks exhibit depolarisation approaching unity: considerably greater than the maximum allowed $^3/_4$ value. Consequently, to overcome this, spectra were acquired from a thin film of polystyrene (pure, purpose built spectroscopic grade) which did not exhibit any polarization scrambling behaviour (see figure 6.7). The sample also appeared to possess rotational symmetry in the measurement plane as there was no orientation dependence of the depolarisation ratio. Whilst it is not possible to state conclusively whether the polystyrene film is representative of the beads it is highly likely that any differences would be very small in nature and subsequent CARS measurements (see chapter 10) suggest, to within the resolution of the system, they are negligible. The polarisation resolved spontaneous Raman measurements notwithstanding, if, using the SIPCARS system, a lack of obvious polarisation scrambling behaviour from the polystyrene beads is assumed, the high degree of spectral information possessed by this particular sample renders it valuable as a potential spatial resolution and multiplexing test sample.

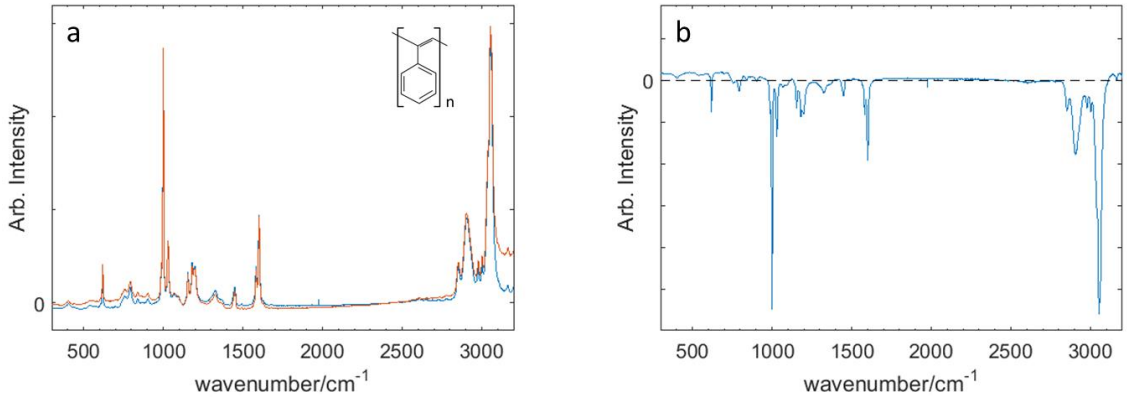

Figure 6.6 a) Polarisation resolved spontaneous Raman scattering spectra of 1 µm polystyrene beads on glass covered by mounting agent. Several of the peaks exhibit an unphysical ρ≥1, such as the ring breathing mode (~ 1000 cm^{-1}). An acquisition time of 120 seconds was used in conjunction with a 10 µm confocal slit width and an incident power of 43 mW. Parallel and perpendicular detection geometries are shown in red and blue respectively. Inset show the chemical structure of polystyrene. b) The corresponding $(I_{\parallel} - 3I_{\perp})$ spectrum.

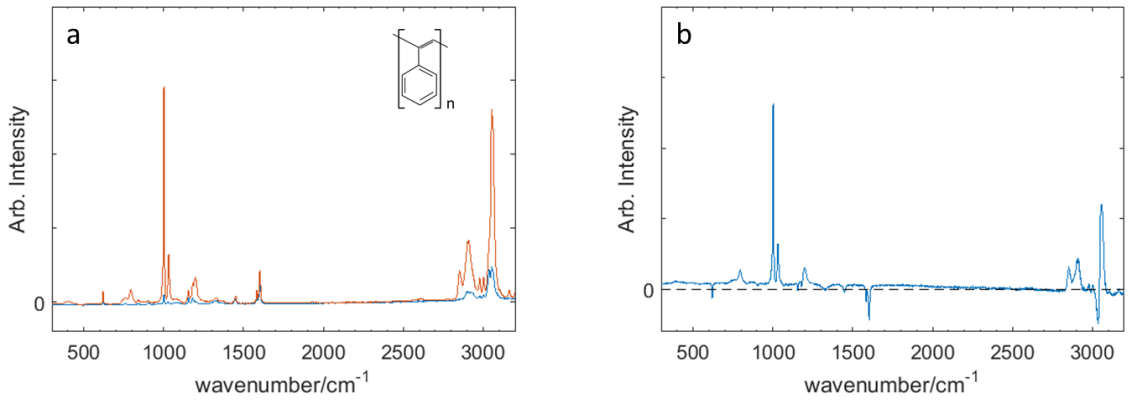

Figure 6.7 Polarisation resolved spontaneous Raman scattering spectra of a pure polystyrene film. a) Parallel and perpendicular detection geometries are shown in red and blue respectively. The depolarisation ratios of all the peaks are within the expected range. Inset show the chemical structure of polystyrene b) The $(I_{\parallel} - 3I_{\perp})$ spectrum containing a significant amount of spectral information thoughout the FPR and CH-stretch region in the form of positive and negative narrow features. An acquisition time of 60 seconds was used in conjunction with a 50 µm confocal slit width and an incident power of 20 mW.

While it was possible to source a suitable thin film sample of polystyrene it proved exceptionally difficult to acquire similarly pure thin films of other polymer materials, including poly methyl methacrylate (PMMA) and 1,3,5-Triazine-2,4,6-triamine (melamine), which were subsequently used as CARS bead samples. It was also impractical to manufacture these in house due to the time and expenditure needed to perform a full chemical characterisation to confirm the chemical structure, and ensure the required purity was achieved.

6.5 Limitations

The limitations of these measurements can be separated into inherent limitations of the technique and of this system specifically.

It would appear, although spontaneous Raman scattering is a ubiquitous analytical chemistry technique [84] that, despite potential advantages, the practice of acquiring polarisation resolved measurement has never really gained traction. The primary reason for this is that the SNR, particularly in the crossed polarisation detection geometry, is typically exceptionally small, even for spontaneous Raman scattering: an already weak scattering effect (relative to Rayleigh scattering). Acquisition of polarisation resolved spontaneous Raman scattering, therefore, requires a high sensitivity detector and either long exposure times, or high incident laser powers, both of which can induce sample heating and/or photodamage. Practically, for conventional spontaneous Raman scattering of delicate biological samples, the preferred route is to limit the incident power and extend the exposure time accordingly [85]. If, however, a 1 mW incident power was used for a polarisation resolved measurement this would result in acquisition times on the order of tens of minutes for a single point spectrum for the strongest bulk scatters (e.g. pure

solvents such as toluene or cyclohexane). In practice this technique is realistically limited to samples that can tolerate high incident powers (up to and, in fact, exceeding 1W), long exposure times and consist of strongly scattering molecules, in other words analysis of inorganic compounds, solvents, and crystals.

The particular modified Renishaw Raman microspectrometer implemented at KCL has, in addition to the specific limitations of the make and model, several unique limitations. Within the body of the Renishaw system there are nine non anti-reflection coated optics in the beam path prior to the sample. If optical components preceding the main body of the system are included this becomes (when configured for polarisation resolved measurements) a minimum of twelve. In practice, however, given the addition of external mirrors on the optical table, to facilitate alignment, and the remote location of the laser (adjacent room requiring the use of a periscope), the number of uncoated optics prior to the sample was sixteen. Taking an optimistic view that the average transmission (reflectance in the case of mirrors and the long pass filter) is 95% this would equate to less than 45% of the laser power onto the sample. In reality the actual percentage throughput onto the sample was less than 15% (40 mW total power on to the sample with a 275 mW laser output). This is likely due to degradation of the optics over time and power losses through the beam expander. If the path of the back scattered light is now considered, an additional nine uncoated optical components, including the diffraction grating, must be traversed prior to the CCD. The net effect of this multitude of uncoated optics it that an already immensely weak scattering effect is significantly attenuated. In many ways the fact that polarisation resolved spontaneous Raman scattering can be attained at all is a testament to the quality of the edge filter couplet and the CCD. It is hardly reasonable to suggest a lack of power as a limitation given the Coherent Innova 70C, when operating optimally, is capable of producing over a 1 W of power at 514 nm. At the time these measurements were performed, however, the laser was also producing sufficiently strong plasma lines, that despite the addition of a pair of 514 nm laser line filters, the laser had to be turned down so as to avoid significant leakage into the acquired spectra and in some cases saturation of the CCD. The addition of otherwise unnecessary optical components into the beam path, resulting in lower incident power onto the sample, served to exacerbate the situation. Another final partial limitation of the system was the low numerical aperture lens (highest available at the time) which would have served to significantly increase the already stretched acquisitions times.

Whilst the above limitations are substantial they are by no means insurmountable. As the polarisation resolved spontaneous Raman scattering signal is so weak it would be beneficial to construct an open optical table system, and in so doing limit the number of optical components through which the incident beam has to pass prior to the sample and the back scattered beam before the CCD. The advantages of simply modifying the Renishaw are, however, numerous as in optimum working condition it allows rapid full spectral range (150-3400 cm^{-1}) conventional

spontaneous Raman scattering to be acquired. The inherent stability of the Renishaw system, coupled with the automatic calibration of the motors (beam expander and diffraction grating), result in a system that should require minimal user intervention. Ideally, if retaining the Renishaw system, the laser should be as close as reasonably possible to the input port, whilst also ensuring optimal alignment though the system and using a high numerical aperture (NA≥ 0.8) lens.

Unfortunately before these limitations could be rectified and the system used to start building a working directory of depolarisation ratios the ability to acquire measurements was lost. As despite being of great importance to the overall development and continued application of SIPCARS, the polarisation resolved spontaneous Raman spectrometry system implemented at KCL was dismembered by unauthorised individuals during the second quarter of 2013 and despite best efforts has yet to be brought back into full working order. Whilst this body of work was undoubtedly cut short and therefore failed to achieve its full potential it did yield enough data/information to identify several potential test samples and illustrate the viability of a polarisation resolved Raman approach.

7. CARS based on a commercially available supercontinuum source

7.1 Motivation

There are several aspects of a BCARS system based around a commercially available supercontinuum source that are appealing; however, before addressing these, a comment should be made about the availability of such a source. When this project was first conceived (2007) commercially available turn-key supercontinuum generation systems were a relatively new technology (post-millennium) as, although supercontinuum generation had been studied since the 1960s [27], progress towards a high power (multi-watt), small foot-print, turn-key solution had only really started in earnest since 1996 following the work of *Knight et al* [86]: establishing a robust fabrication process for PCF.

Set in this context, one of the primary initial aims of this project was simply to establish whether a CARS system using this recently developed 'off the shelf' supercontinuum generation approach was, in fact, viable. The typical approach to generate a supercontinuum for use in BCARS, at the time, was to employ a high peak power titanium-sapphire oscillator in conjunction with a free standing PCF [87]; however, this is far from trivial. A significant amount of practical expertise is required to initially align and maintain such a system. In addition to the novelty of a turn-key solution, the ability to construct a BCARS system requiring little or no user set-up/maintenance (at least of the source) is highly appealing and would potentially widen the user base from highly specialised physics labs to the wider scientific community: including biologists, medics, crystallographers, analytical chemists *etc.*. An additional significant advantage of departing from the conventional titanium – sapphire oscillator model is expense. The cost of a titanium sapphire oscillator including high power CW pump laser (or single-box equivalent) is usually upwards of £120,000 whilst the fibre based turn-key approach, discussed above, costs in the region of £35,000.

In addition to the practical benefits of these novel fibre based supercontinuum systems, if the spectral characteristics of the Fianium (SC-400) system employed at KCL are considered, there are other apparent advantages. Whilst the spectral extent of supercontinuum generated by the Fianium system is in excess of 1600 nm the vast majority of the power is located between 1050 - 1650 nm. This is significantly redshifted with respect to a titanium-sapphire based supercontinuum which, when utilising a PCF pump wavelength in the region of 780 - 800 nm, is typically located between 800 – 1100 nm. The ~1050 nm pump/probe wavelength used with the Fianium system is also significantly longer than 780 - 800 nm typically used in a titanium - sapphire based system. Redshifting the entire CARS process results in an increased sample penetration depth, due to wavelength-dependent absorptivity (Beer-Lamberts law), and a reduction in one- and two-photon sample autofluorescence [88].

Considering the above posited advantages and potentially wide reaching benefits of a BCARS system using a fibre based supercontinuum source there was a strong argument for exploring the merits of such a system in reality. A system was, therefore, constructed at KCL with the aim of investigating these prospective advantages: details given below.

Construction of this system occurred at the beginning of this Ph.D. therefore Dr. Littleton took the lead with the author using the opportunity to gain familiarity with the optical components and alignment techniques. The initial method and set-up were devised by Dr. Littleton, however, subsequent alterations and improvements were accomplished in close collaboration with the author. The data presented in this chapter was acquired by Dr. Littleton, with the exception of section 7.4.3 which was an individual effort on the part of the author.

7.2 Apparatus

7.2.1 Initial setup

7.2.1.1 Fianium SC-400 supercontinuum pulsed laser source

The Fianium SC-400 supercontinuum pulsed laser source used was equipped with a factory installed modification allowing it to produce both the required supercontinuum broadband (405 - 2000 nm) and auxiliary narrowband beams (1045 - 1055 nm), with an average pulse duration of 400 femtoseconds, repetition rate of 20 MHz, and an integrated beam power of 2 watts in each beam [89]. The broad and narrowband beams were produced anti-synchronously, resulting in a 25 nanosecond period between their relative emissions, thus necessitating the presence of an exceptionally long folded delay line in the pump arm to bring them back into temporal overlap.

Narrowband pump/probe beam:

The narrowband output of the Fianium system (i.e. CARS pump/probe beam) was generated via amplification of a low-power passively mode-locked ytterbium fibre laser source: the initial seed produced by an IR laser diode [89]. In greater detail this was achieved by using a fibre resonator in conjunction with a short lasing cavity containing an intensity dependent saturable absorber. This established a fixed phase relationship between lasing modes, consequently allowing the production of a femtosecond pulse train [90]. Amplification was then attained using a double clad optical fibre pumped by a high power multi-emission laser diode [89]. Operating at full power this produced an output beam of 10 nm spectral width centred on 1050 nm.

Supercontinuum Stokes beam:

The supercontinuum broadband Stokes beam was created via the same mechanism as the narrowband pump beam, however, prior to emerging from the Fianium system, the beam passed through a PCF (many metres). The effect of the PCF was to convert the incident narrowband laser

beam into a supercontinuum [27]. Whilst the total spectral extent of the Stokes beam was significant (in excess of 1500 nm) the majority of the laser power was situated between 1050 and 1650 nm. It is worthwhile noting that although the details of the PCF used are proprietary knowledge some inferences may be made: the output of the fibre was unpolarised therefore it is a reasonable assumption that the fibre is not polarisation maintaining, and, given the chromatic dispersion of the supercontinuum (shown in following sections), the major broadening mechanism occurs in the anomalous GVD regime and most likely occurs over many metres of PCF due to the large extent of this effect.

7.2.1.2 The post laser/pre-microscope optics

Narrowband (pump/probe) beam:

The narrowband (∼10 nm) pump beam (see figure 7.1) was passed, via a collimating lens to correct slight beam divergence, immediately into a 7.5 metre delay line (achieved via multiple passes between retroreflectors) on exiting the laser allowing temporal overlap with the Stokes beam to be achieved (eventually verified by the presence of CARS). After this it propagated through an angled tuned 1064 nm band pass filter in order to reduce the bandwidth to 4 nm. The combination of linear polariser, half waveplate and quarter waveplate through which the beam subsequently propagated allowed an elliptical polarisation of arbitrary orientation and ellipticity to be set. The beam then reflected from a 1064 nm long pass filter, propaging collinearly with the Stokes beam from this point onward. In this geometry, at a non-zero degree angle of incidence, this particular 1064 nm long pass filter acted to transmit wavelengths longer than 1060 nm, whilst reflecting those below this.

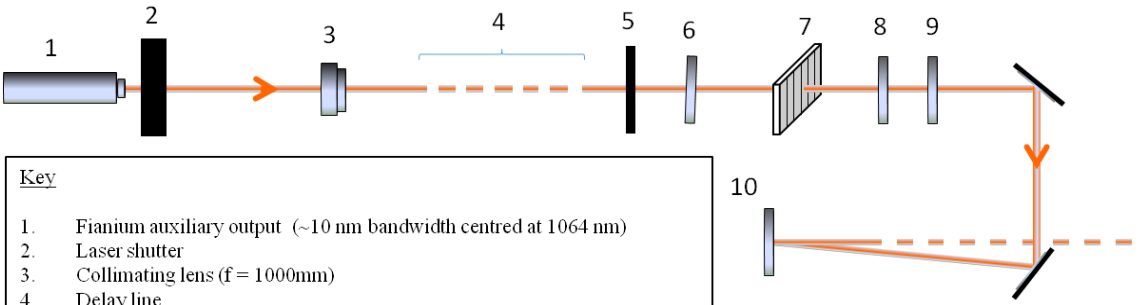

Figure 7.1 The main optical components of the narrowband pump/probe beam arm up to and including the point at which it is recombined with the Stokes beam.

Broadband (Stokes) beam:

After exiting the laser (see figure 7.2) the Stokes beam passed through an initial 1050 nm long pass filter, delimiting the lower extent of the broadband beam, and a beam expander to match the

diameter of the pump/probe beam. After this the beam then passed through an additional 800 nm long pass filter as the blocking band of the 1050 nm filter proved insufficient to remove the shortest wavelength components of the supercontinuum. Following this a linear polariser was used to set the polarisation axis, and the beam recombined with the pump/probe beam by means of an angle tuned 1064 nm long pass filter. The two beams were then passed into the microscope via a final beam expander in order to match the 13 mm back aperture of the top objective lens.

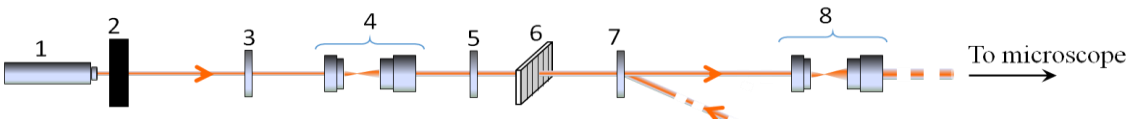

Key

1. Fianium supercontinuum output (~ 1600 nm bandwidth)
2. Laser shutter
3. 1050nm long pass filter
4. Beam expander (mag. = 1.5)
5. 800nm long pass filter
6. Linear polarizer
7. 1064 nm long pass filter (minimal angle tuning < 5 °) (optic 10 in figure 7.3)
8. Beam expander (mag. = 1.5)

Figure 7.2 The main optical components of the broadband Stokes beam arm including the recombination of the pump/probe beam and onward propagation to the microscope

7.2.1.3 Nikon Eclipse TE-2000-E inverted microscope

Key

1. Collinearly propagating pump and Stokes beams
2. Objective lens (x40 NA=1.3 oil immersion)
3. Scanning stage
4. Sample (between two cover slips)
5. 1000nm short pass filter
6. Wollaston prism
7. Lens (f = 100mm)
8. λ/4 – plate
9. Lens (f = 50mm)
10. Spectrometer entrance slit

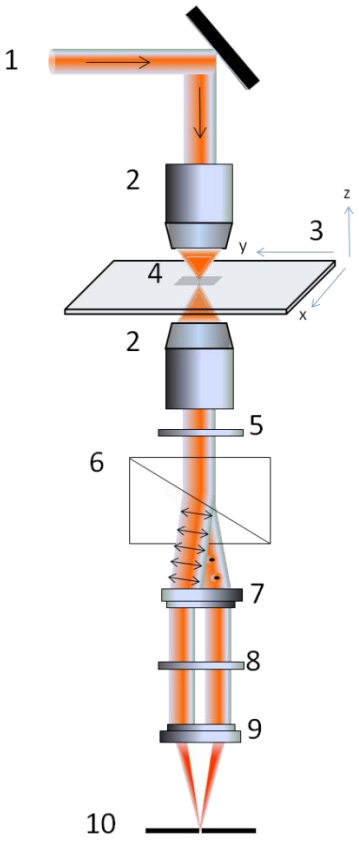

Figure 7.3 The main optical components of the microscope used, including stage assembly and pre-monochromator optics. Inset photograph of the microscope.

The microscope used in this experiment was a customised Nikon Eclipse TE-2000-E (see figure 7.3). Illumination and subsequent collection from the sample was achieved using two identical Nikon Plan Fluor DIC oil immersion lenses (NA 1.30 ×40) in a diascopic geometry. Samples of thickness less than 60 μm were sealed between two coverslips in order to allow focusing. The resultant beam then propagated though a 1000 nm short pass filter to reject any light that may have passed unaffected through the sample and was subsequently split by a Wollaston prism into two orthogonal polarisations which, propagating separately, were then circularly polarized via a quarter waveplate, so as to account for differing grating reflectivities prior to passing into the monochromator. A combination of two lenses in the beam path after the microscope were used to focus the beams onto the entrance slit attempting to match the NA of the monochromator (NA = 0.12). Due to complex alignment requirements (given in section 7.3.1) the eventual configuration was a compromise which left a significant mismatch between the intrinsic NA of the monochromator and the actual NA of the focused beam ($NA_{beam} < NA_{monochromator}$). Although not shown on this diagram there were also two alignment cameras: one situated before the top objective and the other attached to an auxiliary output port at the base of the microscope after the Wollaston prism.

7.2.1.3 Bentham TMc300 monochromator and Andor iXonEM camera

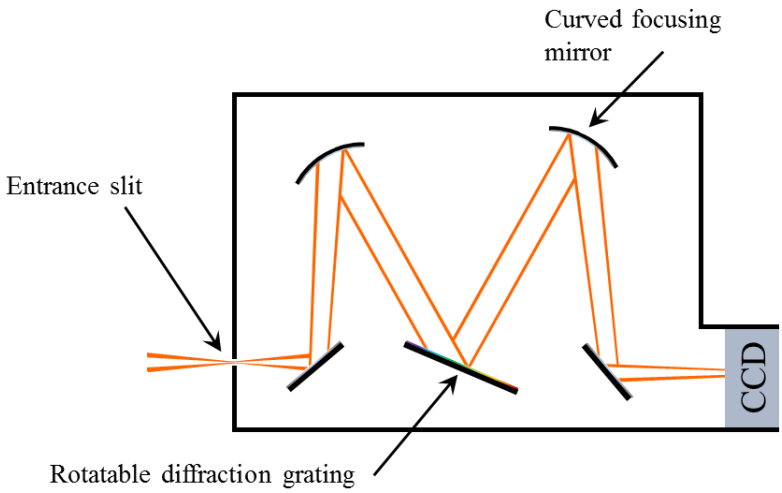

Figure 7.4 Diagram showing the Czerny-Turner type Bentham TMc300 monochromator used and the location of the Andor iXon EMCCD. Note the path through the monochromator of each beam shown is only an approximate representation. In reality the two beams are vertically displaced as opposed to horizontally, as shown on the diagram for ease of depiction.

A Bentham TMc300 Czerny-Turner type monochromator (see figure 7.4) was used in this experiment in conjunction with a Peltier cooled Andor iXon^{EM} 897 camera; the wavelength range of interest selected by rotating the diffraction grating (150 l/mm and 600 l/mm gratings were used for complete spectral range and for high resolution small spectral regions of interest respectively). The Andor iXon^{EM} camera utilized an electron multiplying charge coupled device (EMCCD) consisting of both a lateral and vertical elongation of the shift register in comparison to a normal CCD [91]. The vertical and lateral extensions of the shift register allowed both frame transfer and on-chip electron multiplication to be implemented [91]. Whilst frame transfer was not actually used in this experiment electron multiplication was used extensively, especially during high acquisition rate scans. An EMCCD achieves an appreciable gain whilst minimising the effect of electronic noise by exploiting 'impact ionization', a process whereby, when the charge moves along the register it creates a secondary charge, thus causing amplification of the signal [91]. For this to occur the initial charge must have sufficient energy and, therefore, the probability of this occurring naturally in a normal CCD is negligible; however, by laterally extending the shift register (i.e. creating a multiplication register) and increasing the charge's initial energy, it is possible to stimulate this process [91]. By this method the Andor iXon^{EM} EMCCD may achieve gains of up to 300 times; however, the optimum signal to noise ratio is found at approximately a gain of 30 times. Using the Andor iXon^{EM} EMCCD the intensity, in relation to wavelength, was recorded across the wavelength range of interest. Whilst the beam paths shown in figure 7.3 are not accurate, serving only as an illustration of the concept, they highlight that the two beams stemming from the Wollaston prism propagate entirely separately though the monochromator. In reality, the beams are, in fact, vertically displaced rather than horizontally (with respect to the optical table) as a result of which they are vertically displaced on the EMCCD and thus may be detected in two separate sets of pixels (tracks) simultaneously: see figure 7.5. Additionally, owing to the circular polarisation imparted by the quarter waveplate prior to the monochromator, the transmission through the monochromator should in theory be equivalent for each beam.

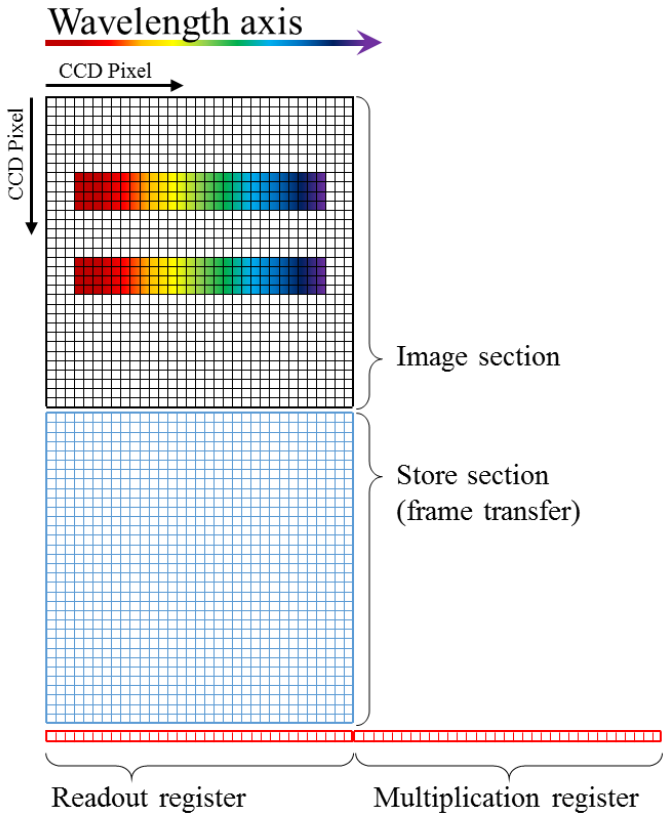

Figure 7.5 Schematic of the Andor iXonEM EMCCD chip. Shown on the primary imaging section (the exposed potion of the chip) are the two tracks. Note that the readout direction of this region is top to bottom. The lateral dispersion of spectra across this region dictates the wavelength axis. Shown in blue is the store section where, if frame transfer mode is utilised, the entire frame is rapidly shifted down prior to reading out. This process allows another frame to be captured whilst the slow process of reading out is performed thus significantly reducing camera dead time. The data may be read out of the readout register in either direction: right to left (conventionally) or left to right through the multiplication register where it undergoes amplification. A slight complication arises from this, as dependent on the direction of readout, the spectra maybe reversed. Whilst this EMCCD may be operated independently of the multiplication register the store section is an intrinsic component and actually acts to slow readout (negligibly in comparison to the exposure times used) if frame transfer is not used [91].

7.2.2 Set-up after alterations

Following the initial setup several technical issues were soon discovered which led to the alteration of both arms of the system. The spectral resolution of the initial CARS experimental setup was dictated by the spectral width of the pump beam and not, as might have been expected, by optical imperfections or by the mismatch in NA of the microscope setup with the monochromator. To reduce the spectral width of the pump beam, and thus improve the spectral resolution of the system, a laser chirp was introduced (see figures 7.6 and 7.7). The initial diffraction grating of the laser chirp acted to disperse the incident beam, resulting in the shorter wavelength components travelling a greater distance to the second diffraction grating than their longer wavelength counterparts. The second diffraction grating then recollimated the beam

resulting in a net reduction of the spectral width (see figure 7.7). The reduction in spectral width derived from this particular laser chirp was 2.0 nm, consequently reducing the spectral width to 2.0 nm. The additional optical path length derived from the laser chirp also allowed the delay line to be unfolded. With the introduction of this laser chirp the limiting factor became the mismatch of NA between the microscope and the monochromator. This was partially alleviated by moving the monochromator and altering the coupling optics, however, the mismatch remained but to a lesser extent.

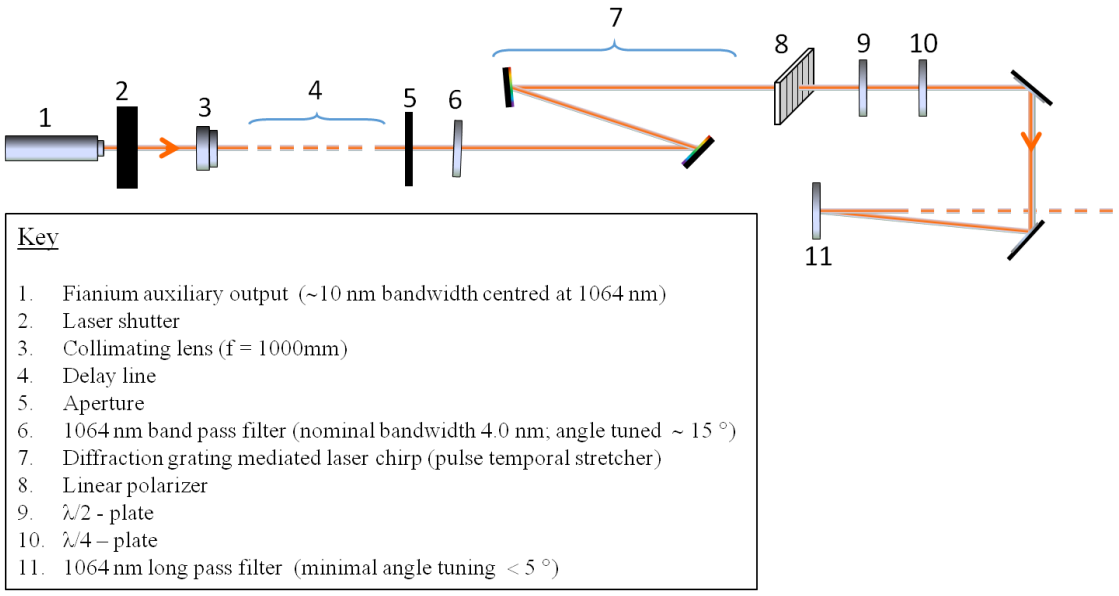

Figure 7.6 Altered narrowband pump/probe beam path incorporating a diffraction grating mediated laser chirp resulting in a ~2 nm narrowband beam.

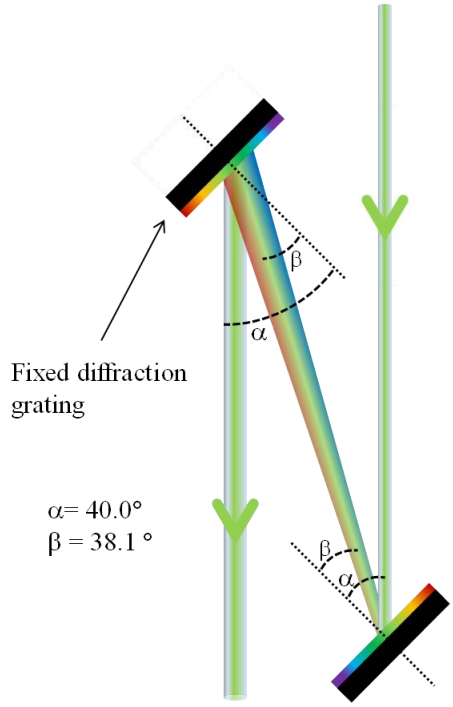

Figure 7.7 Expanded view of the diffraction grating pulse temporal stretcher (two identical 600 l/mm gratings separated by 30 cm). This diagram has been exaggerated in order to illustrate the principle as the total reduction in spectral width was only from 4 to 2 nm.

Whilst reducing the spectral width of the narrowband pump/probe beam and thus improving the spectral resolution of the system required a relatively conventional approach, compensating the exceptionally large negative dispersion of the Stokes beam necessitated a more inventive, unorthodox solution (proposed and implemented by Dr. Littleton).

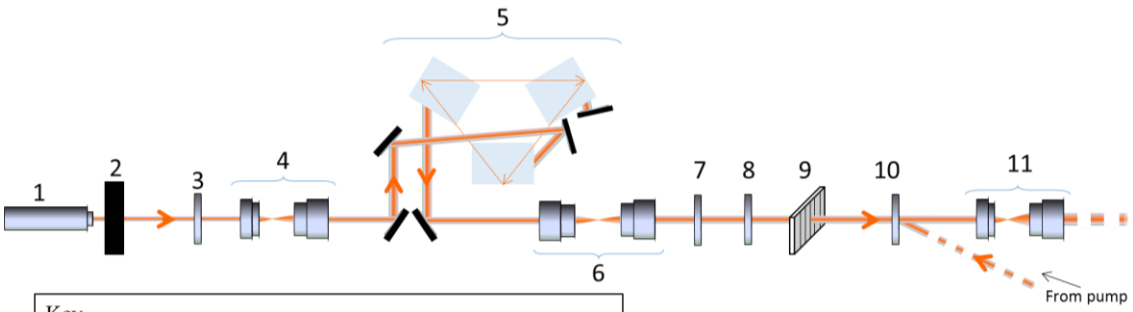

Key

1. Fianium supercontinuum output (~ 1600nm bandwidth)
2. Laser shutter
3. 1050nm long pass filter
4. Beam expander (mag. = 1.5)
5. Beam circulator
6. Beam expander (mag. = 1)
7. 800nm long pass filter
8. 1050nm long pass filter
9. Linear polarizer
10. 1064 nm long pass filter (minimal angle tuning < 5 °)
11. Beam expander (mag. = 1.5)

Figure 7.8 Diagram illustrating the location of the beam circulator and additional beam expander within the altered Stokes beam arm.

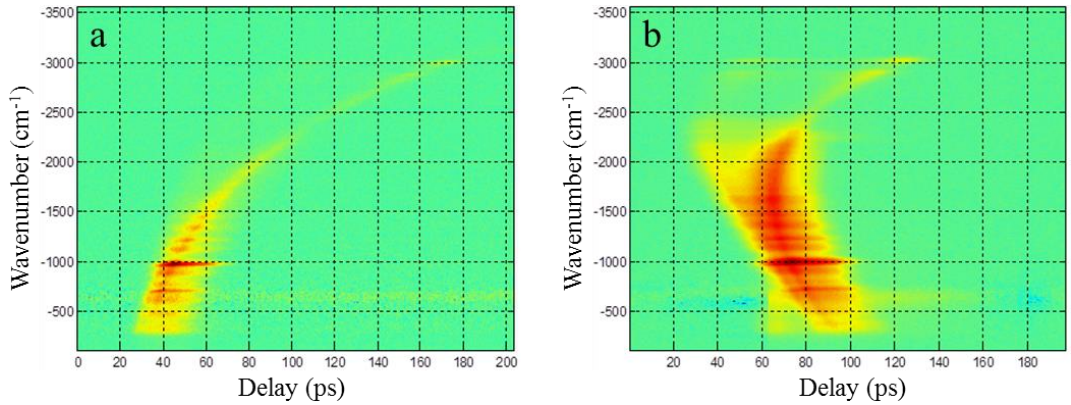

Figure 7.9 Intensity (log) plots (where red denotes the highest intensity) showing the relative dispersion of the Fianium broadband supercontinuum pulse a) before, and after b), the addition of the beam circulator.

The true extent of the initial negative dispersion of the Fianium broadband supercontinuum pulse can be seen by inspection of figure 7.9a: the pulse was dispersed over greater than 160 ps. Even taking into account the temporal elongation of the pump pulse (on the order of 4 ps at the dichroic filter) introduced by the chirp, it was not physically possible to achieve significant temporal overlap of the two beams. This effect significantly reduced the ability of this system to attain single shot broadband spectra, allowing only limited spectral regions to be probed.

The addition of the beam circulator (see figures 7.8 and 7.10), which acted to introduce a positive dispersion by circulating the beam through approximately three metres of glass (~ 17 complete rotations), allowed the longer wavelength components to become temporally overlapped with the shorter components (see figure 7.9b). This resulted in a broadband beam where it was possible, by adjusting the delay line, to achieve a CARS spectrum covering a spectral region including both the FPR and the CH-stretch region.

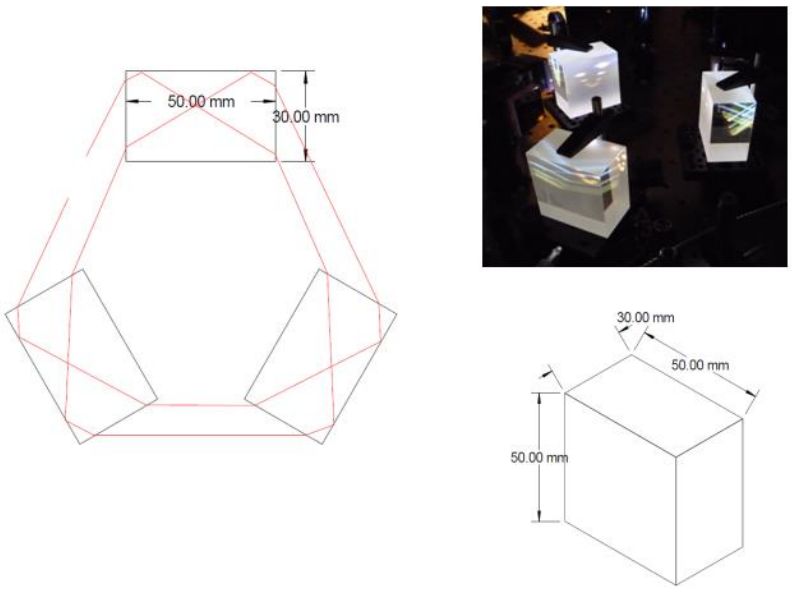

Figure 7.10 Diagram illustrating the physical dimensions of the Stokes beam circulator. The glass blocks used were constructed from of H-ZF13 glass which is functionally equivalent to SF-11 Schott glass.

The introduction of aberrations by the Stokes beam circulator necessitated the addition of a correction 1-to-1 lens couplet: with the second lens slightly angled with respect to the first (tuned by eye).

7.3 Method

7.3.1 Initial alignment

As the system was aligned according to conventional practices, this section will focus on the unusual aspects of this particular alignment (after the initial alterations). Considering the length of the pump/probe beam delay line, even after unfolding, extra special care was taken to ensure the motion of the retro-reflector was axial with respect to the beam. This is exceptionally important as any lateral translation of the pump/probe beam, while tuning the delay between the beams, would manifest as an alteration of the spatial overlap of the beams in the sample plane and thus a reduction in CARS signal. Additionally, the specific location of the beam on the retro-reflector was chosen so as to avoid clipping any of the internal edges/the vertex. The other atypical component of the pump/probe beam was the diffraction grating mediated laser chirp. The appropriate gratings were selected, allowing for space limitations on the optical table, by calculating the required optical path difference between long and short wavelength components of the narrowband beam to result in a 50% reduction in spectral bandwidth. These were then aligned using the first order diffracted beam, as shown in figure 7.7, and rigidly fixed to the optical table. The reduction in spectral bandwidth was not independently verified but inferred from the increased spectral resolution of the subsequent CARS measurements.

The details of the Stokes beam circulator are given above; however, initial implementation required the dispersion of the Stokes beam to be measured, which was achieved by performing a delay line scan with a toluene sample. To clarify, a delay line scan corresponds to continuously moving the pump/probe beam retro-reflector (i.e. continuously lengthening the delay line) at a known velocity, equivalent to a constant change of delay between the beams, whilst CARS spectra of toluene are acquired with an exposure time corresponding to ~ 1.5 mm increments of the delay line (every 5 ps if translated into temporal delay between the beams). This yields a measure of which wavenumber is being probed at each given delay, assuming a minimal chirp of the narrowband pump/probe beam, this is approximately equivalent to the Stokes beam dispersion. The dispersion of the Stokes beam being known, using the Sellmeier equation with tabulated values for the Sellmeier coefficients, the required length of glass (H-ZF13) through which the Stokes beam needed to pass, in order to allow access to the entire 500 - 3500 cm^{-1} region simultaneously, was calculated. Using this analysis it was determined that three metres of glass would be required to correct the Stokes beam chirp. Whilst not impossible, it is highly impractical and expensive to purchase and subsequently utilise a high quality block of scientific glass with

this dimension. To circumvent this problem a circulator was devised that consisted of three glass blocks arranged such that the beam could enter, via a mirror, and circulate at a slight decline with respect to the optical table before re-circulated, at an equal and opposite incline, and being extracted by another mirror, having travelled approximately 17 complete revolutions, prior to re-entering the main beam path. In order to minimise losses throughout this process the beam (p polarised with respect to the blocks) was aligned such that it entered the blocks at the Brewster angle (60.31° for 1064 nm). Not only did this ensure that there would be minimal losses but it also satisfied the criteria for total internal reflection to occur at the back face of each block. An additional desirable secondary effect of multiple incidences at the Brewster angle was exceptionally high polarisation purity.

The location of the Wollaston prism was dictated by the limited access to the microscope body below the bottom objective lens which, in turn, determined the required Wollaston beam separation angle so as to produce two distinct tracks on the EMCCD, whilst avoiding clipping any apertures *en route*. Even given the minimal leeway afforded by the body of the microscope, and thus the predetermined beam profiles (each polarisation) exiting the microscope body, it was still possible with the correct choice of coupling optics to match the native NA of the monochromator. This was a highly desirable situation; however, it led to the beams clipping the edge of the diffraction grating. Only by imaging the Wollaston prism directly onto the diffraction grating could the two beams both fit. This required altering the coupling optics and, as a consequence, introducing a significant mismatch in NA.

7.3.2 Sample preparation

As two high NA lenses were utilised in a diascopic geometry the sample format requirements were very stringent: especially in terms of thickness. The working distance of each lens was 200 μm, therefore, the samples had to be enclosed between two 170 μm (no. 1.5) coverslips with a maximum physical thickness of 60 μm. The samples investigated with the system were predominantly volatile liquids and were prepared by dropcasting 8 μl onto a coverslip and immediately covering with a second coverslip. The choice of sealant was determined by the reactivity of the sample liquid [92]. For relatively inert liquids a nitrocellulose resin was used whilst more reactive liquids merited an epoxy resin sealant. On several occasions the volatility of the liquid resulted in a sample that, after sealing, contained only an exceptionally thin layer to the point where any measurement would encompass a significant quantity of unwanted glass background. To minimise this, spacers were constructed from aluminium foil (3 folds totalling ~ 45 μm thickness [93]), as it is broadly unreactive: with the notable exception of methanol where a spacer was not needed.

7.3.3 Spectrum acquisition

This experiment was carried out at room temperature, with the exception of the Peltier cooled EMCCD (see section 7.2.1.3) which was maintained at - 40 °c. Due to the exceptional sensitivity of the EMCCD it was extremely important to avoid external interference and thus the experiment was carried out in a dark room. The laser (see section 7.2.1.1) was turned on sequentially to avoid damaging the fragile fibre components, allowing the IR - laser diode and ytterbium fibre lasing cavity to warm up before amplifying to full power (4W). The two objective lenses were then retracted, immersion oil placed on the bottom lens, and a sample rigidly affixed to the stage. Immersion oil was also placed on the top surface of the sample prior to replacing the bottom objective lens. Employing white light incandescent illumination, via the top objective, and using the second alignment camera, the bottom objective lens was focused on the sample. The Stokes beam laser shutter was then opened and the top objective lens used to focus it onto the sample. The focus of both objective lenses was then checked and altered as necessary. The variable attenuator and OD4 filter were then placed in the beam path and the pump beam laser shutter opened. The two beams were then visually aligned (to attain maximum spatial overlap) using the first alignment camera. The laser alignment was subsequently verified by the observation of CARS on the EMCCD. Using this sequential alignment procedure, first focusing the bottom objective on the sample and subsequently focusing the top objective using the bottom objective, ensured that both objectives were focused in the same optical plane.

Spectra spanning both the FPR and CH-stretch region were then acquired with a combined total of 40 mW onto the sample (20 mW derived from each beam). Acquisition times were tailored to each sample with the aim of attaining high SNR spectra whilst taking into account the inherent instability of the system (details given below).

7.4 Results and analysis

7.4.1 Troubleshooting

During test measurements, following the introduction of the Stokes beam circulator and pump/probe chirp, it was observed that the power, and consequently the signal, would decrease over time: typically a period of minutes. Initially, as this seemed to coincide with temperature fluctuations within the room, the effect of altering the air conditioning power and temperature was investigated. Closer investigation, measuring the power of each beam relative to the fluctuating room temperature at intermediate points along the beam path, however, showed the temperature fluctuation to be only a small contributory factor. Eventually, by observing the alignment at various points over a period of time, the cause of the signal decrease was determined to be due to miss-alignment of the Stokes and pump beam spatial overlap arising from mechanical drift of the Stokes beam circulator.

In addition to devising a suitable method to minimize the effect of the drift, it was also necessary to determine the polarisation rotation imparted to the beams by the OD2 filter (which temporarily replaced the short pass filter whilst aligning the pump beam). Taking into account this polarisation rotation whilst aligning the beams, and the time constraints due to mechanical drift, it was then possible to acquire basic measurements.

7.4.2 SIPCARS

These measurements allowed the CARS spectrum, as measured along each of the detection axes of the Wollaston prism (S_+ and S_-) and the resultant SIPCARS spectrum (ΔS), to be plotted (see figure 7.11). The features contained within the S_+ and S_- spectra are shifted and dispersive in nature whilst the corresponding features are symmetric and appear at the correct vibrational energies within the SIPCARS spectrum, indicating the NRB has been successfully removed. This can be seen explicitly by comparison with the polarisation resolved spontaneous Raman scattering spectra: relative peak intensity (including negative going peaks) and Raman shift are in complete agreement (see figure 7.12). In addition this comparison highlights the mode symmetry information intrinsically encoded in SIPCARS spectra.

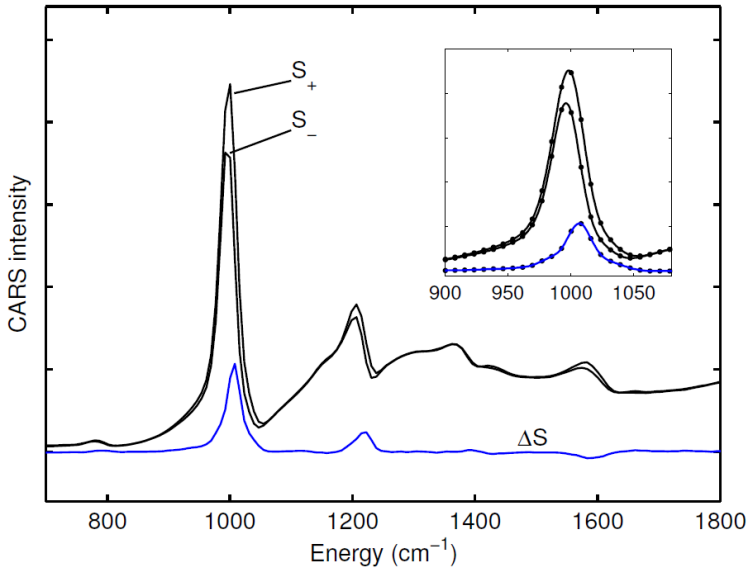

Figure 7.11 CARS spectrum of toluene as measured along each of the detection axes of the Wollaston prism and the resulting SIPCARS spectrum (blue). Inset: shows an expanded view of the breathing mode of toluene. (Acquisition time: 240 seconds).

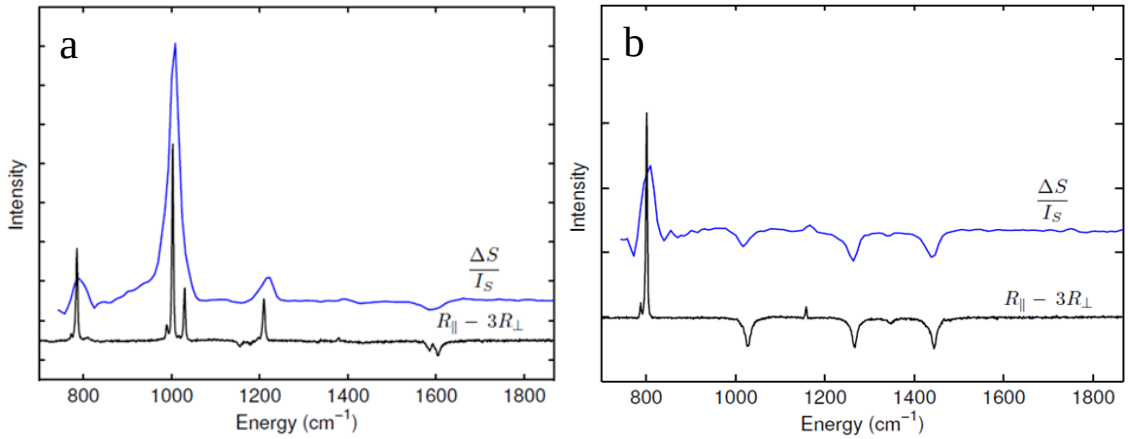

Figure 7.12 Comparison between polarisation resolved spontaneous Raman scattering spectra (black) and the normalised SIPCARS spectra (blue) of a) toluene and b) cyclohexane. Where $R_{\parallel}$ and $R_{\perp}$ correspond the signal stemming from parallel and crossed polarisation geometry respectively and I_s is the spectral variance of the Stokes beam used to normalise the SIPCARS spectrum (to allow direct comparison with polarisation resolved spontaneous Raman scattering). Curves have been scaled and offset vertically for clarity. (Acquisition time: 240 seconds)

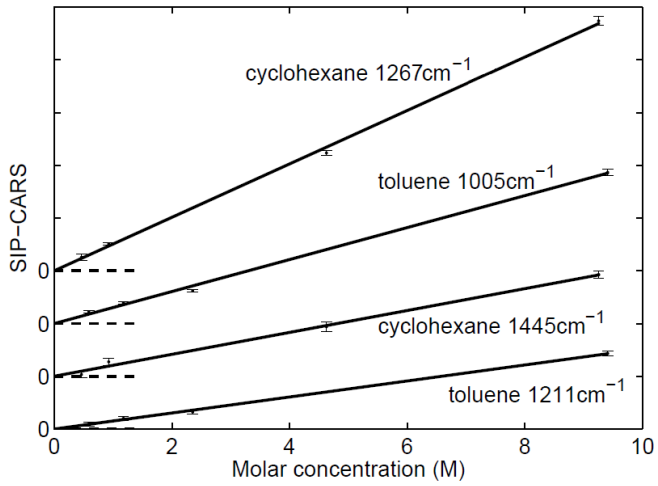

Figure 7.13 Concentration dependence of various resonances of toluene (in methanol: 100% to 6.25% toluene) and cyclohexane (in toluene: 100% to 5% cyclohexane) in the presence of strongly varying NRB.

As previously mentioned (see section 2.3.1) one of the major drawbacks of CARS spectroscopy is the intrinsic non-linearity of the signal intensity precluding its use for quantitative analysis; however, SIPCARS intensity are linear with respect to the number of Raman active species in the focal volume. To illustrate this fact explicitly a series of measurements, at various resonances, of the SIPCARS signal intensity from toluene and cyclohexane in relation to concentration were acquired (see figure 7.13). In order to vary the NRB, thus showing a linear proportionality irrespective of relative NRB strength, the toluene was mixed with methanol and the cyclohexane was mixed with toluene: the third order susceptibility of methanol, cyclohexane and toluene are 2.68×10^{-14} esu, 5.93×10^{-14} esu and 9.81×10^{-14} esu respectively [94].

7.4.3 Maximum entropy method

In addition to acquiring spectra with the SIPCARS polarisation geometry, the quarter waveplate was removed allowing spectra of toluene to be acquired with the parallel linearly polarised pump and Stokes beams necessary to apply the MEM algorithm. Prior to inputting the spectra into the MEM algorithm, thankfully provided by the group of E. M. Vartiainen, Department of Electrical Engineering, Lappeenranta University of Technology [95], a Matlab program was written to remove any superfluous backgrounds not relating to the NRB (see figure 7.14). The MEM algorithm (see figure 7.15) was only marginally successful at retrieving the $Im\{\chi_R\}$. Whilst the peaks that occur at wavenumbers greater than 1100 are, in fact, symmetric and occur at approximately the correct vibrational energies they do not possess the correct relative peak intensities. The peak situated at approximately 1600 cm^{-1} should, in reality, be negative (cf. figure 7.12a) and the asymmetry of the toluene breathing mode at approximately 1000 cm^{-1} was, actually, exaggerated by this process. This is largely due to the constraints imposed by this type of algorithm, such that, during the normalisation procedure, regions that would otherwise amplify noise are removed (or set to zero). This results in spectral features that are not completely encapsulated by non-resonant regions exhibiting an erroneous spectral form in the output spectrum. Whilst it is true that for a continuous spectrum of infinite width this algorithm would reproduce the expected $Im\{\chi_R\}$ exactly, even in cases where spectral features are fully encapsulated, discrete spectra exhibit spectrally varying residual errors of up to 10% at resonances [30].

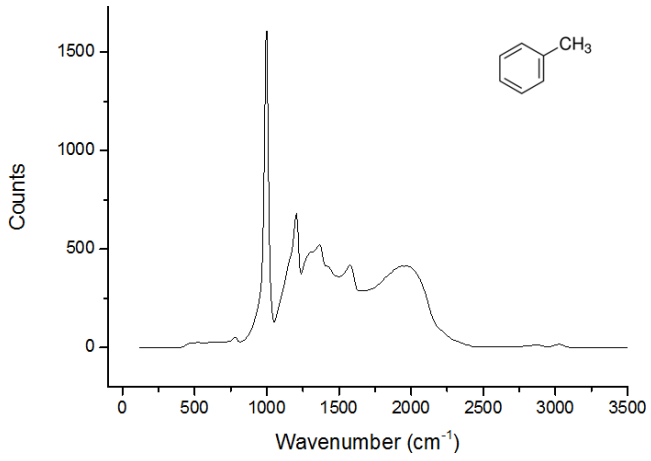

Figure 7.14 The CARS spectrum (linear pump and Stokes polarisation) of toluene which was subsequently input in to the MEM algorithm. (Acquisition time: 180 seconds)

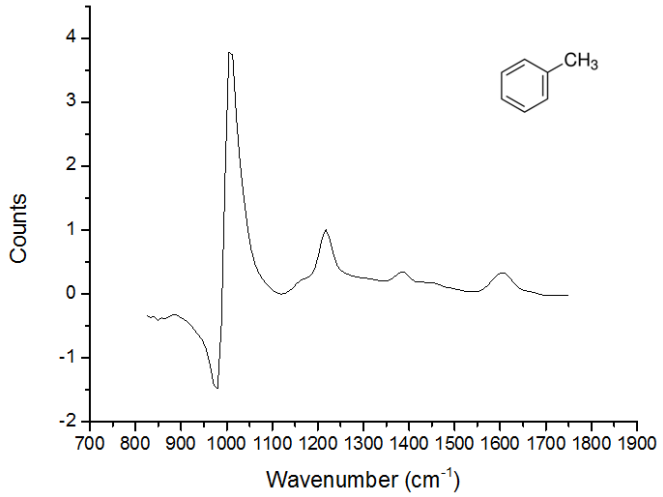

Figure 7.15 The spectrum resulting from the application of the MEM algorithm to toluene. (Acquisition time: 180 seconds)

7.5 Limitations

There are a multitude of limitations of this particular system, however, the majority initially stem from the laser. Whilst, as shown above, the significant negative dispersion of the Stokes beam can be largely corrected using the beam circulator, this particular solution is accompanied by a significant drawback. Given the considerable additional path length introduced by the Stoke beam circulator which, in effect, included a multiplicity of additional interactions with optical components, this solution, although inventive, resulted in a high degree of instability. This manifests as a change in the spatial overlap between the pump/probe and Stokes beam which, owing to the non-linearity of the CARS process, resulted in a vast alteration of the signal. This occurred on the sub-10 minute timescale subsequently significantly limiting possible sample acquisition times.

Whilst in section 7.1 a compelling argument was put forward for performing CARS using a pump/probe beam at 1050 nm, in practice this led to an array of technical issues. The objectives used, indeed the vast majority of objectives, start to considerably degrade in performance at wavelengths beyond the visible. This resulted in a considerably lower CARS signal than would be expected given the incident laser powers, in fact, the signal levels were similar, or worse, than that of a spontaneous Raman measurement. The low signal levels, when coupled with the mechanical drift of the beam circulator, resulted in a situation where only spectra of the strongest Raman scatters can be attained.

An additional, possibly more obstructive, issue encountered operating in this wavelength range was etaloning on the EMCCD chip. Even though the detected anti-Stokes signal is blueshifted with respect to the excitations beams, the entire spectral range of interest is situated beyond 800 nm (with the FPR region located above 900 nm); at these wavelengths the silicon chip used

in the Andor iXon EMCCD is partially transparent leading to etaloning. As the structure of the silicon at an optical scale determines the degree of etaloning, it is exceptionally difficult to account for this effect when two tracks are dispersed onto the EMCCD. It is worth noting that for a given material over a narrow defined physical pixel range (on the EMCCD) a standing calibration may have been possible but as the pixel range altered slightly between measurements and samples this was not the case. This resulted in a significantly more complex analysis process (the details of which will be given in a subsequent chapter) and ultimately a lower SNR.

A final major limitation of this system was the monochromator which, due to its simplistic nature, significantly aberrated the two beams *en route* to the EMCCD. The unfolded Czerny-Turner type configuration of the Bentham TMc 300 monochromator employs two concave mirrors in an off-axis geometry in order to firstly collimate and then refocus the dispersed beams. As this system was designed primarily as a monochromator rather than a spectrometer it contains no additional optics, such as an angled cylindrical lens, to correct the spherical aberration and coma induced by using concave mirrors off-axis. A schematic of the resulting beam profile onto the CCD can be seen in figure 7.16. It should be noted that for clarity of depiction figure 7.16 shows equal aberration across both tracks and also over the entire wavelength range, however, in practice, this was not the case. The elongated concave shape of the beams imaged onto the EMCCD had two effects: degrading the spectral resolution (~ 35 cm^{-1}) and requiring significantly larger track widths (i.e. the number of pixels across which the track is spread vertically in the non-wavelength axis) to be defined in the software. Whilst the requirement for larger track widths (in excess of 30 pixels) may not at first appear detrimental it reduced the SNR and limited any future potential for rapid single axis galvanometer based scanning (*cf.* section 5.2).

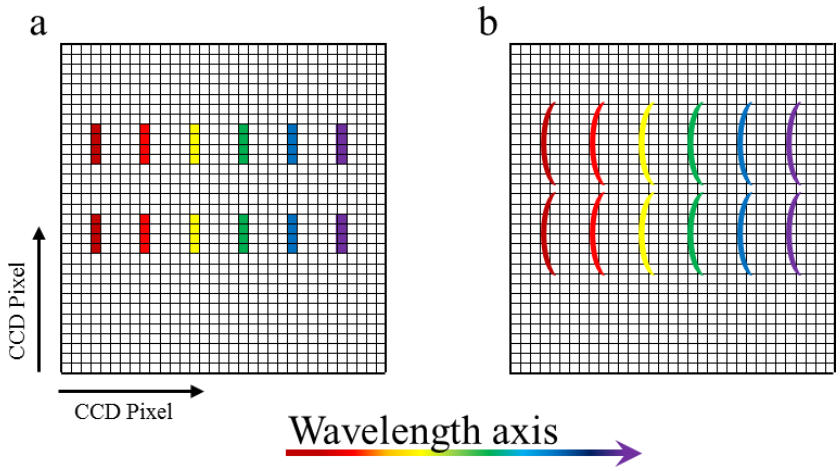

Figure 7.16 A schematic of the EMCCD chip with several spectral bands shown. The idealised case is shown in a) where the bands are all uniform between tracks and along the wavelength axis. b) A simplified view of the actual situation. In reality not only are the lines all concave but differ along the wavelength axis and between tracks.

The above listed limitations appear rather extensive; however, the majority can be largely alleviated by shifting the entire CARS process to lower wavelengths. Reducing the excitation wavelengths of the pump/probe and Stokes beams would immediately improve the performance of the objective lenses (primarily the quality of the foci) as it is considerably closer to their design wavelength range. This would yield a greater throughput and thus improved CARS signal levels allowing the use of shorter acquisition times. An improved spatial resolution would also result from a blue shifting of the process.

In addition the resultant shorter wavelength CARS signal would be detected by the EMCCD with minimal etaloning, as below 1020 nm (at - 40 °c) [96] silicon is essentially opaque (this is dependent on the specifics of the chip however it would typically be the case), vastly simplifying analysis and ultimately resulting in higher SNR spectra.

Beyond purchasing a purpose build imaging spectrometer there was little that could be done to improve aberrations of the beams *en route* to the EMCCD, as modifications of the existing monochromator would need to be to such a tight tolerance as to render them impractical.

Whilst the limitations presented above dramatically reduced the applicability of this system beyond pure solvent measurements and made data acquisition a time consuming task owing to the continual need for re-alignment, it did, however, provide apodictic proof-of-concept with regards to SIPCARS. To that end this system formed an invaluable initial platform from which to improve and build the technique. As stipulated above the single greatest step that could be taken to improve the system was to blueshift the entire CARS process. To this end the system was rebuilt using a titanium-sapphire oscillator to generate both the narrowband pump/probe beam, at 785 nm, and the broadband Stokes beam between 800 – 1040 nm.

8. CARS based on a titanium-sapphire oscillator and photonic crystal fibre: conception and initial results

8.1 Motivation

Although the Fianium based BCARS system had successfully provided results that validated the SIPCARS technique, given that the required acquisition times were in excess of those necessary to acquire the corresponding spontaneous Raman scattering spectra, it was not realistically feasible, using this system, to progress to biological samples. The extensive limitations of this system can be primarily attributed to the characteristics of the laser: an exceptionally large negative chromatic dispersion of the broadband Stokes beam and an overly broad narrowband pump/probe beam. Conceptually, if not practically, a solution to these limitations was relatively simple: employ a more suitable laser source. To this end an entirely new system was constructed utilising a single titanium - sapphire oscillator to produce both the narrowband and, by means of a PCF, broadband beams.

Construction of this system was a collaborative effort between the author and Dr. Littleton. Work within the lab was conducted both jointly and also individually. Development of the method was an iterative process with input from both parties resulting in a process of continual optimisation. The results presented in this chapter were the culmination of several measurements carried out by both the author and Dr. Littleton.

8.2 Apparatus

This system underwent significant and sustained development over the course of the last two years and, as such, it is impractical to display a beam path diagram for all these developmental stages. An optical diagram detailing the first functional configuration will, therefore, be included and the various alterations/improvements will be described in detail.

8.2.1 Coherent Mira 900-D titanium-sapphire oscillator

The Coherent Mira 900-D titanium-sapphire oscillator was used in conjunction with a Coherent Verdi-V6 seed laser. The output was tuneable over a wavelength range of 700-980 nm and could be operated in two distinct modes: femtosecond pulse (<200 fs) and picoseconds pulse (<3 ps) duration (CW lasing was possible in either mode) [97]. As switching between the two operational modes is a non-trivial process a substantial amount of thought was given to the pros and cons of each. Whilst femtosecond pulses are generally preferred for PCF mediated supercontinuum generation due to their higher peak power (supercontinuum generation is a non-linear process, therefore significantly benefits from higher peak powers), this would have had considerable implications for the narrowband pump/probe beam. As the narrowband beam would be derived

directly from the oscillator, if femtosecond mode was employed this would then require significant spectral compression (pulse lengthening) to deliver a meaningful final BCARS spectral resolution. Although possibly resulting in a small loss of phase coherence (due to the requirement of a longer PCF) and spectral width, the picosecond pulse mode was finally chosen, as it is far more expedient to use a slightly longer PCF than have to pass the narrowband beam through several metres of glass to attain the desired final spectral resolution. The titanium-sapphire oscillator was set for a 785 nm output and, once optimised and modelocked, produced a pulse duration of ~ 2 ps with an output power ~ 1 W. This pulse duration was chosen as it approximately corresponded to a spectral width of 7 cm^{-1} ($sech^2$ pulse profile), the typical organic Raman line width, thus maximising the potential spectral resolution of the system.

8.2.2 Post-laser pre-microscope optics

Upon exiting the laser, the beam was passed through a Faraday isolator in order to minimise back reflections and, by way of a collimating lens, onto a 90:10 beam splitter (see figure 8.1). At this point ten percent of the beam was reflected into the pump beam path whilst the remaining ninety percent continued on: forming the Stokes beam. After passing through a half waveplate, in order to correctly align the polarisation with that of the PCF, the Stokes beam was then coupled into the PCF (NKT photonics A/S; model: NL-PM-750) via an objective lens with a numerical aperture and magnification of 0.4 and 20 respectively. The broadband beam was then collected with an identical objective lens and collimated prior to being passed through a 650 nm long pass filter ensuring no shorter wavelength components of the supercontinuum leaked through subsequent filters. The combination of linear polariser and quarter waveplate through which the beam subsequently propagated allowed the beam to be linearly polarised and, additionally, to pre-compensate for any polarisation rotation imparted by subsequent optics in the beam path. The lower wavelength extent of the broadband beam was then further delimited by a 785 nm long pass filter, after which the Stokes beam propagated collinearly with the pump beam. Both beams then passed through a 50 mm HZF-13 glass block which acted to disperse the Stokes beam consequently mitigating the effect of non-spectrally resolved resonant artefacts (these arise when the broadband Stokes beam acts as the probe). The final spectral bandwidth of the broadband Stokes beam was 785 - 1040 nm.

The pump beam (see figure 8.2) was passed immediately into a delay line from the beam splitter allowing temporal overlap with the Stokes beam to be achieved. After this it was linearly polarised and passed through a 650 nm long pass filter to remove unwanted spectral features apparently arising both from the titanium - sapphire laser and backscattered light from the PCF. The combination of half waveplate and quarter waveplate through which the beam subsequently propagated allowed an elliptical polarisation of arbitrary orientation and ellipticitiy to be set prior to recombining with the Stokes beam by way of reflection from the 785nm long pass filter.

The microscope used (see figure 8.3) was identical to Fianium based SIPCARS system with the exception of the short pass filter and Wollaston prism which were replaced to account for the change of excitation wavelength, and altering the coupling optics to better match the NA of the spectrometer. The addition of the 945 nm short pass filter was necessary in order to reject light above (longer wavelengths) the blocking band of the 780nm short pass filter.

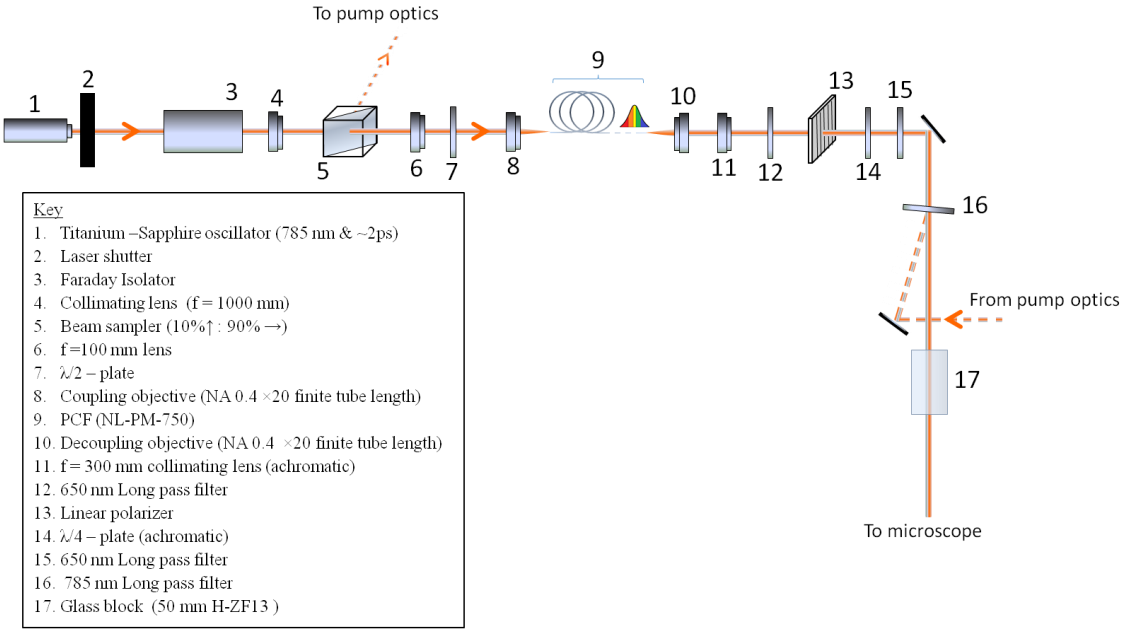

Figure 8.1 The main post-laser pre-microscope optical components of the of the titanium-sapphire oscillator based CARS system excluding the narrowband pump/probe beam optics

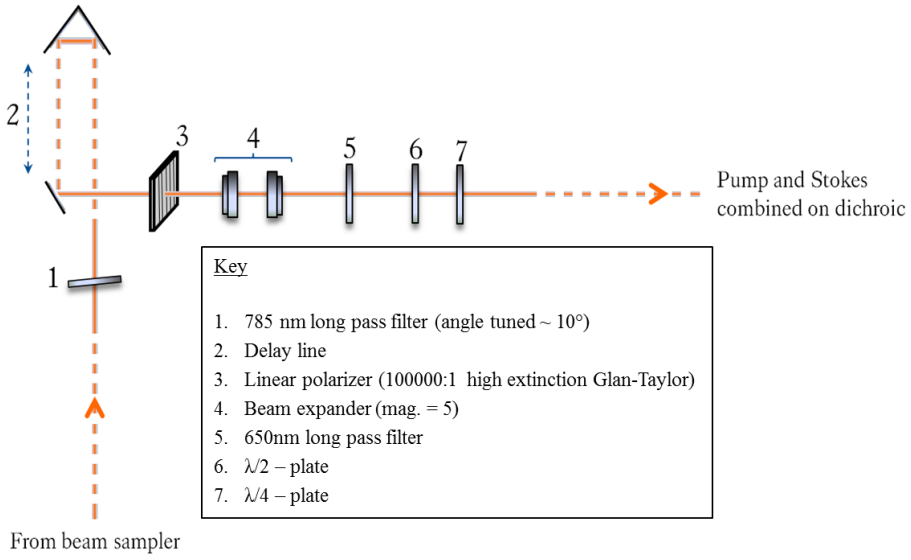

Figure 8.2 The main optical components of the narrowband pump/probe arm. Note the inclusion of an angle tuned 785 nm long pass filter was solely to reject an unwanted fluorescence background originating from the titanium - sapphire oscillator.

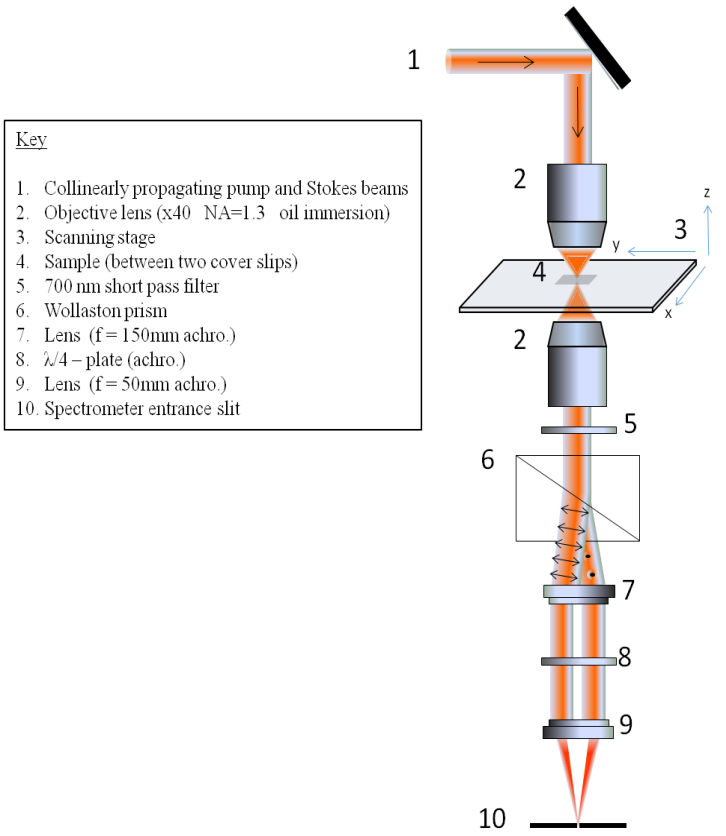

Figure 8.3 The main optical components of the microscope used, including stage assembly and pre-monochromator coupling optics.

Despite the associated disadvantages the Bentham TMc300 monochromator was also retained at this point in time.

Although several advantages of a titanium-sapphire oscillator based BCARS system have already be described in detail above there is a remaining significant advantage yet to be explored: the use of a free-standing PCF. As previously stated (see appendix III) the correct PCF length is imperative. Ideally the length of the PCF should be optimised so as to accentuate the particular spectral area of interest, the FPR, whilst still having sufficient power to allow access to the CH-stretch region. In order to ascertain the most appropriate length of PCF several were trialled ranging from 7 to 20 cm. A PCF length of 12 cm was subsequently chosen. Consulting the seminal paper relating to PCF characteristics, *Dudley et al* [27], which reports on two particular regimes, with respect to pulse duration, less than 100 fs and greater than 10 ps, it was immediately apparent that the spectral broadening observed using a 12 cm PCF fell within the bounds of the former. This paper suggested the shortest possible fibre that yielded sufficient broadening would be advantageous: both reducing energy loss to spectrally unimportant regions and preserving the spectral coherence of the beam. Preliminary tests suggested the spectral extent of the supercontinuum was, in fact, sufficient to access the CH-stretch region whilst concentrating the majority of the power in the FPR. Notably, using a 12 cm length of PCF it was possible, even considering the absolute power of the titanium-sapphire oscillator derived supercontinuum was

significantly less than that of the Fianium system, to have a considerably greater usable power/cm^{-1} across the pertinent spectral range. A further advantage stemming from an appropriate choice of fibre length was, as with the pump beam, the lack of requirement for dispersion compensation measures, such as the beam circulator with its extensive associated alignment issues.

8.3 Method

8.3.1 PCF preparation and alignment

The inherent capillary action of the microtubules surrounding the core of a PCF posed a significant problem with regards to determining the most effective way to strip, and subsequently cleave, a PCF without allowing solvent to wick into the internal structure. The common method of removing the cladding from a PCF is by burning which, while successful, leaves the remaining glass fibre perilously fragile, particularly when working with short lengths and small radii of curvature. In order to circumvent this problem, the ends were glued (using Araldite) prior to exposure to any solvent. The glued ends were then wrapped in a dichloromethane soaked lens tissue for 3 minutes at which point the outer cladding could be easily removed and an electronic fibre cleaver (Photon Kinetics FK11) used. As per the instructions, the PCF was cleaved at 70% the normal required tension of a solid fibre: 140 (no unit given).

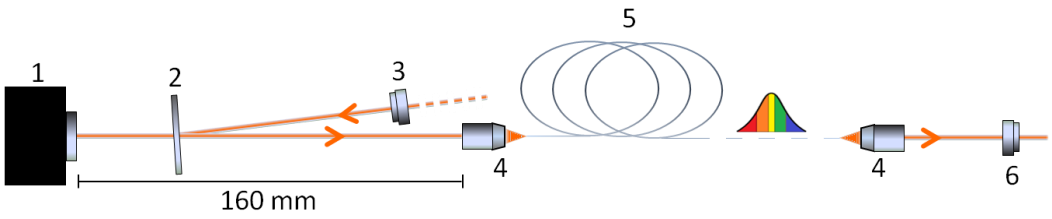

Key
1. Fibre alignment CCD
2. 700 nm short pass filter
3. f = 100 mm focusing lens
4. Coupling/decoupling objective (NA 0.4 ×20 finite tube length)
5. PCF (NL-PM-750)
6. f = 300mm collimating lens (achromatic)

Figure 8.4 Optical components used to couple/decouple into/out of and align the PCF. Note that some additional optics are included here which are not shown in figures 8.1 or 8.2. This is because they are not essential to produce BCARS but used solely for alignment purposes.

Having successfully cleaved the PCF, the input end was installed in a chuck and mounted in a 5-axis stage (x, y, z, pitch and yaw), while the output end was rigidly fixed. Altering the alignment into the input of the PCF, as opposed to the output, was necessary to avoid re-alignment of the downstream optics each time the laser was turned off. Coupling light into a PCF with a core diameter of 1.8 μm without a direct feedback is injudicious and likely to result in a considerable amount of wasted time so a camera was positioned behind a 700 nm short pass filter allowing the

end of the fibre to be directly imaged (see figure 8.4). Utilising this system it was possible to accurately ascertain the correct z-plane (distance between the end of the objective and input of the PCF) and approximately locate the core. Once some light was coupled into the fibre it was merely a process of optimising the power and colour output of the fibre (assessed by eye via diffuse scattered light and partially attenuated by laser safety glasses).

8.3.2 Sample preparation

Sample preparation followed the procedure set out in section 7.3.2 with a minor caveat. During initial test measurements of this system it became apparent that focusing the full incident power on the glass-sample interface led to immediate damage of the glass (possibly through 2-photon absorption or ablation). For measurements where it was necessary to image close to glass surface, cells and sub-micron beads, it was therefore necessary to use fused silica which has an inherently higher damage threshold and does not meaningfully absorb in the near or mid-UV. For all other measurements the method set out in section 7.3.2 was followed using conventional glass coverslips.

As fused silica coverslips are more expensive than conventional glass coverslips they were not discarded after a single use, rather piranha cleaned. This entailed immersing the slides in a 3:1 mixture of highly concentrated sulphuric acid (H_2SO_4) to hydrogen peroxide (H_2O_2) contained within a glass beaker in a fume cupboard for 30 minutes, after which the samples were rinsed copiously with deionised water. Next they were placed in a beaker containing a 3:1 mixture of concentrated ammonium hydroxide (NH_4OH) and H_2O_2 heated to 60 °c. As cleaning with Piranha solution is potentially extremely dangerous it was, and should always be, performed under the most stringent of safety protocols. Whilst it is true that they could have been cleaned using a variety of other methods an additional benefit of piranha cleaning is that the surface of the cleaned slide is hydrophilic/negatively charged improving the adherence of cells and beads.

Given the micrometer or sub-micrometer size of all the beads used, and thus their predilection toward flocculating, an initial 10 minute sonication was carried out prior to all sample creation. A stock mixture of equal quantities, by volume of solids, of 1 μm polystyrene and poly(methyl-methacrylate) was then made and further sonicated for 10 minutes to ensure, as far as possible, the two bead types had completely mixed. 8 μl of the mixture was then dropcast on to a coverslip (15 mm dia. circular no. 1.5 Sigma Aldrich LLC) and allowed to air dry (under ambient conditions) for a minimum of 3 hours in a dust free location. Following this, 8 μl of pure (deionised) water was applied to another coverslip (24×48 mm no. 1.5 Sigma Alrdrich LLC) and the two gently brought together attempting to cause minimal dislocation of the dried beads. Finally the sample was sealed using a nitrocellulose resin. The two bead types, polystyrene and PMMA, were sourced from Sigma Aldrich LLC and Polysciences Europe GmbH respectively.

Whilst it was apparent that a minority of the beads detached and were consequently floating in the sample, the bulk had remained attached. An imaging area of 20×20 μm was chosen as it was possible to identify regions of this size containing a mono-layer of beads. Additionally a small imaging area allowed high SNR spectra to be acquired whilst also accounting for the limitations of this system (addressed in section 8.5).

8.3.3 Polarisation alignment

A method of sequentially aligning the various polarisation optics *in situ* was devised. Using a combination of the linear polariser and the quarter waveplate in the Stokes beam arm (see figure 8.1), in conjunction with an additional analyser placed directly above the microscope (for alignment purposes only), the linearity of the Stokes beam was maximised. Using the Stokes beam, the angle of the Wollaston prism was then set by rotating it to balance the power of the two tracks defined on the EMCCD. This was achieved by rotating the diffraction grating so as to directly image the Stokes beam spectral range (785 - 1040 nm), replacing the 1000 nm short pass filter in the microscope with a neutral density filter (OD4), and using the Andor Solis software suite (proprietary software provided with the EMCCD used only for this purpose and not for general spectral acquisition) to define two equally sized spatial regions-of-interest on the EMCCD chip. The power (i.e. the area under the spectrum acquired in each region-of-interest) was then balanced by rotating the Wollaston prism. Whilst power was ultimately the metric used to determine the balance of the two tracks, using the Solis software, the spectral form of the two tracks could also be observed and the balance optimised with this additional information. This was particularly important, as due to etaloning, stemming from the EMCCD at these wavelengths, power measurements alone could be misleading.

Having used the Stokes beam to set the Wollaston prism, a small rotation of the EMCCD was then required to vertically align the position of the pump/probe beam in the two tracks on the EMCCD: observed as leakage through the 780 nm short pass filter. Although this was judged by eye it was corroborated by comparing the power of the beam in the two tracks within a defined spatial region-of-interest on the EMCCD. This was accomplished by first altering the polarisation state of the pump/probe beam, using the half- and quarter-waveplates (see figure 8.1), to approximately equalise the power in the two tracks (determined by comparing the maximum signal) then defining a very narrow spatial region-of-interest on the EMCCD: just encompassing the leaked pump/probe light. The comparative power measurement was acquired solely from this narrow region-of-interest and therefore, as the EMCCD was rotated, slight vertical misalignment of the two beams resulted in an alteration of the power difference between the two tracks. Using this method the pump/probe beam was correctly aligned when the power difference between the tracks was zero. This was in good agreement with the visual assessment of alignment.

At this point the relative orientation of the various polarisation optics were aligned (both beams balanced within the tracks on the EMCCD), however additional steps were required to align the pump/probe beam polarisation for SIPCARS (max SNR alignment). Once again, the additional alignment analyser above the microscope was used and the pump/probe beam polarisation set orthogonal to that of the Stokes beam. Finally to achieve SIPCARS the EMCCD was allowed to continuously acquire short exposures of a well characterised alignment sample (toluene or cyclohexane) and the half and quarter waveplates rotated to maximise signal whilst completely cancelling the NRB.

Although several aspects of aligning the polarisation states of the individual beams were conceptually challenging, this sequential approach, assuming the output polarisation of the PCF to be the fiducial marker, and altering the Wollaston prism, EMCCD and pump/probe polarisation accordingly, ensured that the correct relative polarisation states were attained. This consequently allowed complete NRB removal and the maximum possible signal to be derived from the SIPCARS process.

The process detailed above corresponds to the full polarisation alignment which, following the initial commissioning of the system, was required only after major alterations that impacted significantly on the polarisation states of the beams. The polarisation alignment was verified at the commencement of each set of measurements by inserting a cyclohexane sample and ensuring complete cancellation of the NRB across the entire spectrum. If this was not the case, then a small adjustment of the polarisation state of the pump/probe beam, affected by rotating the half- and quarter- waveplates, was normally sufficient to re-attain the correct SIPCARS polarisation alignment.

8.3.4 SIPCARS data analysis

Whilst the analysis of SIPCARS data is only marginally more complex than any other form of hyperspectral data, the limitations of this specific system introduce significant complications. In particular accounting for the presence of the persistent interference fringe-like pattern necessitates several additional normalisations, which would otherwise be unnecessary.

To affect the various normalisations requires the isolation of the individual spectral components contributing to the SIPCARS dataset and an additional non-resonant data set (although, if present, a non-resonant area within the sample would suffice to generate this). In reality, this consists of acquiring the SIPCARS data (i.e. a hyperspectral data cube from each track on the EMCCD) followed by a high SNR spectrum from the same sample (a featureless area) exposed to just the narrowband pump/probe beam and then just the broadband Stokes beam. Assuming the sample does not contain a suitable non-resonant area (most samples not immersed in water) the above procedure is repeated with a non-resonant calibration sample: typically water. This non-resonant

calibration data essentially provides a measure of the spectral response of the system. It may be assumed that a darkfield spectrum has been removed from all data as this was performed automatically at the acquisition stage.

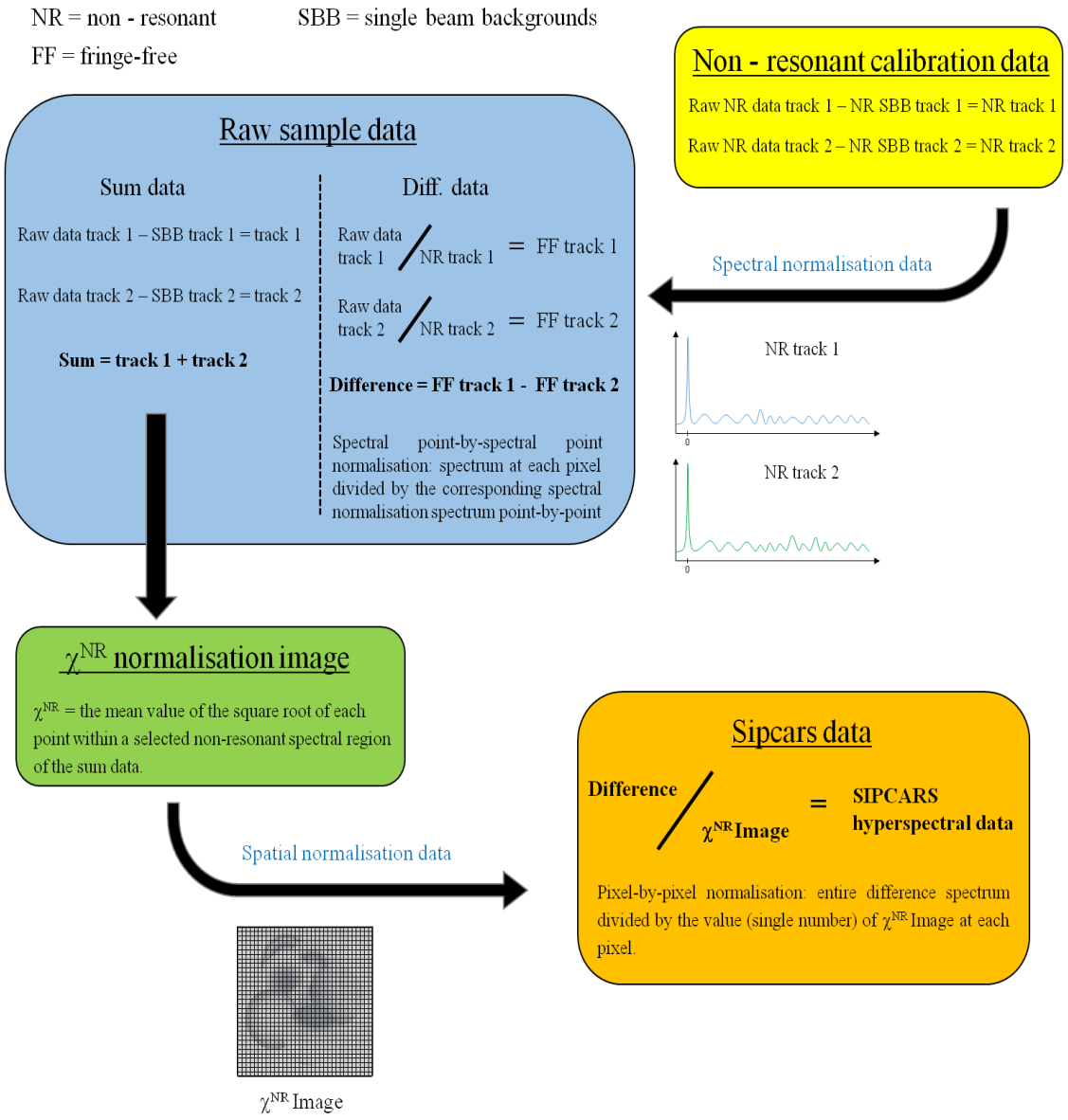

Figure 8.5 The essential SIPCARS hyperspectral data analysis steps. Note a high resolution darkfield spectrum has been removed from all data automatically prior to enacting this analysis protocol.

The full data analysis protocol can be seen in figure 8.5. If the non-resonant calibration data is considered first, the single beam backgrounds (taken to mean the sum of pump/probe beam only and Stokes beam only high SNR spectra) from each track are subtracted from the raw CARS non-resonant calibration data to produce the calibration data for each respective EMCCD track.

Each track of the sample data is now divided by the corresponding calibration data track. All things being equal, this normalisation procedure should remove the fringing/rippling artefact. The difference of the two ripple-free tracks now undergoes a normalisation by the spatial variation of

the non-resonant third order susceptibility, χ^{NR}, over the image. It can be seen, from equation 47 (chapter 4), that this corresponds to normalisation by the homodyne amplification term (i.e. normalising for the amount of amplification at each pixel). This term, in actuality, is approximately proportional to the refractive index at each pixel (see appendix VIII) and, thus the χ^{NR} image is, in many respects, similar to a DIC image: probing optical path length differences [64] [97] [98].

The χ^{NR} normalisation image is extracted from the sample sum data. In order to form the sample sum data cube, the sample single beam backgrounds are subtracted from the corresponding tracks which are then summed. The χ^{NR} normalisation image is generated by taking the mean value of the square root of each point within a selected non-resonant spectral region (corroborated by the inspection of the difference data). Note that to avoid introducing additional noise the selected region is as spectrally broad as is feasibly possible.

Finally the ripple-free difference data, a spectrum at each pixel, is divided in by the χ^{NR} image, a single number at each pixel, in a pixel-by-pixel manner yielding a NRB-free SIPCARS hyperspectral data set.

There are two primary reasons this data analysis is often only partially successful. Firstly, it is imperative the *status quo* is maintained while the single beam and/or non-resonant calibration data set are attained. This is frequently not the case (see limitations below) and leads to artefacts in the final data set. The second possible cause stems from imbalance between the two tracks (i.e. incomplete cancelation of the NRB) either due to initial misalignment, changes in the spectral form of the Stokes supercontinuum, lensing (see next chapter) or sample birefringence. If these effects are significant then the method breaks down and the data/spatial region must be discarded. An initial imbalance between the tracks is likely due to the fringe pattern (see limitations below). An additional effect of this fringe pattern is, due to the width of oscillation approximately matching some broad Raman linewidths, that it often complicates the location of a NRB region from which to construct the χ^{NR} normalisation image.

8.4 Results and analysis

Measurements similar to those taken with the Fianium based SIPCARS system were acquired (see figures 8.6 and 8.7), and as before, were in complete agreement with the polarisation resolved spontaneous Raman scattering data both in terms of peak positions and relative intensity. Notably, however, rebuilding the SIPCARS system based on a titanium-sapphire laser and a freestanding PCF increased the signal by approximately three orders of magnitude. This allowed high SNR spectra to be acquired with acquisition times of the order of milliseconds as opposed to minutes as had previously been the case. Whilst the signal had been increased dramatically the resolution

had remained the same (approximately 30 cm^{-1}): limited by the inability to clearly distinguish the two tracks on the CCD caused by aberrations within the spectrometer.

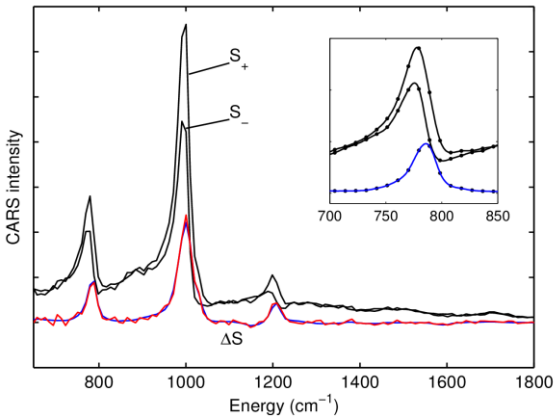

Figure 8.6 CARS spectrum of toluene as measured along each of the detection axes of the Wollaston prism and the resulting SIPCARS spectra (blue and red). Inset: shows an expanded view of the breathing mode of toluene [48]. (blue: 100ms and red/black: 10ms).

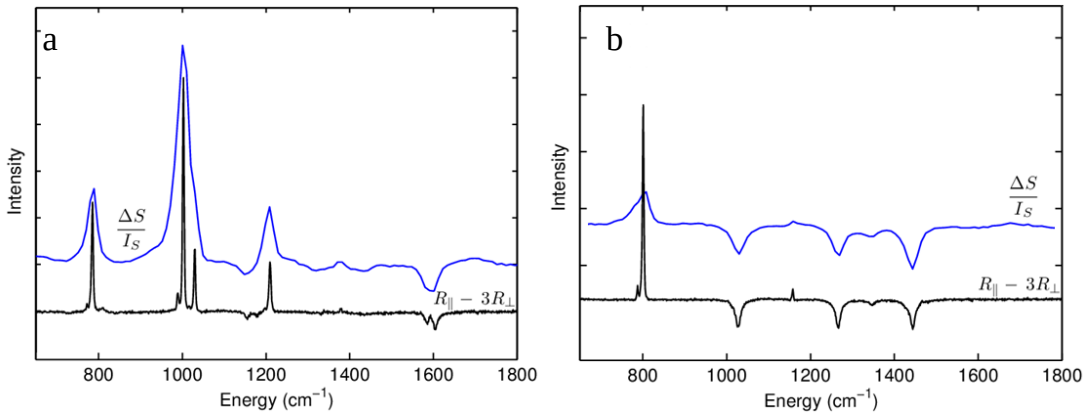

Figure 8.7 Comparison between polarisation resolved spontaneous Raman scattering spectra (black) and the normalised SIPCARS spectra (blue) of a) toluene and b) cyclohexane. Where $R_{\parallel}$ and $R_{\perp}$ correspond the signal stemming from parallel and crossed polarisation geometry respectively and I_s is the spectral variance of the Stokes beam used to normalise the SIPCARS spectrum (to allow direct comparison with polarisation resolved spontaneous Raman scattering). Curves have been scaled and offset vertically for clarity. (SIPCARS: 100 ms acquisition time and 20 mW per beam. Spontaneous Raman scattering 60 seconds acquisition time and 40 mW).

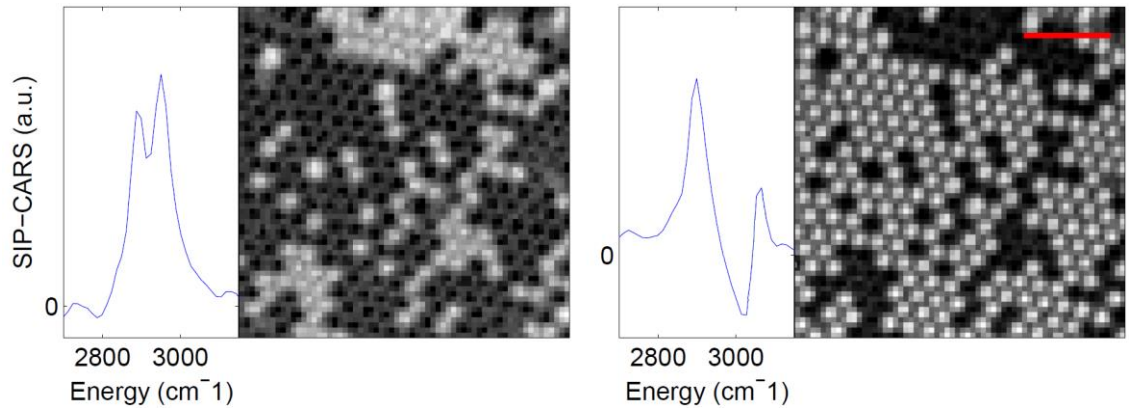

Figure 8.8 Hyperspectral image of 1µm polystyrene and PMMA beads: the component spectra are shown adjacent, as derived by a Pearson clustering algorithm. (pixel dwell time: 100ms, pixel size: 300 nm, scale bar: 5 µm)

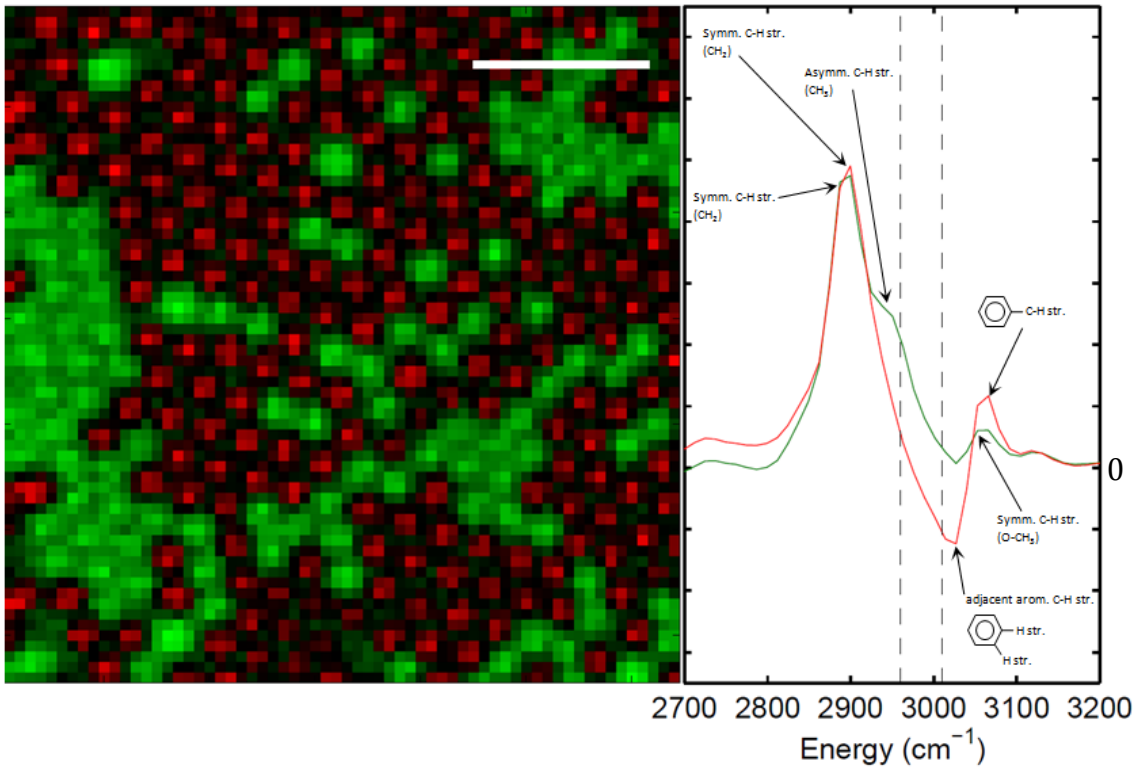

Figure 8.9 Hyperspectral image of 1µm polystyrene and PMMA beads: the red and green regions/spectrum relate to polystyrene and PMMA respectively. Highlight region of spectrum: 2960 - 3010 cm^{-1} (pixel dwell time: 100ms, pixel size: 300 nm, scale bar: 5 µm). Mode assignment was taken from references [100]–[104].

Given the decreased acquisition times attainable with this system biological imaging was now entirely feasible. As an initial test of the hyperspectral imaging capability of this system a bead sample containing a mixture of 1 µm polystyrene and PMMA was created. The images (see figure 8.8 and 8.9) were acquired with a pixel dwell time of just 100 ms, sufficient to attain high SNR spectra at each point and subsequently segment the images. The segmentation of figure 8.9 was derived from the sign of the integrated signal in the highlighted spectral region, which corresponds

to differing mode symmetries of these two bead types. The shoulder of the PMMA spectrum at 2940-2960 cm^{-1}, corresponding to an asymmetric C-H stretch (in a methyl group), [101] is not discernible even on a high resolution room temperature spontaneous Raman spectrum of PMMA and thus serves as a powerful demonstration of SIPCARS ability to discriminate otherwise similar spectra by the symmetry of the modes. In addition to deriving image segmentation from mode symmetry, a Pearson clustering analysis [105] was performed, returning two distinct spectral components thus allowing the two bead populations to be clearly distinguished (see figure 8.8).

8.5 Limitations

Implementing the titanium-sapphire oscillator based system constituted a considerable step toward realising a fully functional biologically applicable SIPCARS system; however a variety of very significant limitations still remained.

Principal amongst these were those stemming from the free standing PCF. Due to a combination of the cleaving process and the design of the fibre chuck/5-axis stage, a small, though not insignificant (~ 2 mm), amount of the PCF input end remained unfixed/free-floating. This, in conjunction with thermal drift of the stage, resulted in an unpredictable partial decoupling, typical on the order of 10 - 20 minutes, of the light into the end of the fibre. Whilst the decoupling/recoupling effect could be oscillatory in nature, the overall outcome of this was to alter both the power and spectral width of the supercontinuum beam in an indeterminate fashion. This, in effect, limited the safe data acquisition time to approximately 20 minutes. Analysis, where possible, was, therefore, hugely complicated by this effect.

An additional problematic aspect of this fibre was that over time, although once again unpredictably, the output of the PCF would suffer a loss of power, and thus spectral width, independent of the coupling strength. Following investigation it was concluded this was due to damage/melting of the output face. This is somewhat counterintuitive (i.e. damage of the output rather than input face which, arguably, would be subjected to the highest power density) and the cause proved elusive. This called in to question the long term durability of these PCFs when pumped according to the specifications detailed above.

To add to the above image acquisition time limitations imposed by the PCF oscillatory decoupling/recoupling, the titanium-sapphire oscillator would frequently drop modelock necessitating a re-alignment/recoupling into the PCF and consequently any ongoing measurement to be aborted.

Whilst it is possible to say with a high degree of confidence that blueshifting the entire CARS process resulted in a significant reduction of the etaloning stemming from the semi-transparency of the EMCCD chip: a fringe pattern never-the-less persisted. Possessing similar properties to an etaloning pattern, oscillatory behaviour varying in intensity between and along the two tracks,

this yielded a similar detrimental result: a significantly more complex analysis process and ultimately a lower SNR. The cause of this fringe/interference-type pattern was not, even after extensive investigation, apparent (this will be revisited in detail in the following chapter).

As expected, even shifting to shorter wavelengths, the spectral resolution did not improve meaningfully as it was still limited by aberrations *en route* to the EMCCD stemming from the simplistic nature of the Bentham TMc 300 monochromator.

A final problematic aspect of the above system was incomplete cancellation of the NRB across the entire spectral range. As figure 8.1 is a schematic it does not show all the mirrors contained within the beam path. Between the Stokes arm linear polariser and the top objective of the microscope there were, however, six mirrors and, owing to space limitation, it was not possible to ensure the beam stuck each at 45°, consequently resulting in a non-linear polarisation (i.e. an elliptical polarisation). Whilst an achromatic quarter waveplate was included immediately after the linear polariser, specifically, to pre-compensate any elliptical polarisation imparted post-linear polariser, this did not prove sufficient, as it was capable only of correcting a limited wavelength range. As it turned out, this broadly corresponded to either the FPR or the CH-stretch region.

As an initial prototype titanium-sapphire oscillator based SIPCARS system utilising a free-standing PCF to generate a supercontinuum, a number of impediments were expected and can be addressed in a variety of ways. The power fluctuations, in conjunction with the unpredictable tendency to rapidly degrade, suggested that a free-standing PCF may not be the most expedient approach. Whilst the cause underlying the power fluctuations was apparent, the origin of the rapid degradation has not been so forthcoming. It is possible that dust settling on the output face may be responsible; however, due to the multiple identical occurrences, it is highly probable that the fundamental cause is systemic in nature. Irrespective of the underlying cause there are two possible mitigation approaches: an encapsulated PCF, and a minimal air current/dust environment, or, in fact, a combination of the two.

It is highly probable that back reflections into the laser cavity stemming from the input face of the PCF (there was an apparent correlation between the modelocking stability and the strength of coupling into the PCF) disrupt the modelocking. The presence of the Faraday isolator should have nullified this effect; however, this was, demonstratively, not the case. The Faraday isolator (Electro-Optics Technology Inc.) was a relatively high rejection threshold (nominally 30 dB isolation) model operable over a wide range of wavelengths, and therefore encompassing a degree of user tunability. If, through fine tuning (with a partially coupled PCF) the stability of the titanium - sapphire oscillator could be improved this isolator could be retained; however, if not then an alternate high isolation model could be sourced.

There is no expeditious solution to resolve the fringing pattern. It is not practical, although possibly necessary, to individually assess the optical behaviour of each optic in the beam path; therefore, the most likely origins (the objectives, the sample and the beam recombination long pass filter) will be eliminated first.

As previously stated the lack of spectral resolution can be realistically addressed only by replacing the Bentham TMc 300 monochromator with an aberration corrected imaging spectrometer.

Whilst, paradoxically, the most conceptually easy problem to rectify, ensuring the Stokes beam polarisation remained as pure as possible on to the sample would require the beam paths to be altered in order to recombine the two beams immediately above the top objective.

All of these limitations, in addition to the continued development of the systems will be addressed in the next chapter.

9. CARS based on a titanium-sapphire oscillator and photonic crystal fibre: continued development and improvements

Owing to the predominantly developmental nature of this project, this chapter will be structured unconventionally. Rather than attempt to address separately the method and ensuing results, a limitation/potential improvement will be identified, analysed, and, where possible, the solution will be given. This structure will facilitate rapid retrieval of information and highlight, unambiguously, many of the difficulties associated with such a system, and the potential solutions. The limitations of the initial system, detailed above, will be addressed along with all others that arose over the course of the project. Limitations/improvements will be addressed in an approximately chronological order with the exception of instances where it is beneficial to group several together.

In a similar vein to the previous chapter the majority of the work presented in this chapter was performed in close collaboration with Dr. Littleton. Isolating and resolving the cause of temporal fluctuations in signal strength, and identifying the asymmetry in the spatial response of the system were, however, performed solely by the author.

9.1 Titanium - sapphire oscillator modelock instability

As outlined in the previous chapter the stability of the titanium - sapphire oscillator modelock was often lower than desirable. After extensive investigation it became apparent that the cause was back reflections into the oscillator from the PCF due to inadequate performance of the Faraday isolator. Whilst this effect initially appeared to be intermittent, a causal link with the coupling strength into the PCF was soon established. Although the exact mechanism was unknown the effect often manifested when the PCF began to decouple: possibly due to increased back reflections from the fibre. A Faraday isolator employs the magneto-optic effect and thus by slightly decreasing/increasing the distance between the magnets and the internal crystal it is possible to attain a higher degree of isolation for a given wavelength. As the reflections from the PCF were not necessarily at the 785 nm titanium - sapphire oscillator output wavelength, by first partially decoupling the PCF, then tuning the Faraday isolator, an empirical setting that offered higher isolation at these problematic wavelengths could be attained. As a result the stability of the titanium - sapphire oscillator, although not ideal, was significantly improved.

9.2 PCF sporadic decoupling and systemic degradation (FemtoWhite800 and NanoTrak)

As outlined in the previous chapter (see section 8.5), the free-standing PCF was prone to both catastrophic degradation and sporadic decoupling/re-coupling. Following the degradation of the third 12 cm length of PCF, without any immediately apparent cause, an encapsulated PCF was considered. This was due not only to the expense of continually replacing the PCF (approximately £1000/metre) but also to time wastage involved: effectively one day every two to three weeks.

An NKT photonics FemtoWHITE800 [106] is, in essence, a 12 cm encapsulated version of the NL-PM-750 PCF fibre already in use within the system. The entire length of the fibre is encased within a protective ridged aluminium cylinder (see figure 9.1). Unlike the free standing PCF, the ends of the FemtoWHITE800 are not microstructured and are, in actuality, a very short section of standard optical fibre which has been spliced with the PCF within the body of the FemtoWHITE800 unit. This has two principal advantages: the input and output damage thresholds are significantly increased, and the ends can be cleaned should they become dirty/dusty. Although marketed for super continuum generation with 50 fs pulses and a maximum average input power 200 mW, having previously used an identical free standing version of this PCF in the system, no unforeseen problems were expected. At a cost of approximately £2500, however, and especially using the FemtoWHITE800 off-spec, every precaution was taken when performing the initial alignment and testing.

Figure 9.1 A FemtoWHITE800 unit. The white line indicates the native polarisation of the PCF contained within [106].

Owing to the radically different format of the FemtoWHITE800, in comparison to the free-standing PCF, the alignment procedure changed appreciably. A brief description of the mounting and alignment will, therefore, be given. Unlike the previous alignment (see section 8.3.1) where, by means of a camera, the approximate location of the core could ascertained, due to the slight recession of the fibre input end, in relation to the aluminium housing, this was not possible. The procedure was, therefore, significantly more laborious. To avoid damaging the FemtoWHITE800 during the alignment process a linear polariser mediated variable attenuator

was constructed in the beam path before the coupling objective, allowing the input power to be attenuated without deviating the beam. Having focused a significantly attenuated (approximately 5% power) beam using the input objective, the FemtoWHITE800, mounted on a 3-axis translation stage equipped with differential micrometers, was rotated to ensure alignment with the polarisation axis of the incident beam and positioned approximately 170 μm away. The position of the input objective (also mounted on a on a 3-axis translation stage equipped with differential micrometers) was fixed and, using an IR indicator card to assess the output, the FemtoWHITE800 was systematically translated in all three axes to achieve coupling. At this input power, if any spectral broadening of the beam occurred, it would not extend into the visible region; therefore, the only indicator that the beam was correctly coupled was a tell-tale increase-decrease-increase sequence of brightness as seen on the IR indicator card (the location of the decrease corresponding to the core). The input power was then iteratively increased, ensuring maximum coupling at each stage, until visible light was observed. After this the power was increased to maximum and fine adjustments of the FemtoWHITE800 translation stage used to optimise (maximum power and spectral width) the output. At this point the FemtoWHITE800 translation stage was locked in place. The decoupling objective was then correctly positioned, ensuring it was both axially and laterally aligned with respect to the FemtoWHITE800 output beam, and rigidly fixed in place. It was possible to verify the axial separation between the FemtoWHITE800 output and decoupling objective by observing the downstream focus of the beam. Owing to the finite correction of the decoupling objective, when this focus was at 160 mm, the focal length, the separation was correct. It is important to note that after this initial alignment the position of the FemtoWHITE800 and decoupling objective were rigidly fixed so as to avoid any re-alignment of the downstream optics each time the laser was turned off. The necessary small adjustments required to re-couple into the FemtoWHITE800 (typically each morning and several times a day) were; therefore, performed using the coupling objective. To date (in excess of 12 months usage) the FemtoWHITE800 has exhibited no symptoms of degradation: either visually, or spectrally.

Having introduced the FemtoWHITE800 unit, catastrophic PCF degradation no longer posed a problem; however, it did not greatly affect the sporadic decoupling/re-coupling. As the FemtoWhite800 and decoupling objective were now rigidly fixed it was highly likely this effect stemmed from thermal drift of the coupling objective.

To minimise this effect a closed loop feedback system (Thorlabs APT NanoTrak) was installed with the aim of stabilising the output of the FemtoWHITE800 by correcting the drift of the coupling objective. This consisted of a 2-channel piezoelectric controller coupled with a high resolution piezo driven 3-axis stage (Thorlabs 3-Axis NanoMax: MAX313D), and a visible light photodiode detector. Using the reflection from the long-pass filter which followed the FemtoWHITE800 (see figure 8.1) in conjunction with the photodiode detector, the included

software (Thorlabs APT V. 3.14.0) acted to translate (x and y axis) the coupling objective (attached to the 3-axis stage) in order to maximise the output of the FemtoWhite800.

This drastically improved the stability of the FemtoWHITE800 output; however, as the algorithm underlying the software was somewhat rudimentary, this introduced another slight impediment. In order to elaborate, it is necessary to describe briefly the action of the software. Within the software a circle is defined on the x-y translation plane of the 3-axis stage. The radius, on the order of microns, is dependent on the magnitude of the power detected by the photodiode: a larger signal results in a smaller circle. The stage is then rapidly (less than 0.1 second) raster scanned over this circle and the point of maximum intensity, as measured by the photodiode, is set as the origin of a new circle and so the optimisation procedure continues.

This approach is perfectly functional; however, it lacks any effective redundancy. That is to say, it cannot self-correct in the event that a power fluctuation occurs. Although rare, whether stemming from sporadic partial dropping of modelock from the titanium-sapphire oscillator or unexpected vibrations, on occasion the power detected by the photodiode would significantly decrease (typically for less than a second). In reaction to this, the optimisation routine would drastically enlarge the circle and continue to raster scan in an attempt to locate the maximum. If the power did not recover (at least enough to register as a maximum) within approximately 0.5 seconds (an average of multiple scans, user set, in an attempt to avoid this scenario) the optimisation would, instead, continue from a local maximum and, in so doing, drive the focus of the coupling objective away from the core of the fibre. Given the large range of travel (over 20 μm) of the piezos relative to the size of the core, if the beam recovered to full strength this would amount to focusing a high power pulsed beam into the cladding of the FemtoWHITE800 fibre and could result in irreparable damage. Due to the possibility of this occurring, the system could not be left unattended, even briefly, while scanning: often for many hours.

The entire assembly, FemtoWHITE800 and the NanoTrak, were then enclosed within a lidded laser resistant box. The reasoning behind this was threefold, firstly, to ensure that dust did not impair the working or cause damage to the fibre ends. Secondly, to minimise the effects of air currents/temperature gradients within the room, and thirdly, to limit user exposure to the broadband beam (particularly dangerous as it cannot be entirely blocked via laser goggles).

9.3 Alterations to the input path and body of the microscope

In order to preserve better the linearity of the Stokes beam, discussed in detail in the previous chapter (section 8.5), the Stokes linear polariser and recombination 785 nm long pass filter were moved from the optical table to a vertical breadboard located above the microscope: only a single mirror from the top objective (see figure 9.2 a and b).

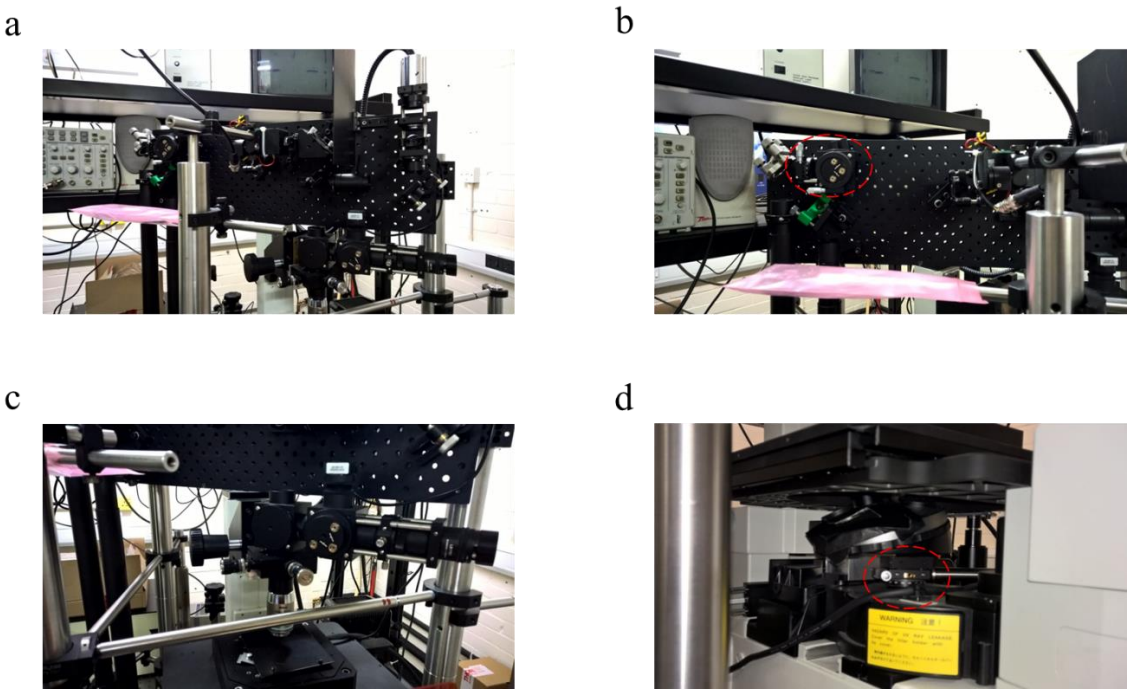

Figure 9.2 a) Positioning of the vertical breadboard above the microscope. Note it was mounted at 45° to the Cartesian scan axes b) Location of the Stokes beam linear polariser and recombination 785 nm long pass filter (encircled with a dashed red line) on the breadboard. c) The top objective and stage. Note the 3 cm uprights onto which the vertical breadboard is mounted and the extensive additional bracing (1 cm horizontal tensioning bars). d) Wollaston prism rotation mount equipped with a micrometer (encircled with a dashed read line).

This served to improve the NRB cancellation across the entire spectrum (i.e. it was possible to achieve a more complete cancelation of the two tracks in a non-resonant region); however, even disregarding the inescapable fringing pattern, the cancelation was still not optimum. A further improvement was realised through small lateral alterations of the recombination 785 nm long pass filter (i.e. the angle with respect to the plane as defined by the surface of the breadboard).

As the large/heavy vertical breadboard located above the microscope was rigidly fixed to the optical table while the body of the microscope was unattached (standing on rubber vibration isolation feet) this resulted in significant vibrations of the focal spot during alignment and data acquisition. So high was the sensitivity of the system to vibrations that footsteps inside the room, and any large movement outside the room, would be immediately apparent in acquired data. This severely limited use of the system.

While the most obvious solution would be to float the optical table this had previously been discounted as the Verdi/Mira laser system was a shared system and needed to be passed between two unattached optical tables (separated by ~ one metre). Simply rigidly fixing the microscope to the table only partially alleviated this effect, as the breadboard, over 80 cm above the optical table, oscillated at a different frequency to the microscope, therefore, introducing vibrations at the difference frequency. The most effective way of limiting the effect of these oscillations was found to be extensive bracing of the struts supporting the breadboard (see figure 9.2c). This was achieved by installing several additional vertical struts and, under high tension, attaching horizontal bars. This, in effect, considerably limited the ability of the vertical breadboard to respond in a meaningful way to anything but the largest of external vibrations (the impact of an 85 kg mass on the floor one metre from the optical table from a height of approximately one metre did not visually register on the alignment monitor).

An additional improvement afforded by the use of a vertical breadboard, was the ability to mount the input mirror to the top objective on a translation stage. Although this may appear to be a small inconsequential adjustment, the input mirror had previously been attached to the body of the microscope with no translational freedom. The reality of this was that the input beam was always very slightly off-axis which introduced additional aberrations to the beams and consequently a larger focal spot. Mounting this mirror on a translation stage significantly improved the quality of focus attained. Similarly, the opportunity was taken to replace the inbuilt top objective mount with a two axis translation stage equipped with micrometers. Owing to the rudimentary thumb screws of the pre-existing Nikon mount, and thus lack of fine adjustment, it was exceptionally difficult to accurately align the top and bottom objective. This was further exacerbated by the fact that the available translation axes of this stage were at 45° to the scan axis of the sample stage.

Another hugely significant upgrade of the system was replacing the sample scanning stage. Prior to implementing this upgrade the stage utilised was a 3-axis, electrostrictive actuator driven, Newport cross-roller bearing stage. Owing to the quadratic relationship between displacement and applied voltage exhibited by this type of actuator, linearisation of the response was necessary. The rudimentary correction applied by the stage controller was, however, not sufficiently precise to allow fine scanning. In addition the coarse movement of the stage was achieved via mechanical micrometers which also exhibited a non-trivial amount of hysteresis. This stage, therefore, required extensive compensation to be incorporated within the software in order to ensure accurate scanning was achieved. Whilst this compensation was largely successful, it introduced a considerable amount of dead time into scans. In addition the maximum travel of the stage was 80 μm × 80 μm × 20 μm (minimum step size x, y: 100 nm and z: 200 nm). In reality, this stage posed the single greatest impediment to meaningful biological tissue imaging: one of the primary objectives of the SIPCARS system.

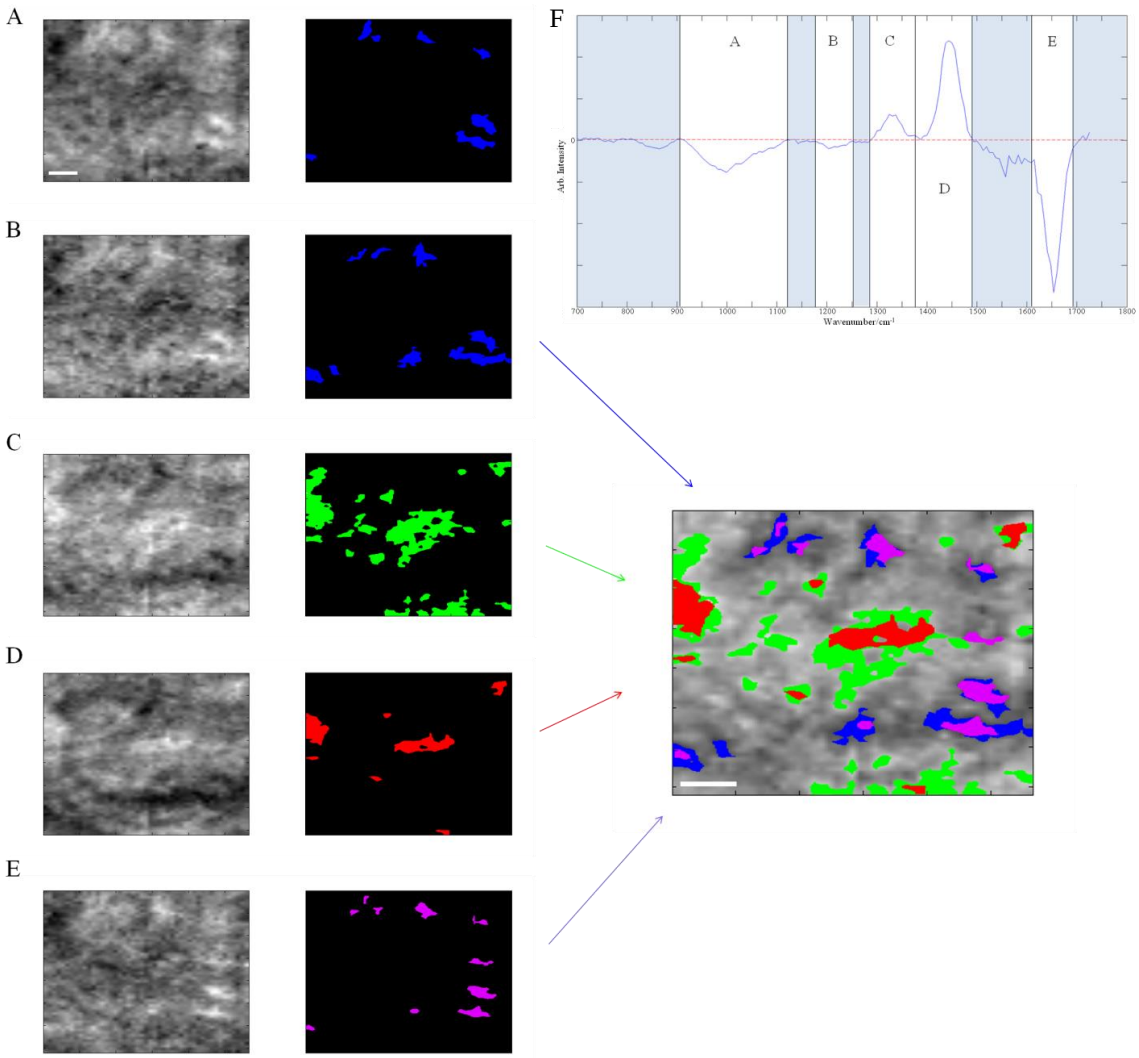

Figure 9.3 A hyperspectral image of murine breast tissue 18 μm × 13.5 μm (60×45 pixels), 300 ms/pixel; scale bar: 1μm; pixel size 300nm. SIPCARS images A-E are derived from the spectral bands indicated on the SIPCARS spectrum (F). The composite image has been formed by applying a threshold at 70% image saturation and imposing a minimum feature size of 0.9 μm^2. Showing that various tissue components can be clearly distinguished. Band assignments: A and B - collagen; C - nucleic acids (tentative); D - CH_2 and CH_3 in lipids; E - C=C in lipids [72].

This is clearly illustrated by figure 9.3: a hyperspectral image of murine breast tissue. In this case murine breast tissue has been imaged with a pixel dwell time of 300ms. Image segmentation was performed using a relatively simple approach whereby spectral bands corresponding to various cell components were selected (figure 9.3 F) from which false colour images have been created using a 70% image saturation threshold and imposing a minimum feature size of 0.9 μm^2. A composite image was then formed by combining these false colour representations and superimposing them on the NRB image. From the composite image it is clearly possible to observe that the various tissue components are localised to spatially distinct regions. Whilst this set of images successfully demonstrated the capability of this system to segment tissue, even using this simplistic analysis, based solely on the molecular vibrations, it was; however, all too apparent that, given the limited scan range of the stage used, this 18 μm × 13.5 μm image is not sufficiently

large to distinguish any of the morphological features of this tissue. Using this stage the idea of producing diagnostically relevant images was not even remotely feasible.

The stage was, therefore, upgraded to a high precision (sub-nanometre resolution) 200 μm × 200 μm × 20 μm piezo flexure stage (Physik Instrumente P-527.3) that incorporates integrated capacitive sensors and a closed loop feedback system. This resulted in virtually backlash-free high precision scanning.

A final minor, though no less important, alteration of the microscope body was the replacement of the exceptionally coarse Wollaston prism rotation mount with a finer micrometer driven equivalent. This in turn allowed the Wollaston prism to be more accurately set allowing for an improved cancellation of the NRB to be attained.

9.4 Isolating and resolving temporal fluctuations in signal strength

In April of 2015 a major external incident (London Kingsway underground fire 01/04/2015) occurred causing significant mains electrical fluctuations (blackouts, spikes and brownouts) which closed the KCL strand campus for over a week and resulted in an unstable power supply for a period of months. As might reasonably be expected, all experiments were postponed while the college was closed. Unfortunately, as it turned out, the lab was already in a cooling off period (i.e. only short/simple experiments being performed) preparing for a pre-planned relocation, which occurred upon re-opening of the Strand campus. The system was, therefore, relocated before any extensive testing could be carried out to ascertain if any damage had resulted from the initial black out and subsequent spikes in electrical power. Fortuitously, as the system was in standby mode at the time of the incident this was thought to have limited any possible damage to the camera (not powered), the Mira oscillator (not powered), the computer (surge protected) and the PCF. The Verdi laser, although powered in standby mode, is equipped with a battery to avoid thermal shock of the crystal in the event of a blackout and was shut down completely within two hours of the incident. A preliminary inspection of the system indicated no warning/faults and so it was relocated on the assumption of no damage. Owing to the complexity of the system, re-building in the new lab took approximately one and half months (including the identification and subsequent resolution of several minor complications). The initial spectra acquired of cyclohexane in the new lab appeared to indicate a successful move with no complications. As soon as images were acquired, however, it became immediately apparent that this was far from the case. Figure 9.4, a SIPCARS image of cyclohexane acquired over 100 minutes, clearly shows periodic fluctuations in signal strength. Whilst the overall balance, figure 9.4a, appears to be exemplary, resulting in an average spectrum that correlates well with the literature [83] and previous polarisation resolved spontaneous Raman scattering measurements (see chapter 6), this belies the fluctuating signal strength illustrated by the figure 9.4 b, c and d.

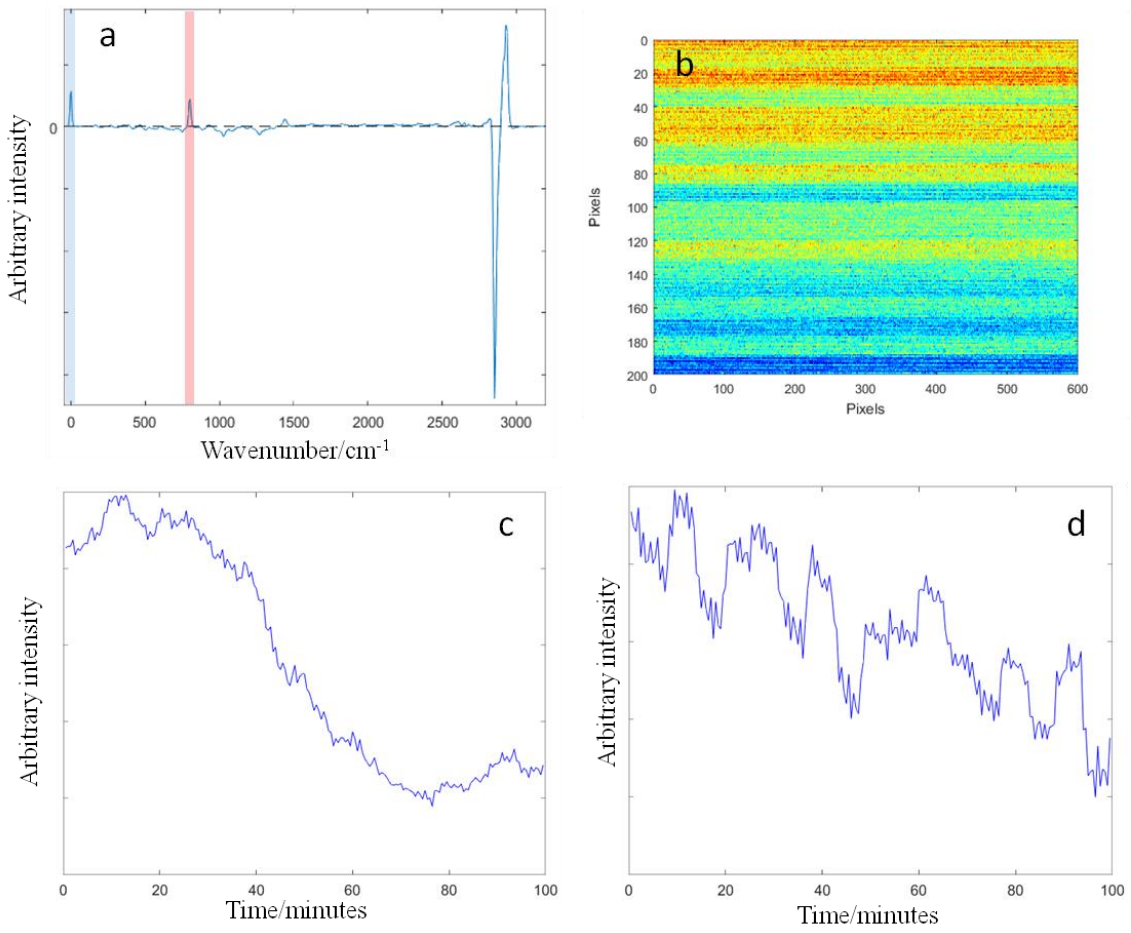

Figure 9.4 a) average SIPCARS spectrum over the entire 100 minute acquisition. The blue and red highlighted regions correspond to the laser line leakage (through the short pass filters) and the C-C stretch peaks respectively [107]. b) SIPCARS image generated by integrating over the of the 801 cm^{-1} C-C stretch peak. Note, as the pixel dwell time was 50 ms, each line along the x axis corresponds to 30 seconds. Signal fluctuation trace over c) the laser line leakage and d) the 801 cm^{-1} peak.

Comparing figures 9.4 c and d, there is a clear decrease in power over the duration of the acquisition; however, it would appear that there are also two distinct periods of oscillation. Owing to the highly complex processes underlying the supercontinuum generation and the SIPCARS process; however, on the strength of this data alone, this could not be confirmed. Consequently, further data sets (only the most decisive data shown here due to space limitations) were acquired in order to corroborate the existence and extent of this effect.

It is worthwhile noting the process of investigating these oscillations was hampered and significantly complicated by an unstable mains supply throughout. This would manifest as power spikes and brownouts which often led to decoupling of the FemtoWHTE800 unit and/or the titanium-sapphire to drop modelock. These power fluctuations, although stemming from an unidentified external source, would also frequently occur if there was a sudden increase/decrease in current drawn from the mains circuit supplying the lab (i.e. if anything was

connected/disconnected from the mains power supply in the SIPCARS or adjacent labs). Practically this complicated diagnosis, as upon commencing an acquisition the *status quo*, with respect to the mains power supply within the lab, had to be carefully maintained. Having limited control over adjacent labs, accounting for any fluctuations originating from these locations was particularly difficult.

Initially, to establish if these fluctuations were non-linear in origin, data from each beam, measured via the EMCCD, was acquired separately and analysed. Using the EMCCD as the detector, however, proved problematic as there was a significant etaloning problem associated with directly observing the Stokes wavelength region (see section 7.5). An accurate logging power meter (Thorlabs PM200 unit with a S302C thermal head) was therefore utilised to attain further measurements. These showed that the effect, although present in each beam, was an order of magnitude greater in the Stokes beam: approximately a 1-3% oscillation of the pump beam and 10-30% of the Stokes beams (see figures 9.5). The range of these percentages, derived from multiple measurements, reflect the considerable instability of the system. It was also apparent that there were two distinct periods of oscillation of differing amplitude: a larger ~ 12.5 minutes and a smaller ~ 52 seconds. As only one logging power meter was available it was not possible to give a definitive answer as to whether the oscillations were temporally coupled; however given that oscillations of the same period appear in both traces it was highly likely they shared a common origin.

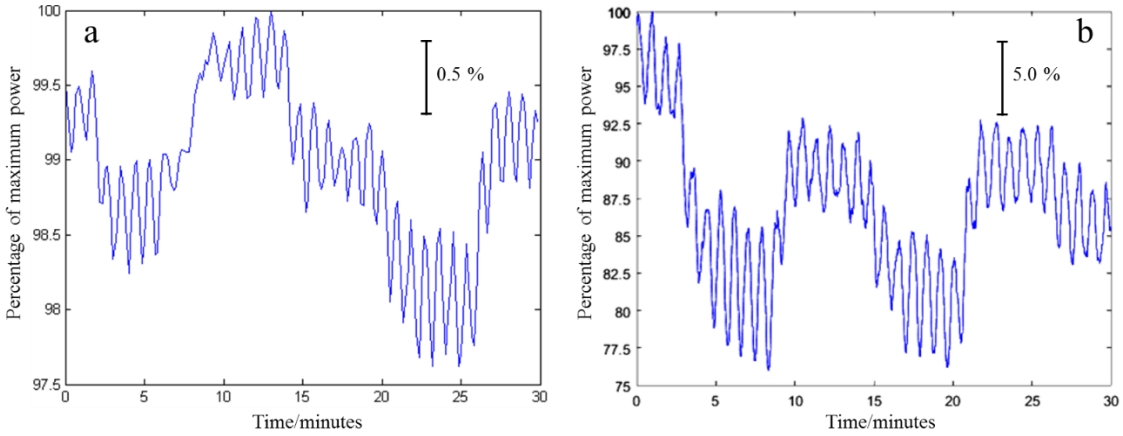

Figure 9.5 A trace of a) the pump beam and b) the Stokes beam normalised and displaced against percentage of their respective maximum beam powers (different scales used). Note, for the sake of clarity, a second order polynomial fit was removed from this data to account for a gradual decrease in power over the 30 minute period. Note that these two traces are not contemporaneous measurements.

In principle, if the observed oscillations were of low enough amplitude and/or over a sufficiently long period (40+ minutes) they could potentially be accounted for by normalisation; however, the largest problem stems from the supercontinuum generation. A fluctuating power input to the

FemtoWHITE800 unit not only resulted in fluctuation of the power output, but also an unpredictably varying spectral output. Whilst this should not, in theory, affect the NRB removal, due to the to the undiagnosed fringe-type spectral pattern, any alteration of the spectral form of the Stokes resulted in an incomplete cancelation of the NRB. As this non-linearly mixed with the SIPCARS signal, it cannot, by any conventional means, be removed by normalisation or subtraction.

Owing to the clear disparity between the two beams, in terms of severity of oscillation, the first factor to investigate was whether the NanoTrak feedback system could have been exacerbating the effect. Even though the oscillations were present in both beams, if the amplitude of the Stokes beam oscillations could be reduced in line with the pump beam this might have been sufficient to acquire usable images. It is difficult to draw any firm conclusions from Stoke beam traces without the feedback mechanism as the observed oscillations increased to over 50% of the maximum power due to thermal drift. It is, however, possible to see that the oscillations appeared to retain a ~ 12.5 minute period, which would seem to confirm that the NanoTrak was not the underlying cause.

Given the apparent common origin of the oscillations, the next solution attempted was to completely clean the Mira and Verdi water chiller (ThermoTek T255P). Previous experience suggested that doing so would, at least temporally, relieve instability originating from the titanium - sapphire oscillator. As there is no prescribed method to clean the chiller, and given that the primary cause of the blockage was probably lime scale (calcium carbonate) build up, a solution of approximately 20% ethanoic acid (pure distilled vinegar) was used. Using a short loop, directly from the output to the input by way of a motorbike fuel filter (essentially multiple layers of filter paper contained within a small chamber), the ethanoic acid was cycled for 24 hours, replaced, and cycled for a further 24 hrs. The chiller was then flushed multiple times with distilled water to ensure no debris or ethanoic acid remained. Cleaning the small gauge tubes within the body of the Mira oscillator proved more challenging. As with the chiller, ethanoic acid was circulated for 24 hours; however, given the significant narrowing of the tubes, as deduced by the minimal flow rate, a more direct approach was required. This entailed careful threading a wire through the channels and mechanically agitating the insides of the calcified tubes. Whilst completely cleaning the chillers and internal tubes of the Mira resulted in a greatly improved flow rate and decreased temperature fluctuations of the cooling water, this had very little effect on the overall amplitude or period of the oscillations.

Although the origin of the oscillation had been narrowed down to either the Mira or Verdi, it was imperative to isolate the exact cause, therefore, further stability measurements were conducted on each (see figures 9.6 and 9.7). In tandem, although unlikely to be a major contributing factor, the room temperature was also monitored. Over the course of a day the room temperature fluctuated

by a total of 1.5 degrees. Excluding the laser warming up and cooling down period, the temperature range was less than 1 degree and, as such, can be discounted as a possible source of the oscillations.

Figures 9.6 and 9.7, traces of the Mira and Verdi, respectively, show a very similar oscillation profile (a significant oscillating component with a period of ~13 minutes). As it is highly unlikely that two independent oscillations would have the same period it is a safe assumption that the underlying cause stemmed from the Verdi laser.

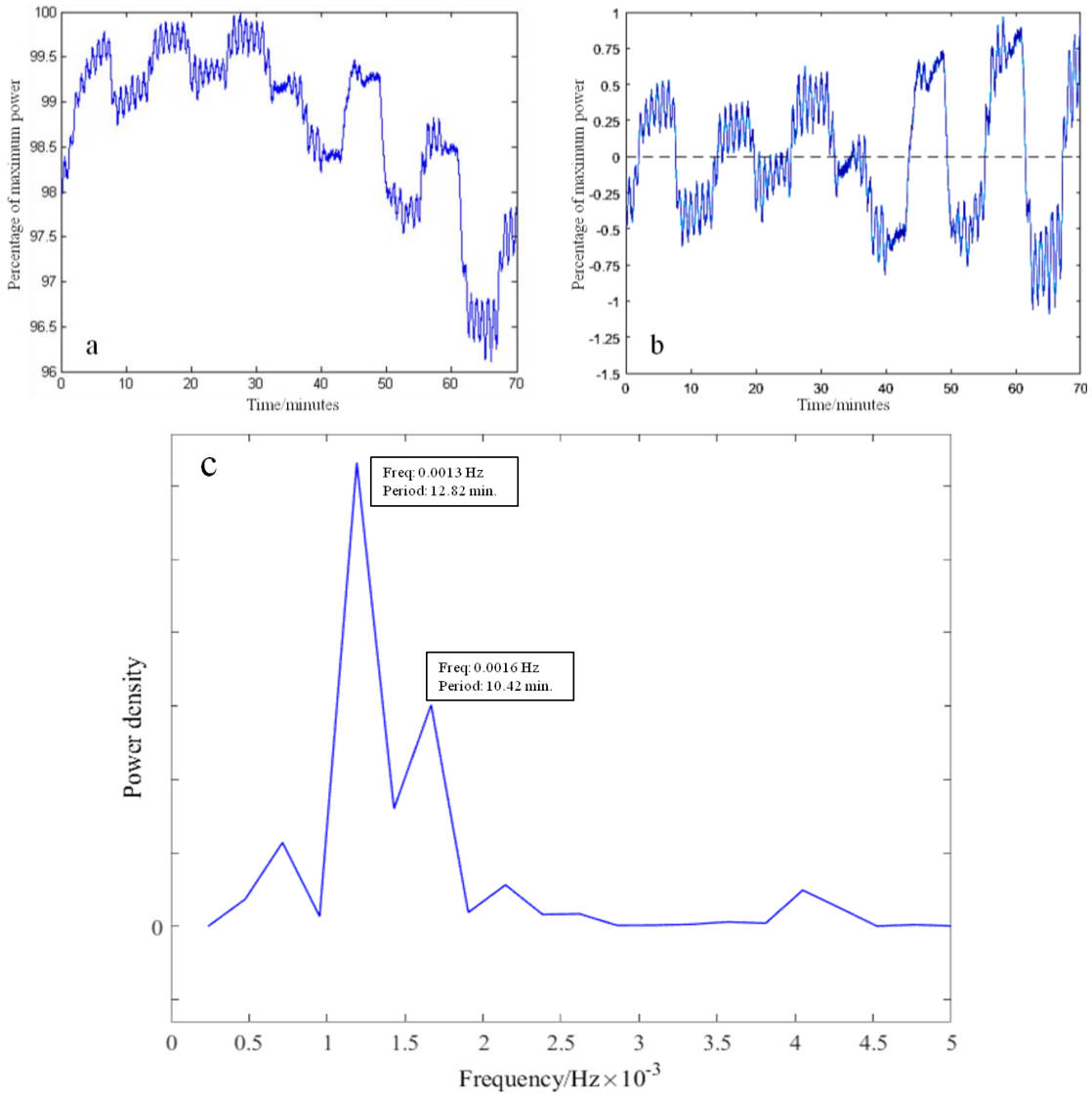

Figure 9.6 a) Unprocessed trace of the Mira output: shown as a percentage of maximum power. b) Processed trace: the underlying slowly varying fluctuation in power removed by subtracting a second order polynomial fit. c) Power spectrum (via Fourier analysis) with the predominant oscillation frequencies highlighted.

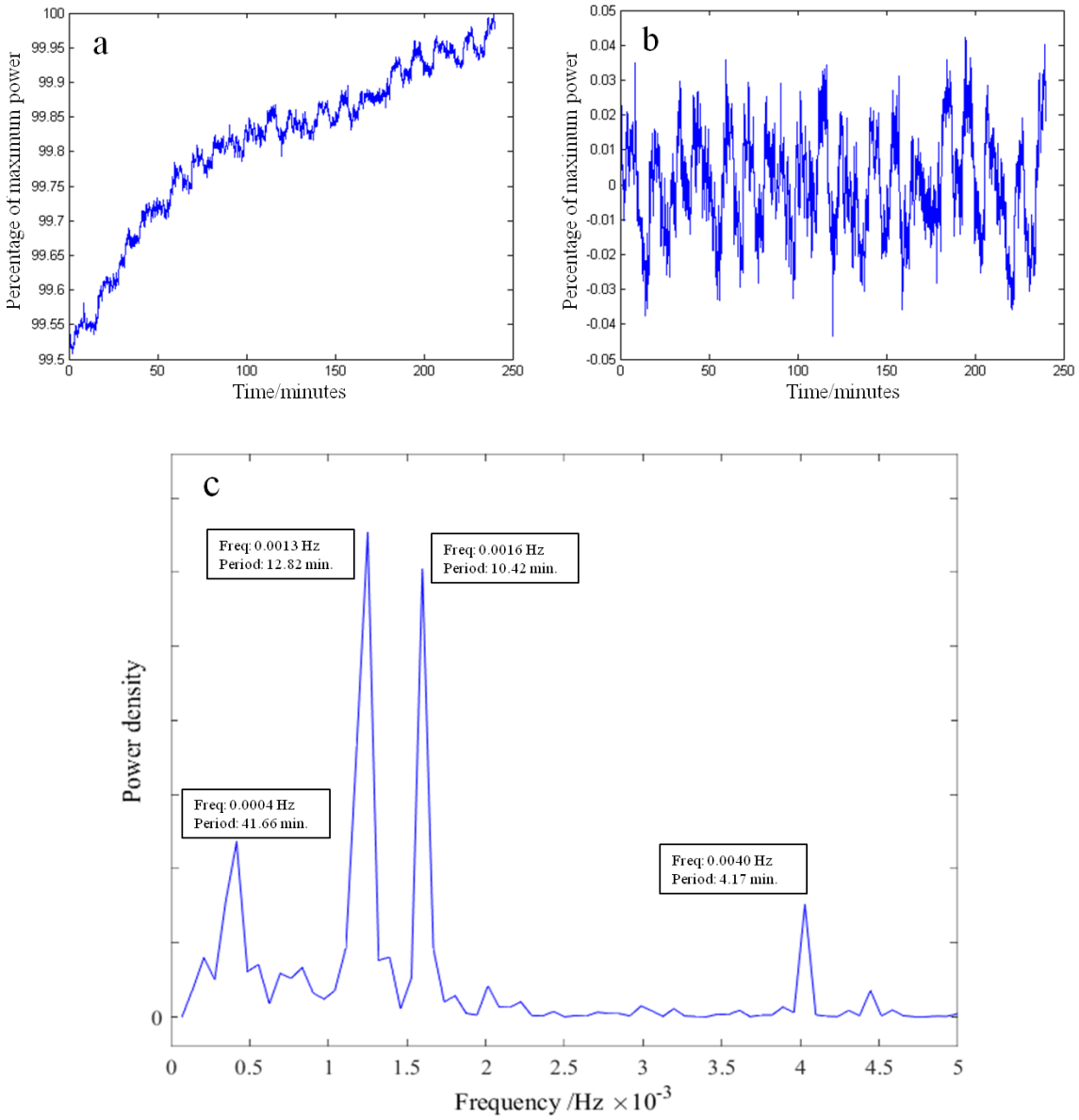

Figure 9.7 a) Unprocessed trace of the Verdi output: shown as a percentage of maximum power. b) Processed trace: the underlying slowly varying fluctuation in power removed by subtracting a second order polynomial fit. c) Power spectrum (via Fourier analysis) with the predominant oscillation frequencies highlighted.

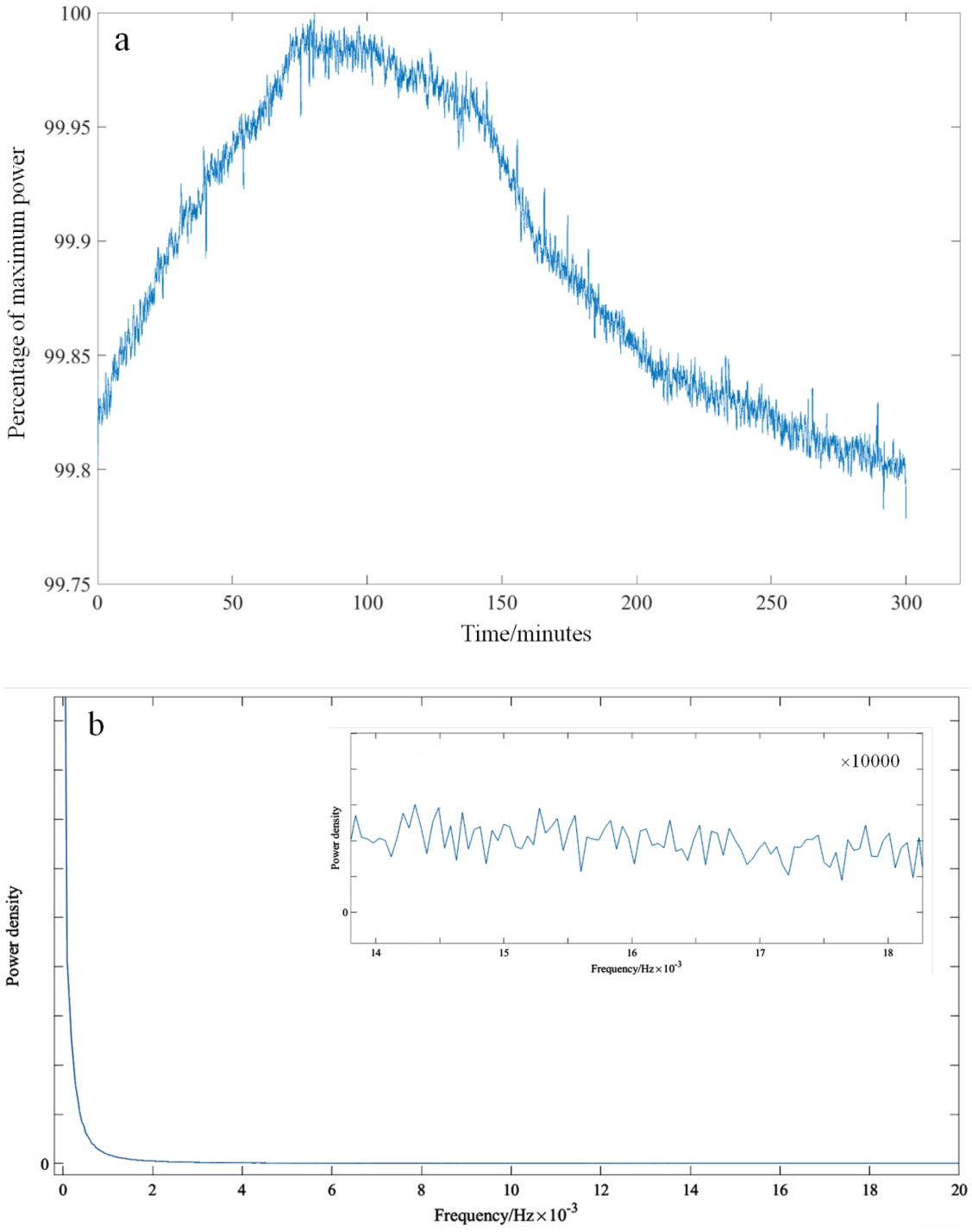

Figure 9.8 a) Unprocessed trace of the Verdi output after reset and re-optimisation of all the thermo-electric coolers: shown as a percentage of maximum power. b) Power spectrum (via Fourier analysis) of the entire 5 hour window. Inset: expanded view of the frequency window corresponding to oscillations with a 50 to 70 second period.

In summary, from these figures and many additional (not shown) corroborating measurements it is possible to state that the source of the oscillations was the Verdi laser. The oscillations, however, were then amplified by an order of magnitude in the Mira and again in the FemtoWHITE800 unit: resulting in a largely unusable system.

The actual amplitude of the Verdi output oscillations was, however, less than the ± 1% (over a two hour period) specification and thus an amount of persuasion and evidence was required for Coherent to make a service call. Even though the Verdi was operating within specification, the engineer agreed that the ~ 13 minute oscillations were not typical of the system and performed a complete diagnosis and recalibration (beyond the simple user optimisation shown in the manual) of the diode thermo-regulation system. The underlying cause of the oscillations was due to the thermo-electric cooler of the Lithium Triborate (LBO) doubling crystal failing to stabilise at its optimised temperature and instead oscillating. Given that these oscillations were not apparent in the previous lab, on the balance of probability they resulted from damage to the Verdi systems caused by the Kingsway fire.

After a full reset and re-optimisation of all the thermo-electric coolers within the Verdi, the stability of the output, figure 9.8, was markedly improved: exhibiting no detectable oscillations with a either ~ 13 minute, or ~ 52 second period. Whilst this is clearly a considerable improvement, figure 9.8a shows that, despite the complete overhaul, fluctuations, albeit smooth, on the order of 0.05% still occurred on a ~ 40 minute timescale. This prolonged investigation to identify the source of the oscillations had also served to expose the ramification of even small power fluctuations on the supercontinuum generation. Even this, seemingly minute, 0.05% fluctuation of the Verdi power would result in a 5% change in power output of the FemtoWHITE800 and, more problematically, an indeterminate alteration of the spectral form and width of the supercontinuum. Owing to the inherent non-linearity and complexity of PCF mediated supercontinuum generation, fluctuations of the input power will always result in significant and difficult to predict alterations of the output. That being said, the effect will be more pronounced at the extremities of the supercontinuum range and will, therefore, have a greater effect on higher wavenumber (i.e. the CH-stretch region). Given the fluctuation is now smooth in nature it can, to a large extent, be normalised (it will be largely removed by the χ^{NR} normalisation procedure); however, particular care needs to be taken to identify any potential artefacts in hyperspectral images derived from the CH-stretch region.

9.5 Installing an imaging spectrometer (Princeton Instruments IsoPlane-320)

The extensive inadequacies of the Bentham TMc 300 monochromator for SIPCARS were given, in detail, in the previous chapter (see section 8.5). It was entirely impractical to attempt to address these shortcomings in-house, and so, a purpose built imaging spectrometer was purchased. The class-leading Princeton Instruments IsoPlane-320 spectrometer employs a folded Schmidt-Czerny-Turner configuration which allows virtually aberration free spectra to be acquired [108] (see figure 9.9). The folded configuration allow for both a more compact footprint and a closer to axial optical path through the concave mirrors. Although the exact details of the

aberration correction methods utilised by this spectrometer are proprietary (and therefore not shown in figure 9.9), given the name assigned by Princeton Instruments (Schmidt-Czerny-Turner) it is a safe assumption that this spectrometer contains a Schmidt compensator/compensation plate. The details of this are beyond the scope of this thesis; however, this type of compensator is extensively used in astronomy and consists of a specifically tailored/shaped glass element introduced into the beam path which acts to pre-compensate any coma and spherical aberrations that are introduced by the use of concave mirrors off-axis. The interested reader would be well served by consulting references [108]–[112].

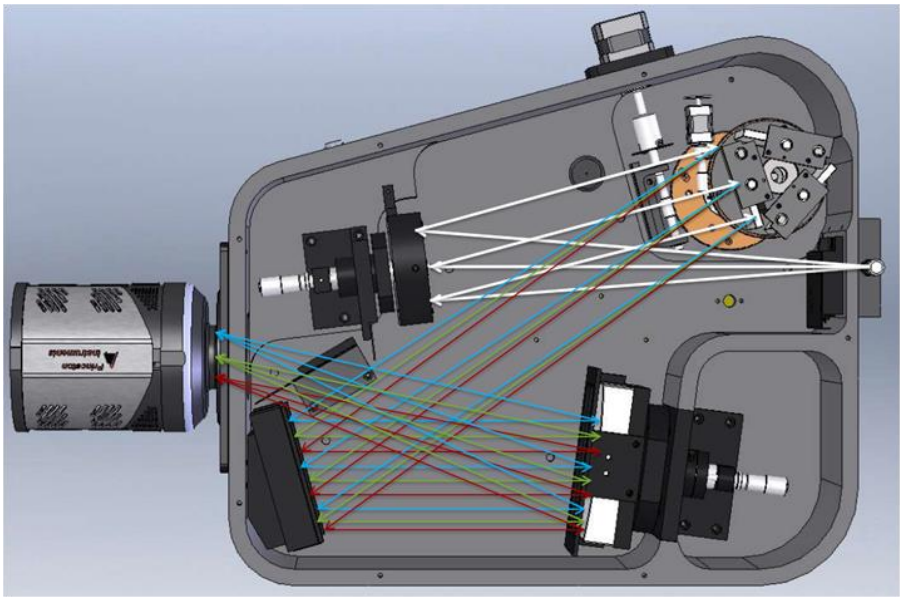

Figure 9.9 Internal workings of a Princeton Instruments IsoPlane-320 (shown to scale) [108]. The majority of the optical elements are not designed to be manipulated by the user; however, the position of the spherical mirror may be altered to fine tune the focus on to the CCD.

The net effect of replacing the Bentham monochromator with the IsoPlane-320 spectrometer was that the resulting tracks were, in fact, virtually aberration free and significantly narrower (i.e. the software defined track width over which the signal was collected could be considerably narrower: 6 as opposed to 40 pixels). In real terms this corresponded to an increase in both spectral resolution, and SNR. It also provided sufficiently narrow tracks for rapid single axis galvanometer based scanning (*cf.* section 7.5) to be a viable. The spectral resolution was now, taken as the FWHM of the leaked laser light through the 780 nm short pass filter, 11.5 cm^{-1}. With the Princeton Instruments 150 l/mm grating, used to interrogate the whole Raman spectral range, the limiting factor is now the pixel size of the Andor iXon EMCCD.

The polarisation alignment procedure outlined in section 8.3.3 presupposes that the track widths are sufficiently large that a small rotation of the EMCCD will have a negligible effect on the balance between the broadband Stokes beam components in each track. With the significantly

reduced track widths resulting from the implementation of the IsoPlane-320 spectrometer this was no longer the case and thus a new alignment procedure was required.

In essence, rather than set the rotation of the Wollaston prism by balancing the components of the broadband Stokes beam, the narrowband pump/probe beam was used. Initially, to ensure the maximum SNR alignment of the system (*cf.* appendix VII) was attained, an additional analyser, placed directly above the microscope, was used to ensure the pump/probe beam polarisation was orthogonal to that of the Stokes beam (with the Stokes beam linear polariser set to maximise transmission). Then, by rotating the Wollaston prism, the power of the two pump/probe beam components was balanced. After this, using the Stokes linear polariser, the power of the Stokes beam components in each track was balanced. It is worth noting that if a significant rotation ($< 5^{o}$) of the Stokes beam linear polariser was required then, although this did not automatically invalidate the alignment, it was double checked as this both reduced the power of the Stokes beam, and introduced a non-trivial deviation from the expected symmetry. In other words, the pump/probe beam elliptical polarisation would not, at the location of the Stokes beam linear polariser, be symmetrical with respect to the Stokes beam linear polarisation (a fundamental tenet of SIPCARS).

9.6 Outstanding limitations

There were two significant remaining outstanding limitations of the system: the fringe/interference-type spectral pattern, and an unexpected asymmetrical response from symmetrical (spherical) test beads.

9.6.1 Fringe/interference-type spectral pattern

The fringe/interference-type pattern, shown in figure 9.10, corresponded to an oscillatory behaviour varying in intensity between and along the two tracks. Owing to the EMCCD etaloning at the Stokes beam wavelengths it was not possible to state conclusively whether fringing was apparent with this beam alone. Under the assumption (Occam's razor) that the underlying cause of this effect stemmed from an individual optical element, the initial approach taken was to systemically remove and replace, if necessary, each optical component in the beam path until the culprit was identified. This was done in the perceived order of highest probability (and ease of realignment): starting with those elements common to both beams.

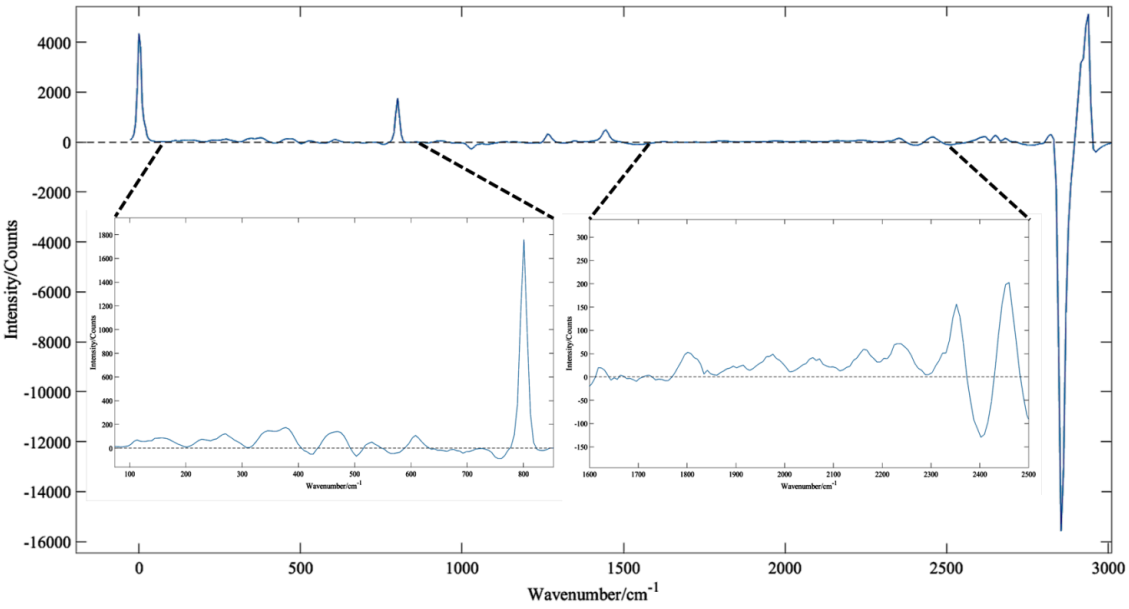

Figure 9.10 Full spectrum of pure cyclohexane. Insets show expanded views of the indicated regions. A clear oscillatory behaviour can be observed.

Over the course of previous alterations/improvements to the system, the objectives (top and bottom), the sample (measurements with just immersion oil between the objectives had also been acquired), the spectrometer, the re-combination long pass filter, the PCF, the Stokes beam linear polariser, the spectrometer coupling optics, the EMCCD, and the vast majority of mirrors throughout the system (silver mirrors upgraded to high reflection dielectric mirrors) had been replaced and the fringing pattern persisted. These optics could, therefore, be eliminated as possible sources. The only optics common to the both beams that had not been replaced were the Faraday isolator, the 90:10 beam splitter, the post sample short pass filter, the Wollaston prism, the prism in the base of the microscope (used to direct the emitted light into a specific exit port), and the post microscope quarter waveplate.

Although it was possible, albeit challenging, to remove several of these components while maintaining a similar alignment into the EMCCD, it was highly impractical to replace the prism in the base of the microscope and suitable replacements for the Faraday isolator and the 90:10 beam splitter could not readily be sourced. It was, however, exceptionally improbable that the latter two, the isolator and beam splitter, were responsible for the pattern as they were subject to a narrowband beam and, in the case of the Stokes beam arm, came before the PCF (which should have scrambled any spectral varying pattern in the input beam).

Owing to the significant irregularity, the period of oscillation could only be approximated to 4.5 nm. If the oscillations are attributed to a Fabry- Pérot type etalon and, assuming near normal incidence and a refractive index of 1.5753 (Schott glass at 785 nm), this corresponds to a cavity length of approximately 33 μm. Whilst this is significantly thicker than the typical $\lambda/4$ single

layer optical coating (anti-reflection coating) utilised on many optical elements it is not beyond the realms of possibility that an optical filter (i.e. a dielectric stack) may contain a layer/layers of this thickness. The first of the optical element common to both beams that was tested was, therefore, the post sample short pass filter. As the excitation beams must be rejected to avoid saturating the EMCCD, the Semrock 780 nm ultra-steep short pass filter (SP01-785RU-25) was replaced firstly by a Thorlabs premium 750 nm short pass filter (FESH0750), and then a Thorlabs standard 750 nm short pass filter (FES0750). Both filters resulted in an increase of leaked pump/probe light (at 785 nm); however, they had a negligible effect on the intensity or period of the fringe pattern. The Semrock filter was, therefore, re-installed and discounted as the source of the oscillations.

As the Wollaston prism was manufactured for this particular system, it could not be replaced with an off-the-shelf equivalent. To eliminate this optic as a possible source of the oscillations it was, therefore, simply removed and the beam allowed to propagate, unsplit, through the spectrometer and onto the EMCCD. The resulting single track on the EMCCD exhibited oscillations of an almost identical period as the split tracks (and SIPCARS spectrum) and, therefore, it was concluded that the Wollaston prism was not the underlying cause.

Removing the post microscope superachromatic quartz $\lambda/_4$ plate (B. Halle RSU 1.4.15) from the beam path affected only the relative intensity of the oscillation between the tracks and, as expected, did not have a discernible effect on the period.

Given that each optic common to both beam paths had now been excluded the single arm optics were now investigated. This did not, however, provide any conclusive evidence as to the cause of the fringe/interference-type spectral pattern.

This pointed towards a more subtle effect, perhaps a combination of several optics (highly unlikely) or (current best educated guess) a structuring of the focal point caused by complex polarisation interactions; however, it should be noted that at present, without any convincing evidence, this is conjectural.

A further possibility, although once again improbable, is that the underlying cause is, in fact, the EMCCD. Whilst the fringe pattern was observed with two separate EMCCDs, the Andor iXon DU-897 and the Princeton instruments ProEM+ 512B, which would seem to exclude this as the cause, they may not be independent. These two scientific camera manufacturers both purchase the silicon sensors used in their EMCCDs from e2v ltd. [113]–[115]. The specific details of the sensors used in each EMCCD are, of course, proprietary knowledge, so there is no way of confirming they are identical. If, however, the same sensor chips are used in both, which owing to the same form factor may not be that improbable, the fringing pattern could, therefore, be a systemic flaw. The recent release, by Princeton instruments, of new EMCCDs based on eXcelon3

technology, which it is claimed significantly reduces etaloning, [115] would seem to suggest this is an established effect.

9.6.2 Unexpected asymmetrical spatial response

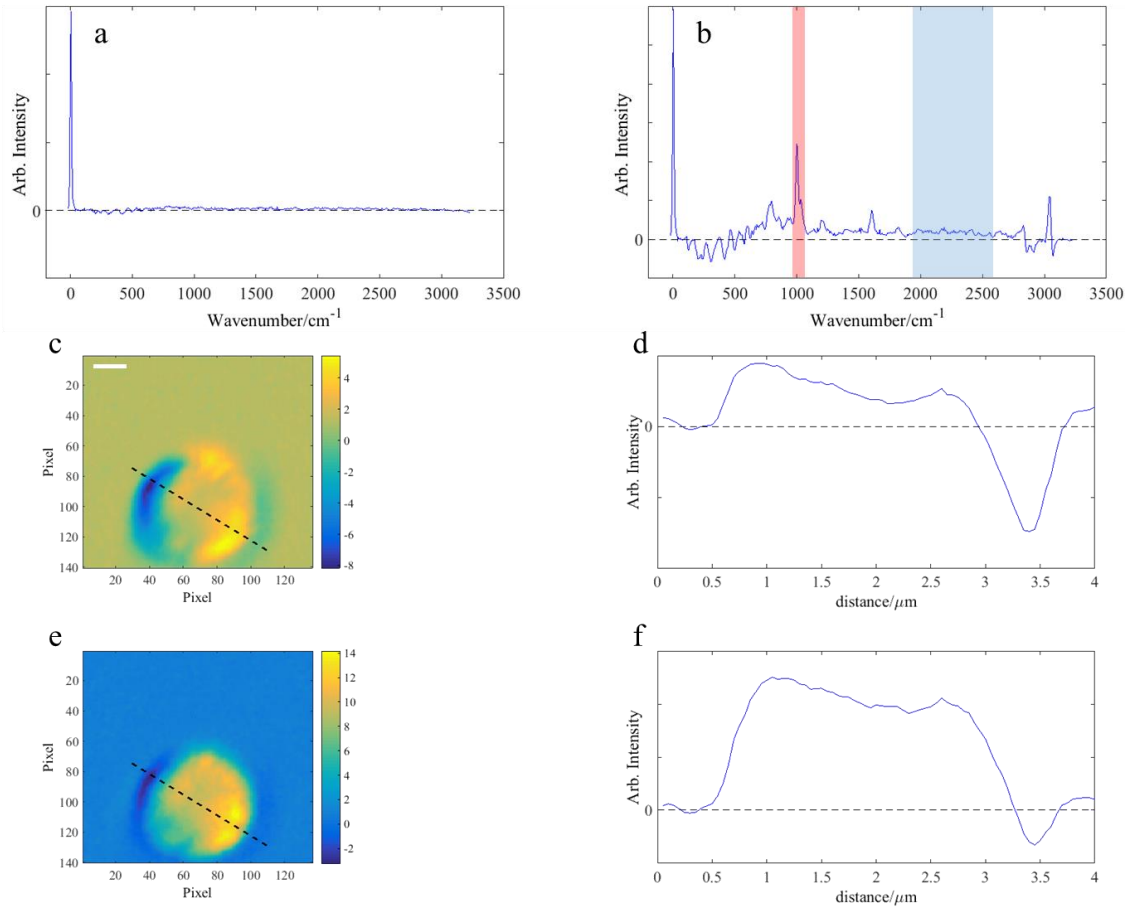

Figure 9.11 Image of a 3 µm polystyrene bead immersed in water. a) Mean spectrum taken from a 20×20 pixel water region. b) Single pixel spectrum taken from the centre of the bead. The 1013 cm^{-1} ring breathing mode peak, and non-resonant region are highlighted in red and blue respectively c) SIPCARS image of the highlighted non-resonant region. Ideally, conforming to the theory, this should be just noise. Dashed line (also shown in e) corresponds to the line transecting the geometric centre of the bead with the largest intensity range of the resonant (1013 cm^{-1}) peak. d) The line profile of intensity in the non-resonant region along dashed line shown in c). e) SIPCARS image of the highlighted polystyrene ring breathing mode peak. f) The corresponding intensity line profile of the dashed line shown in e). Pixel dwell time: 50 ms; pixel size: 50 nm; scalebar 1 µm.

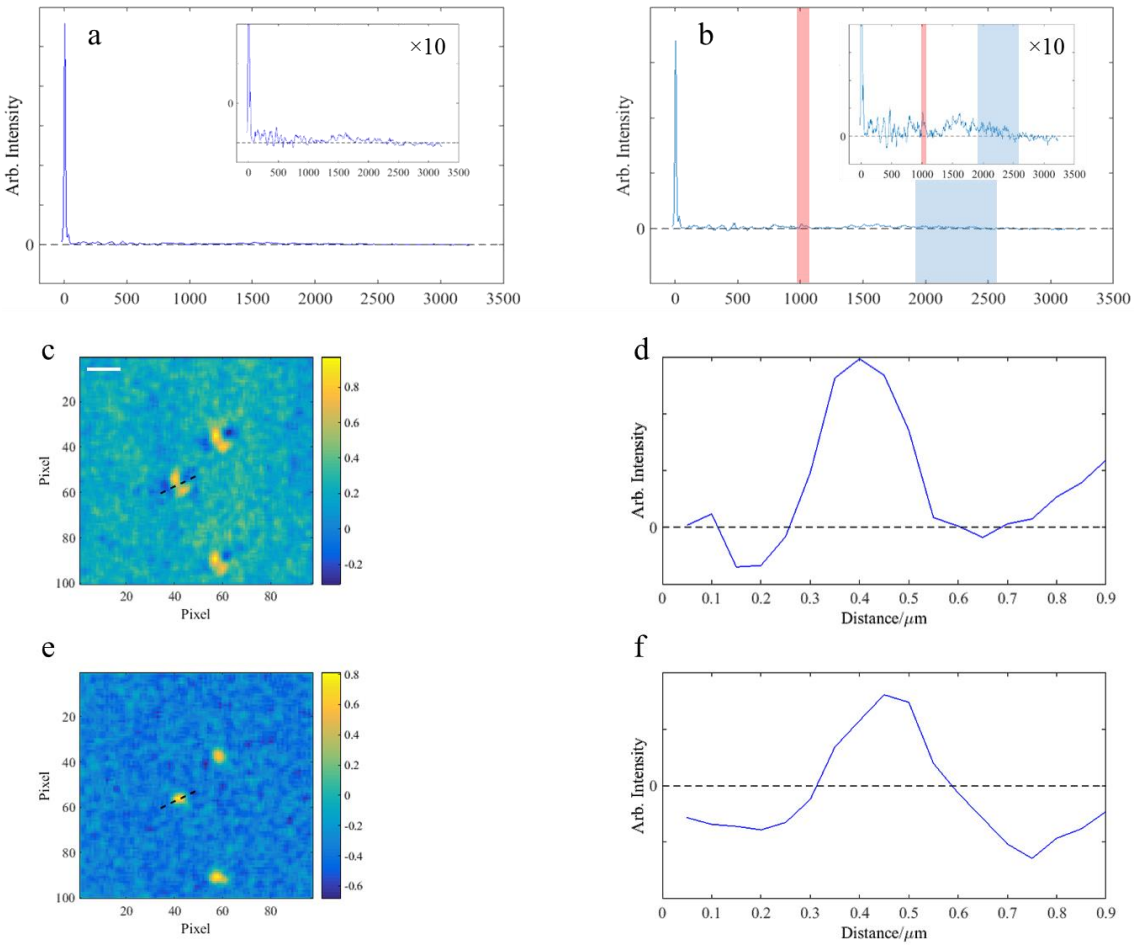

Figure 9.12 Image of a 0.46 µm polystyrene bead immersed in water. a) Mean spectrum taken from a 20×20 water region. Inset: expanded (×10) spectrum. b) Single pixel spectrum taken from the centre of the bead. The 1013 cm^{-1} ring breathing mode peak, and non-resonant region are highlighted in red and blue respectively c) SIPCARS image of the highlighted non-resonant region. Ideally, conforming to the theory, this should be just noise. Dashed line (also shown in e) corresponds to the line transecting the geometric centre of the bead with the largest intensity range of the resonant (1013 cm^{-1}) peak. d) The line profile of intensity in the non-resonant region along dashed line shown in c). e) SIPCARS image of the highlighted polystyrene ring breathing mode peak. Inset: expanded (×10) spectrum. f) The corresponding intensity line profile of the dashed line shown in e). Pixel dwell time: 50 ms; pixel size: 50 nm; scalebar 1µm.

Throughout the course of several bead and biological test samples investigated (some of which are shown in the succeeding chapter) a troubling effect was observed. When acquiring images including spherical or oblate objects, such as beads or droplet-type structures, there was an apparent unphysical asymmetry. The images of polystyrene beads shown in figures 9.11 and 9.12 clearly illustrate this effect. In both cases the cancellation, although not perfect, is acceptable in the water region, panel a), but upon entering the bead, panel b), is significantly perturbed. More significantly, panels c) and e), images over the highlighted resonant and non-resonant regions, respectively, with their associated line profiles emphatically exhibit this asymmetry.

Due to time limitations only a preliminary investigation of this effect could be carried out; however, it was possible to exclude a major potential cause and provide strong circumstantial evidence as to the potential source of this effect.

The initial route of investigation focused on a 'lensing' type of effect. In other words, due to a mismatch in refractive index between the bead/spherical object and the surrounding medium, the location of tracks was shifted on the EMCCD, or even overlapped, resulting in an erroneous result. As the effect was significantly diminished in many biological samples where spherical organelles are embedded in a surrounding medium (tissue) with approximately the same refractive index this theory appeared to have credence. In order to test this, using the same 3 μm bead type, five additional measurements were taken with varying track widths. Employing a similar analysis as used to produce figures 9.11 and 9.12, the percentage difference between maximum and minimum value along the line profile was taken as indicative of the degree of asymmetry. Whilst the percentages recorded over the various track widths ranged from 28.8% to 32.7% this did not show any significant correlation with track width.

Once again previous experience of this effect suggested the line of greatest asymmetry was always aligned in a similar direction. The orientation of the Stokes beam was therefore ascertained by placing an additional polariser above the top objective and minimising the power as measured via a power meter located after the Wollaston prism. The orientation of the Stokes beam entering the top objective was found to be perpendicular to the breadboard. Using four separate 3 μm beads (eight scans were attempted resulting in only four successful acquisitions) and analysing the 1013 cm^{-1} peak, an average angle for the line of greatest asymmetry was calculated. Defining the zero angle as the plane of the breadboard, the angle of the average line of greatest asymmetry was $90^{o}\pm10^{o}$: in other words, approximately aligned along the breadboard. It is not immediately apparent why/how a polarisation effect could manifest as an asymmetry, causing a preferential decrease/increase in resonant signal on one side of a bead relative to the other; however by showing the line of greatest asymmetry was aligned perpendicular to the polarisation orientation of the Stokes beam this does, at least, provide a strong indication that the two are related. As previously stated this was a preliminary study of this effect; however, it undoubtedly warrants further investigation and would form an immediate/short term objective of future work on this system.

10. CARS based on a titanium-sapphire oscillator and photonic crystal fibre: system characterisation

This chapter concerns those bodies of work that are more characterisation as opposed to predominantly developmental in nature. Each section within this chapter represents a standalone piece of work, and, as such, will be presented in a more conventional format. To that end, each will be subdivided into an introduction, followed by an apparatus and methods section, before culminating with results, discussion and conclusions. As the apparatus and general method have been discussed in detail in chapter 8, only unique aspects of the particular experiment will be given in addition to attempting to place the work within the developmental chronology (i.e. these experiments were carried out at various different time points and thus using the system at different developmental stages).

The experiments detailed in this chapter were performed and analysed by the author.

10.1 Spatial resolution

10.1.1 Introduction

The focal volume of any microspectroscopy system is a defining characteristic and is important for determining the spatial resolution and calibrating instrument sensitivity. Unfortunately, owing to the inability to source suitable x and y axes spatial targets (see section 10.2.4), only the axial resolution was determined in this body of work. The axial resolution of the system was determined by scanning through a thin polyacrylonitrile (PAN) film and observing the resonant and non-resonant response.

10.1.2 Apparatus and Method

10.1.2.1 Apparatus

The data presented in this body of work was acquired immediately after the titanium-sapphire oscillator based system was commissioned and prior to the implementation of any improvements (i.e. using the freestanding PCF, cross-roller bearing stage, and Bentham monochromator).

10.1.2.2 Sample preparation

Axial resolution was determined using a 40 nm thick PAN film (provided by collaborators at the National Physics Laboratory): spun-coated on glass and characterised using AFM. Rather than image through a glass coverslip (i.e. enclose the PAN film between two glass coverslips) and risk the formation of air pockets, immersion oil was placed directly on the top surface of the film.

10.1.2.3 Spectral acquisition

Data was acquired by performing a 5 μm axial scan across the oil-PAN-glass interfaces with a step size of 0.2 μm. In order to increase the SNR at each step, a 4×4 pixel area was acquired with an exposure time of 1.5 seconds, and a mean spectrum subsequently derived. These parameters were chosen to maximise the signal whilst still remaining within the limitations of the system: i.e. before the PCF started to decouple. Note, given the limited thickness of the PAN film, it was necessary to both average and utilise long exposures to attain a sufficiently high SNR.

10.1.3 Experimental Results and discussion

Having produced a mean spectrum at each z-plane the axial resolution was determined via two distinct approaches: resonant and non-resonant (see figure 10.1). The resonant approach consisted of integrating over the C≡N bond PAN peak (2245 cm^{-1}) of the SIPCARS spectrum and plotting against axial distance. It was then possible to perform a Gaussian fit of this plot and retrieve a value for the FWHM.

The second approach exploited the NRB, which, whilst differing in intensity between materials, is spectrally equivalent (discussed in detail in section 10.2). Taking the square root of the integrated intensity attained from a non-resonant region (2400-2600 cm^{-1}) within the sum spectrum, allowed the value χ^{NR} (see appendix IV) to be plotted against axial distance, which could subsequently be fit (using the inbuilt Matlab fitting tool) with a simple error function. Taking the derivative of this function with respect to the scan direction produced a Gaussian profile from which it was also possible to attain the FWHM.

There are two distinct advantages to using the NRB signal as opposed to the resonant PAN vibration. Firstly, as the signal is generated from the entire focal volume rather than solely from the PAN film (sub-diffraction limit thickness) it is possible to attain a considerably higher SNR. Secondly, when considering only the NRB signal a judicious choice of materials allows the refractive indices to be matched across the interface ensuring the imaging properties are not altered; therefore ensuring that the contrast stems solely from the change in the non-resonant component of the non-linear response.

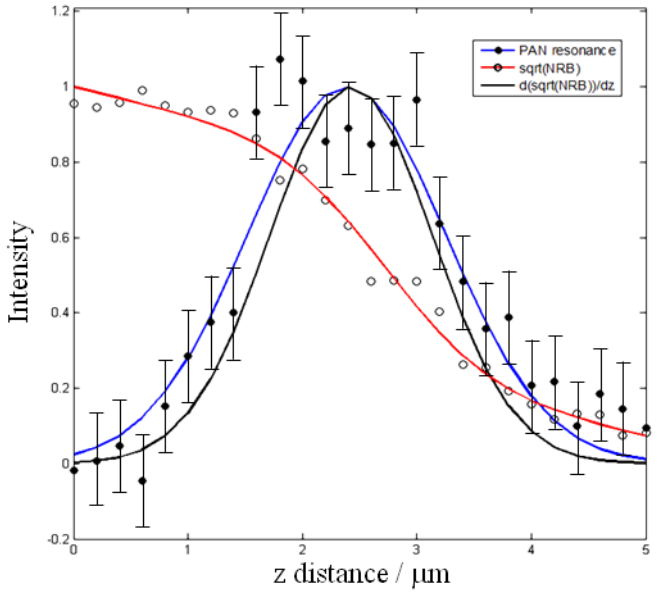

Figure 10.1 z-scan across a 40 nm polyacrylonitrile (PAN) film held between glass and immersion oil. Closed circles: C≡N vibration of PAN at 2245 cm^{-1}; open circles: square root of the NRB signal; blue curve is a Gaussian fit to the resonant PAN signal; black is the derivative of the error function fit to the $\sqrt{Sum_{NR}}$ signal (red curve). Error bars correspond to a best estimate of the true error based on the SNR and the fluctuation of the NRB cancelation over the scan.

The FWHM as determined from figure 10.1 are 2.2 ± 0.4 µm and 1.7 ± 0.2 µm derived from the resonant and non-resonant approach respectively. These values are significantly larger than might be expected; even discounting the intrinsic multiphoton optical sectioning, the theoretical diffraction limit for a single 1.3 NA objective under similar conditions is 1.402 µm (at 785.0 nm). This largely stems from optical aberration introduced by the sub-optimal (corrected for visible wavelengths as opposed to IR wavelengths used) objectives used for these measurements. The value of resolution as determined using the non-resonant approach is likely to be the more accurate representation of the true axial resolution of this system as the higher SNR allowed for a more robust fitting.

10.2.4 Conclusion and future extensions

Whilst the axial resolution of the SIPCARS system has been evaluated using two distinct methods, given the inherently lower SNR of the resonant approach, it is highly likely that the 1.7 ± 0.2 µm value attained via the non-resonant approach is more reliable.

As previously stated significant problems related to sourcing suitable samples were encountered whilst attempting to determine the lateral resolution of the system. It is therefore possible only to provide an upper limit of 460 nm: the smallest clearly resolved polystyrene bead successfully imaged.

As it would be highly desirable to have a full characterised spatial resolution of the SIPCARS system, the most exigent extension of this work would be to procure a reliable, well characterised set of lateral resolution test samples. Ideally the format of these samples would be point-like resonant objects (50 - 200 nm polystyrene beads) embedded within a non-resonant matrix. An analysis, similar to that for the axial resolution, could then be applied to determine the lateral resolution.

Any further extensions to this body of work would be subject to other improvements of the system. In terms of absolute spatial resolution the main limiting factor was the optical aberration introduced by sub optimal objectives; however, in terms of facilitating characterisation of the spatial resolution, improving the stage was a high priority.

10.2 Non Resonant Background (NRB) Calibration

10.2.1 Introduction

The ability to characterise the third order susceptibility $\left(\chi^{(3)}\right)$ of a given chemical species is of significant importance for a variety of reasons: both practical (optical device applications) and fundamental (understanding the non-linear response) [116]. This has, consequently, led to a range of techniques being developed to study the $\chi^{(3)}$ of liquids including, but not limited to, the AC/DC Kerr effect, electric-field-induced-second-harmonic-generation (EFISHG), degenerate/non-degenerated four wave mixing (FWM) and third harmonic generation (THG) [117]. A discussion of the relative merits of each technique is included in the seminal paper (Meredith *et al.*). This paper puts forward a compelling argument for THG as the most accurate probe of $\chi^{(3)}$ and thus the literature values used for comparison purposes were taken from this reference (and the second paper in the same series [94]).

Whilst, as stated above, there are generic reasons why the ability to determine $\chi^{(3)}$ is of importance, it is, however, necessary to compare quantitative coherent anti-Stokes Raman scattering techniques (of which a NRB removal mechanism must be a part) and spontaneous Raman scattering [118] [119] (see section 3.2.1.3). It is, in fact, of greater importance still for the various computational NRB removal approaches which require the raw CARS spectrum to be normalised by $\chi^{(3)}$ in a non-resonant region $\left(\chi^{NR(3)}\right)$ prior to the attempted removal of the NRB [30] [95]. The most widely adopted approach, at present, is to normalise by the $\chi^{NR(3)}$ of a reference material (normally glass). This, however, does not account for the possibility that the reference material itself may have residual resonances present in the non-resonant region of interest. The primary aim of this particular study was, therefore, to assess the applicability of various materials (including glass) as possible $\chi_{NR}^{(3)}$ calibration samples, looking at their spectral forms, ease of use, and reproducibility.

With regards to appendix VIII, which states there is proportionality between the $\chi^{NR(3)}$ and the real components of the linear refractive index (n_0), this is purely an empirical result and cannot be applied to quantitative measurements: merely providing an approximate value for $\chi^{NR(3)}$ given n_0.

10.2.2 Apparatus and Method

10.2.2.1 Apparatus

As per the determination of spatial resolution (section 10.1), the data presented below was acquired immediately after the titanium-sapphire oscillator based system was commissioned and prior to the implementation of any improvements.

10.2.2.2 Sample preparation

The liquid calibration samples used in this study were prepared in accordance with the method set out in section 7.3.2. As ensuring the entirety of the focal spot was situated within the calibration sample measurements was highly critical, each sample included a 45 μm aluminium spacer between the coverslips.

The glass spectra acquired were simply obtained by moving the focal spot into the glass above the water sample prior to acquisition (ensuring sufficient distance before the glass liquid boundary). As only a single sapphire coverslip (170μm - UQG Ltd.) was available, spectra were acquired by simply focusing the laser into it with immersion oil above and below. The quality of resultant spectra is equivalent to those acquired from the liquid samples.

10.2.2.3 Sample choice

Ideally a comprehensive set of NRB samples would include a wide variety of $\chi^{NR(3)}$ with spectrally varying resonance free regions (allowing $\chi^{NR(3)}$ to be determined throughout the entirety of the pertinent wavenumber range), be relatively user friendly and sufficiently commonplace as to be accessible by most CARS labs. In addition to these criteria the choice of reference material was also partially determined by the availability of relevant $\chi^{NR(3)}$ data [94] (see appendix IX). As a result the following reference materials were initially chosen: carbon disulphide (CS_2), carbon tetrachloride (CCl_4), chloroform ($CHCl_3$), toluene (C_7H_8), water (H_2O), immersion oil, glass (Sigma-Aldrich coverslip glass), and sapphire.

Of these initial choices carbon tetrachloride and chloroform proved overly difficult to work with being too volatile, resulting in the liquid instantaneously undergoing convection pumping (thermosyphoning) away from the focal spot. An attempt to address this was made in the form of

thicker samples, however the same result was observed and, as such, these samples were discarded.

Carbon disulphide also proved problematic as it reacts instantaneously with wet epoxy resin forming a yellow highly viscous liquid of unknown chemical composition. To remedy this an empty sample was made up with the two coverslips partially sealed (a ~2 mm hole remained) allowing the epoxy to completely set (over 48 hours) prior to filling with carbon disulphide. This was subsequently sealed with epoxy which, although reactive, proved adequate for such a small gap. Whilst the epoxy still deteriorated it did so over a period of days thus allowing spectra to be acquired.

Having determined the useable calibration samples the number of molecules in their respective focal volumes was calculated using various methods (see section 10.2.3). The validity of each method and assumptions made therein will be commented upon further in the analysis section.

10.2.2.5 Spectral acquisition

Spectral acquisition entailed altering the length of the delay line so as to focus temporal overlap on the 950 – 980 nm region. This equates to the spectral region of the Stokes beam that directly corresponds to the quiescent, resonance free, region of the emitted anti-Stokes signal (centred at approximately 2200 cm^{-1}). Spectra of each calibration sample were acquired (the average of 1000 individual 50 ms exposures) and, by means of a band pass filter and a powermeter (Coherent field master GS), the power of the Stokes beam recorded in the 950 – 980 nm region. This particular approach allowed for relatively accurate normalisation of each spectrum both in terms of the power, and spectral fluctuation of the Stokes beam intensity (a significant hindrance at this point in time: see section 8.5)

10.2.3 Experimental Results and discussion

Whilst acquiring the data presented below it became apparent that significant laser power fluctuations were occurring during and between each acquisition. An initial analysis step, whereby the spectra were normalised with respect to Stokes beam power, has been performed on all data presented below.

The resultant spectra (see figure 10.2), as expected, do not show any resonant spectral features (within the targeted 1700 - 2900 cm^{-1} region) and serve to highlight the distinctly different $\chi^{NR(3)}$ values of each sample. Whilst the magnitude of $\chi^{NR(3)}$ may be different for each sample the spectral forms appear equivalent. This suggests that all of the materials evaluated in this study may be considered valid NRB calibration samples. Given the aforementioned reservations concerning the use of glass as a NRB calibration sample a more in depth analysis was performed. A comparison of spectral forms of glass and carbon disulphide (see figure 10.3) verified the

absence of residual glass resonance as the two forms are identical to within the spectral resolution (~ 30 cm^{-1}). It should be noted that this applies only to this particular glass composition and spectral range; it is not possible to make inferences about glass in general from this result.

The nature of the spectral form observed is that of the interference-type pattern discussed extensively in the previous chapter. In light of this underlying pattern, it is important to note that these spectra actually portray the instrumental response, as over this wavenumber range for the chosen samples the $\chi^{NR(3)}$ is effectively constant (see chapter 2).

Having investigated the spectral form of each potential NRB calibration sample, in an attempt to corroborate the findings of this study with that of early work [94], the ratios of $\chi^{NR(3)}$ between different sample were assessed. Note, as demonstrated in appendix IV, the value of $\chi^{NR(3)}$ is directly proportional to the square root of the sum spectrum derived from a non-resonant region$\left(\sqrt{Sum_{NR}}\right)$.

The intensity of the highlighted region in figure 10.2 was measured for each of the samples and subsequently used to normalise for the different incident Stokes beam power. An initial plot of $\sqrt{Sum_{NR}}$, as normalised by the number of molecules in the focal volume (assuming the focal volume to be independent of refractive index), was created (see figure 10.4).

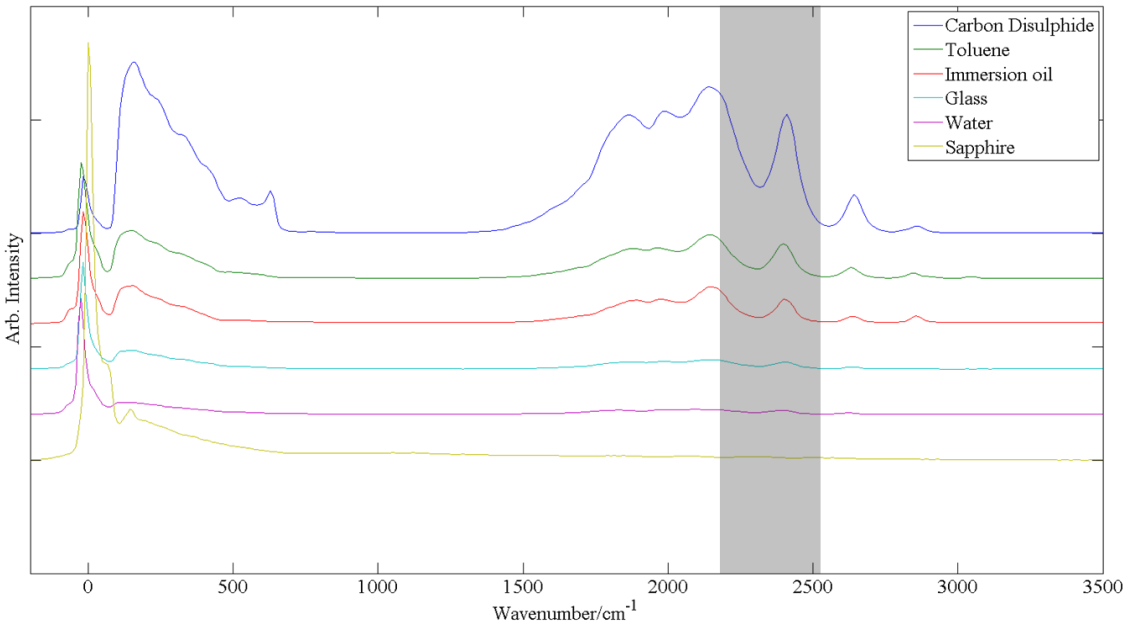

Figure 10.2 Calibration sample sum spectra. The highlighted area indicates the region over which the Stokes power was assessed. Spectra have been offset for clarity.

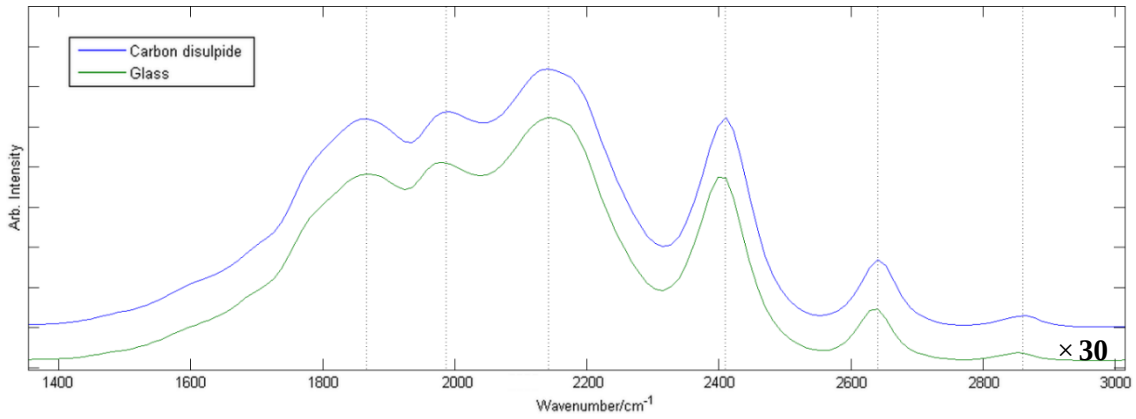

Figure 10.3 A comparison of the spectral forms of carbon disulphide and glass. The dotted lines serve as a guide to the eye. The spectra have been scaled (glass × 30) and offset for clarity.

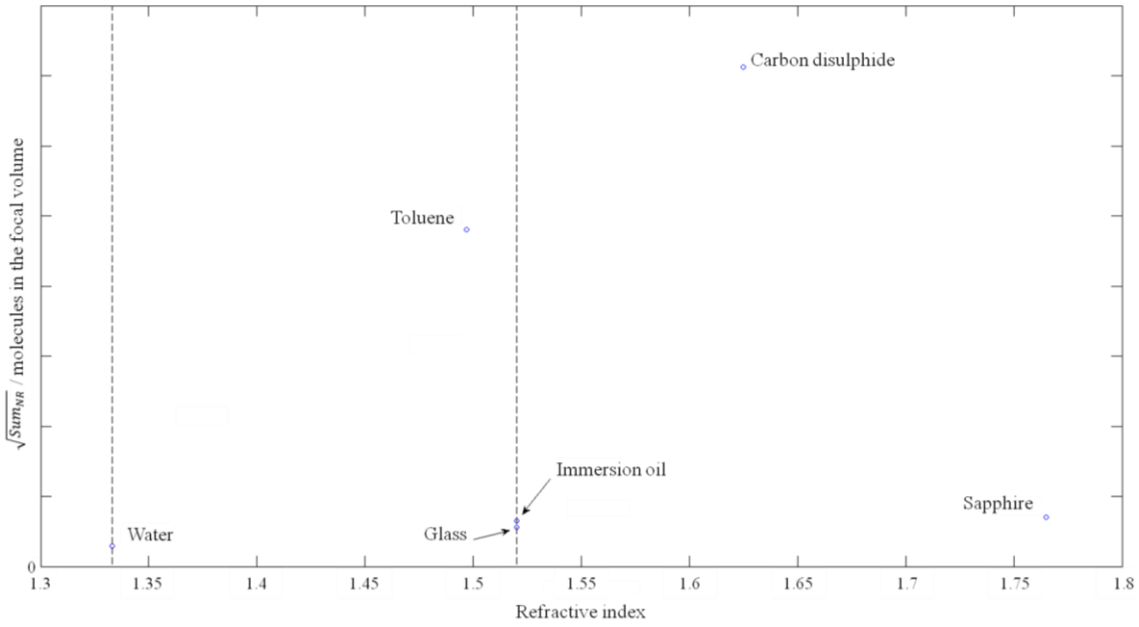

Figure 10.4 Graph showing the $\left(\sqrt{Sum_{NR}}\right)$ as normalised the number of molecules in the focal volume (focal volumes all assumed to be equivalent to the focal volume as calculated in glass) against refractive index. The left and right hand dashed lines correspond to the refractive index of water and glass respectively.

Of the samples studied here, $\chi^{NR(3)}$ values are known only for carbon disulphide and toluene. The $\chi^{NR(3)}$ ratio for toluene : carbon disulphide, determined in reference [94] was 1:2.3 (9.81 esu : 23.0 esu) whilst using the approach outlined above a value of 1:1.5 was attained. The significant difference (49%) between these two values was likely to be due to the assumption of a focal volume independent of sample refractive index.

A less simplified approach for calculating the focal volume was, therefore, implemented. This was achieved by assuming the focal volume was solely dependent on the refractive index of the sample. Additionally the dependence of wavelength on refractive index was also taken into

account which resulted in a $\frac{1}{n^6}$ relationship between focal volume and refractive index (see appendix IX). The ratio obtained using this method was 1:2.3 which is equivalent to the literature value. Whilst this result is certainly promising it is by no means conclusive as it is based solely on two results (further comment will be made in the section 10.2.4).

A $\frac{1}{n^6}$ relationship may, at first, appear unlikely; however, the objectives are being used outside their original specification. That is to say an oil immersion objective lens is typically designed to focus on the glass-sample boundary through a specified thickness of immersion oil and glass; however, in this case the focal volume is completely encapsulated deep (approximately 20 μm) within the sample (see figure 10.5). Additionally these objective are optimised for use with biological samples which are typically found in an aqueous medium and have a refractive index not too dissimilar to water (1.33) In essence, ~10% of the combined working distance of the two lenses is located within the sample which may have a refractive index significantly different to that of water (see figure 10.5). When taking this into account whilst calculating the focal volume (i.e. using a wavelength corrected for the sample refractive index: $\lambda_{sample} = \frac{\lambda_{vacuum}}{n_{sample}}$) using the normal formulae this yields a $\frac{1}{n^6}$ dependency on refractive index.

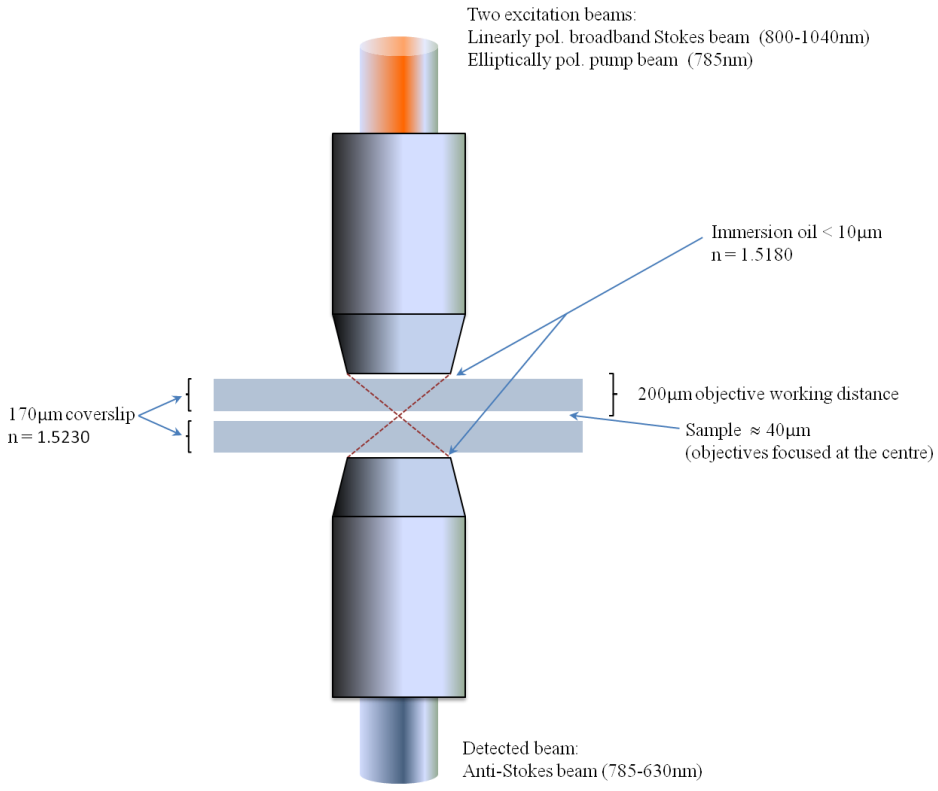

Figure 10.5 The location of focal volume within the sample configuration and relative to the two objective lenses.

This is, without doubt, still a vast over simplification of the system and extensive computational simulation would be required to derive an accurate relationship between the focal volume and

refractive index (especially given the non-trivial input polarisation states). This was not attempted but would form an important and potentially illuminating piece of future work.

10.2.4 Conclusion and future extensions

The primary aim of this study was to assess the viability of several materials as NRB calibration samples. Whilst according to the above results any of the samples tested could potentially be used to calibrate the NRB, the most applicable for any given situation is largely a matter of convenience. The use of water as a calibration sample is particularly attractive for biological specimens which are normally studied in aqueous solution; however, given the relatively low strength of $\chi^{NR(3)}$ of water, necessitating long exposures, it may not be appropriate for fragile samples. Alternatively the majority of microscopy samples are mounted on glass (which would require independent testing to verify the absence of resonances in a given region) and thus by translating into the glass this provides a potential NRB calibration. From a purely spectroscopic point of view, as a NRB calibration sample, carbon disulphide offers the highest signal to noise ratio due to its intrinsically high $\chi^{NR(3)}$. The concept of a 'best' calibration sample to use is, therefore, largely situational.

This experiment, although broadly successful, was limited in terms of the number of samples tested, the spectral region over which the samples were tested, and assumptions made in determining the focal volume. These limitations could potentially be overcome with the implementation of some extensions. There are several extensions that could be applied to this work in the future: the most pressing of which is to increase the number of samples tested. Whilst the number of useable samples for which $\chi^{NR(3)}$ data is available is severely limited, testing additional samples may prove, or disprove, any tentative conclusions made in this work thus far. In addition, attaining an accurate value for the lateral resolution (see section 10.1) of the system, at least in water, would allow for a more accurate estimate of the focal volume at a given refractive index. As physically measuring the focal volume of many of these samples would be exceptionally difficult, if not impossible, owing to their high solvation potentials, deriving a value via computationally modelling would be a valuable extension of this work. The initial region over which the Stokes beam power and thus analysis of NRB was performed was chosen as the filters were readily available and it corresponded to a resonance free region of the samples. To truly calibrate the entire spectral region of interest, however, would require the analysis to be extended to include more spectral regions.

10.3 Investigation of the multiplexing limit

10.3.1 Introduction

Much of the requisite introduction for this body of work was addressed in chapter 5, including the multiplexing limit as related to CARS, and the importance of a high limit when interrogating complex biological systems. As one of the most significant advantages of CARS imaging, in relation to other imaging modalities, is the potential to attain significantly higher multiplexing limit. It was, therefore, important to assess the multiplexing capabilities of the SIPCARS system, especially in light of the 30 cm^{-1} spectral resolution (at the developmental stage when these experiments were performed). This was achieved by acquiring and subsequently analysing hyperspectral data from multicomponent samples.

10.3.2 Apparatus and Method

10.3.2.1 Apparatus

The data presented in this body of work was acquired in the period after the titanium-sapphire oscillator based system was commissioned and prior to the implementation of many improvements (i.e. using the freestanding PCF, cross-roller bearing stage, and Bentham monochromator).

10.3.2.2 Sample preparation

Two stock solutions, the first, containing equal quantities, by volume of solids, of polystyrene, PMMA, silicon dioxide beads of 1 μm diameter, and hydroxyapatite powder (approx. 1 μm). The second, containing polystyrene (1 μm dia.), PMMA (0.5μm dia.), Melamine (2.0 μm dia.) and hydroxyapatite powder (0.2 μm dia.), also in equal quantities, were created. These materials were chosen as their spectra are sufficiently different to make image segmentation a realistic prospect [75] [83] [105] [120]. Given the relatively small diameter (≤ 2 μm) of all the constituents used, an initial 10 minute sonication was carried out prior to all sample creation. Onto individual coverslips (15 mm dia. circular no. 1.5 Sigma Alrdrich LLC) 8 μl of each stock solution was dropcast and allowed to air dry (under ambient conditions) for a minimum of 3 hours in a dust free location. Following this, 8 μl of a glycerol based mounting agent was applied to another coverslip (24×48 mm no. 1.5 Sigma Alrdrich LLC) and the two gently brought together attempting to cause minimal dislocation of the dried beads. Finally the sample was sealed using a nitrocellulose resin. The polystyrene, melamine and hydroxyapatite beads were sourced from Sigma Alrdrich LLC while the PMMA, was sourced from Polysciences Europe GmbH.

10.3.2.3 Image acquisition

To avoid potential polarisation scrambling effects (see section 6.4), stemming from multiple layers of beads, great care was taken to identify monolayer regions within the samples. Once suitable regions were located, images were acquired with a pixel dwell time chosen to maximise SNR whilst still allowing an imaging area sufficiently large so as to give a reasonably high probability of containing all of the various constituent components. Additionally, the sporadic decoupling of the freestanding PCF, a prevalent feature of the system at this developmental stage, also had to be considered when setting the pixel dwell time. Pixel step size was set by assuming an ideal spatial resolution given the NA of the objectives and requiring at least two sample points within the smallest constituent.

10.3.2.4 Data analysis

The data acquired was, in addition to the mandatory SIPCARS analysis (see section 8.3.4), subject to PCA denoising (see section 5.1). Employing a conservative approach, the first ten principle components were retained and the following ten visually inspected to ensure they contained no spatially varying content prior to discarding.

10.3.3 Experimental Results and discussion

The initial sample created (see figures 10.6 and 10.7) consisted of polystyrene, PMMA, silicon dioxide beads of 1 μm diameter and hydroxyapatite powder (approximately 1 μm diameter). Considering figure 10.6, the mean spectrum taken over all of the pixels did not appear to show a significant amount of spectral detail, largely limited to the peak and adjoining shoulder located in the vicinity of a 1000 cm^{-1}; however, this was due to the relative sparsity of beads/powder within the imaged area. Having consulted the literature spectra [75] [83] [105] [120] and following a semi-empirical approach, several spectral regions (highlighted in panel a) were identified that had the potential to facilitate image segmentation. The images generated from these highlighted regions did, in fact, have sufficient contrast to localise each different bead-type/powder with the exception of silicon dioxide. This is further corroborated by the fact that spectra c, e and g are exceptionally similar to the literature spectra of hydroxyapatite and polystyrene and PMMA respectively.

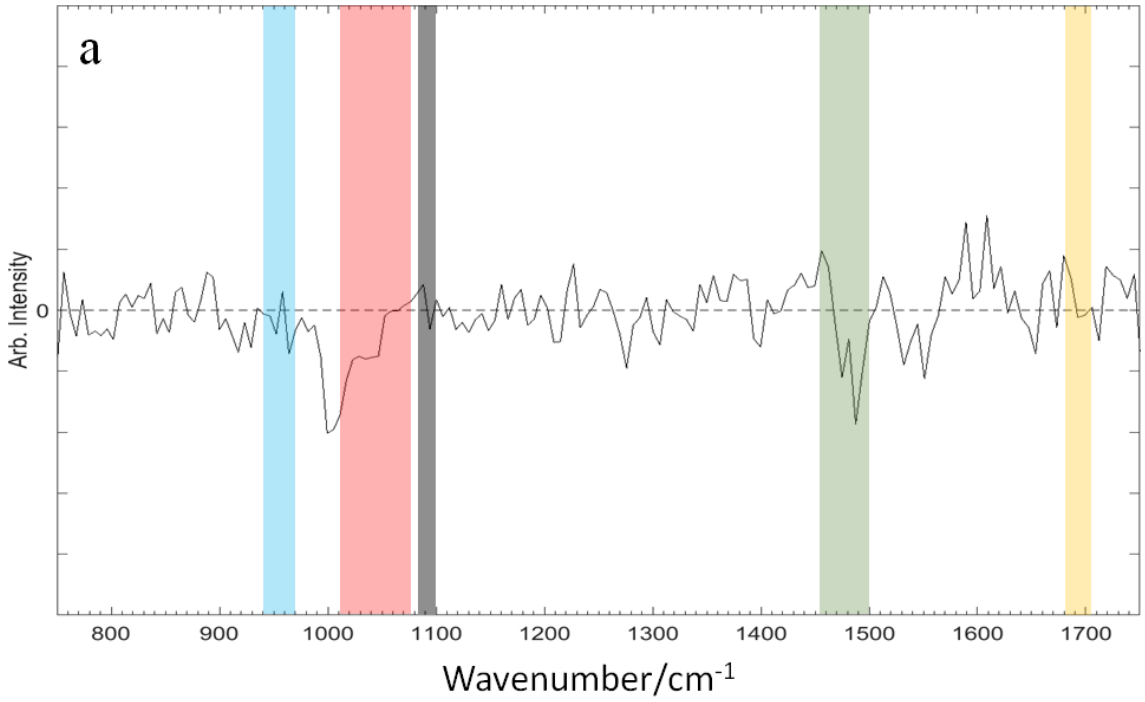
a
Arb. Intensity
0
800
900
1000
1100
1200
1300
1400
1500
1600
1700
Wavenumber/cm-1

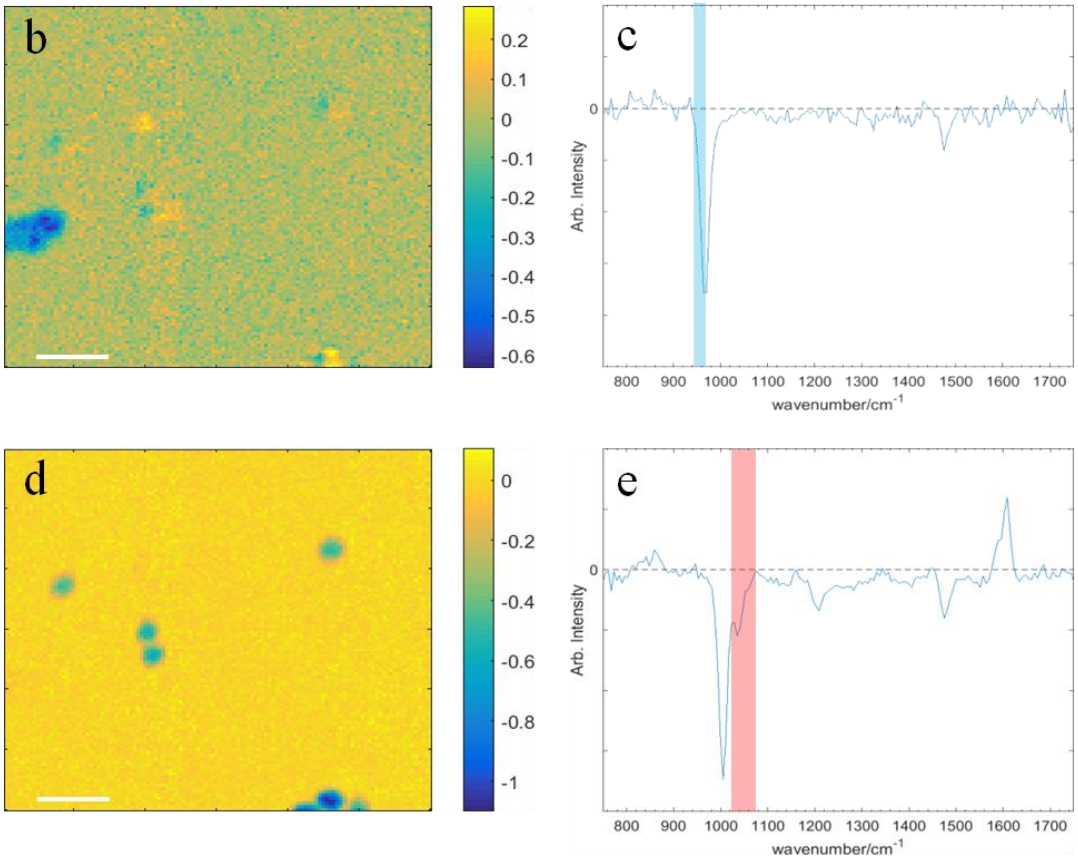
b
0.2
0.1
0
-0.1
-0.2
-0.3
-0.4
-0.5
-0.6
c
Arb. Intensity
0
800
900
1000
1100
1200
1300
1400
1500
1600
1700
wavenumber/cm-1
d
0
-0.2
-0.4
-0.6
-0.8
-1
e
Arb. Intensity
0
800
900
1000
1100
1200
1300
1400
1500
1600
1700
wavenumber/cm-1

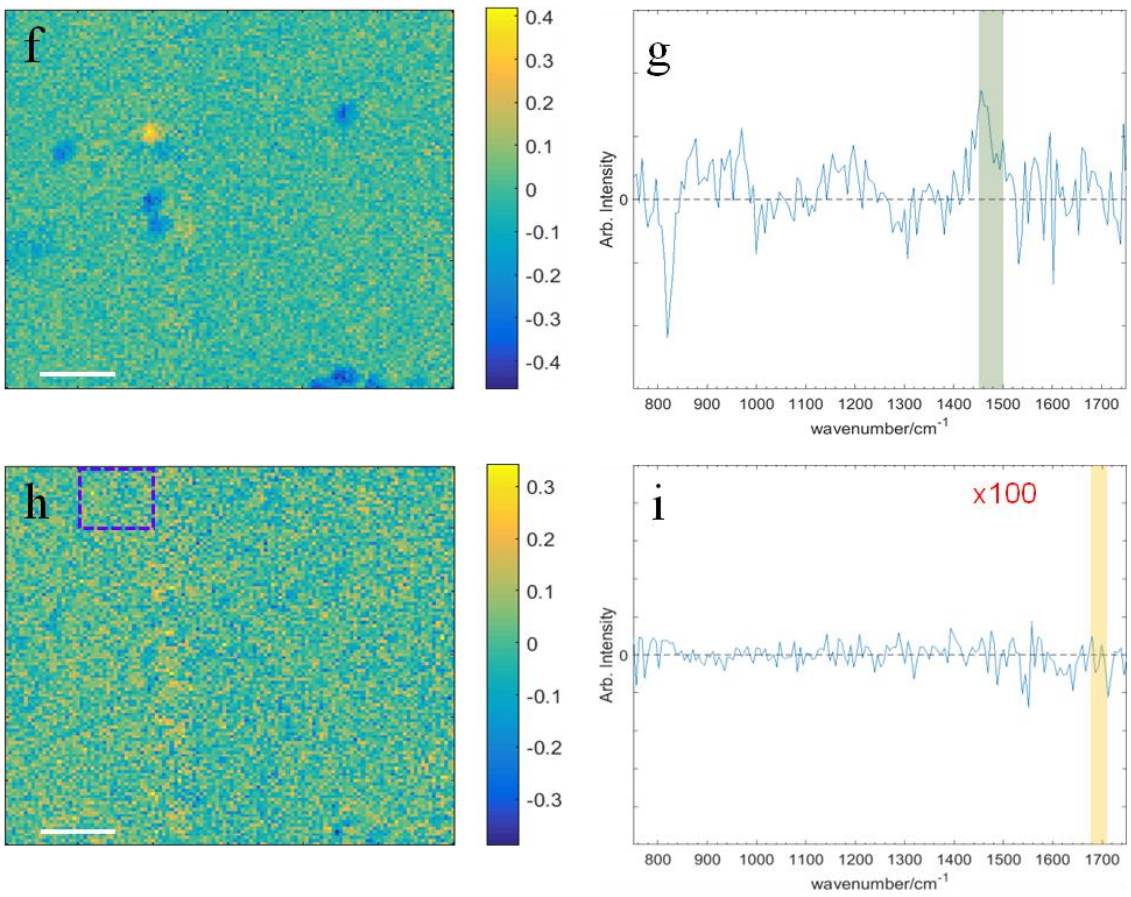

Figure 10.6 Hyperspectral dataset (fingerprint region). Sample containing polystyrene, PMMA, silicon dioxide beads of 1 μm diameter and hydroxyapatite powder (approx. 1 μm). a) Mean difference spectrum take over all of the pixels. The blue, red, green and yellow highlighted regions indicate the wavenumber ranges used to generate images b, d, f and h respectively. The grey highlighted region corresponds to the spectral range used for the χ^{NR} normalisation. Panel c) corresponds to the mean spectrum over the large negative region (blue) region shown in image b). Panel e) corresponds to the mean spectrum over the several negative region (blue) regions shown in image d). Panel g) corresponds to the mean spectrum over the single positive region (yellow) region shown in image f). Panel i) is the mean spectrum (scaled up by a factor of 100) derived from the 20 × 20 pixel region encircled in blue in image h). Note than the highlighted regions shown on spectrum a) have been included in spectra c, e, g, and i as a visual aide. Pixel size: 150 nm; pixel dwell time: 80 ms; scale bar: 3 um

As, due to decoupling of the PCF, non-resonant calibration data (see figure 8.5 in section 8.3.4) could not be attained for this sample, a 20 × 20 pixel region devoid of beads in the upper left quadrant of image was used as a proxy. This region solely consisted of the glycerol based mounting agent, therefore using it to generate the non-resonant calibration data removed both the interference-like fringe pattern and the spectrum of the mounting agent from the final data set. With regard to the silicon dioxide beads, the CARS spectrum of silicon dioxide is comparatively weak and is therefore easily swamped by larger spectral contributions. In this instance due to a considerable overlap between the spectrum of the mounting agent and silicon dioxide it is highly likely the fringe removal process not only removed the mounting agent spectrum but the silicon

dioxide spectrum also. It is worthwhile noting that even though the spectrum shown in panel i) has been scaled there is no visible remnant of the interference fringe-like pattern which speaks to the efficacy of the normalisation approach adopted. Comparing the retrieved spectra and those found in the literature it is immediately apparent that spectra c, d, g correspond to hydroxyapatite, polystyrene and PMMA respectively.

Figure 10.7 clearly illustrates that the identified polystyrene, PMMA, and hydroxyapatite components shown in blue, red and cyan, respectively, can be readily mapped onto the χ^{NR} image. The banding seen in the χ^{NR} image is a product of a fluctuating PCF output due to de-coupling/re-coupling.

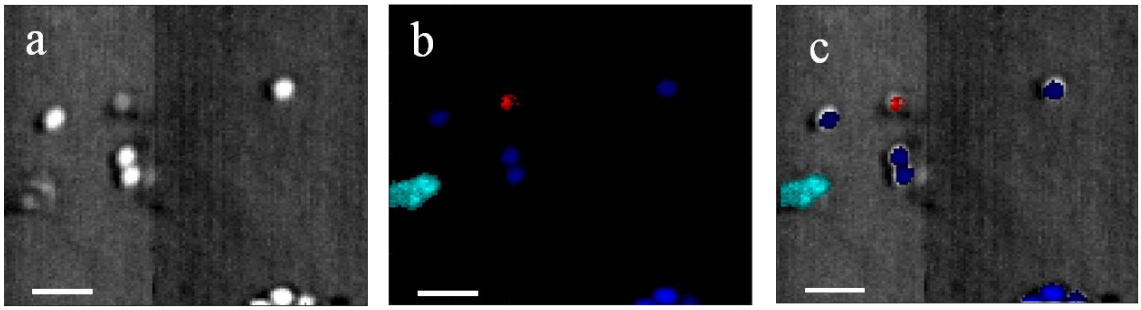

Figure 10.7 a) χ^{NR} image: very approximately relatable to the refractive index at each pixel. b) Composite false colour image (derived from figure 10.6): each component separately thresholded of at 18% of maximum intensity. Polystyrene, PMMA, and hydroxyapatite components shown in blue, red and cyan, respectively c) An overlay of image b) on image a).

This initial measurement proved largely successful, localising all of the constituent components within the image, with the exception of silicon dioxide, based solely on their intrinsic molecular vibrations. Owing to the limited number of constituent components, however, it could not characterise the maximum number of distinct simultaneously identifiable species. In order to rectify this, other potential bead types were investigated; however, only a very limited range of micron size beads were in existence at the time. After extensive investigation the only suitable, in term of spectral form and format, additional bead material that could be sourced was melamine (smallest diameter 2.0 μm).

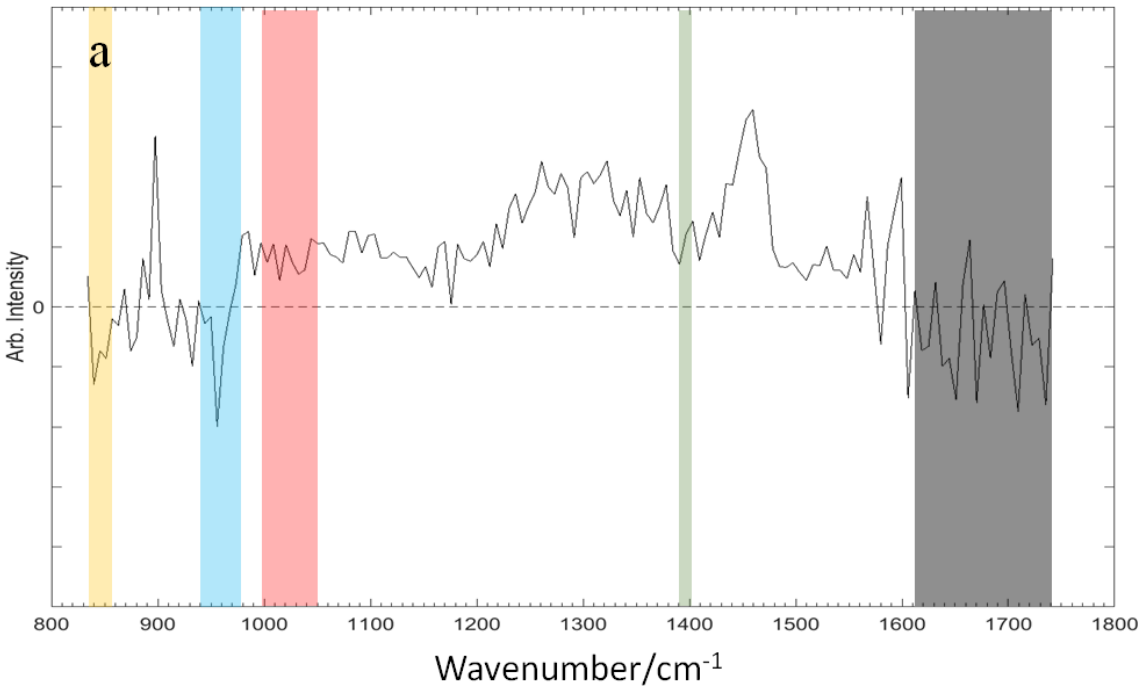
a
Arb. Intensity
0
800
900
1000
1100
1200
1300
1400
1500
1600
1700
1800
Wavenumber/cm-1

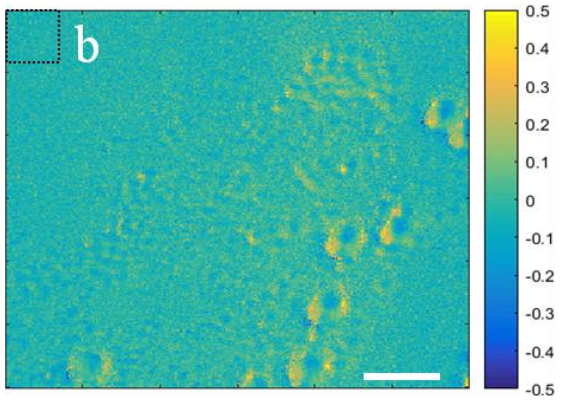
b
0.5
0.4
0.3
0.2
0.1
0
-0.1
-0.2
-0.3
-0.4
-0.5

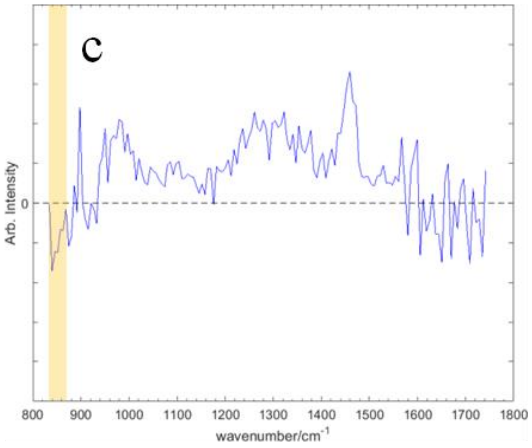
c
Arb. Intensity
0
800
900
1000
1100
1200
1300
1400
1500
1600
1700
1800
wavenumber/cm-1

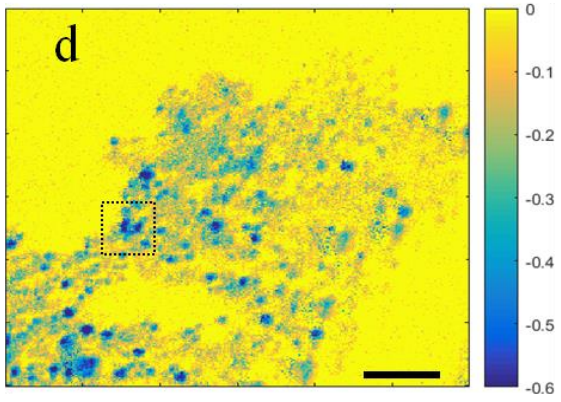
d
0
-0.1
-0.2
-0.3
-0.4
-0.5
-0.6

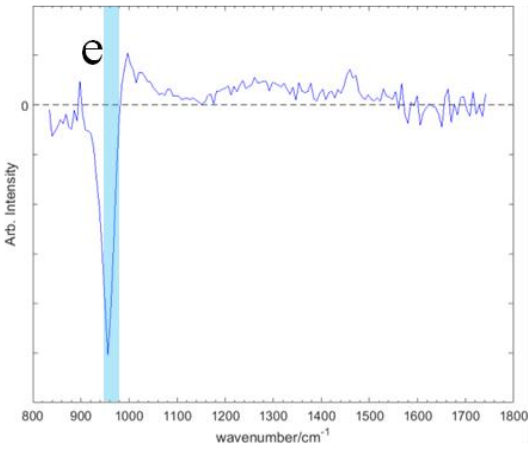
e
Arb. Intensity
0
800
900
1000
1100
1200
1300
1400
1500
1600
1700
1800
wavenumber/cm-1

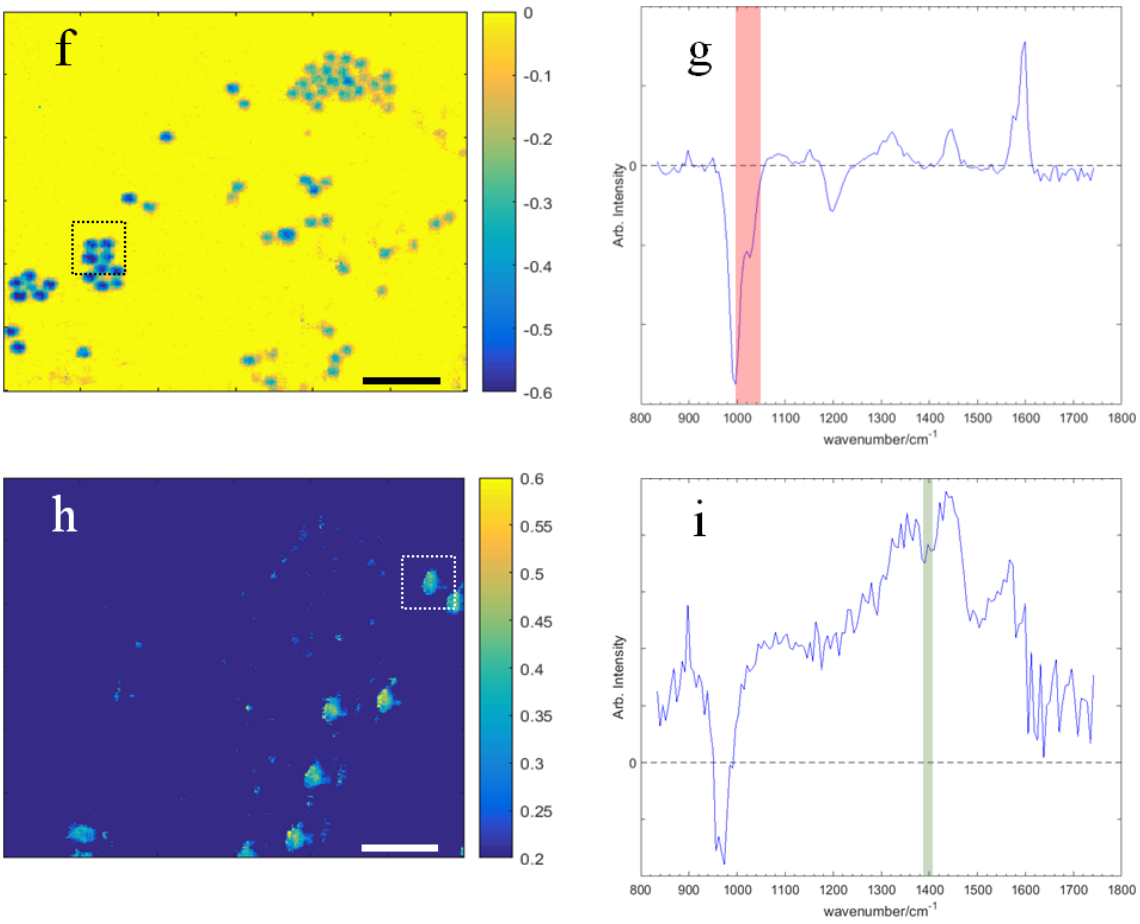

Figure 10.8 Hyperspectral dataset (fingerprint region). Sample containing polystyrene (1 μm dia.), PMMA (0.5μm dia.), Melamine (2.0 μm dia.) and hydroxyapatite powder (0.2 μm dia.) beads. Image a) Mean difference spectrum take over all of the pixels. The yellow, blue, red, green highlighted regions indicate the wavenumber ranges used to generate images b, d, f and h respectively. The grey highlighted region corresponds to the spectral range used for the χ^{NR} normalisation. Mean spectra shown in panels c, e, g and i correspond to the indicated spatial regions (centre 8 × 8 pixels of the dashed box) in images b, d, f and h respectively. Note than the highlighted regions shown on spectrum a) have been included in spectra c, e, g, and i as a visual aide. Pixel size: 100 nm; pixel dwell time: 60 ms; scale bar: 5 um

A second sample was created in which, given the low probability of detection against the underlying fringing pattern, the silicon dioxide beads were replaced with 2.0 μm diameter melamine beads (Sigma Alrdrich LLC). Additionally the diameters of each component bead type were varied, affording a second discriminatory criterion: an independent verification (assuming accurate nominal diameters).

Unlike the first sample, the mean spectrum, panel a), of figure 10.8 shows a significant amount of spectral detail. This is largely due to the use of an additional non-resonant, glass coverslip, calibration sample which results in a normalisation of the interference-like fringe pattern without major impact on the overall genuine, component derived, spectral content. Following the same approach as used for the first sample several spectral regions were identified and images b, d, f,

and h created. Mean spectra of the isolated component were then determined from the indicated regions within the corresponding images. Whilst there is a good correlation between the size of the bead and the derived images it is clearly possible to segment the data without resorting to size as a defining metric. The component spectra also appear to be in agreement with the identified bead (or mounting agent) all sharing pertinent spectral features with their nominal component. In the case of spectrum c) the overall form appears to follow the complex spectral shape of glycerol, including the indicative 1460 cm^{-1} and 900 cm^{-1} peaks. Spectra e) and g) are also exceptionally similar to the literature spectra [83] [105] of hydroxyapatite and polystyrene respectively. Finally spectrum i), although there is some indication that this corresponds to melamine, the 1450 cm^{-1} and 1550 cm^{-1} peaks [75], this is hardly conclusive due to the underlying background. This background stems from imbalance between the two tracks, i.e. incomplete cancellation of the NRB. If images b) and h) are compared, there is clear bleed through of the melamine beads into the former. Additionally, as corroborated by figure 10.9a, the melamine beads present with an asymmetric spatial response (*cf.* section 9.6.2). Whilst, demonstrably, this did not prohibit image segmentation it is not possible to say whether the melamine beads were truly isolated via their intrinsic Raman response or on the strength of this image aberration. It is worthwhile noting that while this asymmetric spatial response is most apparent in the larger melamine beads a close inspection of image b), as compared with the other images, shows that it is present to a lesser extent with all bead types.

Notably although there were four bead components in this sample it was only possible, even after extensive investigation, to isolate three: polystyrene, hydroxyapatite and melamine. Quite why this was the case is not overly clear. There are two possibilities, firstly, there is some spectral overlap, especially with the mounting agent or, secondly, it simply may not have been present in the field of view. On the strength of the previous sample (see figure 10.6), and other scans of PMMA in mounting agent, the presence of PMMA was expected; however, although unlikely, the unorthodox interference-like pattern removal may have highlighted the PMMA. As for the possibility of PMMA beads being absent from the scanning area, the same result was seen in multiple scans, therefore, a subtle entropic separation of the beads notwithstanding, this seems unlikely. The only potentially decisive factor is that the derived segments appear to correspond completely (see figure 10.9) to the outline of the beads (sufficient refractive index mismatch to make all types visible), therefore, on the balance of probability the latter possibly is marginally more probable.

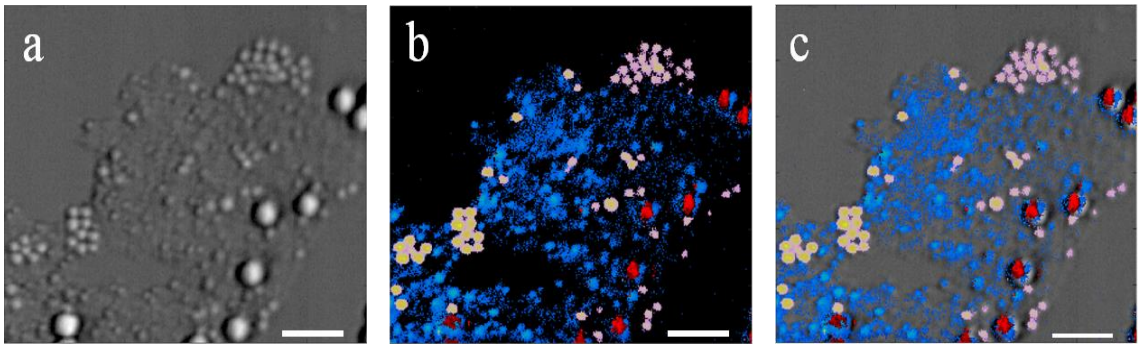

Figure 10.9 a) χ^{NR} image: very approximately relatable to the refractive index at each pixel. b) Composite false colour image containing melamine (red), polystyrene (pink) and hydroxyapatite (blue): each component separately thresholded of at 8% of maximum intensity. c) An overlay of image b) on image a).

10.3.4 Conclusion and future extensions

From the above results it seems that, in the majority of cases, image segmentation using SIPCARS based solely on molecular vibrations and mode symmetry is possible. As expected, the limitations of the system, the asymmetric spatial response (see section 9.6.2) and spectral interference-type fringe pattern (see section 9.6.1), act to significantly reduce sensitivity of the system and introduce image artefacts. This is most deleterious when imaging larger beads which exacerbate the asymmetric spatial response which consequently results in imbalance between the two tracks and subsequently renders the fringe pattern removal ineffectual.

A lack of appropriate beads also hampered this body of work and as a result it was not possible to actually determine the extent of the multiplexing limit with this system other than to state the lower limit is four distinct constituent components.

Further extensions of this work, perhaps moving towards determining multiplex capabilities in well characterised living tissue equivalents, while ultimately feasible, cannot realistically be considered prior to improving the underlying limitations of the system.

11. CARS based on a titanium-sapphire oscillator and photonic crystal fibre: biological applications

This chapter contains two bodies of work relating to the use of SIPCARS to characterise lipid droplets within biological samples: a HeLa cell and *Caenorhabditis elegans* nematodes. As per chapter 10, to avoid repartition only unique aspects of each particular experiment will be given in addition to attempting to place the work within the developmental chronology.

11.1 HeLa (Henrietta Lacks) cells

11.1.1 Introduction

This body of work was performed and analysed by the author.

The lipid droplet (LD), a ubiquitous organelle found in the majority of eukaryotic cells [121], had long been thought to be simply a benign deposit of neutral lipids within a cytoplasmic inclusion; however, recent work [122] has shown it to be a highly complex and dynamic structure vital for a wide variety of different functions including metabolic regulation and membrane synthesis. Despite the importance of LDs, both as a homeostatic regulator and as a primary mediator of many disorders, stemming from either over or under accumulation of lipid, such as obesity, diabetes and atherosclerosis, relatively little is known about their underlying biology [123].

Currently the principal approach employed to identify LDs within cells is by fluorescent staining with lipophilic dyes such as Nile Red, BODIPY-C12, Sudan Black and Oil red O [124]. These, however, all present their own unique pitfalls [125]: either through lack of specificity or the introduction of preparation related artefacts.

In this body of work, the ability of SIPCARS to identify LDs in live, unstained biological cells based solely on their endogenous molecular vibrations, is demonstrated. Whilst there have been various previous attempts to characterise individual LDs within a HeLa cell [70] using CARS, these have largely focused on the CH-stretch spectral region where meaningful analysis is complicated by broad spectral features and Fermi resonances stemming from fingerprint region overtones [77]. Where the fingerprint region has been assessed these studies are limited to the strongest bands and can therefore produce only an unsaturation ratio: the ratio of double bonded to single bonded carbons in a fatty acid. Additionally, all previous results are subject to the approximations required to computationally remove the NRB which leads to spectrally varying errors, especially near resonances, of up to 10% [28] [29] (see section 3.2.1.3).

In this body of work, the unsaturation ratio of LDs within a live unaltered (no introduction of supplementary fatty acids) HeLa cell have been assessed using SIPCARS; additionally, subtle differences between the various LDs are shown and related to their oxidative degradation [76].

11.1.2 Apparatus and Method

11.1.2.1 HeLa Cells

HeLa cells were cultured in high glucose Dulbecco's modified eagle medium supplemented with 10% foetal bovine serum and 1% penicillin and streptomycin. Prior to imaging the cells were cultured on fused silica coverslips for 24 hours after which they were washed with PBS and sealed between coverslips, filled with OptiMEM, using nitrocellulose resin.

11.1.2.2 Apparatus

This body of work was conducted after several upgrades of the SIPCARS system. Whilst the Newport cross-roller bearing stage was yet to be upgraded, the supercontinuum was, by this point, generated via a FemtoWHITE800 unit (NanoTrak feedback not yet implemented) and the Isoplane SCT-320 had been installed. The sample was exposed to 14 mW and 25 mW stemming from the pump beam and Stokes beam respectively.

11.1.3 Experimental Results and discussion

The ability to perform non-resonant background free high signal-to-noise ratio fingerprint region imaging of HeLa cells using SIPCARS is clearly demonstrated in Figure 11.1. Figure 11.1a), the NRB image, produced by taking the square root of the sum spectrum in a non-resonant spectral region, is directly related to the density of the sample. When coupled with Figures 11.1b) and c) this gives a clear indication that the masked objects correspond to LDs: conforming to their expected morphology. The mean spectra generated from the indicated regions highlighted in Figure 11.1d), show differences both in spectral form and relative peak intensities.

In order to explore this further the spectral bands of importance have been identified and highlighted: the 1450 cm^{-1} CH_2 degenerate deformation, 1650 cm^{-1} C=C bond, 1684 cm^{-1} and 1704 cm^{-1} (the different peaks relating to differing chain lengths) C=O aldehyde bonds, 1740 cm^{-1} C=O ester bond in red, light blue, green and grey respectively. Additionally the presence of the triglyceride and CH_3 twist modes provide further verification as to the lipid identity of the masked structures [72] [73].

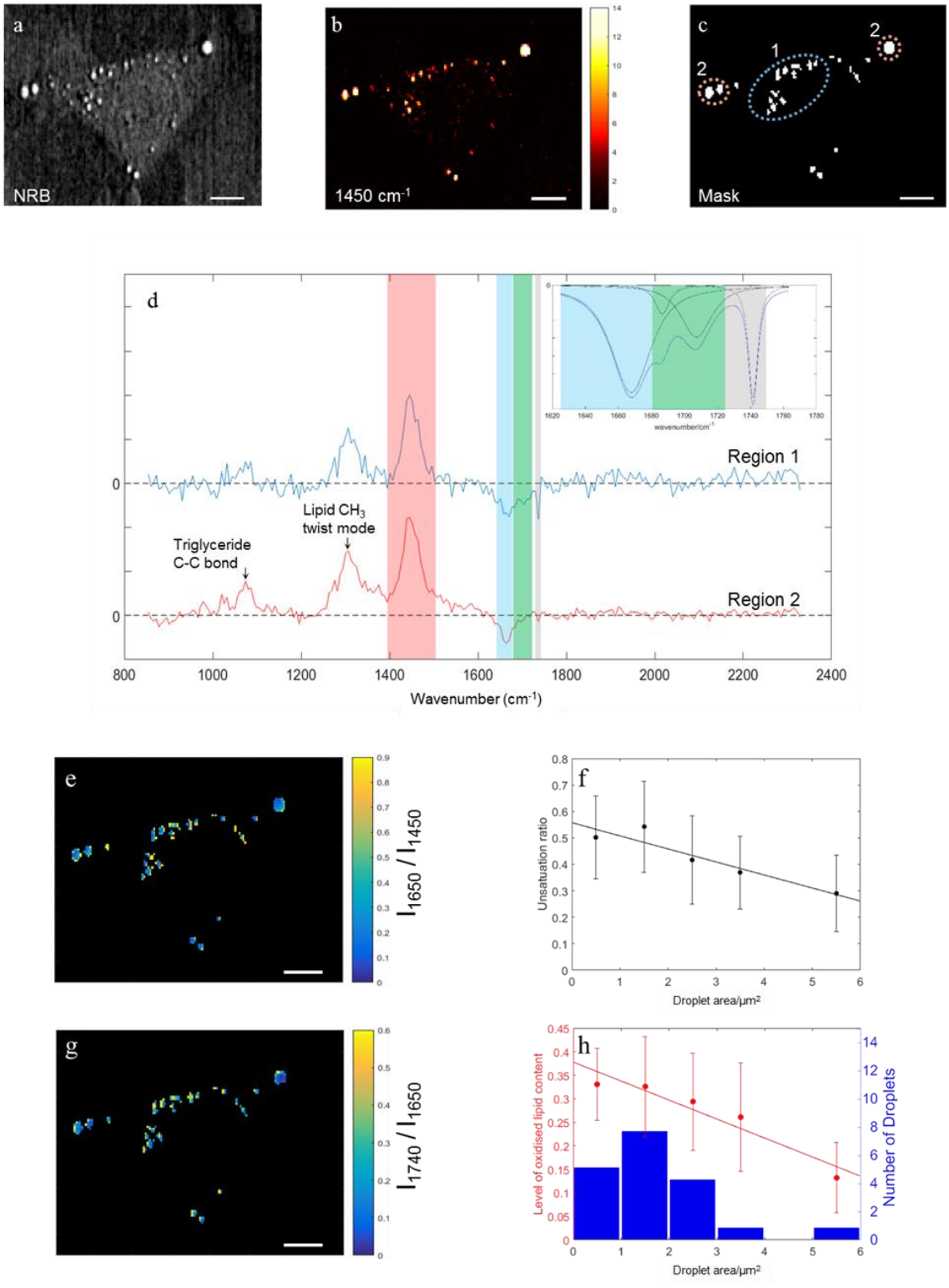

Figure 11.1 : a) NRB image: which is directly related to cell density. b) The 1450 cm^{-1} (CH_2 degenerate deformation) total lipid SIPCARS image [77]. c) A mask generated from image b: minimum feature size of 0.64 μm^2 and thresholded just above the noise floor. Two regions: a small lipid droplets cluster, region 1, and isolated large lipid droplets, region 2, are highlighted. d) The mean spectra corresponding to the highlighted regions (scaled and offset for clarity). General fingerprint region lipids bands are directly labelled [72] [73] while bands important to further discussion are shown by the shaded regions: CH_2 degenerate deformation (red), C=C bond (light blue), C=O aldehyde bonds (green), C=O ester bond (grey). Inset: An example of the fitting applied

to the equivalently shaded spectral region. e) Cell unsaturation image generated by taking the ratio of 1650/1450 cm^{-1} peaks in the masked area. f) The lipid droplet unsaturation ratio dependence on droplet area. g) Image indicative of the degree of lipid oxidation generated by taking the ratio of 1740/1650 cm^{-1} peaks in the masked area. h) Level of oxidised lipid content dependence on droplet area in red and the number of droplets within each bin in blue. For both graphs 1 μm^2 bins were chosen to reflect the realistic spatial discrimination of the system with a 0.4 μm step size. The error bars shown on each graph were derived from the standard deviation of the individual pixel values within each bin. All scale bars correspond to 8μm. Pixel dwell time: 150ms. Pixel step size: 0.4 μm.

By applying fitting based on a mixture of Gaussian and Lorentzian line shapes, chosen to minimise residual fitting error [126], to the 1650 cm^{-1} and 1450 cm^{-1} peaks and taking the ratio it was possible to produce an unsaturation image [78] as shown in figure 11.1e from which it is apparent that the average unsaturation is higher in the central cluster of LDs, average unsaturation ratio value of 0.53 ± 0.11, than the larger isolated LDs, average unsaturation ratio value of 0.35 ± 0.04 (standard deviation of the pixels stated in both cases). This strongly suggests a difference in lipid composition which merited further investigation. Figure 11.1f, explicitly shows the relationship between lipid droplet area and unsaturation ratio confirming the negative correlation between LD area and unsaturation ratio.

The most striking difference between the spectra of these two LD regions is the relative intensity of the 1740 cm^{-1} C=O bond. Previous work related to the storage of lipids within *Caenorhabditis elegans* [76] has shown the ratio of the 1740 cm^{-1} to 1650 cm^{-1} peaks to be indicative of the level of oxidised lipid present. Applying a similar fitting process as used to produce the unsaturation image, figure 11.1g) was created showing a clear difference in oxidised lipid quantity between the two regions which was further verified by the negative correlation shown in figure 11.1h). Additionally the mean spectrum of the small LD cluster contains a significant 1680 cm^{-1} shoulder and 1704 cm^{-1} peak, indicating the presence of aldehyde: a terminal product of lipid peroxidation [127]. Lipid peroxidation is predominantly an unsaturated lipid process and thus the extent to which a given LD is liable to undergo lipid peroxidation, resulting in an oxidised lipid, is intrinsically linked to its degree of unsaturation: heavily favouring polyunsaturated fatty acids [127]. Comparing the two derived ratio images there does, in fact, appear to be a strong correlation between degree of unsaturation and level of oxidised lipid content.

11.1.4 Conclusions and Extensions

High signal-to-noise ratio SIPCARS imaging of a HeLa cell in the vibrational fingerprint region with a competitive 150 ms pixel dwell time was successfully demonstrated, from which it is possible to identify LDs and subsequently, by producing ratio images, assess their degree of lipid unsaturation and the level of oxidised lipid content. Additionally, the strong correlation between these two ratio images corresponds well with the expected underlying lipid oxidative degradation process.

Whilst this proof-of-principle investigation was limited only to a single HeLa cell and focused solely on the LD composition, it has shown that this technique has the potential to detect both the degree of LD unsaturation and the level of oxidised lipid content. Although this cell appears typical, in the future applying this technique to a larger population of cells and/or a population exposed to lipid metabolism altering compounds, would further validate the technique. This, however, is contingent on improving the stability of the supercontinuum.

This technique has been shown to have the ability to determine LD unsaturation and degree of oxidised lipid content and with further development may be a viable route to provide rapid cellular lipid assays without the need for invasive staining.

11.2 *In vivo* lipid saturation study of *Caenorhabditis elegans*

11.2.1 Introduction

This work was performed in in conjunction with Dr. Littleton; this typically entailed the full involvement of both the author and Dr. Littleton in any given measurement with either, or both parties, performing system alignment and optimisation, SIP-CARS scans and data analysis. For example several measurement were started by one only to be completed by the other. All *C. elegans* measurements were performed in collaboration with Dr. Nie (toxicogenomics group, KCL) who isolated the drug compound, cultivated the nematodes, prepared the sample slides and provided insight into the anatomy of *C. elegans*. All details concerning the isolation of the drug compound are provided in the King's College London PhD thesis of Dr Nie [128]. The drug compound is proanthocyanidin trimer gallate purified from grape (Vitis vinifera) extract.

C. elegans, a transparent non-parasitic nematode, is found ubiquitously in the soil of temperate regions. In the adult developmental stage it is typically 1 mm in length with a sagittal diameter of approximately 100 μm. The life span is approximately 20 days, maturing from an egg to a fully-fledged adult specimen in under 72 hours [129]. Development within these first 72 hour is split into several stages: L1, L2, L3, L4 and adult. Each of the L-stages (larval stages) lasts for approximately 8 hours (at 25 ºC) corresponding to an increase in both length and cross-sectional area [130].

One of the defining features of *C. elegans* is their simplicity, containing only 959 somatic cells in an adult specimen. Not only is this number constant between non-mutated "wild-type" specimens but so is the location of each cell within the nematode [130]. This simplicity coupled, with the optical transparency of *C. elegans*, actually allowed the lineage of each constituent cell to be determined in full [131]. In addition *C. elegans* nematodes were the first multicellular organism for which the genome was sequenced in its entirety and the only organism for which the connectome has been fully mapped [132]. There are two truly remarkable features of the

C. elegans genome: its compact length, $\frac{1}{30}^{th}$ of the length of simian DNA, and its similarity with human DNA (~ 40% homologous).

The above features allow *C. elegans* to be an ideal model organism; both in terms of physical characteristics (transparency, short duration and predictability of life cycle, compact size, ease of maintenance and cultivation), and genetic simplicity which allows the robust and reliable production/creation of mutants, and, owing to the similarity with human DNA, lends itself to study of human diseases [130].

Since being first identified as a potential model organism in 1974 by Brenner *et al*. [133] *C. elegans* has been studied both as an integral organism (learning and mating behaviour, chemotaxis, thermotaxis), and as an organism to facilitate early phase medium/high throughput screening of the effects of novel drug candidates on their designated gene.

This body of work is focused on one particular type of organelle within the nematode: LDs (intestinal and hypodermal). As in humans, obesity within nematodes is expressed as an overproduction of LDs, either in terms of size or number. Given the increasing prevalence of worldwide obesity (one of the highest risk factors likely to cause death [134]) a significant amount of recent research has been directed towards understanding LDs and potential lipid metabolism altering drug candidates.

As stated in section 11.1.1 the typical approach used to identify LDs *in vivo* is via potentially invasive staining which may or may not be representative of the true lipid content. The characteristics, given above, of a *C. elegans* nematode not only render it an exceptionally important model organism but also make it ideal for SIPCARS imaging. The primary aim of this study was to assess the effect of a naturally derived phytotherapeutic lipid metabolism altering drug on the LDs contained within "wild type" *C. elegans.* Over the course of this study several mutants were also imaged.

11.2.2 Apparatus and Method

11.2.2.1 *C. elegans*

Throughout this study L2-stage nematodes (see figure 11.2) were used since, although this developmental stage occurs during the rapid growth period, the LD phenotype should be fully expressed. Additionally, this developmental stage also corresponds to the highest density of LDs within the nematode. It should be noted that although on average the diameter of these nematodes, is less (~ 35 μm) than the maximum permitted inter-coverslip distance (60 μm) of the SIPCARS system these nematodes are generally amenable to gentle deformation.

Nematodes (procured from the *Caenorhabditis* Genetics Centre) were cultivated on agar plates and fed a standard bacterial diet (*Escherichia coli* strain OP50). Whilst developing they were maintained in sterile environment at 20 ºC. Nematodes that were exposed to the lipid metabolism altering drug were done so via inoculating the bacteria upon which they fed. Previous work conducted by Dr. Nie had confirmed uptake of the bacteria was unaffected by this inoculation.

In an effort to ensure all nematodes were imaged in the L4-stage, prior to the SIPCARS imaging session (typically a day), several batches of nematodes were prepared so as to mature at different times throughout the day. Additionally, whilst not actively being used, the agar plates were stored in a fridge which should have largely arrested any growth of the nematodes.

SIPCARS imaging samples were prepared by carefully removing a nematode from the surface of the agar plate and placing it into a drop of 50 mM sodium azide solution (a fast acting non-lethal anaesthetic) on a glass coverslip. A second coverslip was then gently placed on top of the drop and sealed with a nitrocellulose resin. Great care was taken at all times to avoid undue pressure on the coverslips as this could cause the nematode to rupture and consequently die.

Whilst the primary objective of this body of work was to establish the effect of this lipid metabolism altering drug on wild type N2 nematodes, several other mutants/diets were also imaged. The technical/genetic details of these mutants are far beyond the scope of this thesis; however, a brief description of the resulting phenotypes and uses of each will be given.

glo-4 mutation: the *glo-4* gene controls biogenesis of the lysosome-related organelles (LRO) located within the intestine. One of the most significant limitations of fluorescent staining as an investigative technique for *C. elegans* is that it lacks specificity. It is often unclear as to whether just the LDs, or the LDs and LROs have been stained. This mutant, which lacks LROs, was therefore developed to remove this source of interference.

High-cholesterol diet: this simply corresponds to a wild type N2 nematode where the standard bacterial diet has been supplemented with cholesterol. This nematode preparation is used to investigate the cholesterol storage mechanisms and location of *C. elegans.*

daf-22 mutation: Whilst the specifics the *daf-22* mutation are very complex, it essentially plays a role in regulating degradation of intestinal lipid. The net result of this is a nematode with enlarged intestinal LDs. As the composition of the LDs should remain relatively unperturbed by this mutation it is well suited for optical analysis.

glo-4;*daf-22* double mutation (produced by the Toxicogenomic group, KCL): This double mutant processes the traits of both its precursors and, as such, exhibits enlarged LDs without the interference of LROs. In terms of optical characterisation of just the LDs this double mutant is ideal.

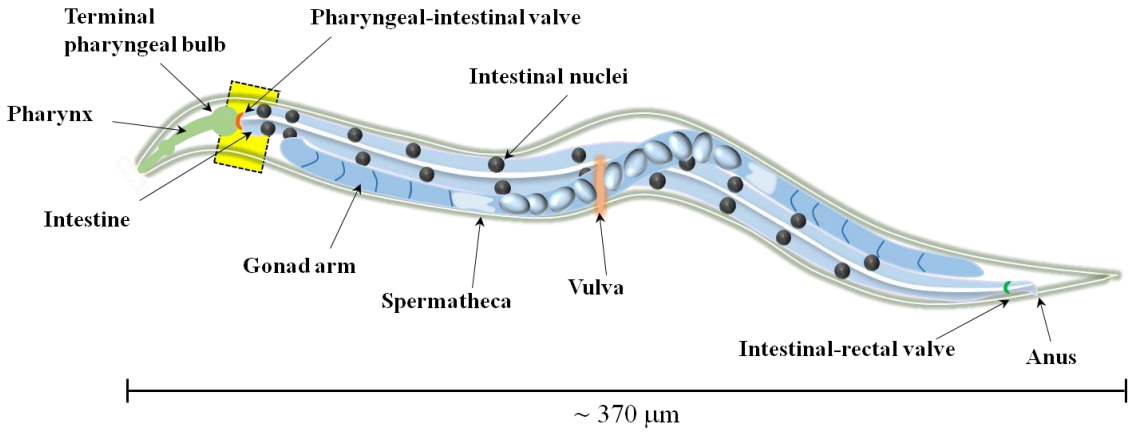

Figure 11.2 The basic anatomy of a C. elegans nematode. The highlighted post-terminal pharyngeal bulb area corresponds to the scanned region.

11.2.2.2 Apparatus

As one of the most recently completed bodies of work with the SIPCARS system, it was conducted with the latest iteration of the system and after the majority of the power fluctuations were resolved. Rather than give a complete recapitulation of the system, the main additions and amendments beyond the initial specification (section 8.2) will be stated here. Note that all the improvements discussed in chapter 9 were implemented prior to commencing this body of work.

Briefly, the supercontinuum was generated via a FemtoWhite800 unit in conjunction with the NanoTrak feedback system and combined with the narrowband beam above the microscope on the vertical breadboard. A high precision (sub-nanometre resolution) 200 μm × 200 μm × 20 μm piezo flexure stage was employed to scan the samples and an imaging IsoPlane-320 spectrometer used to collect the signal.

11.2.2.3 Data acquisition and analysis

As it is not physically possible to image entire nematodes with the SIPCARS system, a specific 45 μm × 45 μm region was chosen. Scanning a constant region within all nematodes also served to ensure a legitimate comparison could be made. The area chosen, highlighted in figure 11.2, corresponds to the post-pharyngeal region at the onset of the gastro-intestinal tract. There are several reasons as to why this area was chosen. Firstly, ease of recognition, the visible morphology of *C. elegans* is particular distinct in this region facilitating easy recognition in each individual nematode. Secondly, this region has the highest probability to be similar between nematodes in the same condition/with the same mutation. Thirdly, the largest phenotypical differences between the different mutants/conditions are observed in this region: largely owing to the high density of LDs. Finally, the morphology of this region is comparatively simple, i.e. only intestinal structures should be present within the resultant images, simplifying analysis.

The scan parameters, 90 × 90 pixels with a step size of 0.5 μm and a pixel dwell time of 150 ms, were used as they afforded sufficient spatial resolution to enumerate and characterise the LDs whilst also retaining a plausible scan time (approximately an hour including alignment and preparation) given the necessity of population statistics. Although not a primary objective of this particular study (i.e. not the predicted mode of action) the extent of the scan region was chosen to be sufficient to include the edges of the nematode so that, if present, smaller hypodermal LDs would also be imaged.

To assess the efficacy of the drug, it was necessary to collect multiple replicates of the inoculated and control wild type N2 nematodes; however, given the one hour turnaround per sample, and the persistent system instability it was possible to attain only five replicates of each (n=5). Three replicates (n=3) were acquired for each of the mutations/other conditions. Although by no mean ideal n=5 is sufficient to draw tentative conclusions as to the effects of the drug.

The basic SIPCARS analysis is given in section 8.3.4; however, in order to extract the pertinent information from the nematode data required a significantly more involved approach. Given the stringent time limitations, a water region within each sample was used to generate a non-resonant calibration spectrum (see below for caveat), which was then subsequently used, as per figure 8.5, to remove the spectral interference-type pattern. The difference data was then subject to PCA denoising (see section 5.1) prior to spatial normalisation via the χ^{NR} value at each pixel. The above broadly corresponds to the essential SIPCARS analysis and thus at this stage the hyperspectral data set was completely free of NRB and the fringe-like pattern had been suppressed via normalisation.

Having produced a 'clean' hyperspectral dataset, it was necessary to extract the relevant LD data. This was achieved by first creating a lipid mask by thresholding over the entire CH-stretch region (2850 - 3000 cm^{-1}) [70]. This threshold was chosen by eye remove obvious noise whilst also conforming to the expected LD morphology. Using the mask to ensure only LD were assessed, the FPR with the indicated pixels was then used to a calculate lipid unsaturation. Note to allow for a meaningful comparison between each nematode the same threshold was used throughout. The lipid area fraction (i.e. the total lipid area/area of the nematode) was calculated directly from the lipid mask, whilst unsaturation heat maps were generated from the FPR. Statistical analysis was also performed on this retrieved data.

There is a slight caveat with regards to the derivation of the non-resonant calibration data from a water region within the sample. Whilst every effort was made to ensure only the nematode was transferred to the coverslip for imaging, it proved impossible to avoid the inadvertent transfer of *E. coli*. It was therefore necessary to identify a water region within each sample that was free of *E. coli*, lest it interfered with the calibration. This was achieved by inspecting the raw difference spectrum (just the subtraction of the raw track signals from which the presence or absence of

E. coli in the laser focus could easily be determined). It proved possible to achieve a full normalisation for all of the samples.

11.2.3 Experimental Results and discussion

As it is not practical to show images related to each and every nematode, figure 11.3 serves to illustrate the typical output following the analysis protocol stated above. The particular nematode shown in figure 11.3 is a *daf-22*;*glo-4* double mutant and, as such, is expected to contain enlarged LDs and be devoid of LROs. The χ^{NR} image, included in panel a), shows the basic morphology of the nematode including several large drop-like structures. The total lipid image (produced by integrating over the 2850 - 3000 cm^{-1} CH-stretch region) and corresponding lipid mask confirm the identity of these structures as LDs. Using the mask, a histogram of lipid intensity was constructed showing a wide range of intensities. Figure 11.3c, the lipid unsaturation portion of the results, contains the average spectrum of the masked regions which clearly illustrates that there is an ample SNR with which to generate unsaturation maps and unsaturation histograms.

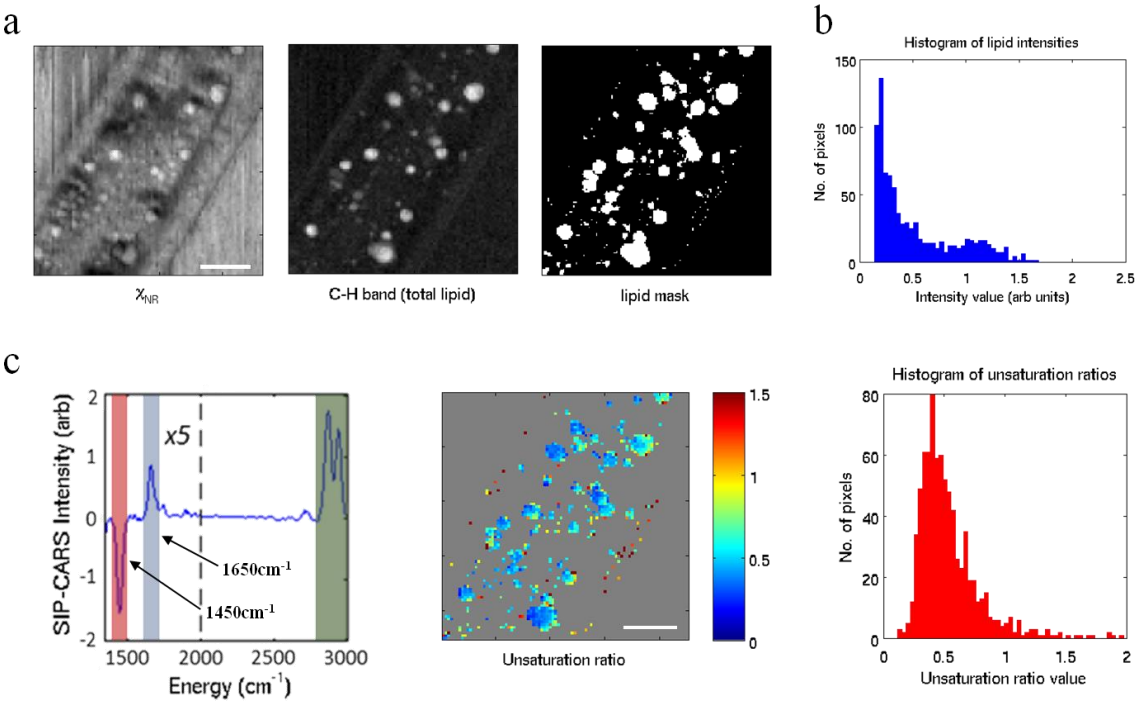

Figure 11.3 Complete analysis of SIPCARS data from a *daf-22*;*glo-4* double mutant. a) χ^{NR} image which approximately relates to linear refractive index of the nematode. Total lipid image which was produced by integrating over the 2850 - 3000 cm^{-1} CH-stretch region. Lipid mask generated by thresholding the total lipid image. b) Histogram corresponding to the lipid intensities within the masked areas. c) SIPCARS spectrum showing both the FPR (×5) and the CH-stretch region. The red, blue and green highlighted regions indicate the 1450 cm^{-1} CH_2 degenerate deformation, 1650 cm^{-1} C=C bond, and the CH-stretch total lipid region (used to generate the total lipid image) respectively. The ratio of the 1650 cm^{-1} and 1450 cm^{-1} peaks (1650 cm^{-1} peak intensity / 1450 cm^{-1} peak intensity) yields the unsaturation ratio. This is presented both as a saturation map and a histogram. All scale bars correspond to 10µm. Pixel dwell time: 150ms. Pixel step size: 0.5 µm.

This unsaturation map clearly illustrates that the larger intestinal LDs are composed of, on average, significantly less unsaturated lipids than the small hypodermal LDs. This serves to provide a visual example of the attainable contrast of this technique. The associated histogram is skewed heavily towards lower unsaturation; however, as expected, exhibits a significant tail incorporating higher unsaturations stemming from the hypodermal droplets.

This analysis approach is sufficiently rigorous and yields quantitative information about the lipid intensity and unsaturation of a given nematode. Utilising this analysis, it should, therefore, be possible to draw some preliminary conclusions as to the efficacy of the drug.

The results derived from ten wild type N2 nematodes, five control and five exposed to the drug, are displayed in figure 11.4. The images in figure 11.4a provide a comparison between control and exposed nematodes in terms of unsaturation (both individuals are typical of their condition). It is immediately apparent that there is a significant increase in average unsaturation and range of unsaturation values in the exposed nematode relative to the control. As shown by the total unsaturation ratio histogram this trend persists across all the individuals within the respective groups.

Figure 11.4b contains the other comparison metrics unrelated to unsaturation. It is clear that in terms of total lipid intensity, lipid area fraction, and total lipid phase, that there is no statistical difference between the two groups of nematodes. Note that the total lipid phase, a measure of the LD viscosity, was calculated by taking the ratio of the CH_2 symmetric stretch at 2845 cm^{-1} and the combination CH_3 symmetric stretch and CH_2 asymmetric stretch at 2930 cm^{-1} (2845 cm^{-1} peak intensity / 2930 cm^{-1} peak intensity). As the combination band, situated at 2930 cm^{-1}, is enhanced in the liquid phase (polyunsaturated lipids are liquid at room/biological temperature) so this ratio can be taken as indicative of lipid phase. This was attempted as it had the potential to be highly informative; however, any decisive information yielded would have had to be heavily scrutinised as lipid phase retrieval in the CH-stretch region is highly complex and often unreliable (see section 11.1.1).

The results shown in figure 11.4 strongly suggest that this drug acts to alter the saturation of stored lipids within *C. elegans* nematodes without affecting the total lipid intensity, lipid area fraction, and/or the total lipid phase. Whilst these conclusions are only tentative, owing to the limited population size analysed, they would appear to correlate with biochemical assays/analysis performed by the toxicogenomic group in KCL [128] which suggest up to a 30% reduction in storage of saturated fats after drug exposure.

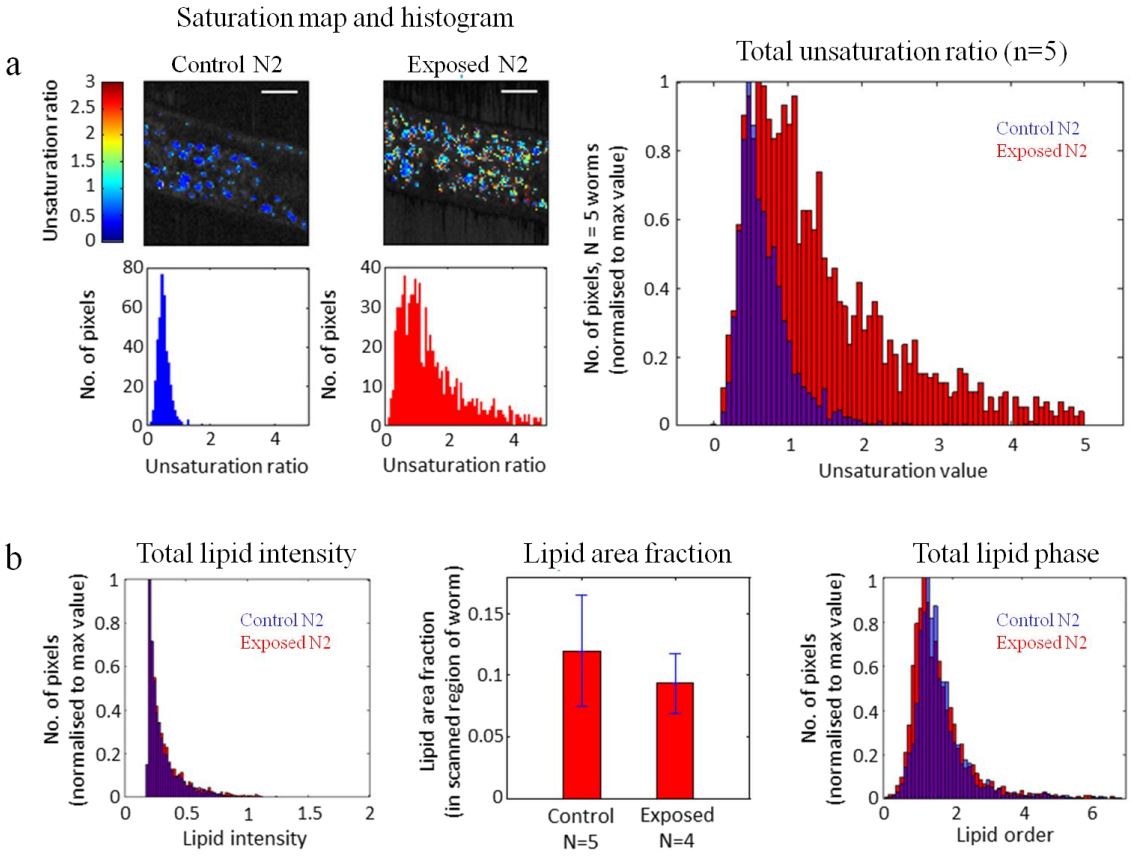

Figure 11.4 Comparison between control and exposed wild type N2 nematodes. a) Comparison between two individual nematodes, control and exposed, presented both as a saturation map and a histogram. This illustrates the immediate striking difference between the two cases. These nematodes are typical of their condition. Shown adjacent is the combined total unsaturation ratio for both conditions (n=5 for both conditions). b) Contains the other comparative metrics: total lipid intensity, lipid area fraction and total lipid phase. The lipid order is calculated by taking the ratio of the CH_2 symmetric stretch at 2845 cm^{-1} and the combination CH_3 symmetric stretch and CH_2 asymmetric stretch at 2930 cm^{-1} (2845 cm^{-1} peak intensity / 2930 cm^{-1} peak intensity). As the combination band, situated at 2930cm^{-1}, is enhanced in the liquid phase (polyunsaturated lipids are liquid at room/biological temperature) so this ratio can be taken as indicative of lipid order.

.

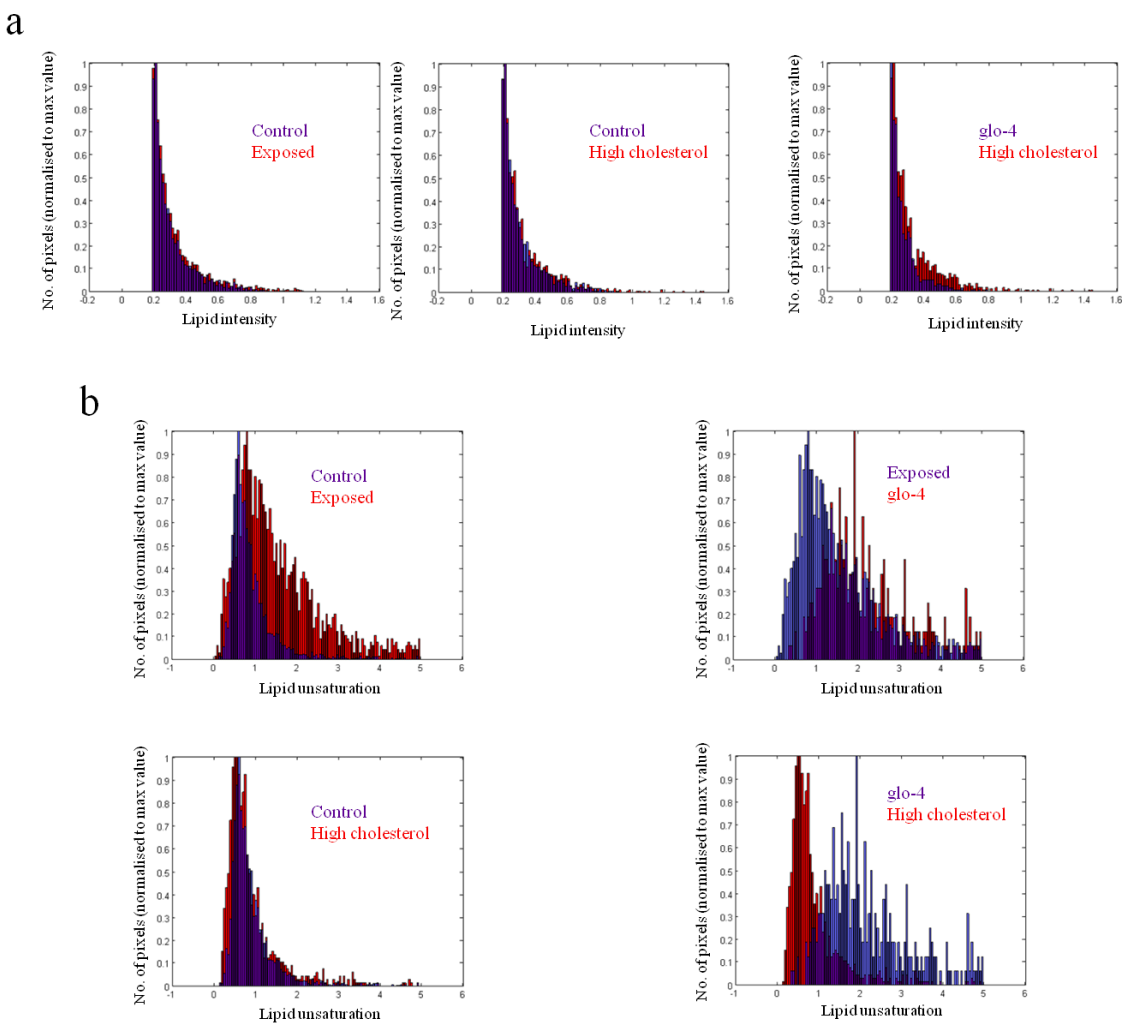

Figure 11.5 Comparison between several of the mutants (n=3 in each case). Out of the multitude of possible combinations these histograms have been displayed due to their biological significance. The a) lipid intensity and b) lipid unsaturation histograms have been displayed due to their biological significance. The a) lipid intensity and b) lipid unsaturation histograms have been given for control, exposed, high cholesterol and *glo-4* mutants/conditions. The identities of the histograms within each panel are given in their respective colours.

Whilst not directly related to assessing the effectiveness of the drug, data was acquired from several other mutants. This was conducted to access the discriminatory power of SIPCARS with regards to unexposed mutants. These mutants are often used whilst attempting to ascertain the exact mechanism of action of lipid metabolism altering drugs in *C. elegans* as their phenotypes allow them to be used as positive and negative controls (see section 11.2.2.1).

Figure 11.5a explicitly shows that these mutations/conditions do not have an appreciable effect on lipid intensity distribution: essentially remaining constant throughout. Figure 11.5b, in contrast, is considerably more remarkable showing differences in unsaturation ratio between several of the mutants. The difference between control and exposed has been commented upon above and is included here for comparative purposes. There appears to be no significant difference between the control and high cholesterol N2 nematodes. This may, at first, appear to be

paradoxical as the introduction of high cholesterol should fundamentally alter the composition of lipids stored in the nematode; however, *C. elegans* does not require a high cholesterol diet [135] and thus it is likely that any uptake of the additional cholesterol would be minimal. If, as suspected, *C. elegans* can attain all its required cholesterol from the *E. coli* alone, this would explain the lack of apparent difference.

If the *glo-4* mutation is compared with the high cholesterol case (demonstrably the same as comparing with the control) it is immediately apparent that although the *glo-4* mutation is supposed only to suppress the production of LROs it also considerably alters the composition of LDs. Although sterol-esters are a known constituent of LDs in many organisms, there is significant contention as to the location of their storage within *C. elegans*, with various sources suggesting either LDs or LROs [136]–[138]. A possible explanation of the observed results is that suppressing the formation of LROs led to an influx of cholesterol into the LDs. It is not clear how this would manifest, however, it could potentially account for the observed distribution of lipid unsaturations within the *glo-4* mutants.

Finally, comparing the exposed and *glo-4* mutation nematodes there is clear overlap between the two distributions; however, this may not be indicative of the underlying mechanism of the drug. Given the highly complex interactions it is very difficult to draw any conclusion from this comparison alone, other than the mechanism of action of the drug is different to the *glo-4* mutation.

11.2.4 Conclusion and future extensions

The above comparative histograms are not, in and of themselves, conclusive; however, they serve as a piece of the puzzle, a small but valuable component of collaborative work, to be further analysed in the context of wider bio-chemical and biological considerations by the KCL toxicogenomic group.

In terms of SIPCARS, however, the above results demonstrate that using this technique it is possible; even with the persistent instability of the present system, to successfully acquire data and produce compelling results. Whilst the SNR ratio attained ultimately limited the number of individuals in each population, five of each condition is still sufficient to draw valid conclusions.

An obvious extension to this body of work would be to acquire a larger number of individuals for each mutation/condition producing a more statistically significant set of results. This is, at present, limited by SNR considerations and system instability. The solution to this will likely be in the form of a new laser which is addressed in the following section.

These initial results illustrate that the SIPCARS system can differentiate between several mutants; however, these mutants have yet to be exposed to the drug. Acquiring data and comparing these

mutants unexposed and exposed could provide invaluable insight into the underlying mechanism of action of this drug.

Whilst attaining two dimensional cross-sections through each nematode was sufficient for comparative measurements, an additional extension of this work would be to acquire in three dimensions. Some preliminary data has already been successfully acquired to this effect; however, owing to a lack of SNR, it takes many hours to acquire a single three dimensional scan. It is, therefore, not feasible with this current system to perform population based studies in three dimensions; however, it may be possible to provide elucidatory information about the mechanism of the drug via high spatial resolution three dimensional imaging of a single nematode.

A final potential extension, SNR permitting, would be to assess the level of oxidised lipid within the LDs. This could be achieved using a similar approach as was used in HeLa cells (see section 11.1.3). Not only would this be interesting from a purely biological stand point but, this may also help determine the potency of the drug's anti-oxidant effect.

12. Future work and conclusions

12.1 Future work

As, where applicable, preceding chapters already address potential extensions, this section will briefly address several possible directions of study and their associated challenges.

Throughout the various iterations of the SIPCARS system, detailed in the previous chapters, many impediments have originated, either directly or indirectly, from the laser source. As such, in the near future a more suitable laser source will be installed. This system, manufactured by Toptica GmbH, is based on erbium fibre technology and is, in essence, identical to the system used by the NIST group (see section 3.2.1.1). It will be capable of producing a flat-top 1.8 ps pulse at 785 nm, and a 16 fs broadband supercontinuum pulse (corresponding to a Raman shift of 2400 - 3200 cm^{-1}), and will be aligned for hybrid two colour/three colour SIPCARS. Upgrading to this new laser system and approach (hybrid two colour/three colour SIPCARS) is expected to yield significant advantages in terms of both SNR, and source stability. This, in turn, will allow shorter pixel dwell times and larger scan areas.

As the Stokes and pump/probe wavelengths derived from this new system are approximately the same as those currently derived from the Coherent Mira titanium-sapphire oscillator based system, installation should be relatively uncomplicated. The SIPCARS methodology is independent of the laser source (i.e. is suitable for any laser source capable of producing a conventional BCARS spectrum), therefore, polarisation alignment will be no different from the existing titanium-sapphire oscillator based system.

One of the major priorities with this new system is to compare the level of contrast and structural discrimination attained in tissue sections, using SIPCARS imaging and haematoxylin and eosin (H & E) staining. As H & E staining is typically conducted on tissue sections considerably larger than the maximum scan size afforded by the current stage and is primarily used to identify and delimit sizeable neoplastic structures, this could pose a potential problem. Owing to its intrinsically detailed morphology, murine pancreas has been identified as a possible tissue sample. This tissue type, even with limited scan range afforded by the current stage, should allow, with a judicious choice of region, several different structures to be imaged in a single scan. A successful comparison with H & E staining should, therefore, be possible. Additionally, suitably dimensioned pre-prepared tissue sections (i.e. sequential stained and unstained sections for comparison) may be directly purchased.

As the scans of *C. elegans* nematodes represent the most successful application of SIPCARS to date and, further data, using this new system, will be acquired after the pancreatic tissue scans. In light of the expected increase in SNR, data from a larger population of nematodes will be

collected, strengthening conclusions based on statistical analysis. Additionally, this will allow whole nematode and/or three dimensional scans to be acquired which were previously impractical.

Following the two indicated samples, data relating to the secondary targets, as set out in previous chapters, would be the next priority.

12.2 Conclusion

This project has not necessarily followed the conventional results orientated path that might be expected using commercial apparatus, but has been predominantly developmental in nature. The overarching objective was to realise a novel CARS imaging system encompassing an all optical NRB removal mechanism: a brief which, to a great extent, the current SIPCARS system fulfils. Further to this principle objective, the ultimate ambition of this research programme was to bring a low cost SIPCARS system to market. Whilst significant progress has been made toward this objective it is yet to be fully accomplished.

With regards to developing the system sufficiently to secure additional funding and/or garner commercial interest, implementing the new laser system, see above, will hopefully allow the true potential of the SIPCARS methodology to be demonstrated without the retarding limitations of the current system. Once the applicability of the SIPCARS methodology for high sensitivity, rapid hyperspectral imaging of tissue (sub-10 ms pixel dwell times) has been categorically demonstrated, the prospects for securing said funding/investment will be radically improved.

Throughout the course of this project many technical impediments have been encountered, including but not limited to, laser output temporal instability, limited spatial scan range (due to the stage), and monochromator derived optical aberrations, all of which have been largely alleviated. Whilst the vast majority of technical obstacles have been surmounted, regrettably there are still outstanding limitations in the form of a fringe/interference-type spectral pattern and an unexpected asymmetrical spatial response (see chapter 9).

Even in light of these outstanding limitations it has proved possible to completely validate the SIPCARS methodology, demonstrating its ability to produce hyperspectral data that is entirely free from NRB. Additionally, it was possible to produce high signal-to-noise ratio SIPCARS imaging of both HeLa cells, and *C. elegans* nematodes.

In the case of HeLa cells, it was possible to identify LDs and subsequently, by producing ratio images, assess their degree of lipid unsaturation and the level of oxidised lipid content and in so doing provide strong circumstantial evidence as to the prevalent underlying lipid oxidative degradation process.

With regards to *C. elegans*, using the SIPCARS system it was possible to differentiate between several mutants based on the unsaturation of their component lipid droplets and also provide compelling evidence demonstrating that a lipid metabolism altering drug had the desired effect within wild type N2 nematodes.

This thesis details the implementation and development of SIPCARS, a new variant of CARS imaging that affords the same spectroscopic insight as conventional Raman scattering, but with inherent optical sectioning and significantly reduced acquisition times.

13. References

[1] C. Balas, 'Review of biomedical optical imaging—a powerful, non-invasive, non-ionizing technology for improving *in vivo* diagnosis', *Measurement Science and Technology*, vol. 20, no. 10, p. 104020, Oct. 2009.

[2] G. J. Brakenhoff, H. T. M. Voort, E. A. Spronsen, and N. Nanninga, 'Three-dimensional imaging in fluorescence by confocal scanning microscopy', *Journal of Microscopy*, vol. 153, no. 2, pp. 151–159, Feb. 1989.

[3] W. Denk, J. H. Strickler, W. W. Webb, and others, 'Two-photon laser scanning fluorescence microscopy', *Science*, vol. 248, no. 4951, pp. 73–76, 1990.

[4] Invitrogen, *Molecular Probes: The Handbook*. .

[5] C. Kittel, *Introduction to solid state physics*, 8th ed. Hoboken, NJ: Wiley, 2005.

[6] J.-X. Cheng and X. S. Xie, 'Coherent Anti-Stokes Raman Scattering Microscopy: Instrumentation, Theory, and Applications', *The Journal of Physical Chemistry B*, vol. 108, no. 3, pp. 827–840, Jan. 2004.

[7] J.-X. Cheng and X. S. Xie, Eds., *Coherent Raman scattering microscopy*. Boca Raton: CRC Press, Taylor & Francis Group, 2013.

[8] W. Demtröder, *Laser spectroscopy: basic concepts and instrumentation*, 3rd ed. Berlin ; New York: Springer, 2003.

[9] M. Tanaka and R. J. Young, 'Review Polarised Raman spectroscopy for the study of molecular orientation distributions in polymers', *Journal of Materials Science*, vol. 41, no. 3, pp. 963–991, Feb. 2006.

[10] D. A. Long, *The Raman effect: a unified treatment of the theory of Raman scattering by molecules*. Chichester ; New York: Wiley, 2002.

[11] P. W. Atkins and R. Friedman, *Molecular quantum mechanics*, 5th ed. Oxford ; New York: Oxford University Press, 2011.

[12] G. L. Eesley, *Coherent Raman spectroscopy*, 1st ed. Oxford ; New York: Pergamon Press, 1981.

[13] J.-X. Cheng, 'Coherent anti-Stokes Raman scattering microscopy', *Appl Spectrosc*, vol. 61, no. 9, pp. 197–208, Sep. 2007.

[14] H. Lotem, R. T. Lynch, and N. Bloembergen, 'Interference between Raman resonances in four-wave difference mixing', *Physical Review A*, vol. 14, no. 5, pp. 1748–1755, Nov. 1976.

[15] J.-X. Cheng, A. Volkmer, and X. S. Xie, 'Theoretical and experimental characterization of coherent anti-Stokes Raman scattering microscopy', *Journal of the Optical Society of America B*, vol. 19, no. 6, p. 1363, Jun. 2002.

[16] A. Volkmer, 'Vibrational imaging and microspectroscopies based on coherent anti-Stokes Raman scattering microscopy', *Journal of Physics D: Applied Physics*, vol. 38, no. 5, pp. R59–R81, Mar. 2005.

[17] C. L. Tang and T. F. Deutsch, 'Generation of Anti-Stokes Radiation in the Higher Order Coherent Raman Processes', *Physical Review*, vol. 138, no. 1A, pp. A1–A8, Apr. 1965.

[18] P. D. Maker and R. W. Terhune, 'Study of Optical Effects Due to an Induced Polarization Third Order in the Electric Field Strength', *Physical Review*, vol. 137, no. 3A, pp. A801–A818, Feb. 1965.

[19] M. D. Duncan, J. Reintjes, and T. J. Manuccia, 'Scanning coherent anti-Stokes Raman microscope', *Optics Letters*, vol. 7, no. 8, p. 350, Aug. 1982.

[20] A. Zumbusch, G. R. Holtom, and X. S. Xie, 'Three-Dimensional Vibrational Imaging by Coherent Anti-Stokes Raman Scattering', *Physical Review Letters*, vol. 82, no. 20, pp. 4142–4145, May 1999.

[21] A. Volkmer, L. D. Book, and X. S. Xie, 'Time-resolved coherent anti-Stokes Raman scattering microscopy: Imaging based on Raman free induction decay', *Applied Physics Letters*, vol. 80, no. 9, p. 1505, 2002.

[22] C. L. Evans and X. S. Xie, 'Coherent Anti-Stokes Raman Scattering Microscopy: Chemical Imaging for Biology and Medicine', *Annual Review of Analytical Chemistry*, vol. 1, no. 1, pp. 883–909, Jul. 2008.

[23] T. W. Kee and M. T. Cicerone, 'Simple approach to one-laser, broadband coherent anti-Stokes Raman scattering microscopy', *Optics Letters*, vol. 29, no. 23, p. 2701, Dec. 2004.
[24] I. T. Jolliffe, *Principal component analysis*, 2nd ed. New York: Springer, 2002.
[25] J. C. Knight, 'Photonic crystal fibres', *Nature*, vol. 424, no. 6950, pp. 847–851, Aug. 2003.
[26] NKT Photonics A/S, 'Compact ultra-bright supercon-tinuum light source'. [Online]. Available: http://www.thorlabs.de/images/TabImages/Application_note_-_Supercontinuum%20-%20SC-5.0-1040.pdf. [Accessed: 29-Aug-2016].
[27] J. M. Dudley, G. Genty, and S. Coen, 'Supercontinuum generation in photonic crystal fiber', *Reviews of Modern Physics*, vol. 78, no. 4, pp. 1135–1184, Oct. 2006.
[28] Thorlabs, Inc., 'Nonlinear Photonic Crystal Fibres'. [Online]. Available: www.thorlabs.de/newgrouppage9.cfm?objectgroup_id=2044. [Accessed: 22-Jun-2016].
[29] M. T. Cicerone, K. A. Aamer, Y. J. Lee, and E. Vartiainen, 'Maximum entropy and time-domain Kramers-Kronig phase retrieval approaches are functionally equivalent for CARS microspectroscopy: Maximum entropy and TDKK phase retrieval approaches are functionally equivalent for CARS microspectroscopy', *Journal of Raman Spectroscopy*, vol. 43, no. 5, pp. 637–643, May 2012.
[30] J. P. R. Day *et al.*, 'Quantitative Coherent Anti-Stokes Raman Scattering (CARS) Microscopy', *The Journal of Physical Chemistry B*, vol. 115, no. 24, pp. 7713–7725, Jun. 2011.
[31] R. K. Chang, J. Ducuing, and N. Bloembergen, 'Relative Phase Measurement Between Fundamental and Second-Harmonic Light', *Physical Review Letters*, vol. 15, no. 1, pp. 6–8, Jul. 1965.
[32] S. H. Parekh, Y. J. Lee, K. A. Aamer, and M. T. Cicerone, 'Label-Free Cellular Imaging by Broadband Coherent Anti-Stokes Raman Scattering Microscopy', *Biophysical Journal*, vol. 99, no. 8, pp. 2695–2704, Oct. 2010.
[33] M. Cui, B. R. Bachler, and J. P. Ogilvie, 'Comparing coherent and spontaneous Raman scattering under biological imaging conditions', *Optics Letters*, vol. 34, no. 6, p. 773, Mar. 2009.
[34] F. Lu, W. Zheng, C. Sheppard, and Z. Huang, 'Interferometric polarization coherent anti-Stokes Raman scattering (IP-CARS) microscopy', *Optics Letters*, vol. 33, no. 6, p. 602, Mar. 2008.
[35] F. Lu, W. Zheng, and Z. Huang, 'Heterodyne polarization coherent anti-Stokes Raman scattering microscopy', *Applied Physics Letters*, vol. 92, no. 12, p. 123901, 2008.
[36] K. Orsel *et al.*, 'Heterodyne interferometric polarization coherent anti-Stokes Raman scattering (HIP-CARS) spectroscopy', *Journal of Raman Spectroscopy*, vol. 41, no. 12, pp. 1678–1681, Dec. 2010.
[37] L. Lepetit, G. Chériaux, and M. Joffre, 'Linear techniques of phase measurement by femtosecond spectral interferometry for applications in spectroscopy', *Journal of the Optical Society of America B*, vol. 12, no. 12, p. 2467, Dec. 1995.
[38] V. R. Supradeepa, D. E. Leaird, and A. M. Weiner, 'Optical arbitrary waveform characterization via dual-quadrature spectral interferometry', *Optics Express*, vol. 17, no. 1, p. 25, Jan. 2009.
[39] C. L. Evans, E. O. Potma, and X. S. Xie, 'Coherent anti-Stokes Raman scattering spectral interferometry: determination of the real and imaginary components of nonlinear susceptibility χ^(3) for vibrational microscopy', *Optics Letters*, vol. 29, no. 24, p. 2923, Dec. 2004.
[40] P. D. Chowdary, W. A. Benalcazar, Z. Jiang, D. M. Marks, S. A. Boppart, and M. Gruebele, 'High Speed Nonlinear Interferometric Vibrational Analysis of Lipids by Spectral Decomposition', *Analytical Chemistry*, vol. 82, no. 9, pp. 3812–3818, May 2010.
[41] S.-H. Lim, A. G. Caster, O. Nicolet, and S. R. Leone, 'Chemical Imaging by Single Pulse Interferometric Coherent Anti-Stokes Raman Scattering Microscopy', *The Journal of Physical Chemistry B*, vol. 110, no. 11, pp. 5196–5204, Mar. 2006.
[42] D. Oron, N. Dudovich, and Y. Silberberg, 'Femtosecond Phase-and-Polarization Control for Background-Free Coherent Anti-Stokes Raman Spectroscopy', *Physical Review Letters*, vol. 90, no. 21, May 2003.

[43] E. M. Vartiainen, 'Phase retrieval approach for coherent anti-Stokes Raman scattering spectrum analysis', *Journal of the Optical Society of America B*, vol. 9, no. 8, p. 1209, Aug. 1992.
[44] R. Selm *et al.*, 'Ultrabroadband background-free coherent anti-Stokes Raman scattering microscopy based on a compact Er:fiber laser system', *Optics Letters*, vol. 35, no. 19, p. 3282, Oct. 2010.
[45] A. Sell, G. Krauss, R. Scheu, R. Huber, and A. Leitenstorfer, '8-fs pulses from a compact Er:fiber system: quantitative modeling and experimental implementation', *Optics Express*, vol. 17, no. 2, p. 1070, Jan. 2009.
[46] A. F. Pegoraro, A. Ridsdale, D. J. Moffatt, Y. Jia, J. P. Pezacki, and A. Stolow, 'Optimally chirped multimodal CARS microscopy based on a single Ti:sapphire oscillator', *Opt Express*, vol. 17, no. 4, pp. 2984–2996, Feb. 2009.
[47] A. F. Pegoraro, A. D. Slepkov, A. Ridsdale, D. J. Moffatt, and A. Stolow, 'Hyperspectral multimodal CARS microscopy in the fingerprint region: Hyperspectral multimodal CARS microscopy in the fingerprint region', *Journal of Biophotonics*, vol. 7, no. 1–2, pp. 49–58, Jan. 2014.
[48] I. Pope, W. Langbein, P. Watson, and P. Borri, 'Simultaneous hyperspectral differential-CARS, TPF and SHG microscopy with a single 5 fs Ti:Sa laser', *Optics Express*, vol. 21, no. 6, p. 7096, Mar. 2013.
[49] F. Masia, A. Glen, P. Stephens, P. Borri, and W. Langbein, 'Quantitative Chemical Imaging and Unsupervised Analysis Using Hyperspectral Coherent Anti-Stokes Raman Scattering Microscopy', *Analytical Chemistry*, vol. 85, no. 22, pp. 10820–10828, Nov. 2013.
[50] M. Okuno, H. Kano, P. Leproux, V. Couderc, and H. Hamaguchi, 'Quantitative coherent anti-Stokes Raman scattering microspectroscopy using a nanosecond supercontinuum light source', *Optical Fiber Technology*, vol. 18, no. 5, pp. 388–393, Sep. 2012.
[51] K. Bito, M. Okuno, H. Kano, P. Leproux, V. Couderc, and H. Hamaguchi, 'Three-pulse multiplex coherent anti-Stokes/Stokes Raman scattering (CARS/CSRS) microspectroscopy using a white-light laser source', *Chemical Physics*, vol. 419, pp. 156–162, Jun. 2013.
[52] Y. J. Lee, Y. Liu, and M. T. Cicerone, 'Characterization of three-color CARS in a two-pulse broadband CARS spectrum', *Opt Lett*, vol. 32, no. 22, pp. 3370–3372, Nov. 2007.
[53] C. H. Camp Jr *et al.*, 'High-speed coherent Raman fingerprint imaging of biological tissues', *Nature Photonics*, vol. 8, no. 8, pp. 627–634, Jul. 2014.
[54] C. Pohling, T. Buckup, A. Pagenstecher, and M. Motzkus, 'Chemoselective imaging of mouse brain tissue via multiplex CARS microscopy', *Biomedical Optics Express*, vol. 2, no. 8, p. 2110, Aug. 2011.
[55] H. Frostig, T. Bayer, N. Dudovich, Y. C. Eldar, and Y. Silberberg, 'Single-beam spectrally controlled two-dimensional Raman spectroscopy', *Nature Photonics*, vol. 9, no. 5, pp. 339–343, Apr. 2015.
[56] V. Kumar *et al.*, 'Balanced-detection Raman-induced Kerr-effect spectroscopy', *Physical Review A*, vol. 86, no. 5, Nov. 2012.
[57] K. Hiramatsu, M. Okuno, H. Kano, P. Leproux, V. Couderc, and H. Hamaguchi, 'Observation of Raman Optical Activity by Heterodyne-Detected Polarization-Resolved Coherent Anti-Stokes Raman Scattering', *Physical Review Letters*, vol. 109, no. 8, Aug. 2012.
[58] C. W. Freudiger *et al.*, 'Label-Free Biomedical Imaging with High Sensitivity by Stimulated Raman Scattering Microscopy', *Science*, vol. 322, no. 5909, pp. 1857–1861, Dec. 2008.
[59] N. Bloembergen, 'The Stimulated Raman Effect', *American Journal of Physics*, vol. 35, no. 11, p. 989, 1967.
[60] P. Berto, E. R. Andresen, and H. Rigneault, 'Background-Free Stimulated Raman Spectroscopy and Microscopy', *Physical Review Letters*, vol. 112, no. 5, Feb. 2014.
[61] Y. Ozeki *et al.*, 'High-speed molecular spectral imaging of tissue with stimulated Raman scattering', *Nature Photonics*, vol. 6, no. 12, pp. 845–851, Nov. 2012.

[62] Y. Yu, P. V. Ramachandran, and M. C. Wang, ‘Shedding new light on lipid functions with CARS and SRS microscopy’, *Biochimica et Biophysica Acta (BBA) - Molecular and Cell Biology of Lipids*, vol. 1841, no. 8, pp. 1120–1129, Aug. 2014.
[63] C.-S. Liao *et al.*, ‘Spectrometer-free vibrational imaging by retrieving stimulated Raman signal from highly scattered photons’, *Science Advances*, vol. 1, no. 9, pp. e1500738–e1500738, Oct. 2015.
[64] C.-S. Liao *et al.*, ‘Microsecond scale vibrational spectroscopic imaging by multiplex stimulated Raman scattering microscopy’, *Light: Science & Applications*, vol. 4, p. e265, Mar. 2015.
[65] M. T. Cicerone, ‘Rapid label-free chemical imaging of cells and tissues’, presented at the Spie Photonics West, Multiphoton Microscopy in the Biomedical Sciences, San Francisco, 14-Feb-2016.
[66] R. W. Boyd, *Nonlinear optics*, 3rd ed. Amsterdam ; Boston: Academic Press, 2008.
[67] D. A. Kleinman, ‘Nonlinear Dielectric Polarization in Optical Media’, *Physical Review*, vol. 126, no. 6, pp. 1977–1979, Jun. 1962.
[68] M. Cui, M. Joffre, J. Skodack, and J. P. Ogilvie, ‘Interferometric Fourier transform Coherent anti-Stokes Raman Scattering’, *Optics Express*, vol. 14, no. 18, p. 8448, 2006.
[69] E. C. Stack, C. Wang, K. A. Roman, and C. C. Hoyt, ‘Multiplexed immunohistochemistry, imaging, and quantitation: A review, with an assessment of Tyramide signal amplification, multispectral imaging and multiplex analysis’, *Methods*, vol. 70, no. 1, pp. 46–58, Nov. 2014.
[70] M. Bonn, M. Müller, H. A. Rinia, and K. N. J. Burger, ‘Imaging of chemical and physical state of individual cellular lipid droplets using multiplex CARS microscopy’, *Journal of Raman Spectroscopy*, vol. 40, no. 7, pp. 763–769, Jul. 2009.
[71] Y. H. Ong, M. Lim, and Q. Liu, ‘Comparison of principal component analysis and biochemical component analysis in Raman spectroscopy for the discrimination of apoptosis and necrosis in K562 leukemia cells’, *Optics Express*, vol. 20, no. 20, p. 22158, Sep. 2012.
[72] A. C. S. Talari, Z. Movasaghi, S. Rehman, and I. ur Rehman, ‘Raman Spectroscopy of Biological Tissues’, *Applied Spectroscopy Reviews*, vol. 50, no. 1, pp. 46–111, Jan. 2015.
[73] F. R. Dollish, W. G. Fateley, and F. F. Bentley, *Characteristic Raman frequencies of organic compounds*. New York: Wiley, 1974.
[74] University of Toronto Scarborough, Traces centre, ‘Raman Band Correlation Table’, 06-Jun-2016. [Online]. Available: http://www.utsc.utoronto.ca/~traceslab/raman%20correlation%20table.pdf.
[75] National Institue of Advanced Industrial Science and Technology, ‘Spectral Database for Organic Compounds’. [Online]. Available: http://sdbs.db.aist.go.jp/sdbs/cgi-bin/cre_index.cgi. [Accessed: 08-Jan-2016].
[76] P. Wang, B. Liu, D. Zhang, M. Y. Belew, H. A. Tissenbaum, and J.-X. Cheng, ‘Imaging Lipid Metabolism in Live *Caenorhabditis elegans* Using Fingerprint Vibrations’, *Angewandte Chemie International Edition*, vol. 53, no. 44, pp. 11787–11792, Oct. 2014.
[77] H. A. Rinia, K. N. J. Burger, M. Bonn, and M. Müller, ‘Quantitative Label-Free Imaging of Lipid Composition and Packing of Individual Cellular Lipid Droplets Using Multiplex CARS Microscopy’, *Biophysical Journal*, vol. 95, no. 10, pp. 4908–4914, Nov. 2008.
[78] C. Di Napoli, I. Pope, F. Masia, P. Watson, W. Langbein, and P. Borri, ‘Hyperspectral and differential CARS microscopy for quantitative chemical imaging in human adipocytes’, *Biomedical Optics Express*, vol. 5, no. 5, p. 1378, May 2014.
[79] Leica Microsystems, ‘Field of view scanner’. [Online]. Available: http://www.leica-microsystems.com/products/confocal-microscopes/technology/fov-scanner/. [Accessed: 22-Jun-2016].
[80] I. S. Ryu, C. H. Camp, Y. Jin, M. T. Cicerone, and Y. J. Lee, ‘Beam scanning for rapid coherent Raman hyperspectral imaging’, *Optics Letters*, vol. 40, no. 24, p. 5826, Dec. 2015.
[81] P. A. Temple and C. E. Hathaway, ‘Multiphonon Raman Spectrum of Silicon’, *Physical Review B*, vol. 7, no. 8, pp. 3685–3697, Apr. 1973.
[82] T. R. Hart, R. L. Aggarwal, and B. Lax, ‘Temperature Dependence of Raman Scattering in Silicon’, *Physical Review B*, vol. 1, no. 2, pp. 638–642, Jan. 1970.

[83] R. L. McCreery, ‘Photometric Standards for Raman Spectroscopy’, in *Handbook of Vibrational Spectroscopy*, J. M. Chalmers and P. R. Griffiths, Eds. Chichester, UK: John Wiley & Sons, Ltd, 2006.
[84] S. Stewart, R. J. Priore, M. P. Nelson, and P. J. Treado, ‘Raman Imaging’, *Annual Review of Analytical Chemistry*, vol. 5, no. 1, pp. 337–360, Jul. 2012.
[85] C.-K. Huang, H. Hamaguchi, and S. Shigeto, ‘In vivo multimode Raman imaging reveals concerted molecular composition and distribution changes during yeast cell cycle’, *Chemical Communications*, vol. 47, no. 33, p. 9423, 2011.
[86] J. C. Knight, T. A. Birks, P. S. J. Russell, and D. M. Atkin, ‘All-silica single-mode optical fiber with photonic crystal cladding’, *Optics Letters*, vol. 21, no. 19, p. 1547, Oct. 1996.
[87] T. W. Kee, H. Zhao, and M. T. Cicerone, ‘One-laser interferometric broadband coherent anti-Stokes Raman scattering’, *Optics Express*, vol. 14, no. 8, p. 3631, 2006.
[88] E. O. Potma, C. L. Evans, and X. S. Xie, ‘Heterodyne coherent anti-Stokes Raman scattering (CARS) imaging’, *Optics letters*, vol. 31, no. 2, pp. 241–243, 2006.
[89] Fianium Ltd., ‘Supercontinuum SC400 and SC400-PP’. .
[90] R. Paschotta, ‘Femtosecond Lasers’. [Online]. Available: www.rp-photonics.com/femtosecond_lasers.html. [Accessed: 30-Aug-2016].
[91] Andor Technology Ltd., ‘Electron Multiplying CCD Cameras’. [Online]. Available: http://www.andor.com/learning-academy/electron-multiplying-ccd-cameras-the-technology-behind-emccds. [Accessed: 06-Feb-2016].
[92] Cole-Parmer Instrument Co. Ltd., ‘Chemical Compatibility Database’. [Online]. Available: http://www.coleparmer.co.uk/Chemical-Resistance. [Accessed: 28-May-2016].
[93] European Aluminium Foil Association, ‘Facts about aluminium foil’. [Online]. Available: http://www.alufoil.org/facts.html. [Accessed: 28-May-2016].
[94] G. R. Meredith, ‘Third-order susceptibility determination by third harmonic generation. II’, *The Journal of Chemical Physics*, vol. 78, no. 3, p. 1543, 1983.
[95] E. M. Vartiainen, H. A. Rinia, M. Müller, and M. Bonn, ‘Direct extraction of Raman line-shapes from congested CARS spectra’, *Optics Express*, vol. 14, no. 8, p. 3622, 2006.
[96] J. Komma, G. Hofmann, C. Schwarz, D. Heinert, P. Pastrik, and R. Nawrodt, ‘Optical properties of silicon at low temperatures’, presented at the ELiTES, University of Tokyo, 10-Apr-2012.
[97] Coherent Inc., ‘MIRA 900 modelocked Ti:Sapphire Lasers Datasheet’, 2002. [Online]. Available: http://www.coherent.com/downloads/MIRA900.pdf#page=1. [Accessed: 15-Jul-2013].
[98] J. Wei, *Nonlinear super-resolution nano-optics and applications*. Beijing: Science Press, 2015.
[99] K. Rottwitt and P. Tidemand-Lichtenberg, *Nonlinear optics: principles and applications*. Boca Raton: CRC Press/Taylor & Francis Group, 2015.
[100] P. Nandakumar, A. Kovalev, and A. Volkmer, ‘Vibrational imaging based on stimulated Raman scattering microscopy’, *New Journal of Physics*, vol. 11, no. 3, p. 033026, Mar. 2009.
[101] A. Matsushita *et al.*, ‘Two-dimensional Fourier-transform Raman and near-infrared correlation spectroscopy studies of poly(methyl methacrylate) blends’, *Vibrational Spectroscopy*, vol. 24, no. 2, pp. 171–180, Dec. 2000.
[102] W. M. Sears, ‘Raman scattering from polymerizing styrene. I. Vibrational mode analysis’, *The Journal of Chemical Physics*, vol. 75, no. 4, p. 1589, 1981.
[103] W. M. Sears, ‘Raman spectra at low temperatures and depolarization ratios for styrene and polystyrene’, *The Journal of Chemical Physics*, vol. 77, no. 4, p. 1639, 1982.
[104] M. Haris, S. Kathiresan, and S. Mohan, ‘FT-IR and FT-Raman spectra and normal coordinate analysis of poly methyl methacrylate’, *Der Pharma Chemica*, vol. 2, no. 4, pp. 316–323, 2010.
[105] A. Almahdy *et al.*, ‘Microbiochemical Analysis of Carious Dentine Using Raman and Fluorescence Spectroscopy’, *Caries Research*, vol. 46, no. 5, pp. 432–440, 2012.
[106] NKT Photonics A/S, ‘femtoWHITE800 datasheet’. [Online]. Available: http://www.nktphotonics.com/wp-content/uploads/2015/03/femtoWHITE-800.pdf. [Accessed: 01-Dec-2015].

[107] T. Shimanouchi, ‘Tables of molecular vibrational frequencies. Consolidated volume II’, *Journal of Physical and Chemical Reference Data*, vol. 6, no. 3, p. 993, 1977.
[108] J. McClure, ‘The Schmidt-Czerny-Turner Spectrograph’, presented at the Advanced Materials Characterization Workshop, University of Illinois, 07-Jun-2012.
[109] E. Hecht, *Optics*, 3rd ed. Reading, Mass: Addison-Wesley, 1998.
[110] G. H. Rieke, *Measuring the universe: a multiwavelength perspective*. New York: Cambridge University Press, 2012.
[111] R. Delmas and F. Baratange, ‘Spectrometer with cylindrical lens for astigmatism correction and demagnification’, US 7812949, Oct-2010.
[112] V. Sacek, ‘Full-aperture Schmidt corrector: Schmidt camera’, 2015. [Online]. Available: http://www.telescope-optics.net/Schmidt-camera.htm. [Accessed: 07-Jul-2016].
[113] Photometrics Inc., ‘eXcelon Technical Note’. .
[114] Andor Technology Ltd., ‘Andor iXon3 EMCCD Brochure’. .
[115] Princeton Instruments, ‘Products: eXcelon CCD and EMCCD Technology’. [Online]. Available: http://www.princetoninstruments.com/products/eXcelon. [Accessed: 13-Jul-2016].
[116] F. Kajzar and J. Messier, ‘Third-harmonic generation in liquids’, *Physical Review A*, vol. 32, no. 4, pp. 2352–2363, Oct. 1985.
[117] G. R. Meredith, ‘Third-order optical susceptibility determination by third harmonic generation. I’, *The Journal of Chemical Physics*, vol. 78, no. 3, p. 1533, 1983.
[118] B. Littleton, T. Kavanagh, F. Festy, and D. Richards, ‘Spectral Interferometric Implementation with Passive Polarization Optics of Coherent Anti-Stokes Raman Scattering’, *Physical Review Letters*, vol. 111, no. 10, Sep. 2013.
[119] M. Jurna, J. P. Korterik, C. Otto, J. L. Herek, and H. L. Offerhaus, ‘Background free CARS imaging by phase sensitive heterodyne CARS’, *Optics Express*, vol. 16, no. 20, p. 15863, Sep. 2008.
[120] H. . Willis, V. J. . Zichy, and P. . Hendra, ‘The laser-Raman and infra-red spectra of poly(methyl methacrylate)’, *Polymer*, vol. 10, pp. 737–746, Jan. 1969.
[121] A. R. Thiam, R. V. Farese Jr, and T. C. Walther, ‘The biophysics and cell biology of lipid droplets’, *Nature Reviews Molecular Cell Biology*, vol. 14, no. 12, pp. 775–786, Nov. 2013.
[122] S. Martin and R. G. Parton, ‘Lipid droplets: a unified view of a dynamic organelle’, *Nature Reviews Molecular Cell Biology*, vol. 7, no. 5, pp. 373–378, May 2006.
[123] D. Débarre *et al.*, ‘Imaging lipid bodies in cells and tissues using third-harmonic generation microscopy’, *Nature Methods*, vol. 3, no. 1, pp. 47–53, Jan. 2006.
[124] H. Y. Mak, L. S. Nelson, M. Basson, C. D. Johnson, and G. Ruvkun, ‘Polygenic control of Caenorhabditis elegans fat storage’, *Nature Genetics*, vol. 38, no. 3, pp. 363–368, Mar. 2006.
[125] Y. Ohsaki, Y. Shinohara, M. Suzuki, and T. Fujimoto, ‘A pitfall in using BODIPY dyes to label lipid droplets for fluorescence microscopy’, *Histochemistry and Cell Biology*, vol. 133, no. 4, pp. 477–480, Apr. 2010.
[126] T. O’Haver, ‘A Pragmatic Introduction to Signal Processing’, 2015. [Online]. Available: https://terpconnect.umd.edu/~toh/spectrum/InteractivePeakFitter.htm#comman. [Accessed: 18-Nov-2015].
[127] D. Del Rio, A. J. Stewart, and N. Pellegrini, ‘A review of recent studies on malondialdehyde as toxic molecule and biological marker of oxidative stress’, *Nutrition, Metabolism and Cardiovascular Diseases*, vol. 15, no. 4, pp. 316–328, Aug. 2005.
[128] Y. Nie, ‘Oligomeric Proanthocyanidins Extracts are Putative Anti-Obesity Drug Leads in the Nematode Caenorhabditis Elegans’, King’s College London, London, 2016.
[129] T. Kaletta and M. O. Hengartner, ‘Finding function in novel targets: C. elegans as a model organism’, *Nature Reviews Drug Discovery*, vol. 5, no. 5, pp. 387–399, May 2006.
[130] Laboratory for Optical and Computational Instrumentation, ‘A Short History of C. elegans Research’, 2016. [Online]. Available: http://wormclassroom.org/short-history-c-elegans-research. [Accessed: 13-Jul-2016].
[131] J. E. Sulston, E. Schierenberg, J. G. White, and J. N. Thomson, ‘The embryonic cell lineage of the nematode Caenorhabditis elegans’, *Dev. Biol.*, vol. 100, no. 1, pp. 64–119, Nov. 1983.

[132] T. A. Jarrell *et al.*, 'The Connectome of a Decision-Making Neural Network', *Science*, vol. 337, no. 6093, pp. 437–444, Jul. 2012.
[133] S. Brenner, 'The genetics of Caenorhabditis elegans', *Genetics*, vol. 77, no. 1, pp. 71–94, May 1974.
[134] World Health Organisation, 'The top 10 causes of death', 2014. [Online]. Available: http://www.who.int/mediacentre/factsheets/fs310/en/. [Accessed: 16-Jul-2016].
[135] 'Key to Cholesterol's Role in Nematode Development', *PLoS Biology*, vol. 2, no. 10, p. e345, Sep. 2004.
[136] H. J. Lee *et al.*, 'Assessing Cholesterol Storage in Live Cells and C. elegans by Stimulated Raman Scattering Imaging of Phenyl-Diyne Cholesterol', *Scientific Reports*, vol. 5, p. 7930, Jan. 2015.
[137] T. C. Walther and R. V. Farese, 'Lipid Droplets and Cellular Lipid Metabolism', *Annual Review of Biochemistry*, vol. 81, no. 1, pp. 687–714, Jul. 2012.
[138] S. O. Zhang, R. Trimble, F. Guo, and H. Mak, 'Lipid droplets as ubiquitous fat storage organelles in C. elegans', *BMC Cell Biology*, vol. 11, no. 1, p. 96, 2010.

14. Appendices

Appendix I

The polarisability tensor, α_{ij}, is a second rank tensor that describes the overall polarisability of a molecular bond. It is important to note that the components of the α_{ij} are dependent on the symmetry of the molecular bond. Simplistically the symmetry of the molecular bond dictates the symmetry of the polarisability tensor as follows [9]:

Fully expanded α_{ij}

$$\alpha = \begin{pmatrix} \alpha_{xx} & \alpha_{xy} & \alpha_{xz} \\ \alpha_{yx} & \alpha_{yy} & \alpha_{yz} \\ \alpha_{zx} & \alpha_{zy} & \alpha_{zz} \end{pmatrix}$$

Spherical symmetry

$$\alpha = \begin{pmatrix} a & b & b \\ b & a & b \\ b & b & a \end{pmatrix}$$

Cylindrical symmetry

$$\alpha = \begin{pmatrix} a & b & c \\ b & a & c \\ c & c & d \end{pmatrix}$$

No symmetry

$$\alpha = \begin{pmatrix} a & b & c \\ b & d & e \\ c & e & f \end{pmatrix}$$

This is of particular importance for calculating the depolarisation ratio which, in an isotropic medium, is:

$$\rho = {3\gamma'^2}/{(45\alpha'^2 + 4\gamma'^2)}$$

where:

$$\alpha' = \frac{1}{3}\left(\alpha_{xx} + \alpha_{yy} + \alpha_{zz}\right)$$

$$\gamma'^2 = \frac{1}{2}\left[\left(\alpha_{xx} - \alpha_{yy}\right)^2 + \left(\alpha_{yy} - \alpha_{zz}\right)^2 (\alpha_{zz} - \alpha_{xx})^2 + 6\left(\alpha_{xy}{}^2 + \alpha_{yz}{}^2 + \alpha_{zx}{}^2\right)\right]$$

From the above equation the upper and lower limits of ρ can be readily deduced. If $tr(\alpha) = 0$ then the $\rho = 0.75$: a depolar mode, and the upper limit. If, however, $tr(\alpha) \neq 0$ and in the limit of $\gamma'^2 \to 0$ the value of $\rho = 0$: the lower limit.

This is no more than a very brief introduction to the Raman polarisability tensor a full review detailing the effect of material anisotropy and incident beam ellipticlity can be found elsewhere [10].

Appendix II

The rigorous quantum field deviation of the spontaneous Raman scattering intensity is significantly involved and far beyond the scope of this thesis. It can be found elsewhere in great detail [12] .

The direct proportionality between the spontaneous Raman scattering intensity and $Im\left\{\chi^{R^{(3)}}\right\}$ will be used in several places throughout this thesis and, therefore, it would seem remiss not to give an intuitive interpretation of this result. Note that as this will be an explicatory description of the underlying principle it is not designed to be entirely rigorous.

Firstly it is important to identify the failings of the classical approach which fails to take into account the differing strengths of the pump and Stokes field (i.e. the spontaneous emission process): instead making the assumption that both fields are of equivalent intensity. In reality the pump field is many orders of magnitude more intense than the Stokes field and thus this is an erroneous assumption. The classical approach, therefore, inexorably delivers only an approximate spontaneous Raman intensity value.

If the spontaneous Raman scattering energy level diagram is considered (see figure 2.1) it is possible to see that while the value of interest is the Raman shift (Ω) this is actually inferred from the wavelength of the detected Stokes scattered light. The Raman shift value is simply $\Omega = \lambda_{Stokes} - \lambda_{pump}$ given in wavenumbers. Although, at first, this may appear counterintuitive it is possible to characterise the interaction by constructing a trivial equation which results in the frequency (or wavelength) of the Stokes field: $\omega_{Stokes} = \omega_{pump} + \omega_{Stokes} - \omega_{pump}$. Whilst this equation appears to be null, it is, in essence, without resorting to a rigorous mathematical formalism, the most ingenuous method to show the energy flow/required photons of the spontaneous Raman process. Essentially, the interaction of the initial two photons with the material serve to create a coherence between the ground and vibrational state. The four photons involved in this optical process are indicative of the required order of non-linear optical susceptibility and, as such, it is possible to fully describe spontaneous Raman process via the third order non-linear susceptibility: $\chi^{(3)}$. As this is a resonant effect the resulting dependence is on the imaginary component of resonant third order susceptibility: $Im\left\{\chi^{R^{(3)}}\right\}$.

Appendix III

As the details of DQSI CARS, although similar, differ subtly from DSQI this appendix will broadly outline the method with particular emphasis on the role of the LO and removal of the NRB (the full method is available in reference 39). In DQSI CARS an externally generated LO (typically derived from a glass coverslip) takes the place of the reference beam in the vernacular of DQSI.

Without the use of any polarisation resolved detection (i.e. omitting the Wollaston prism), the detected spectral intensity resulting from the interference (using the apparatus shown in figure 3.5) between a LO field (E_{LO}) and the raw CARS field (E_{CARS}) with a temporal delay (τ) is described by the following equation:

$$I(\omega) = |E_{LO}(\omega)|^2 + |E_{CARS}(\omega)|^2 + 2|E_{LO}(\omega)E_{CARS}(\omega)| \cos\Phi(\omega)$$

Where the total phase difference between the arms is given by $\Phi(\omega) = \omega\tau + \phi_s(\omega) + \phi_{Inst}(\omega)$ with $\phi_s(\omega)$ and $\phi_{Inst}(\omega)$ corresponding to the phase difference introduced by the sample and the optical components respectively.

Employing a similar method to DQSI, whereby the CARS field signal is circularly polarised using a quarter waveplate prior to interference with the linearly polarised LO field and can, therefore, be thought of as a superposition of two orthogonal linearly polarised components, $[E_{CARS}(\omega), iE_{CARS}(\omega)]$. Detecting in two orthogonal polarisations (± 45° with respect to the linear polariser in the LO arm) by means of a Wollaston prism the intensities are given by:

$$I_1(\omega) = |E_{LO}(\omega)|^2 + |E_{CARS}(\omega)|^2 + 2|E_{LO}(\omega)E_{CARS}(\omega)| \cos\Phi(\omega)$$

$$I_2(\omega) = |E_{LO}(\omega)|^2 + |E_{CARS}(\omega)|^2 + 2|E_{LO}(\omega)E_{CARS}(\omega)| \sin\Phi(\omega)$$

As in DQSI the non-interferometric terms, ($|E_{LO}|^2 + |E_{CARS}(\omega)|^2$), maybe ascertained and subsequently removed by sequentially blocking each arm of the interferometer. By simply dividing the remaining interferometric terms and taking the arctangent it is possible to retrieve Φ:

$$\Phi(\omega) = \tan^{-1}\left(\frac{2|E_{LO}(\omega)E_{CARS}(\omega)| \sin\Phi(\omega)}{2|E_{LO}(\omega)E_{CARS}(\omega)| \cos\Phi(\omega)}\right)$$

In order to extract $\phi_s(\omega)$ from $\Phi(\omega)$ a reference spectral phase measurement (Φ_{ref}) is required to characterise the relative phase difference between the two arms not stemming from the sample (i.e. stemming from the individual optical components of each arm and the temporal delay between the beams):

$$\Phi_{\mathrm{ref}} = \omega\tau + \phi_{Inst}(\omega)$$

As phase imparted by the sample is a purely resonant effect by replacing the sample with a non-resonant analogue the reference spectral phase is readily obtained. A simple subtraction of the reference spectral phase from the total phase difference between the two arms yields the required $\phi_s(\omega)$.

As the phase contributions of the system and temporal delay between the beams have now been discounted it is possible to state the CARS intensity derived solely from the sample (E_{sample}) [88]:

$$I_{sample}(\omega) = |E_{LO}(\omega)|^2 + \left|E_{sample}(\omega)\right|^2 + 2E_{LO}(\omega)E_{sample}(\omega)$$

Given that the CARS process is proportional to the product of the incident fields, $E_{in}(\omega) = {E_p}^2(\omega)E_s^*(\omega)$, and the third order susceptibility it is possible to make the substitution $E_{sample}(\omega) \propto E_{in}(\omega)\,\chi^{(3)}$ into the above equation.

$$I_{sample}(\omega) = |E_{LO}(\omega)|^2 + \left|E_{sample}(\omega)\right|^2 + 2E_{LO}(\omega)E_{in}(\omega)\,\chi^{(3)}$$

$\chi^{(3)}$ can be expressed as [88]:

$$\chi^{(3)} = \left(\left[\chi^{NR(3)} + Re\left\{\chi^{R(3)}\right\}\right]\cos(\phi_s(\omega)) + \left[Im\left\{\chi^{R(3)}\right\}\right]\sin(\phi_s(\omega))\right)$$

The CARS intensity (stemming from the sample) can then be expressed in full as:

$$\begin{aligned} I_{sample}(\omega) = {} & |E_{LO}(\omega)|^2 + \left|E_{sample}(\omega)\right|^2 \\ & + 2E_{LO}(\omega)E_{in}(\omega)\left(\left[\chi^{NR(3)} + Re\left\{\chi^{R(3)}\right\}\right]\cos(\phi_s(\omega))\right. \\ & \left. + \left[Im\left\{\chi^{R(3)}\right\}\right]\sin(\phi_s(\omega))\right) \end{aligned}$$

As the values of $E_{LO}(\omega)$, $E_{sample}(\omega)$ and $\phi_s(\omega)$ are now explicitly known and $E_{NR}(\omega)$ can be ascertained from the non-resonant sample used to generate the reference spectral phase, it is now possible to isolate the real and imaginary components of the CARS spectrum as follows [39]:

$$\begin{aligned} Re\left\{\chi^{R(3)}\right\}: &\quad \left(\left|E_{sample}(\omega)\right|\cos(\phi_s(\omega)) - |E_{NR}(\omega)|\right) \\ Im\left\{\chi^{R(3)}\right\}: &\quad \left|E_{sample}(\omega)\right|\sin(\phi_s(\omega)) \end{aligned}$$

The retrieved $Im\left\{\chi^{R(3)}\right\}$, as previously stated in the main body of text, is directly proportional to the spontaneous Raman scattering intensity and, therefore, constitutes a complete NRB removal. In reality, prior to plotting the retrieved $Im\left\{\chi^{R(3)}\right\}$, a normalisation by $E_{LO}(\omega)$ is required. This pre-factor, which persists until this final normalisation, provides heterodyne amplification.

The use of PCF generated supercontinua are not suitable for DQSI CARS for two primary reasons. Firstly, as this technique requires sequential measurements from the sample and a non-resonant analogue (to determine the reference spectral phase) to be acquired, the system must be stabilised between measurements. Even in a carefully controlled environment, whether through thermal fluctuations causing opto-mechanical drift, or air currents, optical coupling into/out of a PCF is never entirely stable. Secondly, and more fundamentally, the myriad of processes by which a PCF generates a supercontinuum have a profound effect on the phase stability attained. The output of a PCF will typically have a very low degree of coherence (determined by autocorrelation): only retaining any significant level of coherence in the immediate vicinity of the pump wavelength [27]. An additional, though related, impediment exists for PCF in which the primary broadening mechanism is soliton fission (the majority of PCF used in CARS) as the process is essentially stochastic in nature leading to inherent 'shot-by-shot' fluctuation in both phase profile and spectral intensity (also resulting in a lower SNR CARS spectrum). It is, in principle, possible to partially circumvent this decoherence conundrum by employing a very short PCF (<2 cm^{-1} for a 100 fs pulses) or an exceptionally short pulse ($<<50$ fs); however, this is by no means an elementary practical feat [27].

As this technique is intrinsically dependent on a coherent phase relationship between the LO and the CARS signal (efficient CARS generation also relies on intra-pulse coherence), in addition to an exceptionally high stability requirement, this prevents the use of PCF generated supercontinua [39].

Appendix IV

For completeness the sum signal, $\sum S = S_+ + S_-$, is shown to have an equivalent form to a conventional CARS signal, which for convenience is restated here:

$$I_{CARS} \propto |\chi|^2 \propto |\chi^R|^2 + 2\chi^{NR} Re\{\chi^R\} + (\chi^{NR})^2$$

As previously derived the SIPCARS sum signal is:

$$\sum S \propto \left(P_x P_x^* + P_y P_y^*\right)$$

Taking each of the terms separately, substituting in equations 31 and 32, and separating into resonant and non-resonant components produces the following expressions:

$$P_x P_x^* = \frac{1}{2}\left(\chi^R_{1111}{\chi^R_{1111}}^* + \chi^R_{1111}{\chi^{NR}_{1111}}^* + \chi^{NR}_{1111}{\chi^R_{1111}}^* + \chi^{NR}_{1111}{\chi^{NR}_{1111}}^*\right) I_P^2 I_s$$

$$P_y P_y^* = \frac{1}{2}\left(\chi^R_{2112}{\chi^R_{2112}}^* + \chi^R_{2112}{\chi^{NR}_{2112}}^* + \chi^{NR}_{2112}{\chi^R_{2112}}^* + \chi^{NR}_{2112}{\chi^{NR}_{2112}}^*\right) I_P^2 I_s$$

Noting that χ^{NR} is a purely real quantity and making use of the identity $z + z^* = 2\,Re\{z\}$ these expressions can be simplified to:

$$P_x P_x^* = \frac{1}{2}\left[\left|\chi^R_{1111}\right|^2 + 2\chi^{NR}_{1111} Re\{\chi^R_{1111}\} + (\chi^{NR}_{1111})^2\right] I_P^2 I_s$$

$$P_y P_y^* = \frac{1}{2}\left[\left|\chi^R_{2112}\right|^2 + 2\chi^{NR}_{2112} Re\{\chi^R_{2112}\} + (\chi^{NR}_{2112})^2\right] I_P^2 I_s$$

At this stage it is pertinent to consider the value of $\sum S$ in a non-resonant region where χ^R is equal to zero. In this regime the sum signal reduces to:

$$\sum S \propto \frac{1}{2}[(\chi^{NR}_{1111})^2 + (\chi^{NR}_{2112})^2]\, I_P^2 I_s$$
$$\propto \frac{1}{2}\left[(\chi^{NR})^2 + \left(\frac{\chi^{NR}}{3}\right)^2\right] I_P^2 I_s \propto \frac{5}{9}(\chi^{NR})^2\, I_P^2 I_s$$

As the value of $\sum S \propto \chi^{NR}$ in a non-resonant region, this allows SIPCARS to be self-calibrating in the sense that spatial variations of the non-resonant $\chi^{(3)}$ can always be normalised if the spectrum contains a non-resonant region.

If resonant component of $\chi^{(3)}$ is included, the derivation proceeds as follows:

$$P_x P_x^* = \frac{1}{2}\,|\chi_{1111}|^2\, I_P^2 I_s$$

$$P_y P_y^* = \frac{1}{2}\,|\chi_{2112}|^2\, I_P^2 I_s$$

$$\sum S \propto (|\chi_{1111}|^2 + |\chi_{2112}|^2) I_P^2 I_s$$

The first term of this expression is equivalent to the signal detected in a conventional CARS experiment whilst the second term stems from the additional polarisations probed in SIPCARS.

Appendix V

$Im\{\chi^R_{1111}\,\chi^R_{2112}{}^*\} = 0$

As χ^R_{1111} and $\chi^R_{2112}{}^*$ correspond to (resonant) tensor elements of the same resonance it follows that the resonant frequency and line widths should be the same.

A CARS resonance takes the following form:

$$\chi^R_{ijkl} = \frac{A_{ijkl}}{\Omega - \Delta\omega - i\Gamma}$$

where A is the amplitude, Ω is the resonant frequency, $\Delta\omega = \omega_p - \omega_s$ is the detuning from the resonant frequency and Γ is the linewidth all of which are purely real quantities. The produce of $\chi^R_{1111}\,\chi^R_{2112}{}^*$ can therefore be written as:

$$\chi^R_{1111}\,\chi^R_{2112}{}^* = \frac{A_{1111}}{\Omega - \Delta\omega - i\Gamma} \times \frac{A_{2112}}{\Omega - \Delta\omega + i\Gamma}$$

At the resonant frequency, i.e. no detuning ($\Omega - \Delta\omega = 0$), the above equation simplifies to:

$$\chi^R_{1111}\,\chi^R_{2112}{}^* = -\frac{A_{1111}}{i\Gamma} \times \frac{A_{2112}}{i\Gamma}$$
$$= \frac{A_{1111}\,A_{2112}}{\Gamma^2}$$

This quantity is purely real and thus the imaginary component is zero.

$Im\{\chi^R_{1111}\,\chi^R_{2112}{}^*\} = 0$

Appendix VI

In this appendix I hope to give a description of the SIPCARS theory, forgoing the normal mathematical approach, for a more elucidatory explanation that should be accessible to a wider, less specialist, audience. This is not designed to be entirely rigorous but to give a simplified view of the concept as a whole.

It is first necessary to give a description of resonance. This ubiquitous natural phenomenon can be best explained by taking an example. If a slowly oscillating force is applied to a young tree approximately half way up the trunk initially both the trunk and the head of the tree will move simultaneously: in phase. As the frequency of oscillation increases so the head of the tree will start to lag behind the trunk until the resonant frequency is reached at which point the head of the tree will be a quarter of a complete cycle (90° or $\pi/2$) behind the applied driving force. This effect is true irrespective of size or constituent components. In the case of Raman scattering the driving force is the lasers incident on the sample and the oscillating bodies are molecular bonds.

An important thing to note is that this is an effect of 'damped' harmonic oscillators. In an undamped system the motion of the oscillating body will be in phase with the driving force independent of the frequency of oscillation.

It is instructive to plot this effect on an Argand diagram as this highlights that fact that the resonant response, shifted by $\pi/2$ with respect to the driving force, is aligned along the imaginary axis (figure A1a). In other words the CARS signal stemming from resonances within the sample corresponds to the imaginary component while other contributions are from unwanted non-resonant processes.

Whilst normal conventional CARS using two (or three) linearly polarised beams results in spectra that contain a NRB (which has to be removed by complex post-processing), SIPCARS, using a circularly polarised Stokes and a linearly polarised pump/probe beam, exploits the phase shift at resonance to automatically remove the NRB.

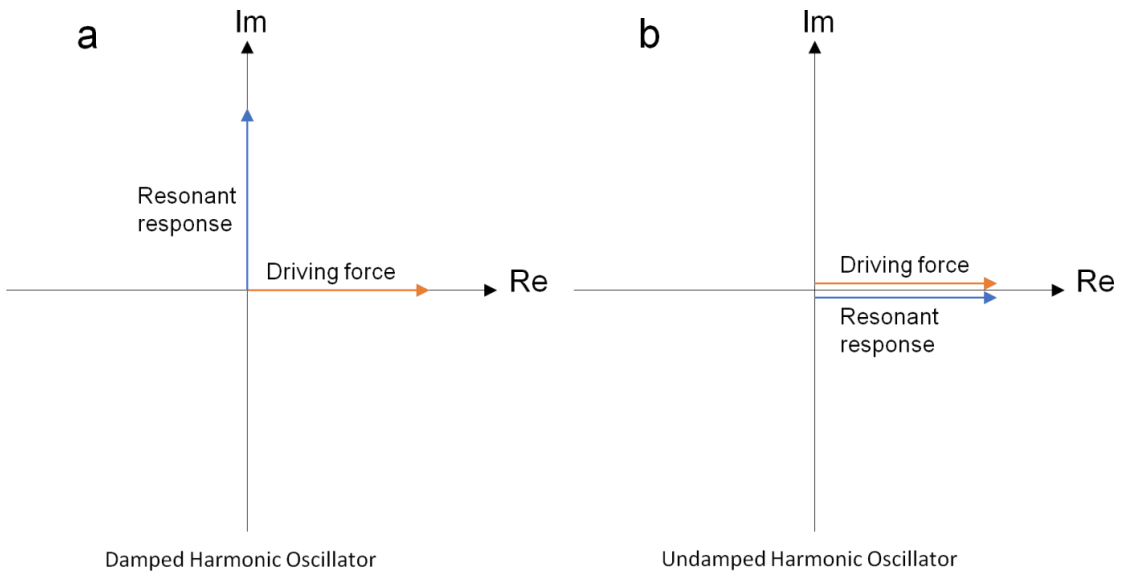

Figure A1: Argand diagrams showing the driving force, in red, and the resultant resonant response in blue, for a) a damped harmonic oscillator and b) an undamped harmonic oscillator.

It is important to emphasize that the NRB (figure A1b) can be thought of as an undamped harmonic oscillator (as it consists of four wave mixing processes that do not coincide with any real energy levels within the molecule).

The automatic NRB removal mechanism of SIPCARS can best be explained by considering a right-handed circularly polarised Stokes beam, figure A2a, which may be envisaged as a clockwise corkscrew proceeding along the direction of travel of the beam, and a pump/probe beam polarised along the x axis. When the driving force, the Stokes beam polarisation in this case, is aligned along the S_- axis any resonant (imaginary) signal will lag in phase by $\pi/2$ and align along the S_+ axis whilst the non-resonant (real) signal will follow the driving force and is consequently aligned along the S_- axis. A similar effect occurs when the driving force is along S_+ however, in this case, the resonant (imaginary) signal is aligned along the negative S_- axis which is equivalent to the negative resonant (imaginary) signal aligning along the S_- (these effects can be clearly seen in figure A2b). The resulting signal along each axis is then:

$$\text{Along } S_+ : \; NRB\ signal\ (real) + \text{Resonant } signal\ (imaginary)$$

$$\text{Along } S_- : \; NRB\ signal\ (real) - \text{Resonant } signal\ (imaginary)$$

After which a simple subtraction of these signals leads to the SIPCARS signal that contains only the resonant (imaginary) components.

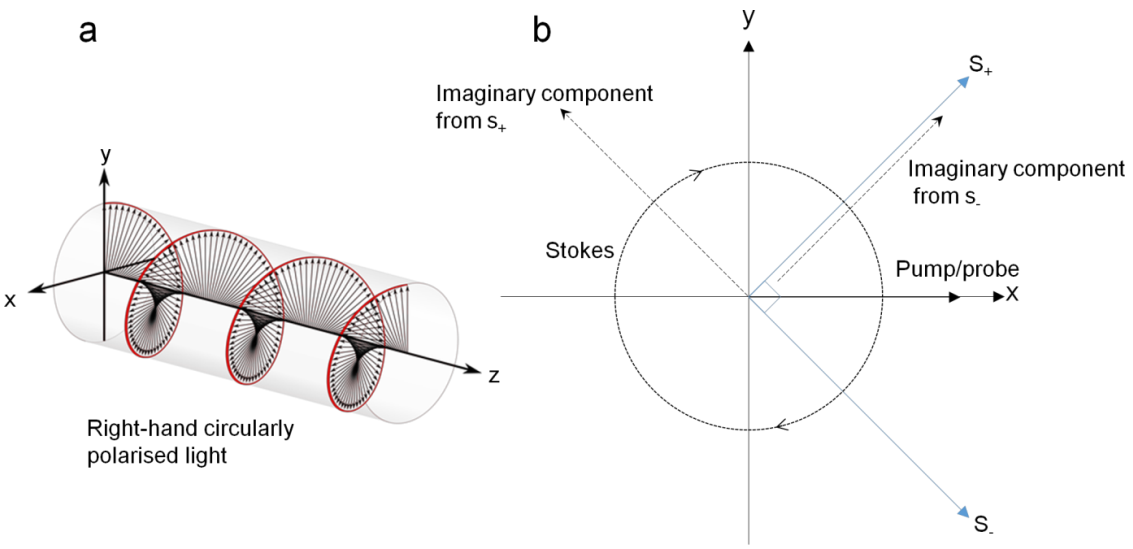

Figure A2: a) diagrammatical representation of right-hand circularly polarised light where the beam is travelling along the z axis and the small arrows denote the direction of polarisation at any given moment. b) Polarisations for SIPCARS where the dashed circle represents the circularly polarised Stokes beam and the solid line along the x axis denotes the linearly polarised pump/probe beam. The blue arrows are the directions along which the signals (S_+ and S_-) are collected and the dashed arrows indicate the direction and origin of the imaginary components.

In addition to the above description a note on how to interpret the, somewhat dense, tensor notation used in the main body of text, and many of the other appendices, is included here. As before this is far from being a comprehensive instruction on tensor notation: just serving as a specific aide to understanding the notation used within this thesis.

$$\chi_{ijkl} = \chi_{anti-Stokes;\, pump,probe,Stokes}$$

As stated in the main text the tensor components *ijkl* correspond to the detected and incident beams. These components may take the value one, two or three; the permutation of which specifies a particular element within the 81 element $\chi^{(3)}$ tensor. It may, however, be easier when reading the derivations in this thesis to think of the components 1, 2 and 3 as corresponding to the Cartesian axes x, y and z respectively. Note that in this thesis the z axis (component 3) does not feature as it is the direction of propagation.

$$\chi_{1111} = \chi_{xxxx}$$

$$\chi_{1221} = \chi_{xyyx}$$

$$\chi_{2211} = \chi_{yyxx}$$

For example if the tensor element χ_{1221} is considered this may be interpreted as the value of the $\chi^{(3)}$ tensor when the polarisations of the anti-Stokes and Stokes are aligned along the x axis and the pump/probe aligned along the y axis. A full treatise on tensor notation and specifically its application to non-linear optics can be found in reference [66].

Appendix VII

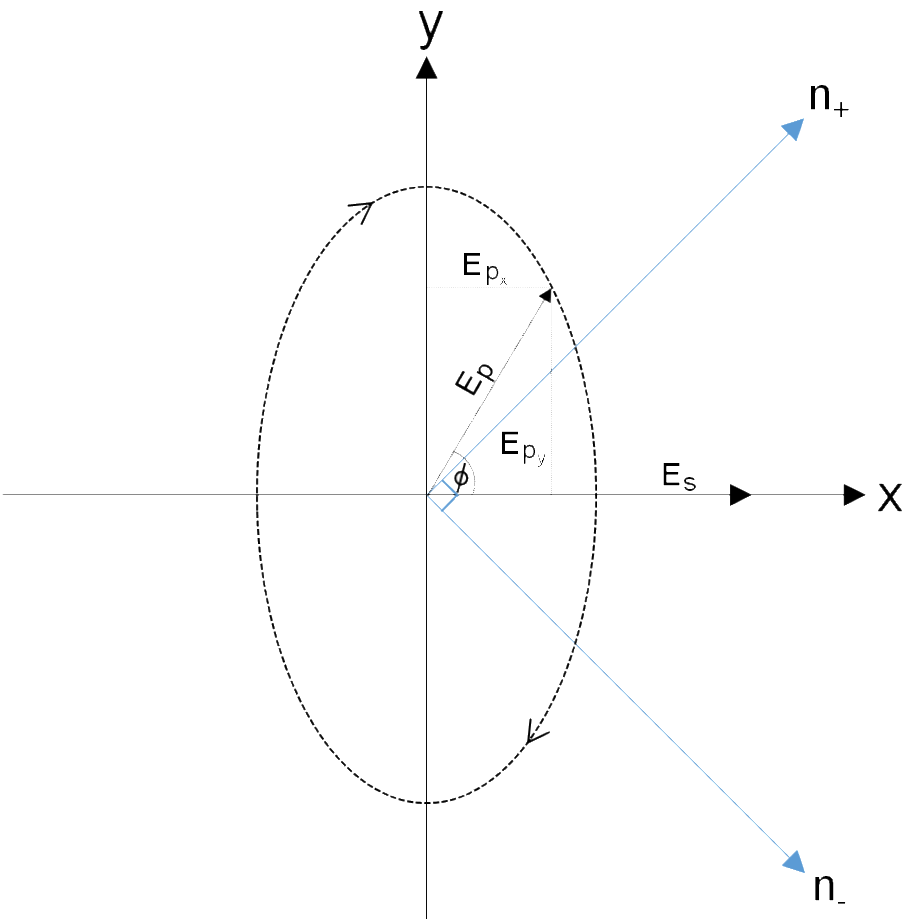

Figure A3: Polarisations for SIPCARS with a linearly polarised Stokes, E_s, beam and a right-hand elliptically polarised (degree of ellipticity characterised by ϕ) pump/probe beam, E_p, ($E_{p_x}$and E_{p_y} are the orthogonal components of E_p) indicated by the dashed circle. Detection is performed along the n_+ and n_- axis (orthogonal blue lines).

This derivation is true to the actual experimental procedure utilizing a linearly polarised Stokes beam and a right-hand elliptically polarised pump/probe beam: as depicted in figure A3. The ellipticity of the pump/probe beam is characterised by ϕ. As per the previous, simplified, derivation, using a circularly polarised Stokes beam, the elliptically polarised pump/probe beam can be decomposed into orthogonal components: $E_{p_x}$and E_{p_y}. These can be simply expressed as:

$$E_{p_x} = E_p \cos\phi \qquad \& \qquad E_{p_y} = iE_p \sin\phi$$

It is then possible to express E_{p_y} as a function of E_{p_x}:

$$E_{p_y} = iE_p \sin\phi = i\left(E_{p_x}/\cos\phi\right)\sin\phi$$
$$= i\tan\phi\ E_{p_x}$$

Substituting k, where $k = \tan\phi$, into the previous equation yields:

$$E_{p_y} = ikE_{p_x}$$

Subsequently the expressions for the induced polarisations P_{x} and P_{y} are:

$$\begin{aligned} P_{\mathrm{x}} &= \chi_{1111}\, {E_{p_x}}^2\, E_s^* \;+\; \chi_{1221}\, {E_{p_y}}^2\, E_s^* \\ &= \chi_{1111}\, {E_{p_x}}^2\, E_s^* \;+\; i^2\, k^2\, \chi_{1221}\, {E_{p_x}}^2\, E_s^* \\ &= (\chi_{1111} - k^2\chi_{1221})\, {E_{p_x}}^2\, E_s^* \end{aligned}$$

$$\begin{aligned} P_{\mathrm{y}} &= \chi_{2121}\, E_{p_x} E_{p_y}\, E_s^* \;+\; \chi_{2211}\, E_{p_y} E_{p_x}\, E_s^* \;+ \\ &\quad \chi_{2221}\, {E_{p_y}}^2\, E_s^* + \chi_{2111}\, {E_{p_x}}^2\, E_s^* \\ &= \chi_{2121}\, E_{p_x} E_{p_y}\, E_s^* \;+\; \chi_{2211}\, E_{p_x} E_{p_y}\, E_s^* \\ &= (\,\chi_{2121} \;+\; \chi_{2211})\, i\, k\, {E_{p_x}}^2\, E_s^* \end{aligned}$$

From equation 38:

$$\Delta S \propto \left(P_x P_y^* + \left(P_x P_y^*\right)^*\right)$$

Taking each of these terms separately:

$$\begin{aligned} P_x P_y^* &= \left[(\chi_{1111} - \, k^2\chi_{1221})\, {E_{p_x}}^2\, E_s^*\right]\left[(\,\chi_{2121} \;+\; \chi_{2211})\, i\, k\, {E_{p_x}}^2\, E_s^*\right]^* \\ &= -(\chi_{1111}\, \chi_{2121}^* + \chi_{1111}\, \chi_{2121}^* - \, k^2\chi_{1221}\, \chi_{2121}^* \;-\; k^2\chi_{1221}\, \chi_{2211}^*)i\, k\;\; {I_{p_x}}^2\, I_s \\ &= [\,-i\, k\, (\chi_{1111}\, \chi_{2121}^* + \chi_{1111}\, \chi_{2121}^*) + \; ik^3(\chi_{1221}\, \chi_{2121}^* + \; \chi_{1221}\, \chi_{2211}^*)]\;\; {I_{p_x}}^2\, I_s \end{aligned}$$

$$\left(P_x P_y^*\right)^* = [i\, k\, (\,\chi_{1111}^*\, \chi_{2121} + \chi_{1111}^*\, \chi_{2121}) - \; ik^3(\chi_{1221}^*\, \chi_{2121} + \; \chi_{1221}^*\, \chi_{2211})]\;\; {I_{p_x}}^2\, I_s$$

Recombining these two terms and rearranging to group similar powers of *k* together, results in the following:

$$\Delta S \;\propto \underbrace{i\, k\, [\,(\,\chi_{1111}^*\, \chi_{2121} + \chi_{1111}^*\, \chi_{2121}) \;-\; (\chi_{1111}\, \chi_{2121}^* + \chi_{1111}\, \chi_{2121}^*)\,]\; {I_{p_x}}^2\, I_s}_{\textit{Part A}}$$

$$+ \underbrace{i\, k^3\, [(\chi_{1221}\, \chi_{2121}^* + \; \chi_{1221}\, \chi_{2211}^*) \;-\; (\chi_{1221}^*\, \chi_{2121} + \; \chi_{1221}^*\, \chi_{2211})]\; {I_{p_x}}^2\, I_s}_{\textit{Part B}}$$

Once again separating this equation into two individually parts, *A* and *B*, rearranging into the required form and applying the identity $z - z^* = 2i\,Im\{z\}$ it is possible to significantly simplify ΔS.

$$\begin{aligned} Part\ A &= i\,k\,[\,(\,\chi^*_{1111}\,\chi_{2121} + \chi^*_{1111}\,\chi_{2121}) - (\chi_{1111}\,\chi^*_{2121} + \chi_{1111}\,\chi^*_{2121})\,] \\ &= -i\,k\,[(\chi_{1111}\,\chi^*_{2121} + \chi_{1111}\,\chi^*_{2121}) - (\,\chi^*_{1111}\,\chi_{2121} + \chi^*_{1111}\,\chi_{2121})\,] \\ &= 2k\,Im\{\chi_{1111}\,\chi^*_{2121} + \chi_{1111}\,\chi^*_{2121}\} \end{aligned}$$

$$\begin{aligned} Part\ B &= i\,k^3\,[(\chi_{1221}\,\chi^*_{2121} + \chi_{1221}\,\chi^*_{2211}) - (\chi^*_{1221}\,\chi_{2121} + \chi^*_{1221}\,\chi_{2211})] \\ &= -i\,k^3\,[(\chi^*_{1221}\,\chi_{2121} + \chi^*_{1221}\,\chi_{2211}) - (\chi_{1221}\,\chi^*_{2121} + \chi_{1221}\,\chi^*_{2211})] \\ &= 2k^3\,Im\{\chi^*_{1221}\,\chi_{2121} + \chi^*_{1221}\,\chi_{2211}\} \end{aligned}$$

This results in the following expression for ΔS:

$$\Delta S \propto 2\,(k\,Im\{\chi_{1111}\,\chi^*_{2121} + \chi_{1111}\,\chi^*_{2121}\} + k^3\,Im\{\chi^*_{1221}\,\chi_{2121} + \chi^*_{1221}\,\chi_{2211}\})\,{I_{p_x}}^2\,I_s$$

As before, under the assumption of an isotropic medium, this equation can be further simplified to:

$$\begin{aligned} \Delta S &\propto 2\,(k\,Im\{\chi_{1111}\,(\chi^*_{2121} + \chi^*_{2121})\} + k^3\,Im\{\chi^*_{1221}\,(\chi_{2121} + \chi_{2211})\})\,{I_{p_x}}^2\,I_s \\ &\propto 2\,(k\,Im\{\chi_{1111}\,(\chi^*_{1111} - \chi^*_{1221})\} + k^3\,Im\{\chi^*_{1221}\,(\chi_{1111} - \chi_{1221})\})\,{I_{p_x}}^2\,I_s \\ &\propto 2\,(k\,Im\{\underbrace{(\chi_{1111}\,\chi^*_{1111}}_{\text{Real}} - \chi_{1111}\,\chi^*_{1221})\} + k^3\,Im\{(\chi^*_{1221}\chi_{1111} - \underbrace{\chi^*_{1221}\,\chi_{1221}}_{\text{Real}})\})\,{I_{p_x}}^2\,I_s \end{aligned}$$

The indicated terms are purely real and as such equal to zero, therefore:

$$\begin{aligned} \Delta S &\propto 2\,(-k\,Im\{\,\chi_{1111}\,\chi^*_{1221}\} + k^3\,Im\{\chi^*_{1221}\chi_{1111}\})\,{I_{p_x}}^2\,I_s \\ &\propto (k^3 - k)\,Im\{\,\chi_{1111}\,\chi^*_{1221}\}\,{I_{p_x}}^2\,I_s \end{aligned}$$

This equation is identical to equation 39 with the exception of the pre-factor $(k^3 - k)$ therefore, without the need for further derivation, it is possible to state:

$$\Delta S \propto (k^3 - k)\,(1 - 3\rho)\,\chi_{NR}\;Im\{\,\chi^R_{1111}\}\;{I_{p_x}}^2 I_s$$

Given that this pre-factor is for the pump/probe beam solely aligned along the x axis it is necessary to convert this to the general form allowing for the full range of beam ellipticities. As previously stated $E_{p_x} = E_p\,\cos\phi$ therefore:

$$I_{p_x}{}^2 = I_p{}^2 \cos^4\phi$$

Considering this the pre-factor becomes $(k^3 - k)\cos^4\phi$ which can be simplified as follows:

$$\begin{aligned}
(k^3 - k)\cos^4\phi &= (\tan^3\phi - \tan\phi)\cos^4\phi \\
&= \left(\sin^3\phi \Big/ \cos^3\phi - \sin\phi\cos^2\phi \Big/ \cos^3\phi\right)\cos^4\phi \\
&= \left[(\sin^3\phi - \sin\phi\cos^2\phi) \Big/ \cos^3\phi\right]\cos^4\phi \\
&= (\sin^3\phi - \sin\phi\cos^2\phi)\cos\phi \\
&= (\sin^2\phi - \cos^2\phi)\sin\phi\cos\phi \\
&= (2\sin^2\phi - 1)\sin\phi\cos\phi \\
&= -\cos 2\phi \ \sin\phi \ \cos\phi \\
&= -\frac{1}{2}(\cos 2\phi \ \sin 2\phi) \\
&= -\frac{1}{4} \ \sin 4\phi
\end{aligned}$$

Therefore for an elliptical pump/probe beam and a linear Stokes beam:

$$\Delta S \propto \sin 4\phi \ (1 - 3\rho)\, \chi^{NR}\, Im\{\chi^R_{1111}\} \ I_{p_x}{}^2 I_s$$

It is important to consider two implications of this result. Firstly, when the pump/probe beam is circularly polarised, i.e. $\phi = \frac{\pi}{4}$, the resulting SIPCARS signal is zero. In this regime both the sum and SIPCARS signals are zero resulting in a null spectrum. The second regime in need of consideration is when $\sin 4\phi = 1$ which occurs at $\phi = \frac{\pi}{8}$ and $\phi = \frac{3\pi}{8}$. In terms of the experimental setup these two conditions correspond to the major axis of the pump/probe ellipse aligned parallel and perpendicular to the Stokes linear polarisation respectively. Whilst complete NRB removal is guaranteed for either of these conditions and the intensity of the SIPCARS signal is equivalent, the noise floors differ. A full derivation of this is given in the supplementary info of [118] however considering $\sqrt{\sum S\left(\frac{\pi}{8}\right)} > \sqrt{\sum S\left(\frac{3\pi}{8}\right)}$ (where the $\sqrt{\sum S(\phi)}$ is a measure of the noise floor) the higher SNR regime is when $\phi = \frac{3\pi}{8}$.

The most important combinations of pump/probe and Stokes beam polarisations have been addressed however for the interested reader a full derivation with arbitrary pump/probe and Stokes ellipticities is given in the supplementary info of [118]. The final result of which is:

$$\Delta S \propto (\sin 4\phi + \sin 2\theta + \sin 2\theta \cos 4\phi)\,(1 - 3\rho)\, \chi^{NR}\, Im\{\chi^R_{1111}\} \ I_{p_x}{}^2 I_s$$

Appendix VIII [66] [98] [99]

There exists an approximate proportionality between the $\chi^{NR(3)}$ and linear refractive index (n_0). The empirical Miller's rules state that:

$$\chi^{(3)} \propto \left(\chi^{(1)}\right)^3$$

Given that:

$$n_0{}^2 = 1 + Re\{\chi^{(1)}\}$$

From which it is a reasonable conclusion that the real $\chi^{NR(3)}$ is approximately proportional to the linear refractive index

$$\chi^{NR(3)} \propto (n_0)^6$$

Although this is based on an empirical rule, in view of the typical components found in bead/biological samples and over the wavelength range considered, it is approximately correct.

In essence the χ^{NR} normalisation image provides an approximate map of the refractive index of the sample. By extension, contrast is provided by differences in optical path length through the sample: analogous to DIC microscopy.

Appendix IX

Lenses: 1.3 NA (oil immersion)			**NB.** NA = n sin(α)	
Immersion oil ref. index: 1.510			**NB.** λ = λ_0/n	
α calculated fron native NA and Immersion oil ref. Index				
α (degrees)=	59.42			
α (radians)=	1.037			
x,y resol. d = 1.22λ_o/(2NA) n			Assuming α from above	
z resol. d = 2λ_o/n^2sin^2(α)	or d = 2λ_o/(NA)^2	where λ_o = 785nm		
Sample	**Concentration (moles dm^{-3})**	**Molecular weight (g/mole)**	**Density (@25 deg) g/ml (unless solid)**	
Water (H2O)	Pure (dionised)	18.02	1.000	
Carbon Disulphide (CS2)	Pure (anhydrous)	76.14	1.266	
Toluene (C7H8)	Pure (anhydrous)	92.14	0.865	
Sapphire (Al2O3)	Pure (solid)	101.96	4.000	g/cm^3
Immersion oil	-	-	-	
Glass	Mixture (solid) - (see below)	67.3	2.51	g/cm^3
Glass composition	**%**	**Molecular weight (g/mole)**		
SiO2	64.0	60.084		
B2O3	8.4	69.620		
Al2O3	4.2	101.961		
Na2O	6.4	61.979		
ZnO	5.9	81.379		
TiO2	4.0	79.855		
K2O	6.9	94.196		
Sb2O3	0.1	291.518		
Glass		67.3		
Sample	**Refractive index (RT.)**	**x,y resolution (nm)**	**z resolution (nm)**	**Focal volume (μm^3)**
Water (H2O)	1.3290	314.9	1199.3	0.3737
Carbon Disulphide (CS2)	1.6058	215.7	821.5	0.1201
Toluene (C7H8)	1.4865	251.7	958.6	0.1908
Sapphire (Al2O3)	1.7603	179.5	683.6	0.0692
glass	1.5104	243.8	928.5	0.1734
No. of Molecules in the focal vol				
Sample	**molecules in focal volume**	**Normalised wrt water**		
Water (H2O)	1.25E+10	1		
Carbon Disulphide (CS2)	1.20E+09	0.096271637		
Toluene (C7H8)	1.08E+09	0.086378302		
Sapphire (Al2O3)	1.63E+09	0.130903445		
glass	3.89E+09	0.311616627		